Extreme ultraviolet frequency combs for precision measurement and strong-field physics

by

Craig Benko

BS, Santa Clara University, 2010

A thesis submitted to the

Faculty of the Graduate School of the

University of Colorado in partial fulfillment

of the requirements for the degree of

Doctor of Philosophy

Department of Physics

2016

This thesis entitled:
Extreme ultraviolet frequency combs for precision measurement and strong-field physics
written by Craig Benko
has been approved for the Department of Physics

Prof. Jun Ye

Prof. John L. Hall

Date

The final copy of this thesis has been examined by the signatories, and we find that both the content and the form meet acceptable presentation standards of scholarly work in the above mentioned discipline.

Benko, Craig (PhD, Physics)

Extreme ultraviolet frequency combs for precision measurement and strong-field physics

Thesis directed by Prof. Jun Ye

The extreme ultraviolet (XUV) is a relatively unexplored spectral region for high-resolution laser spectroscopy. Many atomic and molecular systems of fundamental interest lie in wait of investigation, but the lack of highly coherent sources has forgone the ability to experiment. The XUV frequency comb offers exciting new frontiers for fundamental physics and measurement science by enabling direct and highly coherent laser access to the XUV. Prior to 2012, our group demonstrated the best levels of phase coherence in the XUV at the 10 MHz level and the most powerful XUV light source originating from high-order harmonic generation with powers of 220 μW/harmonic. The work in this thesis improves upon both of these metrics demonstrating coherence at the 62.5 mHz level (eight orders of magnitude improvement) and power levels approaching 1 mW/harmonic (five times improvement). Our work shows that it is possible to produce XUV light with coherence properties that rival that of visible light using the high-order harmonic generation process.

Leveraging XUV frequency comb technology, we also extend the work to probe strong field physics in atomic and molecular systems. We use the phase stable light produced during high-order harmonic generation to probe attosecond phenomena in atoms manifested in the intensity dependent dipole phase. We also study strong-field light-matter interactions in molecular systems. Using our femtosecond enhancement cavities, we perform field-free molecular alignment at unprecedented repetition rates. This allows for a sensitive study of the strong-field interaction and allows the high-order harmonic generation process to be performed in an aligned molecular target.

As XUV frequency comb technology continues to mature, further gains in power levels are anticipated. Additional applications in high-resolution spectroscopy, strong-field physics, solid-state physics, and laser science will come to fruition.

Dedication

Briefly, you can only find truth with logic if you have already found truth without it.

–G. K. Chesterton

To my parents, for never ceasing to love and support me.

To my wife, for helping me keep my head on straight and always reminding me of what is truly most important.

To Gram, for always being there for me (even when we were miles apart). I hoped dearly you would see me finish, but I rest assured that you do indeed know and are at peace.

Acknowledgements

First and foremost, I need to thank my parents, Randy and Kay Lynn, for their continual sacrifice on behalf of myself and my education. I am also very thankful when they did not panic when I decided to switch from engineering to physics and for trusting me that I was making the right decision. I also have to thank them for not being too suspicious for passing up graduate school at a fancy east coast school to attend the University of Colorado. But, I think they would agree that I made the right choice and I would do it again in less than a femtosecond (if you could possibly make a decision that fast).

Santa Clara University made every effort to ensure my future success as a physicist. While the entire physics department deserves my thanks, two in particular stand out. A special thanks to Betty Young for giving me my first job in a lab. But possibly more important, she selflessly teamed me up with, then a brand new, professor Chris Weber. I cannot thank Betty enough for setting me up to work with Chris as it would mark the point at which I became addicted to working with lasers. And to Chris, thanks for showing me how to build an experiment and be a physicist. I still do not completely understand how effortless it seemed for him to let me just start getting my hands dirty building the lab's first Ti:Sapphire and constructing the rest of the apparatus. I still try to recall how he guided me along when I find myself in similar situations. His patience and instruction are nearly unrivaled. I am ever grateful for him showing me how cool lasers are, for stretching the lab budget to take me to a Gordon conference, for taking me up to see a beamtime at the ALS, for all the help in applying for graduate school, and for being a great friend along the way. I also have to thank my first lab mate, Dustin Ngo. It always seemed like he was a few steps ahead of

my understanding of things. I owe a lot of my success to his help. I will never forget some of our adventures outside of lab, especially sitting on the top of Half Dome. It is also hard to believe our first experiment worked as well as it did, considering a $50 chunk of copper almost broke the budget.

It is hard to imagine where I would be if Jun Ye did not give me the opportunity to join his group back in 2010. He graciously offered me a position on the strontium experiments even though I might have had my heart set on the XUV frequency comb experiment. Walking in to Jun's lab for the first time was certainly intimidating, but Jun was very welcoming and enthusiastic. It was very easy to feel right at home amongst what might look like total chaos to the casual observer. However, as I would quickly learn, it was far from chaos but a living and breathing lab battling at the forefront of what is experimentally possible. The lab he has nurtured is unrivaled in breadth and ability, a strong testament to his ability as a leader and a scientist.

I think one of the most important and beneficial decisions Jun has made on my behalf was when upon my arrival he partnered me with a senior graduate student Michael Martin. My early days in the lab were spent under Mike's guidance. He was wonderfully patient and a great experimentalist. Hopefully some of it rubbed off, but, as Mike would probably agree, maybe not his lab notebook practices. My first couple years were spent on the not-so-glamorous aspects of trying to build the most stable laser in the world, but it was certainly a good way to build up experimentalist chops. And, as it would turn out, that laser ended up being pretty good with all due credit going to Mike. I think my time working with Mike ultimately gave me the confidence to ask Jun if I could take over the XUV frequency comb experiment, my first interest in Jun's lab. Jun graciously agreed and I would depart from my short tenure on the strontium experiment to venture off into the XUV.

I would be remiss if I did not acknowledge the fellow strontium-ites I worked with during my time on the experiment. To Michael Bishof, for keeping the work lighthearted without ever losing the ability to be productive. And for welcoming me into the Knights (you still owe me a sword fight). To Matthew Swallows, for answering all my atomic physics questions almost effortlessly and without getting too grumpy. And to Yige Lin, for being one of the nicest people to work along side.

I am only sorry I did not get to overlap with him more.

Making the jump from the strontium experiments to the XUV frequency comb could have been a disaster if it were not for Thomas Allison, Arman Cingöz, and Dylan Yost to welcome me. Unfortunately, my time with Dylan was brief, but it was nevertheless productive. He was able to explain things with great clarity and his ability approach an experimental problem and immediately see the solution was uncanny. Even in his absence, I regularly benefited from his time on the experiment. Arman was also a great labmate and probably the only one I have had that thoroughly documents his electronics. He was always willing to patiently help me. I still do not think I can wipe the cavity's . . . well you know . . . as well as he could. I overlapped with Tom the longest. I will not forget how we fought to his very last day in lab to see a heterodyne beat deep in the XUV and sure enough we saw it on his last day. It certainly was not for lack of trying or lack of singing "Beat It" [1] to coax it out of the machine. Even after leaving JILA, Tom was always one of my most useful resources and he was always available to help. For that, I am very grateful.

The second and third wave of post docs have also been a great help. François Labaye is owed a great deal of thanks for battling with the fiber broadening and nonlinear pulse compression. Linqiang Hua was always willing to work hard and learn the experiment. He certainly made data taking possible and he was the first one brave enough to start putting molecules in the cavity for HHG. Nadine Dörre was a visitor for only a brief amount of time, but she was instrumental in improving the XUV comb flux by nearly 5×. I think some of the tricks we learned will even become commonplace in future XUV combs. The newest arrivals are Gil Porat, Stephen Schoun, and Christoph Heyl. The experiment will be in good hands as they push to turn the XUV comb into a soft x-ray comb (and possibly come up with a more clever name).

A special thanks is due to our collaborators at IMRA. Ingmar Hartl, Axel Ruehl, and Martin Fermann delivered an excellent laser that I had the pleasure of using extensively. Ingmar and Axel continue to be a great resource and I am indebted to their hospitality during a visit to their new home at DESY in Hamburg, Germany.

[1] While it was an earnest attempt to sing the popular song, the rendition certainly qualifies as a "Tom original".

Of course, I would like to thank the rest of the Ye lab team, especially the Mid-IR guys who were the XUV team's companions in the weekly group meeting. A special thanks to Jan Hall who is probably the lab's greatest treasure. He has helped the XUV experiment and myself in more ways than one. He always brought a smile to lab (along with the Peanuts lunch box) and he was always willing to share his knowledge of all things lasers, RAM, and what often seemed like pure wizardry. Attempting to mention everyone else that I have worked with will certainly end in failure. Nevertheless, you know who you are and for all the help you have given me along the way, I am very thankful.

A final acknowledgment is to my wonderful wife Monica. I owe a great deal of my sanity to her constant love and support. It is funny how life happens, but I never anticipated moving to Colorado for graduate school only to find my best friend out in Wyoming. I cannot wait for what comes next.

Contents

Chapter

1 Extreme ultraviolet frequency combs **1**

1.1 Introduction . . . 1

1.2 Optical frequency combs . . . 9

1.2.1 Carrier-envelope offset frequency detection and measurement . . . 10

1.2.2 Frequency comb stabilization . . . 12

1.2.3 Frequency comb performance characterization . . . 18

1.3 Extreme ultraviolet frequency combs . . . 20

1.4 Applications . . . 23

1.4.1 Spectroscopic applications . . . 23

1.4.2 High-flux extreme ultraviolet source applications . . . 25

1.5 Thesis outline . . . 26

2 Experimental apparatus **27**

2.1 Amplifying ultrafast laser pulses . . . 27

2.2 The femtosecond enhancement cavity . . . 28

2.2.1 Cavity finesse, buildup, and contrast . . . 30

2.2.2 Gaussian beams and gaussian beam manipulation . . . 35

2.2.3 Cavity geometry . . . 38

2.2.4 Cavity mirror dispersion and the femtosecond enhancement cavity . . . 43

2.2.5 Laser-cavity stabilization . . . 46
2.2.6 Output coupling . . . 51
2.3 The laser . . . 54
2.3.1 Nonlinear pulse compression . . . 56
2.4 Typical laser-cavity operating parameters . . . 60
2.5 The chamber . . . 60
2.5.1 Ozone and plasma cleaner . . . 62

3 High-order harmonic generation **69**
3.1 Single atom response to a strong laser field . . . 69
3.1.1 Ionization by an intense laser pulse . . . 69
3.1.2 Simple model of high-order harmonic generation . . . 72
3.1.3 The quantum description of high-order harmonic generation . . . 74
3.1.4 Beyond the strong-field approximation . . . 76
3.2 Macroscopic response and phasematching . . . 79
3.2.1 Single-pass case . . . 80
3.2.2 Enhancement cavity case . . . 82
3.3 Power scaling . . . 86
3.3.1 Methods . . . 86
3.3.2 Results . . . 88

4 Interferometry in the extreme ultraviolet **96**
4.1 Motivation and brief history . . . 96
4.2 The extreme ultraviolet interferometer . . . 97
4.2.1 The acousto-optic modulator . . . 98
4.2.2 Construction of the beam combiner . . . 103
4.2.3 Beam combiner theory and scaling . . . 106
4.2.4 Extreme ultraviolet detectors . . . 108

4.2.5 Extreme ultraviolet optics . . . 109
4.2.6 The Seya-Namioka monochromator . . . 111
4.3 Putting it all together . . . 113

5 Phase noise and phase sensitive detection in the extreme ultraviolet 119
5.1 Optical phase noise . . . 119
5.2 Noise scaling of high-order harmonic generation . . . 124
5.3 Testing the limits of coherence in the extreme ultraviolet . . . 126
5.4 Measurement of intensity dependent dipole phase . . . 130
5.4.1 Theory of measurement . . . 132
5.4.2 Measurement systematics . . . 135
5.4.3 Results and data analysis . . . 136
5.4.4 Conclusion . . . 138

6 Strong-field physics with molecules 142
6.1 Impulsive stimulated Raman scattering . . . 142
6.2 Field-free molecular alignment . . . 144
6.3 Field-free molecular alignment experiments . . . 148
6.3.1 Single-pulse case . . . 149
6.3.2 Multi-pulse case . . . 151
6.4 High-order harmonic generation with molecules. . . . 155
6.5 Future potential of cavity-based field-free molecular alignment . . . 155

7 Conclusion and Future Prospects 160
7.1 Conclusion . . . 160

Bibliography **162**

Appendix

A Numerical Code Repository **173**

B Publication list **175**

Tables

Table

1.1 Ionization potentials 7

2.1 $ABCD$ matrix table 39

6.1 Molecular parameters for field-free molecular alignment 148

Figures

Figure

1.1 NIST frequency chain . . . 3

1.2 High-order harmonic generation . . . 8

1.3 Optical frequency comb. . . . 11

1.4 Super continuum generation and f_0 detection . . . 13

1.5 Yb:fiber frequency comb . . . 17

1.6 Frequency comb characterization . . . 19

1.7 HHG and frequency combs . . . 21

2.1 Fabry-Perót ring cavities . . . 29

2.2 Finesse measurement . . . 36

2.3 Cavity geometry . . . 41

2.4 Impact of mirror dispersion . . . 47

2.5 Pound-Drever-Hall laser stabilization . . . 48

2.6 Intensity servo . . . 50

2.7 Output couplers . . . 53

2.8 80 W Yb:fiber frequency comb . . . 57

2.9 Nonlinear Schrödinger equation . . . 59

2.10 Nonlinear pulse compression . . . 61

2.11 Vacuum chamber . . . 63

2.12 Vacuum chamber vibration isolation . . . 64
2.13 Gas dump design . . . 65
2.14 *in-situ* plasma cleaner . . . 67

3.1 Ionization probability by an intense laser pulse . . . 71
3.2 Simple man model . . . 73
3.3 Strong–field approximation . . . 77
3.4 Beyond the strong-field approximation . . . 78
3.5 Absorption limited phase matching . . . 83
3.6 Phase matching in a fsEC . . . 85
3.7 HHG detection . . . 87
3.8 Super sonic jet and cavity mode . . . 89
3.9 Effects of steady state plasma . . . 91
3.10 Phase matching in a fsEC . . . 93
3.11 Extreme ultraviolet power comparison . . . 95

4.1 Mach-Zehnder interferometers . . . 99
4.2 XUV Interferometer . . . 100
4.3 AOM . . . 102
4.4 XUV beam combiner . . . 104
4.5 XUV beam combiner schematic . . . 107
4.6 XUV reflectivity for boron carbide and gold . . . 110
4.7 Harmonic spectrum . . . 112
4.8 XUV reflectivities . . . 114
4.9 Relative harmonic powers . . . 115
4.10 High harmonic heterodyne beats . . . 117

5.1 Phase noise scaling . . . 125

5.2 Phase modulated XUV beatnote . . . 127
5.3 Test of XUV comb coherence . . . 129
5.4 Intensity dependent phase time domain . . . 131
5.5 Measurement schematic of intensity dependent phase . . . 133
5.6 Intensity dependent dipole phase summary . . . 137
5.7 Data set from an intensity dependent dipole phase measurement . . . 139
5.8 Lock-in amplifier data for dipole phase measurment . . . 140

6.1 Field-free molecular alignment . . . 146
6.2 Field-free molecular alignment apparatus . . . 147
6.3 Impulsive stimulated Raman scattering single pulse . . . 150
6.4 Impulsive stimulated Raman scattering multiple pulses . . . 152
6.5 Impulsive stimulated Raman scattering spectral shifts . . . 154
6.6 HHG with aligned molecules . . . 156
6.7 High-order revivals, coherence decay, and spectral modulator . . . 159

Chapter 1

Extreme ultraviolet frequency combs

1.1 Introduction

Optical frequency combs are a remarkable laser technology technology. They seamlessly integrate the disciplines of ultrafast lasers with precision continuous wave (CW) laser stabilization and frequency metrology. The technology is so powerful, it was recognized by a Nobel Prize awarded to John L. Hall and Theodor Hänsch in 2005 [1, 2]. That same year, the extreme ultraviolet (XUV) frequency comb, an extension of the optical frequency comb to wavelengths below 100 nm, was demonstrated by the Ye group and the Hänsch group virtually concurrently [3, 4]. This marked the first step to performing laser spectroscopy at wavelengths previously inaccessible to traditional laser technology. With a few exceptions [5], high-resolution laser spectroscopy below 100 nm is a vastly uncharted territory. To a large degree, the motivation behind the XUV frequency comb is enabling high-resolution spectroscopic exploration in this part of the electromagnetic spectrum. Nevertheless, the XUV comb bridges the worlds of strong-field physics with that of precision measurement in much the same way as the original optical frequency comb bridged ultrafast science and precision metrology.

To put the XUV frequency comb into the broader context of laser technology and the work in this thesis, it is useful to start at the laser's origin, the maser. Gordon and Townes were the first to produce the ammonia maser [6, 7]. To characterize the maser, two versions were built to compare using heterodyne interferometry, a trick we will also use extensively in this thesis. By comparison of two such masers, it was immediately apparent that the spectral purity of the microwave signal and

the stability were quite remarkable. Schalow and Townes followed to show how this demonstration could be feasibly extended to the infrared and optical domain [8]. The promise of being able to perform high-resolution spectroscopy at optical frequencies was certainly tantalizing. In 1960, the first laser was created by Maiman [9]. It was pulsed source that used ruby as a gain medium. This was followed in 1961 with the demonstration of the first CW laser using a helium-neon mixture as the gain medium [10]. These two historical breakthroughs in technology essentially lead to, among many other applications, the birth of nonlinear optics and laser spectroscopy, two seemingly unrelated fields of research that will coalesce to give optical and XUV frequency comb technology.

As laser technology rapidly advanced, it became apparent that there was a need to be able to measure an optical frequency in an absolute sense. The current definition of the SI unit the second, and hence frequency, is based on a hyperfine transition in Cesium-133 at 9,192,631,770 Hz exactly. Optical frequencies are typically at ~ 400 THz, which is much too high for direct electronic measurement. Before the late 1990's, the only way to bridge this frequency gap was a large, magnificently complex system of multiple lasers and microwave sources spanning the electromagnetic spectrum compared at radio frequencies. An example of these heroic efforts is shown in Fig. 1.1.

The device that rendered such frequency chains virtually extinct was the femtosecond optical frequency comb[1] . Ultrashort laser pulses were routinely produced starting in the 1980's. However, it was not until the first demonstration of passive, Kerr-lens modelocking that lasers with femtosecond pulse durations became robust [12]. It became apparent that the train of femtosecond pulses produced by a modelocked laser creates a comb structure in the frequency domain provided that the repetition rate of the pulses is stable *and* provided the phase relationship between the successive pulses' electric field is stable or slipping regularly from pulse to pulse. Under these conditions, the frequency ν_n of each tooth of the comb can be identified by a simple equation $\nu_n = n \times f_r + f_0$, where n is an integer, f_r is the repetition rate of the pulses, and f_0 is the carrier-envelope offset frequency which is defined as the rate the electric field slips in phase from pulse to pulse. The

[1] For this thesis, we will use "femtosecond optical frequency comb", "optical frequency comb", and "frequency comb" virtually interchangeably to refer to frequency combs generated by modelocked, femtosecond pulse duration lasers. There are various other frequency comb technologies and if we are referring to them, it will be clear from context.

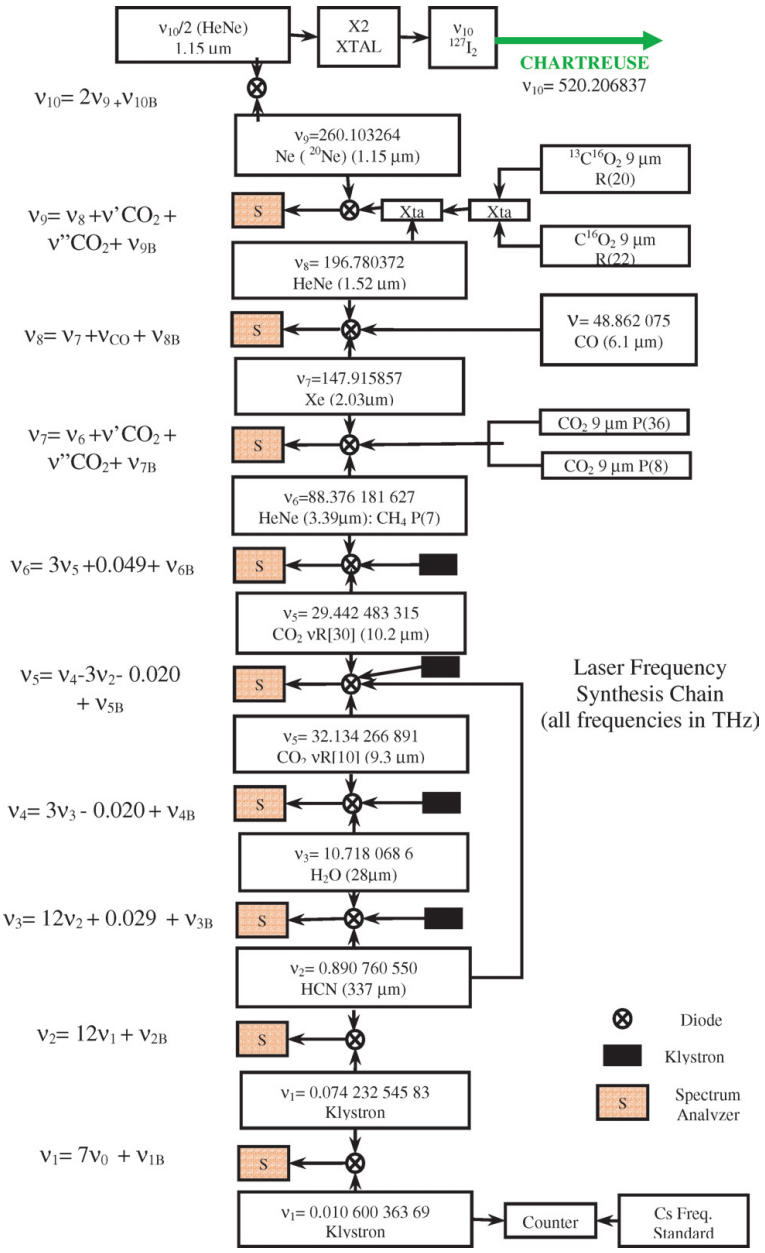

Figure 1.1: This diagram is of the NIST frequency chain used to directly link an iodine transition at ~ 520 THz to the Caesium-133 standard at ~ 9 GHz. Reproduced from [11].

beauty of this equation is that f_r and f_0 are both radio frequencies and can be easily measured with conventional electronics. The optical frequency comb provides a radio frequency (RF) indexed ruler for a large bandwidth of optical frequencies. With this laser, there is a way to directly relate an optical frequency to an radio frequency, the essence of the NIST frequency chain show in Fig. 1.1. Direct frequency comparison could now be accomplished with a single modelocked laser emitting ultrashort laser pulses. By making a heterodyne beat between the laser under investigation and the optical frequency comb (in a way analogous to Gordon and Townes original maser demonstration), one can precisely know the frequency of a laser to very high degree and be able to directly compare it to an absolute standard like the cesium atomic fountain clock operating in the microwave domain (or various other atomic clock technologies).

Spectroscopy in the XUV (10 nm – 100 nm) is a difficult business [13] and it would be great if we could make it easier with the laser technology that has been developed in the visible and near infrared parts of the electromagnetic spectrum. However, building a laser in the XUV is no simple task. The problem is essentially two-fold [14]. The power required to maintain a population inversion and achieve lasing scales $\sim 1/\lambda^4$. Since XUV wavelengths are typically an order of magnitude shorter than their visible counterparts, $\sim 10^4$ times more power is required for their operation. Secondly, solid materials are typically not transparent below 100 nm, limiting gain media to gaseous samples. There is also a very severe problem in that high reflectivity mirrors are extremely rare in the XUV. Despite the apparent difficulty in producing laser light below 100 nm, there is still strong scientific interest in overcoming this challenge. A quintessential example is atomic hydrogen spectroscoy [15]. Moving spectroscopic investigation beyond hydrogen to hydrogen-like systems, or even helium-like systems, will offer new insights to bound-state QED because the corrections scale favorably with the nuclear charge Z [16]. Using the Bohr model as a reference, the energy levels of a hydrogen-like ion are

$$E_n = Z^2 \frac{R_E}{n^2}, \tag{1.1}$$

where R_E is the Rydberg energy of 13.6 eV and n is the principle quantum number. Simply moving from hydrogen to singly-ionized helium (a system similar to atomic hydrogen), the $n = 1 \rightarrow n = 2$ transition is already at 40.8 eV, deep into the extreme ultraviolet and well out of the reach of traditional laser technology. Ultimately we are seeking a source of light that has laser-like properties but we are flexible as to how it is produced. Therefore, we can take advantage of nonlinear frequency conversion techniques. Immediately following Maiman's ruby laser demonstration [9], the field of perturbative nonlinear optics was born with the production of optical harmonics [17]. The high peak power of the pulsed ruby laser source was used to create a nonlinear polarization in a material and thus produced harmonics of the driving laser frequency. We can understand such phenomena by expressing the polarization induced by the laser field in a material or gas by a simple power series expansion expressed as [18]

$$P = \chi^{(1)}E + \chi^{(2)}E^2 + \chi^{(3)}E^3 + \dots , \tag{1.2}$$

where P is the polarization, $\chi^{(k)}$ is the k^{th} order susceptibility, and E is the electric field. The $\chi^{(1)}$ term is describes ordinary, linear optics. The $\chi^{(2)}$ and $\chi^{(3)}$ susceptibilities give rise to now common nonlinear phenomena such as second and third harmonic generation, four-wave mixing, and self-phase modulation. These nonlinearities are routinely exploited to produce optical pulses with nearly single-cycle durations ($\sim 1 - 5$ fs) and down to wavelengths around 200 nm [19]. One might expect that as the intensity of the laser is increased, higher and higher optical harmonics will be produced. To a certain degree, this is true. However, our understanding based on the perturbative expansion of Eq. 1.2 will quickly run into trouble once the electric fields of the laser pulse become comparable to the fields that hold the atom together. If we ignore bound-free transitions (ionization) it is possible to relate the $k + 1$ order susceptibility to the k order of an atomic system with a resonance at ω_0 by using perturbation theory to obtain [19]

$$\frac{\chi^{(k+1)}E^{k+1}}{\chi^{(k)}E^k} \approx \frac{\mu E}{\hbar\Delta} \approx \frac{eEa_B}{\hbar\Delta} \tag{1.3}$$

where a_B is the Bohr radius, the bound-bound transition detuning is $\Delta = |\omega - \omega_0|$, and μ is the bound-bound transition dipole. This is not an extremely rigorous equation, but it gives us a sense for the orders of magnitude with which we are dealing. For a detuning of about 1 eV, the ratio approaches unity when E is on the V/Å level. This corresponds to laser peak intensities on order 10^{14} W cm^{-2}. These sorts of field strengths will cause the expansion in Eq. 1.2 to diverge as the laser field is clearly no longer a perturbation. As it turns out, recent theoretical advances have shown that this expansion starts to break down at much lower laser intensities [20, 21].

At these intensities, it is impossible to ignore bound-free transitions (ionization) making the perturbative treatment even further unjustified. Intense electric fields lead to the ability for a bound electron to quantum mechanically tunnel through the potential barrier and be ionized. There is also the possibility of multiphoton absorption that will also lead to ionization. It is interesting to note that the first strong-field laser-atom, multiphoton absorption experiment was performed at JILA in 1965. An intense laser pulse incident was focused on a beam of I^- and the subsequent ionized electrons were measured [22]. After ionization, the freed electron propagates in the electromagnetic field. A useful metric for understanding the transition to the strong-field regime was introduced in 1965 by Keldysh [23]. The Keldysh parameter is given by

$$\gamma = \sqrt{\frac{I_p}{2U_p}}\,, \tag{1.4}$$

where I_p is the ionization potential of the atom, see Table 1.1 for a list of common atomic targets and the values for I_p. The U_p is the pondermotive energy defined as

$$U_p = \frac{e^2E^2}{4m_e\omega^2}\,, \tag{1.5}$$

where e is the charge of the electron, m_e is the mass of the electron, and ω is the laser frequency. The Keldysh parameter can be understood as a ratio between the laser frequency and the tunneling rate. For $\gamma >> 1$, multiphoton absorption is dominant because the tunnel rate is slow compared to the laser frequency. This is the case for laser pulses with short wavelengths and high intensities. By

lowering the laser frequency, thereby increasing the laser wavelength, it is possible to make $\gamma \approx 1$. This is where the tunnel ionization rate and laser frequency are comparable, a situation found in many strong-field experiments and where the process of high-order harmonic generation is typically performed. For $\gamma << 1$, the electron can begin to topple over the potential barrier or tunnel ionize. While this description has its usefulness, a more detailed review and criticism will be mentioned later in Sect. 3.1.

Atom	I_p [eV]
He	24.5874
Ne	21.5645
Ar	15.7596
Kr	13.9996
Xe	12.1298

Table 1.1: A table containing the ionization potentials of the noble gases used for HHG.

When an electron is tunnel ionized in an oscillatory field, to first order, the electron will propagate in the electromagnetic field like a free, charged particle. At first, the electron will be driven away from the ion core. Since the field is oscillatory, eventually the field will change sign and the electron can return to the ion core it originally left. At this point, there is a small chance the electron will recombine with the ion and emit a very high energy burst of light. This is essentially the three step semi-classical model of high-order harmonic generation (HHG) [24]. This process is schematically shown in Fig 1.2. The three step model predicts that the maximum photon energy (the cutoff) that can be emitted is

$$\hbar\omega_{max} = I_p + 3.17U_p. \tag{1.6}$$

Since the HHG process is an ionization-related phenomena, it is best performed with pulse durations comparable to the ionization rates. The ionization rates can be calculated using the theory of Amosov, Delone, and Krainov (ADK) [25]. For the noble gases assuming a near infrared laser, it is easily possible to completely ionize a gas target in less that 100 fs if the peak intensity is

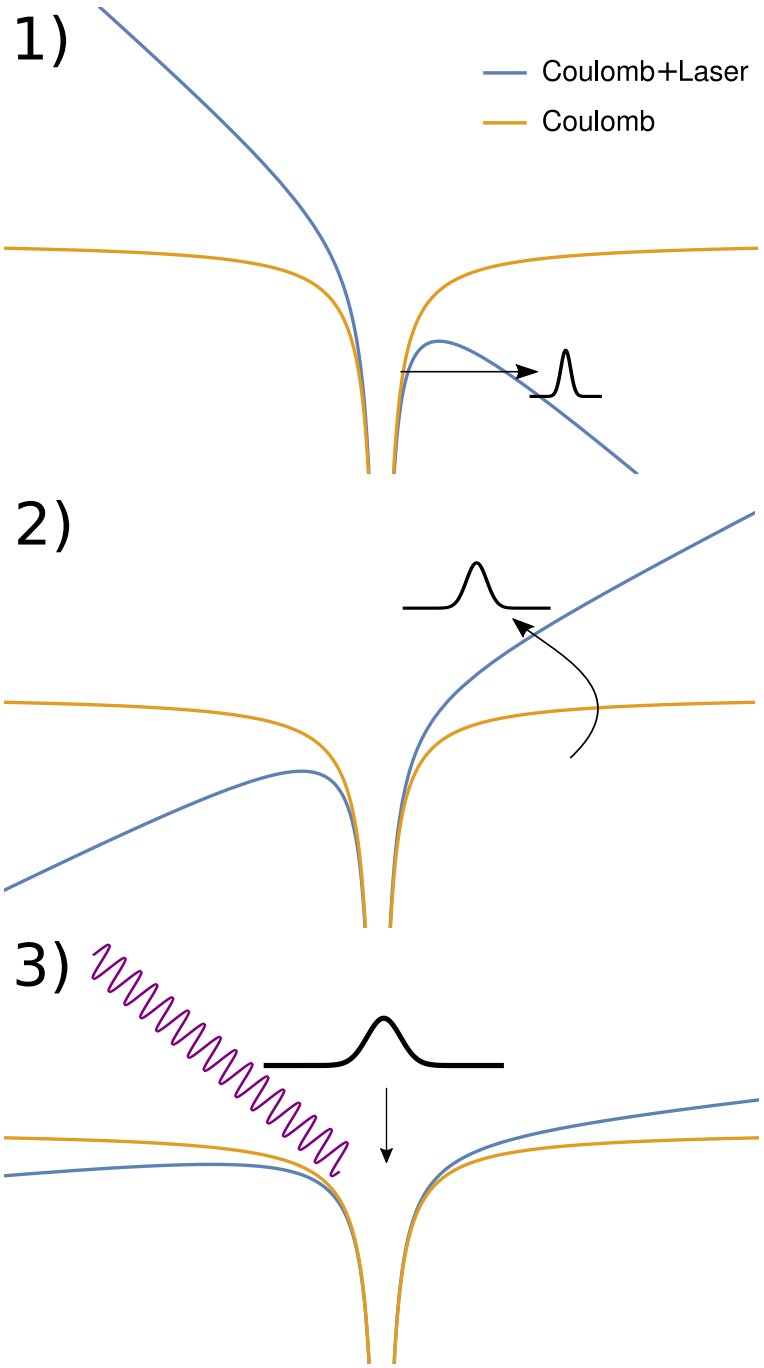

Figure 1.2: Schematic of the three step model of high-order harmonic generation. **Step 1** is ionization by an intense electric field. **Step 2** is the acceleration of the free electron in the electromagnetic field. The oscillatory nature of the electromagnetic field will cause the electron to return to the ion core. **Step 3** is the possible recombination of the electron and ion resulting in a burst of high energy light.

$> 10^{14}$ W cm^{-2}. It is therefore necessary to use ultrashort pulse lasers to prevent complete ionization of the gas before the pulse has passed through the target. To show the power of the scaling of Eq. 1.6, a laser 1070 nm wavelength and at a peak intensity of 1×10^{14} W cm^{-2} focused into argon can produce photons up to an energy of about 48 eV! Assuming a pulse duration of 100 fs, <1% of the gas target will be ionized. The harmonic light is at a high enough photon energy to excite a singly-ionized helium atom between the $n = 1 \rightarrow n = 2$ energy levels that were mentioned earlier. A more detailed description of HHG as it pertains to the work in this thesis will be saved for Chapter 3.

1.2 Optical frequency combs

We will now turn our attention to the optical frequency comb before moving to how an XUV frequency comb is produced. A review of the basic femtosecond optical frequency comb technology can be found in Ref. [26]. The train of pulses coming from a modelocked laser looks very similar to a Dirac comb

$$\text{Ш}_T(t) = \sum_{n=-\infty}^{\infty} \delta(t - nT). \tag{1.7}$$

In reality, the pulses of a modelocked laser are typically $\sim$ 100 fs in duration and are separated by typically $\sim$ 10 ns. At 1070 nm, the period of a light wave is 3.57 fs so there are many oscillations within a single pulse. The Fourier transform of the Dirac comb $\text{Ш}_T(t)$ is well known and is given by

$$\text{Ш}_T(t) \xrightarrow{\mathscr{F}} \text{Ш}_{\frac{1}{T}}(f)\,, \tag{1.8}$$

so it should be of no surprise that the comb-like structure of a modelocked laser in the time domain will lead to a comb-like structure in the frequency domain. The pulse train coming from the modelocked laser has an additional complication. The maximum of the electric field need not occur at the maximum of the intensity envelope. Rather, it can shift from pulse to pulse. The offset of

the electric field relative to the peak of the envelope in a single pulse is often referred to as the carrier-envelope phase $\Delta\phi$. For a pulse train, it is more useful to describe the rate at which the phase slips and this is the carrier-envelope offset frequency f_0 defined as

$$f_0 = \frac{\Delta\phi}{2\pi} f_r \,, \tag{1.9}$$

where $\Delta\phi$ is the pulse to pulse phase slip of the electric field relative to the envelope. This is schematically shown in Fig. 1.3. In the frequency domain, this has very important consequences. All of the comb teeth are uniformly offset from zero by f_0. We can therefore identify any comb tooth at *optical frequencies* by a combination of two *radio frequencies* expressed as

$$f_n = n \times f_r + f_0, \tag{1.10}$$

where n is an integer. Each comb tooth f_n can be used as a frequency marker to compare with CW lasers or it can used in much the same way a CW laser is used. For example, it is possible to perform spectroscopy with an individual comb tooth or simultaneously with multiple comb teeth [27].

1.2.1 Carrier-envelope offset frequency detection and measurement

Modelocked lasers, the basis for femtosecond optical frequency combs, have been routinely used since the 1980's. However, it was not until the year 2000 that an optical frequency comb was demonstrated [28, 29]. This is because detection of the carrier-envelope phase is quite difficult and it was not until the realization that the carrier-envelope phase slip had important consequences in the frequency domain. It also took time to apply the tools of laser stabilization in the frequency domain to ultrafast lasers. To stabilize the carrier-envelope phase of a modelocked oscillator, one must be able to detect it, or at least the rate at which it slips, as previously defined in f_0. One method, and the one originally demonstrated in 2000, is an $f - 2f$ interferometer [28]. If we can compare two comb teeth n and m (or sets of comb teeth) that satisfy the condition $2n = m$, we will be able to detect f_0. The problem is that this requires the optical spectrum to be at least one octave

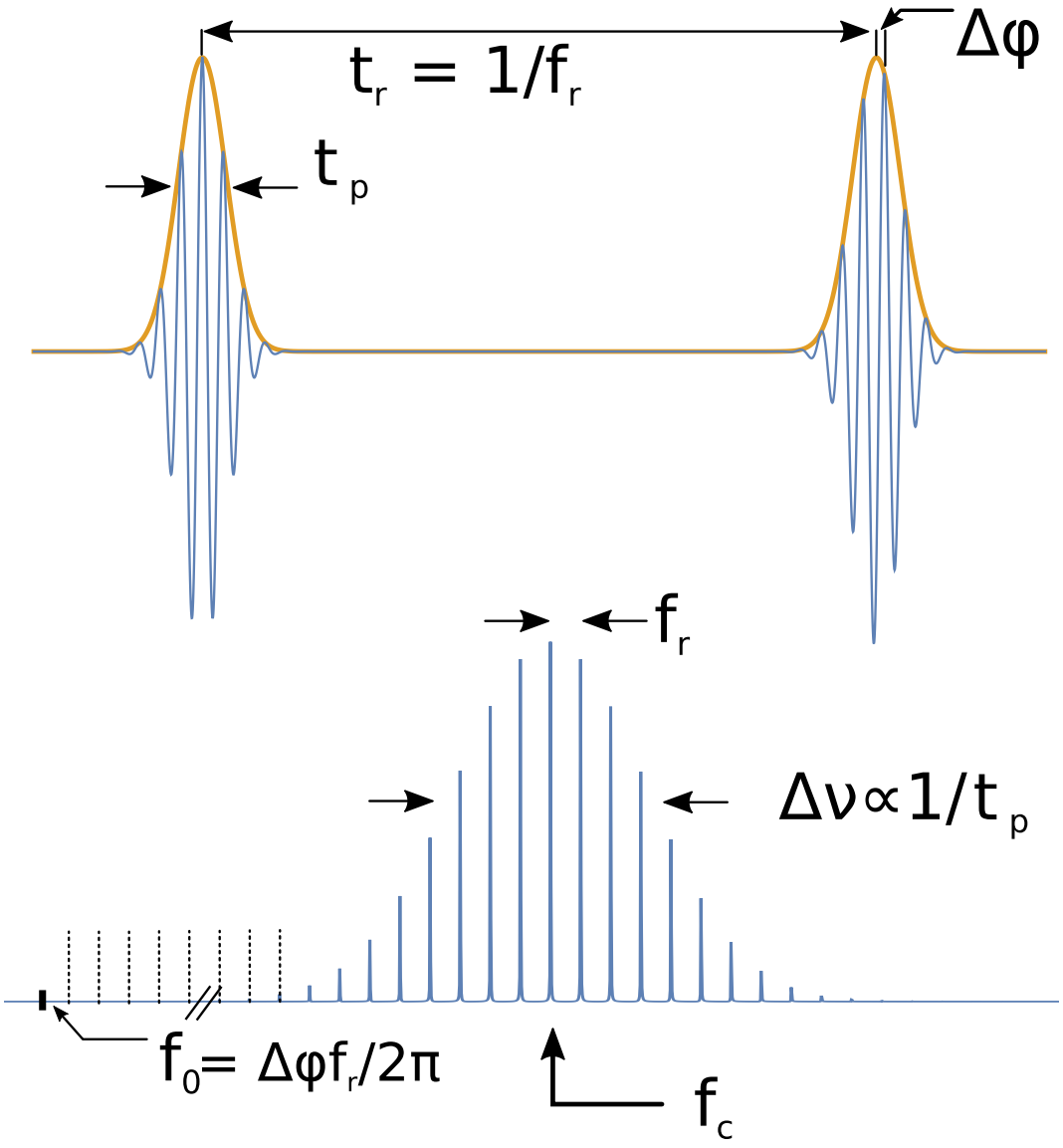

Figure 1.3: Schematic drawing of an optical frequency comb in the time domain and the frequency domain. Relevant time scales and frequency scales are identified in the schematic.

wide. A typical modelocked oscillator spectral width is inversely proportional to the pulse duration $\Delta\nu \propto 1/t_p$ and for pulses of $t_p \approx 100$ fs at the 1070 nm central wavelength, the spectrum only spans $\Delta\nu \approx 4.4$ THz (or ~ 15 nm) which is nowhere near a spectral octave this optical range. To overcome this bandwidth issue, highly nonlinear optical fibers offered an elegant solution [30]. Currently, the highly nonlinear fiber technology is very mature, but at the time, it was still in its infancy. Highly nonlinear fibers rely on a variety of nonlinear optical phenomena (self-phase modulation, Raman scattering, soliton formation, etc.) to spectrally broaden the pulse to reach an octave. An example of this approach from our lab [31] is shown in Fig. 1.4. The spectrum is ideally matched for the strontium optical lattice clock experiments because the octave spanning spectrum covers most of the near infrared and provides access to telecom wavelengths near 1.5 μm. Currently, it is possible to directly produce octave spanning spectra directly from a Ti:Sapphire-based modelocked laser, but they are often not as robust and low maintenance as the fiber-technology counterparts [32, 33].

Once the laser spectrum spans one octave, the long wavelength side of the spectrum can be frequency doubled (by using nonlinear crystals) to spectrally overlap with the blue side of the same comb spectrum. Fig. 1.4 contains shaded regions highlighting the relevant parts of the spectrum used for f_0 detection. By doing this, we can overlap comb teeth that satisfy $2n = m$. We can then observe a heterodyne beat that measures f_0 by

$$2 \times (n\, f_r + f_0) - (m\, f_r + f_0) = 2n\, f_r + 2f_0 - m\, f_r - f_0 = f_0. \tag{1.11}$$

With the ability to detect f_0 and f_r (accomplished with a simple, fast photodetector), there is often still a need to stabilize these quantities. Once stabilized, the potential of the frequency comb is clear; there are millions of stable and well defined frequency markers across the optical spectrum available for use.

1.2.2 Frequency comb stabilization

There are a multitude of ways to stabilize a frequency comb. For the sake of clarity, we will focus on a situation applicable to modern optical atomic clocks [34]. The laser to be described [31]

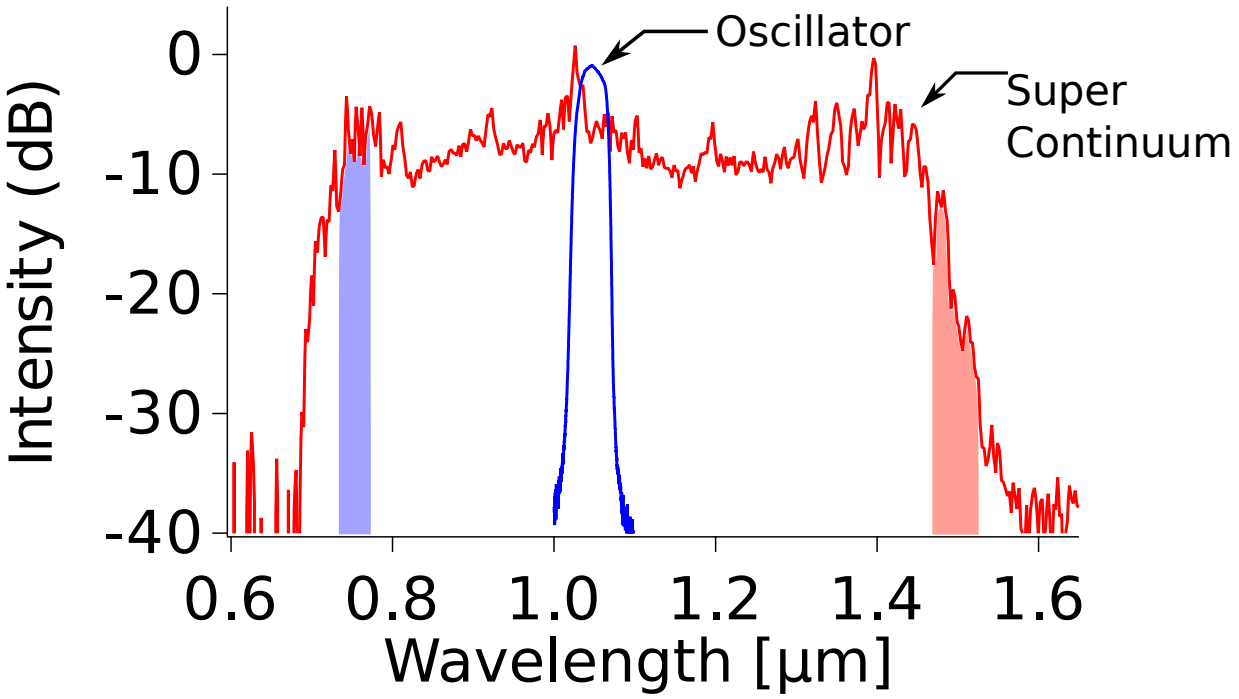

Figure 1.4: A Yb:fiber oscillator spectrum is shown in blue. After nonlinearly broadening the spectrum in photonic crystal fiber, the red spectrum spans over one spectral octave. The red shaded region can be frequency doubled using a nonlinear crystal to spectrally overlap with the blue shaded region to allow f_0 detection.

was used for the strontium lattice clock [35] and precision laser comparison experiments [36]. Nevertheless, the techniques are fairly universal. Precision laser and frequency comb stabilization is an exercise in control systems. It is often joked that you can either engineer a laser system very well, or just build a good feedback system. In reality, the best system is a combination of good engineering and good feedback system design. To avoid obfuscating the point by going into the details of feedback loop design, it is useful to just consider the basic operating principle as it pertains to laser stabilization.

Imagine we want to stabilize a laser frequency Ω_L to a reference laser frequency Ω_R. The first thing we need is some means to measure how far away our laser frequency is from Ω_R. We typically call this a discriminator. Our discriminator will typically give us a signal in the form of an electrical voltage V that tells us how far off we are from the goal so that $V \propto \Omega_L - \Omega_R$. We can take that signal, filter it, invert it, and apply it to the laser to try and steer the laser frequency to the correct value. Our discriminator then reports how well we have done and the process continues until the system settles on our desired result or $V \approx 0$. The real trick involves filtering the signal properly and re-applying with just the right strength. While this is a vast oversimplification, there are a few important subtleties to mention. While, mathematically speaking, a phase-lock and a frequency-lock are an integral away from each other, the physical processes that can generate phase noise or frequency noise can be quite different and have very different spectra. The actuators used for phase-locking or frequency-locking typically typically fall into two categories: fast actuation with low dynamic range or slow actuation with large dynamic range. Typically, both are needed. Fast actuators are essential to remove broadband noise (or high-frequency noise) in a phase-lock or frequency-lock. However, they tend to run out of actuation range very quickly as optical systems drift and respond to slow (but sometimes large) environmental perturbations such as a temperature change. Therefore, slow but high dynamic range actuators are employed to keep the fast actuators within optimal operating ranges.

An optical frequency comb is a complicated laser and it is schematically drawn in Fig. 1.5 with numerous parts and stabilization components labeled. This laser system is almost identical to the

front-end of the high power system used for the HHG work in this thesis (see Chapter 2). There are two fundamental quantities that need to be stabilized in a frequency comb, f_r and f_0. The first is possibly the easiest to understand. Two control f_r, the simplest method is to change the laser cavity length. This changes the round-trip time of the pulse in the cavity and hence the repetition rate. A drawback to this method is that changing the cavity length usually requires moving a macroscopic mirror. This usually introduces temporal delay in the system's response and this is the bane of a feedback loop. In Fig. 1.5, these cavity length changes are accomplished by piezoelectric transducer (PZT) actuators. One is attached to a saturable absorbing mirror (SAM) to provide fast changes to the cavity length and a circular PZT stretches some fiber in the cavity to slowly change the cavity length. However, some applications require feedback to be faster than what a PZT can accomplish. We can then make use of an electro-optic modulator (EOM) to change the cavity length. This works by applying a voltage to the EOM crystal to change the index of refraction of the crystal and hence increase or decrease the optical path making the laser cavity effectively longer or shorter. This can have feedback bandwidth almost an order of magnitude larger than common PZTs as demonstrated in Ref. [31].

To stabilize f_0, we must refer to more sophisticated laser dynamics. Relative changes in the intracavity dispersion (relative amounts of group delay and phase delay) will lead to f_0 shifts. To accomplish this in the frequency comb of Fig. 1.5, the fiber Bragg grating (FBG) temperature is changed. The FBG is responsible for dispersion management inside the laser cavity and by changing the temperature, the grating's dispersive properties change. This process is effective but very slow. Faster control is accomplished by modulating the pump power of the laser. Modulating the pump power will change the amount of self-phase modulation in the laser and modulate the dispersion of the gain medium, both of which will cause f_0 to change [37, 38]. However, it is often nice to use the pump modulation actuator to reduce the amount of phase noise in the laser because fiber lasers typically have large amplitude-to-phase noise couplings [31, 39]. With the pump laser intensity tied up reducing phase noise in the laser by reducing the laser intensity noise, it is unavailable for direct f_0 control. However, this problem can be circumvented by the use of an acousto-optic modulator

(AOM) placed *outside* the laser cavity. An AOM uniformly shifts all the frequency comb teeth by a given radio frequency which is typically near 40 MHz but can be up to and over 1 GHz. The AOM can provide high feedback bandwidths and is a nearly perfect f_0 actuator.

With detection of f_0 described, detection of f_r seems almost trivial as a photodetector with a response faster than f_r is sufficient to measure it. However, it is often unwise to use this method if the highest level of stabilization is required. As an example, stabilizing f_r directly will only fractionally preserve the stability at optical frequencies. Assuming a $f_r = 100$ MHz signal can be stabilized to 1 Hz, that is a fractional uncertainty of $\Delta f_r/f_r = 1$ Hz/100 MHz $= 10^{-8}$. Assuming a frequency comb at 1070 nm, the central frequency is 280 THz. That means the optical linewidth Δf_{opt} would become $\Delta f_{opt} = 280$ THz $\times\, 10^{-8} = 2.8$ MHz. For some applications, this is sufficient, but for high-performing optical atomic clocks [35], this is not acceptable.

However, we are not limited to direct detection of f_r. CW lasers can routinely be stabilized to $\sim \Delta f/f = 10^{-16}$ [40]. By making a heterodyne beat between a extremely stable laser and a single comb tooth we can derive an excellent signal to use for stabilization. The beat frequency with the f_0 dependence removed would be

$$f_{b'} = n \times f_r + f_0 - f_{opt} \tag{1.12}$$

$$f_b = f_{b'} - f_0 = n \times f_r - f_{opt} \tag{1.13}$$

The beat frequency f_b can then be stabilized to a very stable RF reference frequency by controlling f_r. This accomplishes an important point; the fractional stability of the laser can now be transfered directly to f_r. This has been exploited to generate extremely stable radio frequencies by subsequent detection of f_r on a simple photodetector [41]. This method also facilitates precise comparison of lasers separated by frequencies too large for direct detection [36].

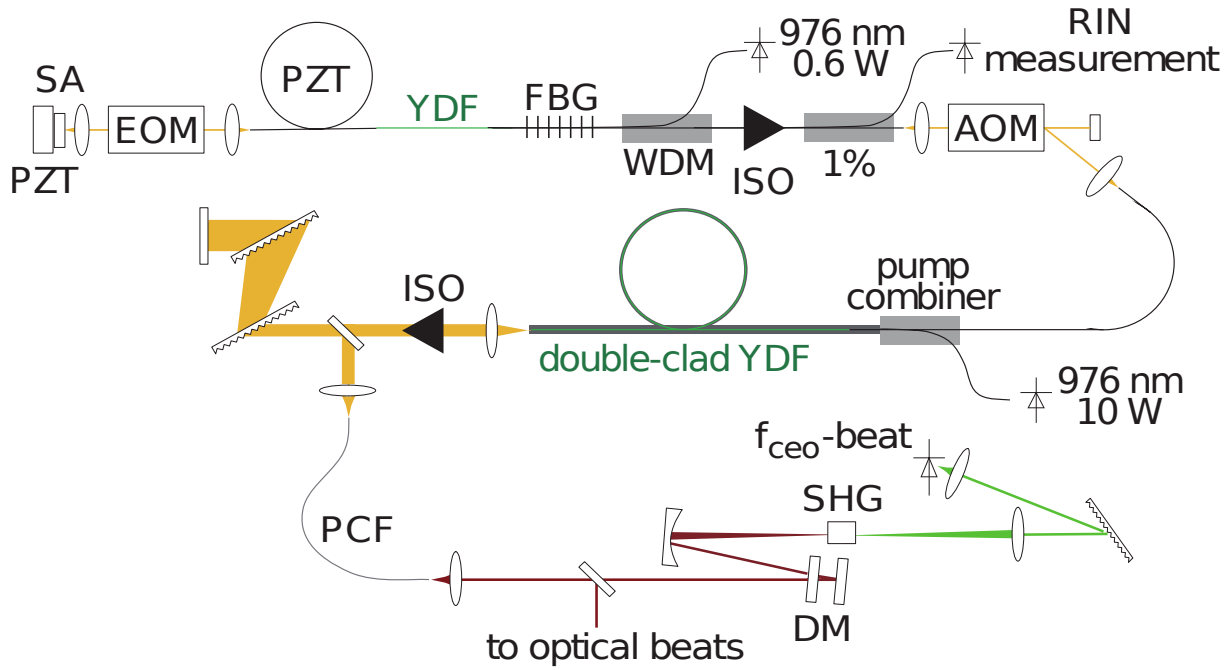

Figure 1.5: A schematic of the Yb:fiber frequency comb used for optical clockwork. PZT, piezoelectric transducer. SA, saturable absorber. EOM, electro-optic modulator. YDF, ytterbium-doped fiber. FBG, fiber Bragg grating. WDM, wavelength division multiplexer. ISO, optical isolator. RIN, residual intensity noise. AOM, acousto-optic modulator. PCF, photonic crystal fiber. DM, dichroic mirror. SHG, second harmonic generation.

1.2.3 Frequency comb performance characterization

After a frequency comb has been stabilized, it is often useful to have multiple methods to characterize it. Fig. 1.6 shows three possible methods. The first is to use a CW laser to compare with an individual comb tooth. To get a true sense of how the comb is performing, it is important that the CW laser is "out-of-loop" (an independent component) meaning that it is not being used as a part of the stabilization scheme. The beat between the CW laser and the comb will yield important information about frequency stability and other possible noise sources. As an example, this method was used to study super continuum processes and how well they preserved the frequency comb coherence across the optical spectrum [42].

The second method and third method rely on the use of a reference frequency comb with known stability properties. The second method uses two combs have the same f_r but different f_0. The heterodyne beat signal will contain information about f_0 stability which can be useful for measuring noise properties coupled to f_0 or to measure optical linewidths across the spectrum by spectrally resolving the comb before heterodyne beat detection. We will use this method later in the thesis when we characterize the coherence properties of the XUV comb [43]. The third method is more complicated, it relies on the two combs having different f_r and possibly different f_0. By doing this, the relative spacing between comb teeth of each comb is growing with the comb tooth number. The heterodyne beat spectrum will contain many signals coming from each pair of comb teether because they are all at slightly different frequencies. This is the basis for the very powerful technique of dual-comb spectroscopy [44, 45]. This method is often used to analyze a new class of frequency combs based on soliton formation in torroidal resonators [46].

There are many figures of merit for frequency comb performance (or CW laser performance) and the most meaningful often depends on the desired application [38, 47]. For the work pertaining to this thesis, we are most concerned with the temporal coherence properties or phase stability. A useful metric for this is the measure of the optical linewidth. Much like an atomic linewidth can give information on an excited state lifetime, an optical linewidth can give information on the coherence

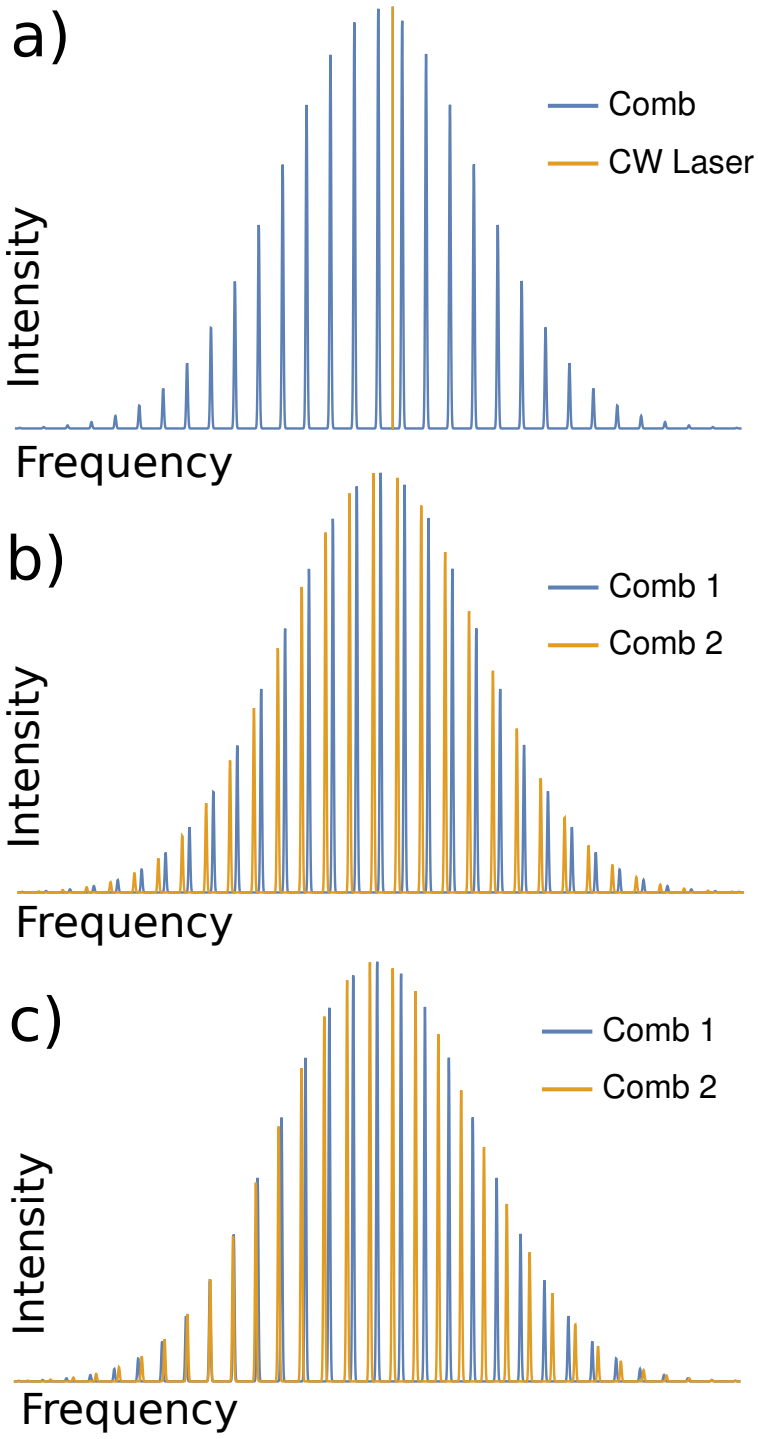

Figure 1.6: **a)** A heterodyne beat between a CW laser and a frequency comb. **b)** A heterodyne beat between two frequency combs with the same repetition rate but different f_0 frequencies. All the beats from different teeth coherently add together to form a single beat. **c)** Heterodyne beats between two frequency combs with different repetition rates. Each pair of teeth form individual beats. It is therefore possible to inspect individual frequency comb teeth in the radio frequency beat spectrum.

time of the light. The coherence time of the light is important because it sets a timescales at which a laser can phase coherently interact with an atomic system. These long light-matter interaction times have the potential to reveal very subtle phenomena in quantum systems. As a quick example, without the ability to resolve sub-Hz features on an atomic transition in strontium, many complex many-body phenomena would have gone unobserved [48]. The resolving power is only possible by having very phase stable light. This fact has driven much of the laser and atomic physics development over the past 50 years – the yearning of high spectral resolution.

1.3 Extreme ultraviolet frequency combs

Creating a frequency comb in the XUV requires performing the aforementioned process of HHG. Most HHG experiments are not performed in a manner that allows investigation of the coherence preserving properties of HHG. Certainly the spatial properties of the light were investigated and are routinely used for coherent diffractive imaging [49]. Since we are interested in using XUV frequency combs for high resolution spectroscopy, we are concerned primarily with the temporal coherence properties. Earlier work has shown that adjacent harmonic orders are locked in phase relative to each other [50]. This results in the HHG process producing a train of attosecond pulses in the XUV. However, this does not test or guarantee absolute phase stability, especially over the time scales of interest.

Before considering coherence properties of the HHG process, it is important to make a technical distinction between performing HHG with a frequency comb compared to a more "traditional" laser system. Calling any laser system designed for HHG "traditional" is troublesome. High-power laser systems are continuously evolving and the technology advances quite rapidly [51]. Nevertheless, a typical approach is to use a high pulse energy laser system. Pulse energies are typically in the few mJ range, repetition rates are in the kHz range or lower, and average powers are in the few W range. Central wavelengths can vary from 800 nm to 4 μm. Some sources offer the ability to customize and shape an optical waveform and others do not even have carrier-envelope phase stability. In principle, even with a very low repetition rate, it would still be possible to observe the

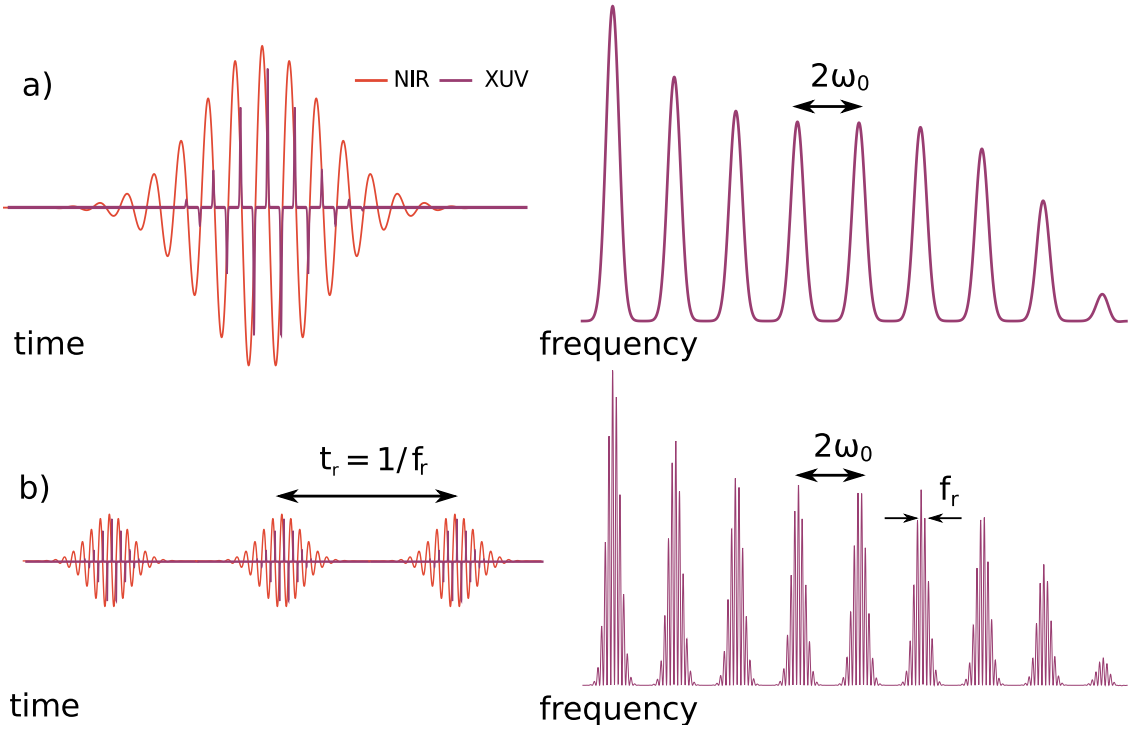

Figure 1.7: **a)** Single pulse HHG in the time and frequency domain. **b)** Multi-pulse HHG and the XUV frequency comb. The harmonic spectrum is the same as in the single pulse case, but the high repetition rate nature of the frequency comb creates a comb structure at each harmonic order.

comb structure, but in reality, when the pulses arrive so infrequently, it makes stabilization of a low repetition rate system nearly impossible. Further, it is an issue of the bandwidth of the noise processes. If the noise-induced modulation bandwidth exceeds f_r, we have no hope in uncovering a comb structure.

The harmonic spectrum produced by a single laser pulse is shown in Fig. 1.7. The is what is observed in low repetition rate laser systems. Near every maximum of the electric field, the three-step process of HHG (see Fig. 1.2) can initiate. The result is a burst of XUV radiation near the zero crossing of the laser field. Therefore, a burst of high energy photons will occur every half cycle of the laser. This is what produces the optical harmonics spaced by $2\omega_0$ where ω_0 is the driving laser central frequency. The harmonics are odd because the sign of the electric field of the high energy photon burst switches every half cycle. Also, since gas targets are typically inversion symmetric, even harmonics are not possible. Even harmonics can be produced if the target lacks inversion symmetry or a multi-color laser field is used to break the electric field symmetry.

The heart of the XUV frequency comb lies with the question of what happens if the HHG process is driven with a high repetition rate pulse train (a pulse train from a frequency comb for example). Provided the HHG process is coherent and reproducible, the XUV electric field produced in a single HHG event will be produced every time by subsequent driving pulses. In this situation, we are driving XUV emission at stable and well defined intervals much like a modelocked oscillator produces optical pulses at stable and well defined intervals. We expect the overall harmonic emission to mimic the single pulse case in terms of the overall spectral shape, but we intend to determine whether a given harmonic order q should have frequency comb teeth separated by the driving laser repetition rate f_r. We expect the carrier envelope frequency to increase with harmonic order as the electric field will be oscillating q times as fast. We can then re-write the frequency comb tooth indexing for the different harmonic orders as

$$f_j = j \times f_r + q \times f_0, \tag{1.14}$$

where j is an integer and f_0 is that of the driving laser. So, provided that the HHG process does not lead to carrier-envelope phase noise, we hope to find a frequency comb structure in the XUV that shares similar properties to the driving laser. For instance, it will then be possible to use the comb structure for high resolution spectroscopy because we can treat each comb tooth similarly to a CW laser [52].

1.4 Applications

There are many examples of spectroscopic application with < 100 nm light that we will briefly summarize below. Another feature of the XUV frequency comb has not been stressed thus far: it is actually one of the highest photon flux sources of XUV radiation available on a table-top. Not only that, it is also nearly as spectrally bright as a synchrotron, the work horse of XUV and x-ray science. We will also highlight some applications unrelated to high resolution spectroscopy but for which the XUV frequency comb is well suited.

1.4.1 Spectroscopic applications

As previously mentioned, precision spectroscopy of atomic hydrogen has been very fruitful and allowed sophisticated bound-state QED calculations to be compared with experiment. The beauty of using hydrogen is that the calculations can be carried out exactly [16]. Singly ionized helium is the next logical step after hydrogen if the goal is to compare to QED calculations [53]. Leading order relativistic corrections to the $1S - 2S$ transition scale as Z^4. Leading order correction to the Lamb shift (splitting between $2S$ and $2P$ levels) also scales as Z^4. This makes QED effects in singly ionized helium over an order of magnitude larger than in atomic hydrogen. Precision spectroscopy of these systems will test the limits of current bound-state QED calculations and possibly reveal new physics.

Helium-like system are also interesting because electron-electron correlations become important. There are currently no methods to perform calculations of helium properties exactly as in the case of hydrogen. Laser spectroscopy on atomic helium has already been performed [54, 55]. At the

time of the test, the experimental uncertainties were close to the achievable theoretical uncertainties. However, more recent experimental efforts aim to beat down the experimental uncertainties to justify improvements on the calculations [56].

Highly charged ions are a relatively untapped source of laboratory spectroscopic investigation. It seems intimidating to trap and cool highly charged ions, but recent experiments are advancing nicely and it will not be long before routine spectroscopic investigation is possible [57]. Highly charged ions are a sensitive testbed to look for variations in the fine structure constant [58–60]. The sensitivity typically scales as Z^2. Highly charged hydrogen-like ions are also postulated to be a useful test bed for looking for parity nonconservation and physics beyond the standard model [61]. In these proposed experiments, highly charged ions would be stored at relativistic velocities to bring the Doppler-shifted resonances into the VUV and XUV where lasers can be used to excite the $1S - 2S$ transition and look for circular dichroism. Since the electrons of highly charged ions are located much closer to the atomic nucleus, looking for strong nuclear affects on the electron spectroscopy could potentially lead to new insights in nuclear physics.

Another interesting target suitable for high resolution spectroscopy is molecular hydrogen and its isotopologues (H_2, HD, D_2). Spectra of molecular hydrogen can be used to constrain the evolution of the electron-proton mass ratio [62]. Further, basic spectroscopic investigation can be used as a test bed for QED in a molecular setting and test our fundamental understanding of the most basic molecular system [63, 64].

A final spectroscopic application of the XUV comb would be a "nuclear" clock. It would work on the same principles of an atomic clock, but rely on a nuclear isomer transition as the frequency discriminator (rather than an electronic transition as in optical clocks). Isomer transitions are typically at x-ray wavelengths. However, thorium is claimed to have a low lying isomer transition near 7.5 eV. To date there is no concrete experimental evidence of this transition and the transition energy is still debated. If it does exist, it would likely make a very nice clock [65]. There is a long-lived isomer transition in uranium with 27 minute lifetime [66, 67] at an energy just under 100 eV. It is unclear whether or not this will be useful for clock operation because the excited state

decay mechanisms are still unknown.

1.4.2 High-flux extreme ultraviolet source applications

The current workhorse for XUV and x-ray radiation sciences is the synchrotron. It produces high flux, spatially coherent, and pulsed light [68]. A small list of its applications contain microscopy, lithography, angle-resolved photoemission spectroscopy (ARPES), crystallography, and structural biology [69]. Most of these would benefit from a light source with similar properties but in a compact, user-friendly package that does not rely on a billion dollar user facility with limited access [69]. For the sake of brevity, we will discuss application to ARPES. What follows will apply to most photoelectron based spectroscopies that rely on XUV light for photoemission.

Many photoelectron based spectroscopies suffer from an effect known as "space charge." For ARPES, the ability to detect photoelectron energy and momentum at high resolution is critical. If too many photoelectrons are simultaneously ejected from the surface of a sample, as they drift to the detector, the momenta will change due to Coulomb repulsion and this effectively blurs out the experimental resolution. To overcome this, scientists usually reduce the brightness of the XUV source that is generating the photoemission, but this comes at the cost of reduced signal size leading to worse statistics in the data (since the experimental shots occur at a fixed rate). The ideal condition is to have a light source that produces maybe only a few photons per pulse but repeats at a high frequency. This is exactly what the XUV frequency comb does very well. The XUV frequency comb is of comparable brightness to a synchrotron *and* operates in a regime where space charge effects are minimal for ARPES application, or other photoelectron-based spectroscopy. An example of how powerful a laser-based source for ARPES can be, we refer to the work of Ref. [70]. The data taken with a laser-based ARPES apparatus clearly has better energy resolution and did not require a trip to the synchrotron. The higher energy resolution was used to observe much more subtle physical phenomena that would have otherwise gone unnoticed in a more traditional ARPES apparatus.

1.5 Thesis outline

For our work, the primary goal of the XUV frequency comb is to combine the precision laser stabilization required to produce an optical frequency comb with the highly nonlinear process of HHG to up convert the near infrared frequency comb into the XUV. The rest of the thesis will describe results of the XUV frequency comb experiments.

- Chapter 2 contains the experimental apparatus including the laser system and the femtosecond enhancement cavities (fsECs).
- Chapter 3 contains a description of HHG as it pertains to power scaling XUV frequency combs and the microscopic phenomena the XUV comb can probe.
- Chapter 4 contains the construction and operating principles of the XUV interferometer used to test the temporal coherence properties of the XUV light originating from HHG.
- Chapter 5 contains our results in performing heterodyne interferometry in the XUV to study the XUV comb phase coherence and how we can use it to probe strong-field phenomena.
- Chapter 6 contains our efforts to use the XUV comb technology to study strong-field effects in molecular systems.
- Chapter 7 contains conclusions and an outlook for future XUV comb work.

Chapter 2

Experimental apparatus

In this chapter, we cover the main experimental apparatus and its working principles. Details about the XUV interferometer will be saved until Chapter 3. Here, we present the femtosecond enhancement cavity, the linchpin of XUV frequency comb generation. We also present the laser system and its modifications since its original construction. We will also discuss the experimental vacuum chamber and operations unique to the XUV frequency comb.

2.1 Amplifying ultrafast laser pulses

Most HHG experiments use lasers that have 100 μJ – 10 mJ pulses energies while maintaining ultrafast pulse durations ($<$ 100 fs). With these parameters, it is very straightforward to focus the laser beam to achieve peak intensities $< 10^{14}$ W cm^{-2}, a sufficient intensity for HHG. These high pulse energies are achieved with low repetition rate amplifiers [71, 72]. The low repetition rate is necessitated by the amplifier pumping laser (or flashlamp) technology. The XUV frequency comb requires similar pulse energies of 10 μJ – 100 μJ while still maintaining the full repetition rate of the initial frequency comb of typically 100 MHz. The amount of average power required for a 100 μJ frequency comb at 100 MHz would be 100 μJ $\times$ 100 MHz = 10 kW! Currently, no "active" amplification technology can achieve this. However, there is a "passive" approach that relies on high finesse optical resonators. We call these special resonators femtosecond enhancement cavities (fsECs). The details of operation will be forthcoming. However, what they achieve is quite remarkable. By coupling a frequency comb to an enhancement cavity, the pulses resonating

inside the cavity can have an average power potentially $> 200\times$ greater than the injected laser while preserving the full repetition rate of the frequency comb and its ultrafast pulse duration. Using this technology, the intracavity pulse is "passively" amplified and can be used for strong-field experiments. Therefore, only a 50 W average power frequency comb (a power completely within current technology [73]) can achieve 10 kW of average power while maintaining ultrafast pulse durations.

2.2 The femtosecond enhancement cavity

An optical cavity is a routinely used piece of instrumentation. Here, we will outline the basic theory of operation and highlight aspects most relevant for femtosecond pulse enhancement. For most of the discussion, we will focus on enhancement cavities for continuous wave lasers since it simplifies the description. However, the extension to coupling frequency combs to enhancement cavities is quite simple because frequency combs behave as if they were composed of a series of continuous wave lasers evenly spaced by the repetition rate. The enhancement cavity for a frequency comb will be referred to as a femtosecond enhancement cavity (fsEC).

The XUV frequency comb relies on Fabry-Pérot ring resonators. Schematics of ring resonators are shown in Fig. 2.1. Fig. 2.1a is a typical four mirror resonator. We are however not restricted to a four optic cavity. Fig. 2.1b shows a resonator with a fifth optic placed between the curved mirrors. This optic, the "Yost grating" [74], is used to outcouple HHG light from the cavity and will be discussed later in Sect. 2.2.6. For the current discussion, it can be treated as an additional high reflector in the cavity. As we will discuss, the total length of the cavities shown in Fig. 2.1 are determined mainly by the frequency comb repetition rate. Therefore, the separation of the curved mirrors can be used to tune the size of the beam waist in the resonator and the transverse mode properties.

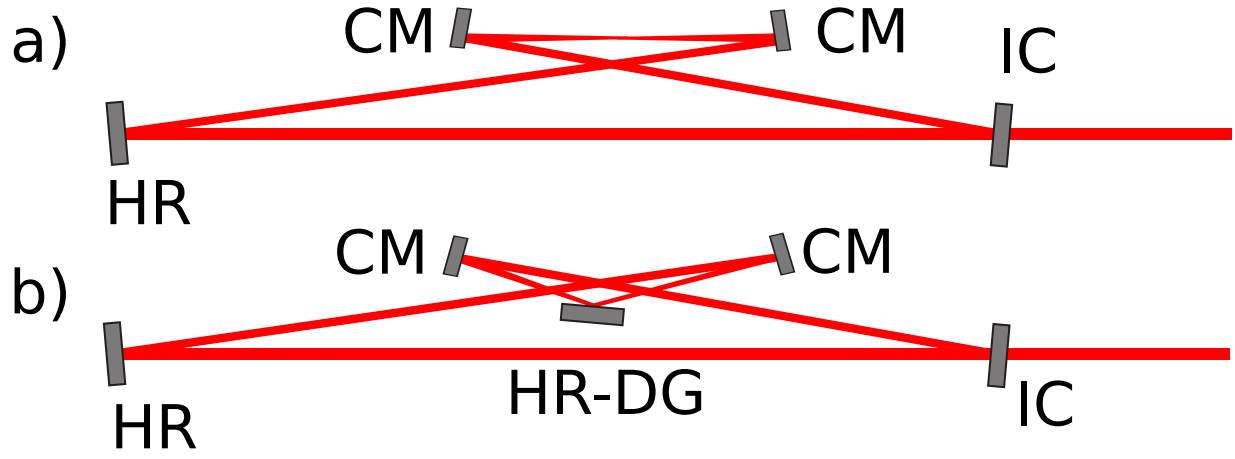

Figure 2.1: **a)** A four mirror ring cavity is schematically shown. HR, high reflector. CM, curved mirror. IC, input coupler. **b)** A five mirror ring cavity is shown. This cavity is equipped with the Yost grating which acts as a high reflecting mirror at the driving laser wavelength. For shorter wavelengths, it behaves as a diffraction grating. HR-DG, high reflector diffraction grating *aka* the Yost grating [74].

2.2.1 Cavity finesse, buildup, and contrast

Referring to Fig. 2.1, we can write the intracavity laser electric field E_{cav} as it traverses around the cavity for multiple round trips as a series given by

$$E_{cav}(\omega) = \sqrt{\epsilon} E_0 t_i \left(1 + r_i r_c e^{i\phi(\omega)} + (r_i r_c e^{i\phi(\omega)})^2 + (r_i r_c e^{i\phi(\omega)})^3 + \dots\right), \tag{2.1}$$

where E_0 is the incident electric field, r_i is the reflectivity coefficient[1] of the input coupler, t_i is the transmission coefficient of the input coupler, r_c is the effective reflectivity coefficient of the rest of the cavity optics, and $\phi(\omega)$ is the total phase shift on the electric field after one round trip through the cavity. The phase shift term includes propagation and dispersive effects of the mirrors and is therefore sensitive to the laser operating frequency ω. The mirror reflectivity coefficient r and transmission coefficient t values are also in general laser frequency dependent. However, we will not explicitly denote this for clarity. The $\sqrt{\epsilon}$ term is due to imperfect transverse mode overlap between the laser beam and the cavity mode. We refer to this term as a "mode matching factor" and its origin will be discussed in detail later. For now, $\sqrt{\epsilon} = 1$ is for perfect overlap of the laser beam profile and the cavity mode. Since reflectivity coefficients are less than 1, the series in Eq. 2.1 converges to

$$E_{cav} = \sqrt{\epsilon} E_0 \frac{t_i}{1 - r_i r_c e^{i\phi(\omega)}}. \tag{2.2}$$

We perform a similar treatment for the electric field reflected from the cavity. The reflected electric field E_{ref} is written as

[1] The "reflectivity coefficient" is how much of the electric field is reflected. It is more common to refer to a mirror "reflectivity", which is how much electric field intensity is reflected. Generally, quantities that refer to electric field intensity will be capitalized. This is also true for mirror transmission.

$$E_{ref} = -\sqrt{\epsilon}E_0 r_i + \sqrt{\epsilon}E_0 r_c t_i^2 e^{i\phi(\omega)} + \sqrt{\epsilon}E_0 r_i r_c^2 t_i^2 e^{2i\phi(\omega)} + \dots , \tag{2.3}$$

$$= -\sqrt{\epsilon}E_0 r_i + \sqrt{\epsilon}\frac{E_0 t_i^2}{r_i}\left(r_i r_c e^{i\phi(\omega)} + \left(r_i r_c e^{i\phi(\omega)}\right)^2 + \dots\right) , \tag{2.4}$$

$$=\sqrt{\epsilon}E_0 \frac{r_c t_i^2 e^{i\phi(\omega)} - r_i}{1 - r_i r_c t_i^2 e^{i\phi(\omega)}} . \tag{2.5}$$

For optical cavities, we routinely measure laser intensities of the reflected and transmitted light. The incident, reflected and intracavity intensity is defined as $I_{0,ref,cav} = |E_{0,ref,cav}|^2$. We can express I_{ref} and I_{cav} as

$$I_{ref} = \epsilon I_0 \left(\frac{(r_i - r_c)^2 + 4r_i r_c \sin^2(\phi(\omega)/2)}{(1 - r_i r_c)^2 + 4r_i r_c \sin^2(\phi(\omega)/2)}\right) , \tag{2.6}$$

$$I_{cav} = \epsilon I_0 \left(\frac{t_i^2}{(1 - r_i r_c)^2 + 4r_i r_c \sin^2(\phi(\omega)/2)}\right) . \tag{2.7}$$

At this point, we can already extract useful cavity characterization parameters. By inspection, the intracavity field is largest when $\phi(\omega) = 0$ (and modulo intervals of 2π). It is useful to fully express $\phi(\omega)$ as

$$\phi(\omega) = kL + \phi_d(\omega) = \frac{\omega}{c}L + \phi_d(\omega), \tag{2.8}$$

where k is the laser wavevector, L is the round-trip cavity length, c is the speed of light, and $\phi_d(\omega)$ is the phase shift due to mirror dispersion. As mentioned, the intracavity power is maximized when $\phi(\omega)$ is periodic in 2π. In the absence of mirror dispersion (we will consider this later), we have

$$\frac{\omega}{c}L = m\, 2\pi, \tag{2.9}$$

where m is an integer. The frequency spacing at which the cavity repeats itself is thus $2\pi c/L$ in angular frequency units (it is simply c/L in Hz). This is defined as the free spectral range (FSR). We can solve for $\phi(\omega')$ to determine the half maximum intensity, again assuming the absence of dispersion. We assume the resonant frequency is at ω_0 and the frequency detuning required to achieve half of maximum intracavity intensity is ω'. Thus, we have

$$\phi(\omega') = \quad 2\sin^{-1}(\tfrac{1-r_i r_c}{2\sqrt{r_i r_c}})\,, \tag{2.10}$$

$$\phi(\omega') \approx \qquad \tfrac{1-r_i r_c}{\sqrt{r_i r_c}}. \tag{2.11}$$

$$\tag{2.12}$$

With this manipulation, we solve for twice the frequency detuning required to achieve half transmission and define this as the full-width at half maximum (FWHM).

$$\text{FWHM} \equiv \Delta\omega_{1/2} \equiv 2|\omega' - \omega_0|\,, \tag{2.13}$$

$$\omega_0 = m\,\pi\frac{c}{L}\,, \tag{2.14}$$

$$\omega' = \frac{c}{L}\left(\frac{(1-r_i r_c)}{\sqrt{r_i r_c}} - m\,\pi\right)\,, \tag{2.15}$$

$$\text{FWHM} = \frac{c}{L}\frac{2(1-r_i r_c)}{\sqrt{r_i r_c}}\,, \tag{2.16}$$

$$\tag{2.17}$$

where the FWHM is given in angular frequency units (divide by 2π for units in Hz). The finesse $\mathcal{F}$ is defined as the ratio of the FSR to the FWHM. We have

$$\mathcal{F} = \quad \tfrac{\text{FSR}}{\Delta\omega_{1/2}}, \tag{2.18}$$

$$= \quad \tfrac{\pi\sqrt{r_i r_c}}{1-r_i r_c}. \tag{2.19}$$

This definition of $\mathcal{F}$ is much more useful if expressed in terms of mirror reflectivity and not reflectivity coefficients. The mirror reflectivity is defined as $R \equiv r^2$. Similarly, mirror transmission is $T \equiv t^2$. Mirror properties also obey

$$R + T + A = 1, \tag{2.20}$$

where A is the mirror loss. This is the fraction of light that is neither transmitted nor reflected. It usually originates from scatter or absorption of the intracavity elements. If we define a mirrors total

loss as $\mathcal{L}_m = A_m + T_m$, where m is just the mirror label, we can rewrite our definition of finesse is a very useful way.

$$\mathcal{F}^2 = \pi^2 \frac{r_i r_c}{1 - r_i r_c}, \tag{2.21}$$

$$= \pi^2 \frac{\sqrt{R_i R_c}}{1 - \sqrt{R_i R_c}}, \tag{2.22}$$

$$\approx \frac{\pi^2}{[\frac{1}{2}(\mathcal{L}_i + \mathcal{L}_c)]^2}, \tag{2.23}$$

$$\mathcal{F} = \frac{2\pi}{\mathcal{L}}, \tag{2.24}$$

where we have implicitly defined the total loss as $\mathcal{L} = \mathcal{L}_i + \mathcal{L}_c$.

Another useful quantity, and possibly the most important for our application, is a cavity's buildup β on resonance defined as $\beta = I_{cav}/I_0$. When a cavity is driven on resonance, the intracavity power will be greater than the driving laser power. Starting with Eq. 2.7 and performing similar manipulations used to arrive at Eq. 2.24, we have

$$\beta = \frac{I_{cav}}{I_0} = \epsilon T_i \frac{\mathcal{F}^2}{\pi^2}. \tag{2.25}$$

Similarly, we can determine the reflected cavity power expressed as

$$I_{ref} = \epsilon I_0 \left[(\mathcal{L}_{cav} - \mathcal{L}_i) \frac{\mathcal{F}}{2\pi} \right]^2. \tag{2.26}$$

It can be seen that the reflected power goes to zero if the input coupler losses match the rest of the cavity losses. This is known as impedance matching. If $\mathcal{L}_i > \mathcal{L}_{cav}$, this is an overcoupled cavity. If $\mathcal{L}_i < \mathcal{L}_{cav}$, this is an undercoupled cavity. The greatest buildup for a fixed finesse will occur in the overcoupled case. Looking at Eq. 2.25, for a given finesse ($\mathcal{L}_{cav} + \mathcal{L}_i =$ constant), the buildup will be directly proportional to T_i, so bigger T_i is better.

We can also define the cavity contrast $\mathcal{C}$ as

$$\mathcal{C} = \frac{I_0 - I_{ref}}{I_0}\,, \tag{2.27}$$

$$= 1 - \epsilon \left[(\mathcal{L}_{cav} - \mathcal{L}_i) \frac{\mathcal{F}}{2\pi} \right]^2 . \tag{2.28}$$

Measurement of $\mathcal{C}$, $\mathcal{F}$, and β constitute a full characterization of the cavity. However, $\mathcal{C}$ and β are dependent on the modematching factor ϵ. Measurement of $\mathcal{F}$ is the best way to determine cavity loss since it does not depend on mode matching. A straightforward way to measure finesse is to stabilize the cavity on resonance and then rapidly turn off the laser. The cavity intensity (in transmission or reflection) will decay exponentially as a function of time. The time constant of decay can be related to $\mathcal{F}$ in the following way. After a field has been stored up in the cavity and then rapidly turned off, we can write the energy as a function of time $\mathcal{E}(t)$ as

$$\frac{d\mathcal{E}(t)}{dt} = -\frac{\mathcal{E}_0}{\tau}. \tag{2.29}$$

We remember that the loss of intensity per round trip is $\mathcal{L}$ and the energy lost per round trip is $\mathcal{L}\mathcal{E}$. The energy lost per unit time becomes $\mathcal{L}\,\mathcal{E}c/L$ (This is just $\mathcal{L}\,\mathcal{E}\,\mathrm{FSR}/2\pi$ where the FSR is expressed here in Hz). Plugging this in we have

$$\frac{d\mathcal{E}(t)}{dt} = -\mathcal{L}\,\mathrm{FSR}\,\mathcal{E}_0 \tag{2.30}$$

$$\tau \Rightarrow \frac{1}{\mathcal{L}\,\mathrm{FSR}}. \tag{2.31}$$

We can now insert Eq. 2.24, rearrange and obtain

$$\mathcal{F} = 2\pi\,\tau\,\frac{c}{L}. \tag{2.32}$$

It is important to note that this is the energy (or intensity) decay time τ. The field decays twice as slowly, so $\tau_{intensity} = \tau_{field}/2$.

Sometimes it is not feasible to turn the laser off rapidly or to stabilize the cavity. An alternative method is to rapidly sweep the laser frequency across the cavity resonance at a rate much faster

than the cavity lifetime. The cavity field that is briefly resonant will form a heterodyne beat with the reflected sweeping laser beam. The heterodyne nature (rather than homodyne) is due to the fact that the resonant field is at a fixed frequency, but the incident beam is frequency chirped. Therefore, when they are overlapped with the reflected beam from the cavity input coupler, they form a beatnote. This ringdown signal can be seen in Fig. 2.2. The signal is fit to a damped, chirped sine wave. A field decay of 1.05 μs (assuming an FSR = 154 MHz) corresponds to a finesse of about 500. The input coupler for this data was $T_i = .008$. This finesse measurement implies a loss of $\mathcal{L}_{cav} = 0.0046$. Assuming perfect mode matching ($\epsilon = 1$), the expected cavity contrast would be $\mathcal{C} = 0.7$ and the expected buildup would be $\beta = 200$. An experimentally measured buildup or contrast can be used to determine the mode matching factor ϵ. For this example, the cavity loss $\mathcal{L}_{cav}$ was due to an optic with an hole drilled in the center (see Sect. 2.2.6 for information of geometric output coupling). When a normal optic is used, it is very routine to have a cavity with $\mathcal{L}_{cav} \leq 0.0005$.

2.2.2 Gaussian beams and gaussian beam manipulation

So far, we have determined that a ring resonator has resonant frequencies evenly spaced by the FSR, neglecting dispersion. However, we have not considered the transverse mode profile of the cavity. To do this, we rely on the formalism of Gaussian beam propagation and the $ABCD$ matrices [14]. The paraxial wave equation is given by

$$\nabla_t^2 u(x,y,z) - 2ik\frac{\partial u(x,y,z)}{\partial z} = 0, \tag{2.33}$$

where ∇_t^2 is the transverse Laplacian defined $\nabla_t^2 = \partial/\partial x + \partial/\partial y$. Eq. 2.33 has well known solutions. The solution for a Gaussian beam field is

$$u(x,y,z) = \frac{u_0}{\sqrt{1+(z/z_R)^2}}\exp\left[-\frac{r^2}{\omega(z)^2} - ik\left(z + \frac{r^2}{2R(z)}\right) + i\tan^{-1}\left(\frac{z}{z_R}\right)\right], \tag{2.34}$$

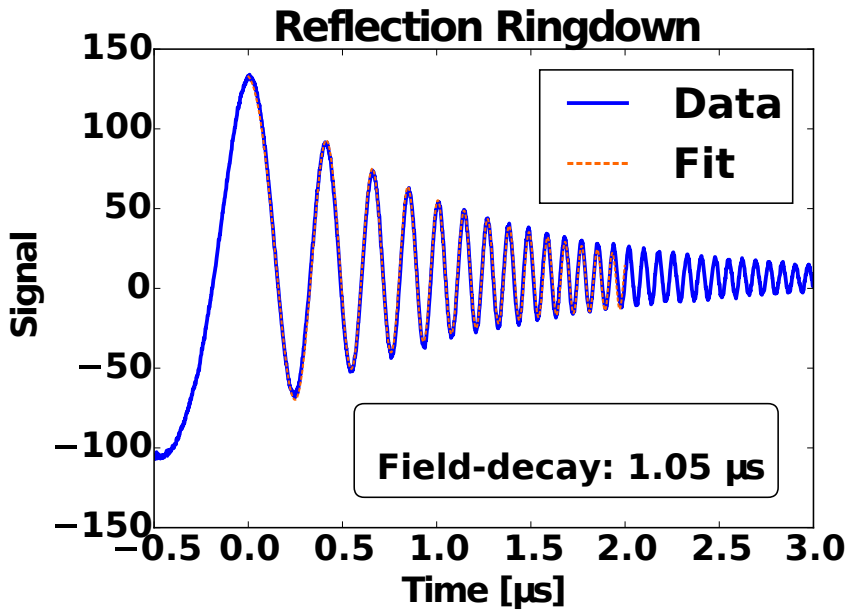

Figure 2.2: Cavity ringdown performed in reflection. A fit using a chirped, damped sine wave is used to extract the electric field lifetime in the cavity. This is used for determination of the cavity finesse. A field decay of 1.05 μs is consistent with a finesse of $\mathcal{F} \approx 500$ (asssuming $c/L = 154$ MHz). This should yield a buildup of $\beta \approx 200$.

where $r^2 = x^2 + y^2$. The Rayleigh range is $z_R = \pi w_0/\lambda$, where w_0 is the beam waist at the focus and $w(z)$ is the beam waist at a position z which can be written as

$$w(z) = w_0\sqrt{1 + \left(\frac{z}{z_R}\right)^2}. \tag{2.35}$$

The wavefront radius at a position z is

$$R(z) = z\left[1 + \left(\frac{z_R}{z}\right)^2\right]. \tag{2.36}$$

Another important feature of Gaussian beams is that there are two terms that lead to a phase shift of the beam during propagation in z. They are

$$\phi = ikz - i\tan^{-1}\left(\frac{z}{z_R}\right) = \phi_{prop} + \phi_{Gouy}. \tag{2.37}$$

While the first term is the usual propagation phase, the second is called the Gouy phase. The Gouy phase shift depends on how tight a Gaussian beam is focused and where the beam is relative to its focus. While the Gouy phase usually does not have significant consequences in dealing with laser beams, it will be very important when we consider phase matching between the driving laser and the high-order harmonics later in this thesis.

While the above discussion is in principle all we need to know about Gaussian beams in order to use them, it is often much more mathematically convenient to deal with the complex beam parameter q defined as

$$\frac{1}{q(z)} = \frac{1}{R(z)} - i\frac{\lambda}{\pi w(z)^2}. \tag{2.38}$$

While at the moment, this may seem arbitrary, it allows us to recast Eq. 2.34 in a slightly different way

$$u(x, y, z) = \frac{u_0}{\sqrt{1 + (z/z_R)^2}}\exp\left[-i\left(P(z) + \frac{k}{2q(z)}r^2\right)\right], \tag{2.39}$$

where we have defined a new parameter $P(z)$ as

$$iP(z) = \ln\sqrt{1 + \left(\frac{z}{z_R}\right)^2} + -i\tan^{-1}\left(\frac{z}{z_R}\right). \tag{2.40}$$

The benefit of this substitution is that manipulation of the q parameter and determining it anywhere along a Gaussian beam becomes very straightforward and it contains most relevant geometric information about the Gaussian beam. At the beam focus q is defined as $q_0 = i\,z_R$. At a further distance z, $q(z)$ becomes a very simple result

$$q(z) = q_0 + z. \tag{2.41}$$

Therefore, with knowledge of the q parameter of a beam, the waist w and wavefront curvature R can be determined. A couple other useful quantities are easy to extract with the q parameter

$$\text{Distance to waist} = -Re[q(z)] \tag{2.42}$$

$$w_0 = \sqrt{\tfrac{\lambda}{\pi} Im[q(z)]}. \tag{2.43}$$

The most powerful result of this discussion of Gaussian beams is that the q parameter can be determined and manipulated using simple matrix operations. To go from $q_1 \to q_2$, simple rules are followed.

$$\begin{pmatrix} q_2 \\ 1 \end{pmatrix} = \begin{pmatrix} A & B \\ C & D \end{pmatrix} \begin{pmatrix} q_1 \\ 1 \end{pmatrix} \tag{2.44}$$

A table of useful $ABCD$ matrices for common optics is given in Table 2.1. By careful determination of a q parameter at a given point in a laser beam, it can be accurately predicted at a later place even if mode changing optics like lenses are employed.

2.2.3 Cavity geometry

We are now ready to use the briefly outlined $ABCD$ matrix formalism to determine the transverse mode structure of the cavity. We are able to use the transverse mode structure to

Optic	$ABCD$
Free Space	$\begin{pmatrix} 1 & z \\ 0 & 1 \end{pmatrix}$
Lens	$\begin{pmatrix} 1 & 0 \\ -1/f & 1 \end{pmatrix}$
Curved mirror x-axis	$\begin{pmatrix} 1 & 0 \\ -2/[R\cos(\theta)] & 1 \end{pmatrix}$
Curved mirror y-axis	$\begin{pmatrix} 1 & 0 \\ -2\cos(\theta)/R & 1 \end{pmatrix}$

Table 2.1: A table of common optical elements and their corresponding $ABCD$ matrices. For this table, f is the focal length of the lens, R is the radius of curvature of the mirror, θ is the angle of incidence on the optic.

accurately measure important cavity parameters such as the spot size in the resonator. Assuming a laser beam with q_1 is incident on the input coupler of a cavity like that of Fig. 2.1a, we can multiply q_1 by all the relevant $ABCD$ matrices to describe the intracavity optics. When the beam returns to the input coupler, in order for the cavity to be stable, the q parameter must return to the original value. What we have just described is a powerful method to determine where the optics should be placed so that a stable cavity is possible. This is equivalent to solving the eigenvalue problem of the $ABCD$ matrix that is product of all the intracavity optics. This will need to be done for the vertical axis of the cavity and the horizontal axis independently as they do not have identical $ABCD$ matrices.

Assuming a generic cavity, we have the following equation

$$q_2 = \frac{A\,q_1 + B}{C\,q_1 + D}\,, \tag{2.45}$$

where we now require that $q_2 = q_1$ after a full round trip. We can then solve for q directly to obtain

$$\frac{1}{q} = \frac{D - A}{2B} \pm \frac{1}{2B}\sqrt{(A - D)^2 + 4BC}. \tag{2.46}$$

Since the $ABCD$ matrix elements are real, we can determine that the first term in the equation must be real and the second must be imaginary because q is in general complex. Therefore, we have

$$R = \frac{2B}{D-A}, \tag{2.47}$$

$$w = \sqrt{\frac{2\lambda|B|}{\pi\sqrt{4-(A+D)^2}}}. \tag{2.48}$$

It is important to remember that these equations are only valid at the reference point of the cavity determined before constructing the $ABCD$ matrix. To determine $R(z)$ and $w(z)$ somewhere else in the cavity, $ABCD$ matrices will be needed to propagate the q parameter to that point. For example, in order to send in a beam with the correct q parameter to the cavity, the intracavity beam determined by the $ABCD$ matrices can be propagated to the input coupler. If there is any spatial mismatch between the intracavity beam and the injected beam, this imperfect overlap leads to the mode matching factor ϵ which was first introduce in Eq. 2.1. Any light that is not mode matched to the cavity will be rejected and is not useful for power enhancement.

It can be seen from Eq. 2.48 that in order to have a real and physical value for the waist, we have a constraint on A and D being,

$$\text{Stability Region: } |A + D| \leq 2. \tag{2.49}$$

Assuming the overall cavity length is fixed [2] , the only way to adjust A and D for our ring resonators is to change the distance between the curved mirrors. There is only a small range of values that will satisfy Eq. 2.49 and hence a small range of suitable curved mirror separations and mirror radius of curvatures. This is referred to as the "stability region."

The results of an $ABCD$ matrix calculation are shown in Fig. 2.3. Assumed is a cavity with an FSR of 154 MHz and with curved mirrors with radii of curvature equal to 15 cm and 10 cm. The angle of incidence on the curved mirrors is 3 deg. Fig. 2.3a shows the focal waist w_0 of the intracavity beam changing as a function of curved mirror separation. The change is most dramatic at the edge of the stability region. Due to the angle of incident on the mirrors, the horizontal beam

[2] This will be required to inject a pulsed laser into the cavity. Typically, the length of the resonator is picked so the FSR is equal to the repetition rate

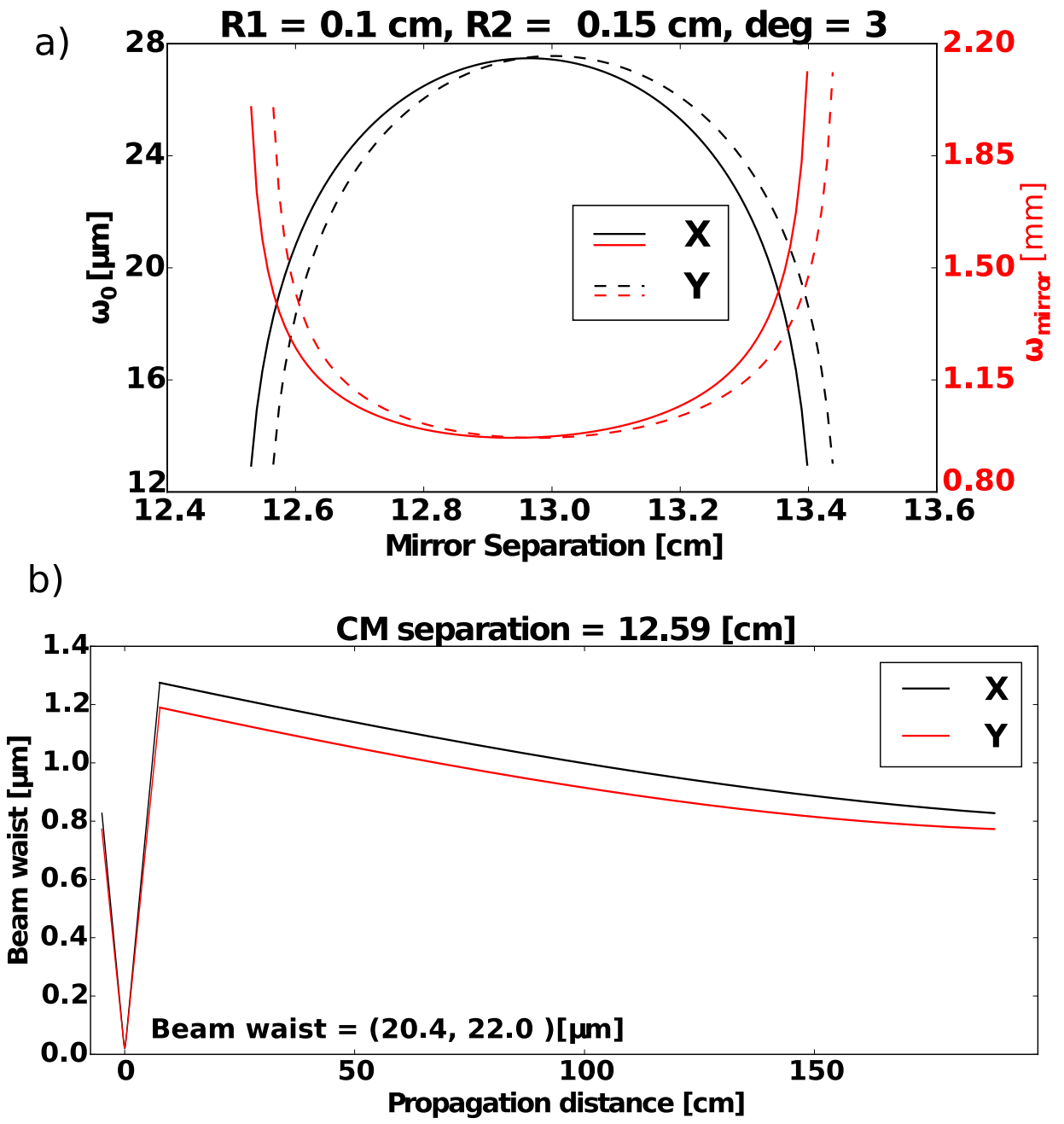

Figure 2.3: **a)** The effect on the cavity focus and the spot size on the second curved mirror as a function of curved mirror separation. **b)** The beam waist as a function of position in the cavity at a fixed curved mirror separation.

size is not necessarily the same as the vertical axis thus leading to astigmatism. At first glance, operating at the outer stability edge would be equivalent to the inner stability edge. However, this is not true. Operating at the outer stability edge will lead to a weak second focus in the cavity. If the second beam waist falls on an optic, the increased peak intensity can lead to optical damage. For the work in this thesis, we generally operate at the inner stability edge. Operating at either stability edge will increase the beam size on the curved mirrors, which will also help with damage considerations. Fig. 2.3a also plots the beam waist on the curved mirror immediately after the focus as a function of curved mirror separation. Fig. 2.3b shows the beam waist as a function of position in the resonator. Again, the astigmatism cause by the non-normal reflection from the curved mirrors is apparent. For Fig. 2.3b, a curved mirror separation of 12.59 cm was assumed. This leads to a focal waist of $w_0 = (20.4, 22.0)\mu$m. In practice, operating the cavity this close to the stability edge as shown in this example is routine and often necessary for HHG work.

While it is in principle possible to determine the cavity spot size by measuring the curved mirror separation, in practice, it is hard to make this very accurate. Instead, we can rely on another feature of the cavity to determine the spot size. A Gaussian beam is only the lowest order transverse mode supported by an optical cavity. In general, the cavity supports Hermite-Gaussian modes [14]. They are denoted by TEM_{mn} where m, n are the transverse mode order. The Gaussian beam we have discussed thus far is the lowest order mode denoted as TEM_{00}. The spatial mode structure becomes much more complex as m, n increases. TEM_{mn} modes behave similarly to a normal Gaussian beam. However, one important difference is that the Gouy phase is modified to be

$$\phi_{Gouy,m,n} = (m + n + 1)\tan^{-1}(z/z_R). \tag{2.50}$$

Since a TEM_{00} beam will have a different round trip phase shift than a TEM_{mn}, the resonant frequencies of the cavity will also be different. Depending on the $ABCD$ matrix that describes the resonator, the resonant frequencies of the q^{th} cavity mode for a TEM_{mn} is written as ν_{qmn}

$$\nu_{qmn} = \text{FSR}\left[q + (m+n+1)\cos^{-1}\left(\sqrt{\frac{1}{4}(2+A+D)}\right)\right]. \tag{2.51}$$

It is often difficult to measure exact resonant frequencies unless a calibrated laser or a frequency comb is employed. However, measuring the relative frequencies of high order transverse modes from TEM_{00} is very straightforward. Therefore, if one can measure the relative frequency spacings of higher order modes, using Eq. 2.51, one can determine to a reasonable degree of accuracy what the $A + D$ coefficients must be. If this is known, then it is straightforward to determine the spot size. This is a very important point because it allows for very accurate peak intensity calibrations for intracavity work. Peak intensity is one of the most important parameters for strong-field physics experiments and is often quite tricky to measure. In the cavity, because the laser mode profile is so well-defined, cavity-based strong-field experiments do not suffer from peak intensity calibration issues; it is very easily inferred from the measurements.

2.2.4 Cavity mirror dispersion and the femtosecond enhancement cavity

We now turn to the effect of mirror dispersion and how it affects cavity operation. This is ultimately the only conceptual difference between operating an enhancement cavity for continuous wave lasers and for frequency comb lasers (femtosecond lasers). Mirror dispersion essentially leads to a different phase shift upon reflection for different wavelengths. For a cavity driven by a continuous wave laser, this is usually of very little consequence because you typically only excite one cavity resonance (or a couple nearby cavity resonances) at a single time. For the work in this thesis, our goal is to inject a frequency comb into the cavity. Recall that the frequency spacing of the comb teeth is determined by f_r. A cavity that has zero dispersion also has perfectly evenly spaced modes separated by the FSR. So, if one matches the frequency comb's f_r to the FSR, then all of the comb teeth can be on resonant at the same time. However dispersion-less mirrors with reflectivity exceeding 99.9% do not exist.

Much in the same way a Gouy phase shift will shift the cavities resonant frequency, so will a phase shift from reflection off of a mirror or if there are any dispersive materials, like a crystal,

inside the cavity. So, the resonant frequencies of the cavity will not be evenly spaced by the FSR, rather they will start to deviate depending on how much dispersion is present. This is a problem for frequency combs because the spacing is always f_r and it is not possible to compensate for the non-uniformity of the FSR spacing in a dispersive resonator.

Dispersion $\phi_d(\omega)$ (originally introduced and dropped from Eq. 2.8) can usually be expanded in a Taylor series as

$$\phi_d(\omega) = \phi_0 + \phi_1(\omega - \omega_0) + \phi_2(\omega - \omega_0)^2 + \phi_3(\omega - \omega_0)^3 + \dots . \tag{2.52}$$

Each dispersion order affects a laser pulse differently. ϕ_0 will cause the electric field to shift in phase relative to the pulse envelope and its original value, but will not affect the position of the envelope. ϕ_1 will cause the pulse envelope to delay in time, but the electric field remains constant (however, the carrier phase relative to the envelope maximum may change). ϕ_2 causes the pulse to broaden symmetrically in time. ϕ_3 and higher will start to distort the pulse in more complex ways. If we consider a cavity with only a ϕ_0, after each round trip through the cavity, the phase of the electric field will have shifted by some small amount relative to the carrier. The injected pulse must be adjusted to avoid destructive interference at the input coupler. Since this happens every round trip, it amounts to setting the carrier-envelope offset frequency $f_0 = \phi_0 f_r$. In the frequency domain, this is a uniform shift of all the cavity resonances from 0. For cavity-comb coupling, ϕ_0 and ϕ_1 can be compensated by judicious choice of f_r and f_0 such that

$$f_0 = -(\phi_o - \omega_0\phi_1)f_r, \tag{2.53}$$

$$f_r = \frac{c}{L}(1 - \phi_1\frac{c}{L}). \tag{2.54}$$

Mirror manufacturers will usually provide group-delay dispersion (GDD) for their mirrors. By integrating the GDD data (typically measured in fs^2), $\phi_d(\omega)$ can be determined. Then, ϕ_0 and $\phi_1(\omega - \omega_0)$ can be subtracted from the data to simulate proper f_r and f_0 choice. The remaining

dispersion can then be plugged into Eq. 2.7. It is useful to express the relation of the intracavity field to the injected cavity field as a transfer function [75, 76]. We then have

$$E_{cav} = B(\omega)e^{i\psi(\omega)}E_0, \tag{2.55}$$

where we have made the following definitions

$$\psi(\omega) = \arg\left[\frac{t_i}{1-r_i(\omega)r_c(\omega)e^{i\phi_d(\omega)}}\right], \tag{2.56}$$

$$B(\omega) = \left|\frac{E_{cav}(\omega)}{t_i\frac{\mathcal{F}}{\pi}E_0(\omega)}\right|. \tag{2.57}$$

where $\mathcal{F}$ was calculated for the peak value of the mirror coating. We can interpret $\psi(\omega)$ as the spectral phase of the circulating pulse and $B(\omega)$ as the frequency dependent coupling efficiency. The cavity electric field can be determined by Eq. 2.2. An example of this analysis of a cavity containing three Layertec high-power, low loss optics plus one low dispersion input coupler of $R = 0.985$ is shown in Fig. 2.4. The injected pulses were assumed to be 70 fs transform limited, centered at 1070 nm, and a Gaussian profile in time. Fig. 2.4a shows the total GDD of all four cavity mirrors. Fig. 2.4b,c shows the phase shift with the zeroth and linear terms removed upon a single mirror reflection and for the whole cavity. The cavity coupling efficiency (and hence bandwidth) is shown in Fig. 2.4d and is a plot of $B(\omega)$. For a 70 fs, transform limited pulse, the time domain and wavelength domain comparisons of the injected pulse and circulating pulse are shown in Fig. 2.4e,f respectively. The bandwidth of the mirrors is quite good and very little spectral filtering is expected. However, the residual phase shift from the cavity, even though it does not affect coupling bandwidth strongly, is still strong enough to alter the pulse in the time domain. For this example, the effect is to increase the pulse duration to about 75 fs. If shorter pulses are used or a cavity with higher finesse, the pulse distortions will become much more severe because of the increased spectral filtering and sensitivity to mirror dispersion. To date, mirrors with lower dispersion than the ones considered here are possible. Cavities with a $\mathcal{F} = 500$ that support 30 fs pulses have been developed [77]. However, their mirror technology relies on the high index material of their quarter wave stack to be Nb_2O_5.

Our mirrors from Layertec use HfO_2 which has a slightly lower index[3] . The contrast between the high index layer and the low index layer (usually SiO_2) sets the mirrors bandwidth. The main drawback to using Nb_2O_5 mirrors is that they have much lower damage thresholds compared to HfO_2 making the cavities less reliable and limit the scalability of the cavity to higher pulse energy. So, when faced with a trade-off between high bandwidth and day-to-day robustness, we sided with robustness.

2.2.5 Laser-cavity stabilization

We have already discussed how resonators have resonant frequencies spaced by the FSR and have a linewidth. If a laser is incident on a cavity with a frequency close to a resonance, but still well outside the linewidth, the cavity will reject the light. If the laser frequency is tuned into resonance, it can be effectively injected and transmitted through the cavity. The cavity is essentially a frequency discriminator. Lasers do not typically stay at a given frequency for very long, but they can be disciplined to an optical cavity that can be made, relatively speaking, frequency stable. In order to lock a laser to a cavity, there needs to be a way of determining the cavity resonant frequency with respect to the laser. The method employed throughout this thesis is the Pound-Drever-Hall (PDH) approach [79]. It is based on a microwave Pound stabilizer but applied to lasers at optical frequencies. It relies on the incident laser having phase modulation sidebands and measuring the reflected cavity light, demodulated at the phase modulation sideband frequency. The approach is very well established and used all throughout atomic physics. For example, it is used to generate the most stable lasers ever made [40, 80] and it is used as the laser stabilization method in the recently successful gravitational wave detectors [81]. Instead of a full derivation (a useful introduction to the matter can be found in Refs. [82, 83]), we will describe how we implement it in our system.

Our frequency modulation sidebands are generated by driving a mechanical resonance of our laser cavity's PZT-driven mirror. The resonance is typically at 700 kHz or 1.3 MHz. After the

[3] Layertec has never confirmed their coating material with us and claim it is a secret. However, due to the damage threshold of these mirrors and their bandwidth, we deduce HfO_2 rather than Nb_2O_5 or Ta_2O_5. See Ref. [78] for further discussion.

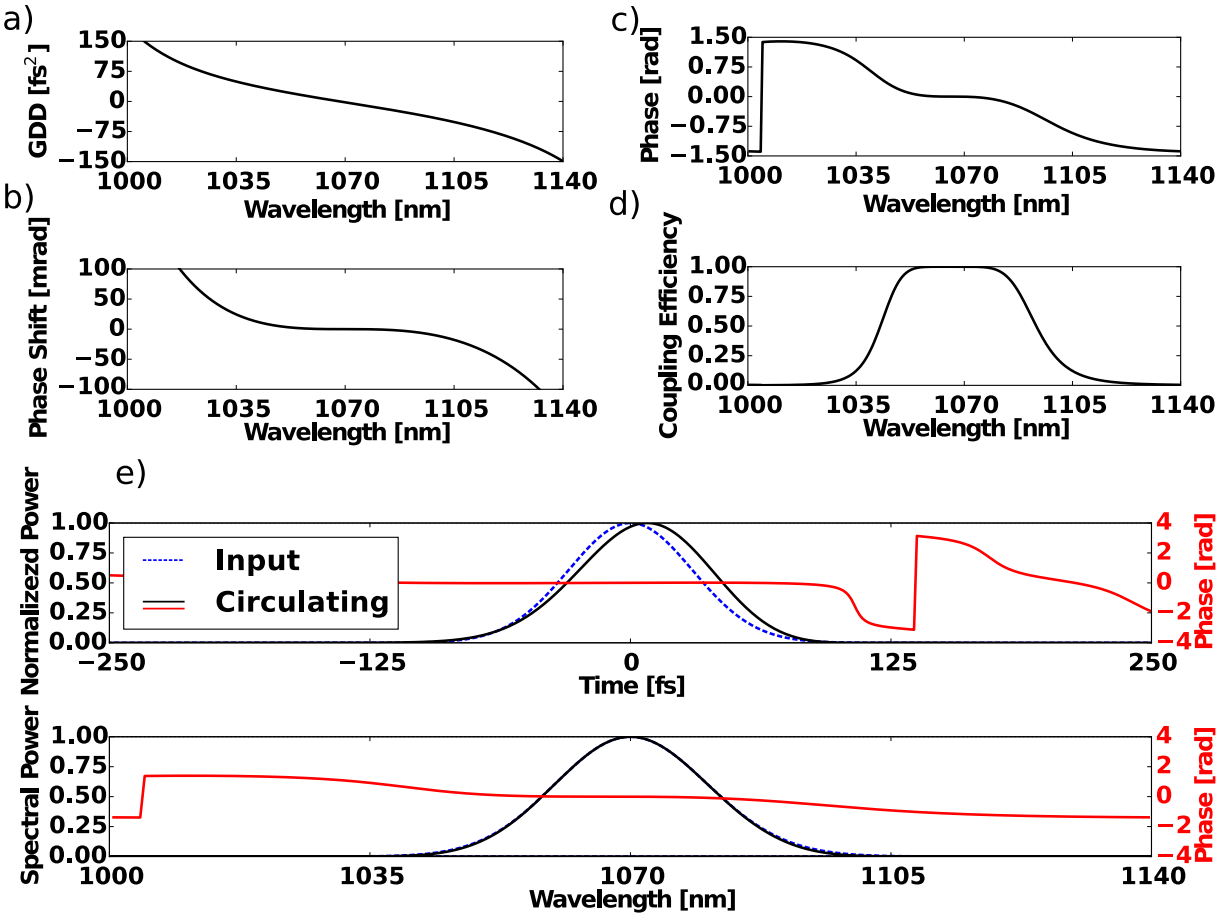

Figure 2.4: **a)** The group delay dispersion (GDD) of a single cavity high reflecting mirror. **b)** The phase shift upon a single reflection from a high reflecting mirror with the zeroth and first order phase terms removed. **c)** The phase shift of a cavity made with the mirrors in a) with the low order phase terms removed. **d)** The spectral bandwidth that will fit inside a cavity made with the mirrors in a) assuming a low dispersion input coupler of an R = 0.985. **e)** The top panel shows how an injected 70 fs pulse is distorted by the mirror dispersion. The bottom panel shows how the pulse spectrum is modified.

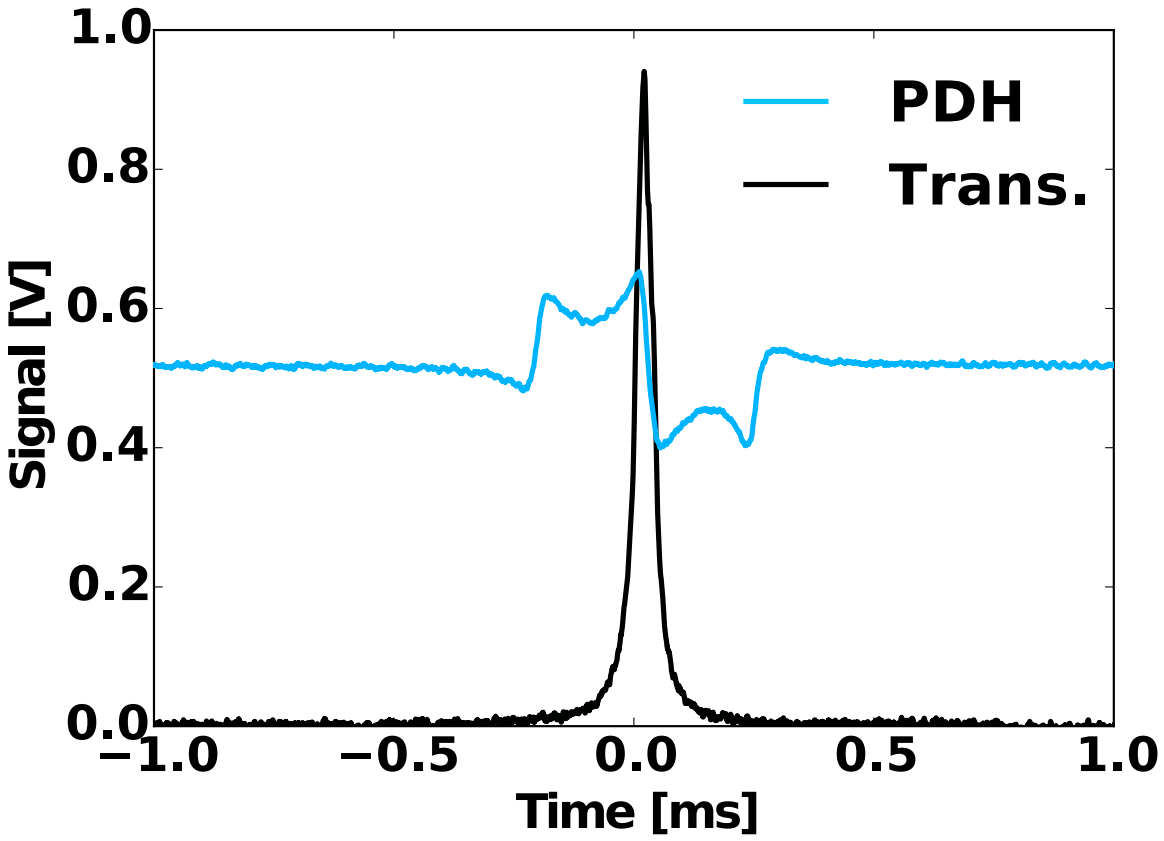

Figure 2.5: Pound-Drever-Hall error signal and the cavity transmission are shown as the laser is slowly swept across a cavity.

comb is injected into the cavity, the reflected light from the resonator is demodulated at the drive frequency with the correct phase to generate the PDH error signal shown in Fig. 2.5. From there, the error signal is filtered and then reapplied to one of two places. The correction signal can be re-applied to the laser using the same PZT that generated the sidebands. Adding these two signals together is accomplished with a bias-T. Alternatively, a cavity mirror equipped with a PZT can also be used. In the former case, the laser follows the cavity fluctuations. In the latter, the cavity follows the laser fluctuations. In either case, the laser can be maintained on resonance with a servo bandwidth of about 50 kHz. Slow feedback is provided by a PZT stage in the fsEC or by fiber stretching in the laser cavity. At night, when the lab is very quiet, the cavity-laser stabilization scheme can stay locked over the course of a few hours without interruption if both fast and slow feedback loops are active.

The frequency comb has two degrees of freedom, f_r and f_0. The scheme described above typically makes f_r modifications to maintain lock. The passive stability of f_0 is sufficiently good that it does not require active locking. Rather, f_0 is set by tuning the temperature of the fiber Bragg grating (FBG) in the laser cavity until maximum buildup is achieved. Adjustments by hand (the graduate student feedback loop), are made every 10 minutes or so if the laser is warmed up. With both locks engaged, optimal power enhancement can be achieved. Ultrafast lasers with larger optical bandwidth typically require active feedback on f_r and f_0 because it is easier for the comb modes to walk off when the optical spectrum is very broad. However, due to our low finesse cavity and the relative narrowness of our spectrum, only one active lock is necessary.

If there is a large amount of relative frequency noise between the laser and the cavity, feedback loops often don't have enough bandwidth to maintain perfect synchronization. Therefore, frequency fluctuations of the laser (or cavity) will lead to amplitude fluctuation in the cavity. This can be very problematic for HHG (which is *very* nonlinear in intensity) or if the transmitted light needs to be used for subsequent detection. An example of the transmitted intensity noise for one of our cavities with $\mathcal{F} = 1000$ is shown in Fig. 2.6. The vertical axis is the residual intensity noise (RIN) power spectral density (PSD) expressed in decibels below the carrier (dBc). This frequency to amplitude

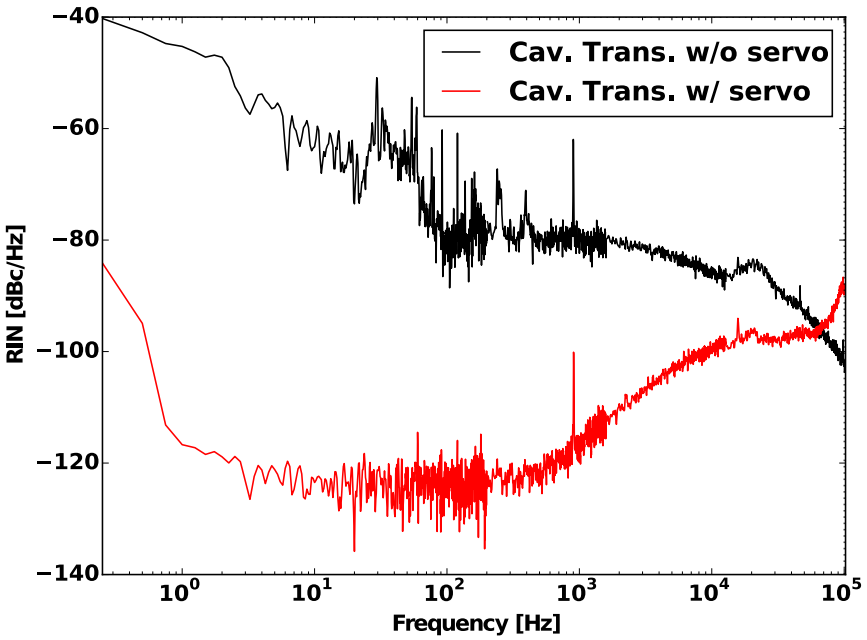

Figure 2.6: The residual intensity noise (RIN) power spectral density is shown when a cavity intensity servo is on and off. The actuator for the servo was an acousto-optic modulator placed before the cavity that can steal power from the undiffracted beam. The servo bandwidth is limited by acoustic wave propagation delay in the acousto-optic crystal.

noise conversion process can be combated in two ways: make the laser and cavity more frequency stable or make an intensity servo. In Fig. 2.6, we demonstrate an intensity servo. The transmitted light is taken and compared to a constant value to generate an error signal. The error signal is filtered and applied to an acousto-optic modulator (AOM) that has the ability to steal power away from the laser beam. The AOM is placed before the cavity. When the lock is engaged, there is a 40 dB suppression of noise out to 1 kHz with the unity gain crossing at nearly 100 kHz. This is extremely powerful for making the laser-cavity system more stable, especially for applications where the transmitted light needs to be analyzed [84, 85]. We will discuss later that there is an amplitude to phase noise coupling in the HHG process as well [43, 86, 87]. This makes a quiet cavity of paramount importance if coherent XUV light is to be generated. This process will be discussed in detail in Sect. 3.1.3.

2.2.6 Output coupling

We plan to use all of the described cavity technology to perform HHG. Since the HHG process will be performed inside of the cavity, we need to have some method of getting the XUV light out of the cavity. Most optical materials are completely opaque at XUV wavelengths. This is problematic because immediately after the focus, if the XUV light is not directed out of the cavity, it will be absorbed by the next curved mirror. There are three experimentally verified methods of outcoupling XUV light from a fsEC. However, others such as crossing two cavities to implement noncollinear HHG, have been proposed [88]. The first method is to use a thin piece of glass or a crystal and place it at Brewster's angle for the driving laser inside of the cavity. Since the index of refraction of the material is different at XUV wavelengths, there will be a Fresnel reflection for the XUV and the XUV light can be reflected out of the cavity. Brewster angle operation is essential to not induce any extra loss to the cavity at the driving wavelength. A common material to use is c-plane sapphire with a thickness around 300 μm. It is very important that the sapphire is very flat and has a very low surface roughness, otherwise the XUV beam quality and intensity deteriorate. Another concern with using Brewster plates is that the sapphire will be nonlinear at the high intracavity powers

required for HHG. Secondly, sapphire is dispersive, so it will ultimately limit how short a pulse can be stored inside a cavity. For example, sapphire typically has a GVD of 90 fs^2/mm. So, even a 300 μm piece has much worse dispersive properties than our other cavity optics.

The second method is the Yost grating and is described in detail in Refs. [74, 89]. The method relies on placing an optic at a 70 degree angle of incidence immediately after the focus of the resonator (See Fig. 2.1b). The optic is actually a high-reflector for the driving laser wavelength. The topmost layer of the optic is SiO_2 with a small period grating etched on it. The period of the grating is too small for the fundamental light to cause diffraction. Thus, for the driving laser it behaves just like a normal high-reflecting optic. However, for the shorter harmonic wavelengths, it behaves like a diffraction grating. It causes the harmonic light to spectrally disperse, separate from the driving laser, and outcouple from the cavity all in one step. This is a perfect output coupler for spectroscopy applications because they usually have the requirement that the harmonic light needs to be spectrally dispersed or filtered before shining it on a target [52]. For ultrafast applications, it is obviously not ideal. If one were to start with a Brewster plate output coupler and then attempt to spectrally disperse the light, there will be severe power loss as optics in the XUV are in general terribly inefficient.

The third method is often referred as "geometric output coupling" or "holey mirror output coupling." The method was first proposed in our group immediately after the first demonstrations of fsEC-based HHG [88] and was recently demonstrated a group in Garching [90]. Since the harmonic wavelengths diverge at much slower rates than the fundamental wavelength, a small hole can be drilled in the curved mirror immediately following the focus. The hole must be small enough to not cause large amounts of additional loss to the cavity, but large enough to allow the XUV light to leak out of the hole. Our initial attempts were not successful due to a poor effort in drilling that cause small cracks in the optical coating near the hole. In recent years, new attempts were made inspired by the results of Ref. [90]. The method for fabrication is to take an optical substrate, laser drill a hole with a conical shape, re-polish the substrate, and finally coat with a high-reflection coating. Our initial attempts have been encouraging with output coupling $\sim \mu$W/harmonic power levels,

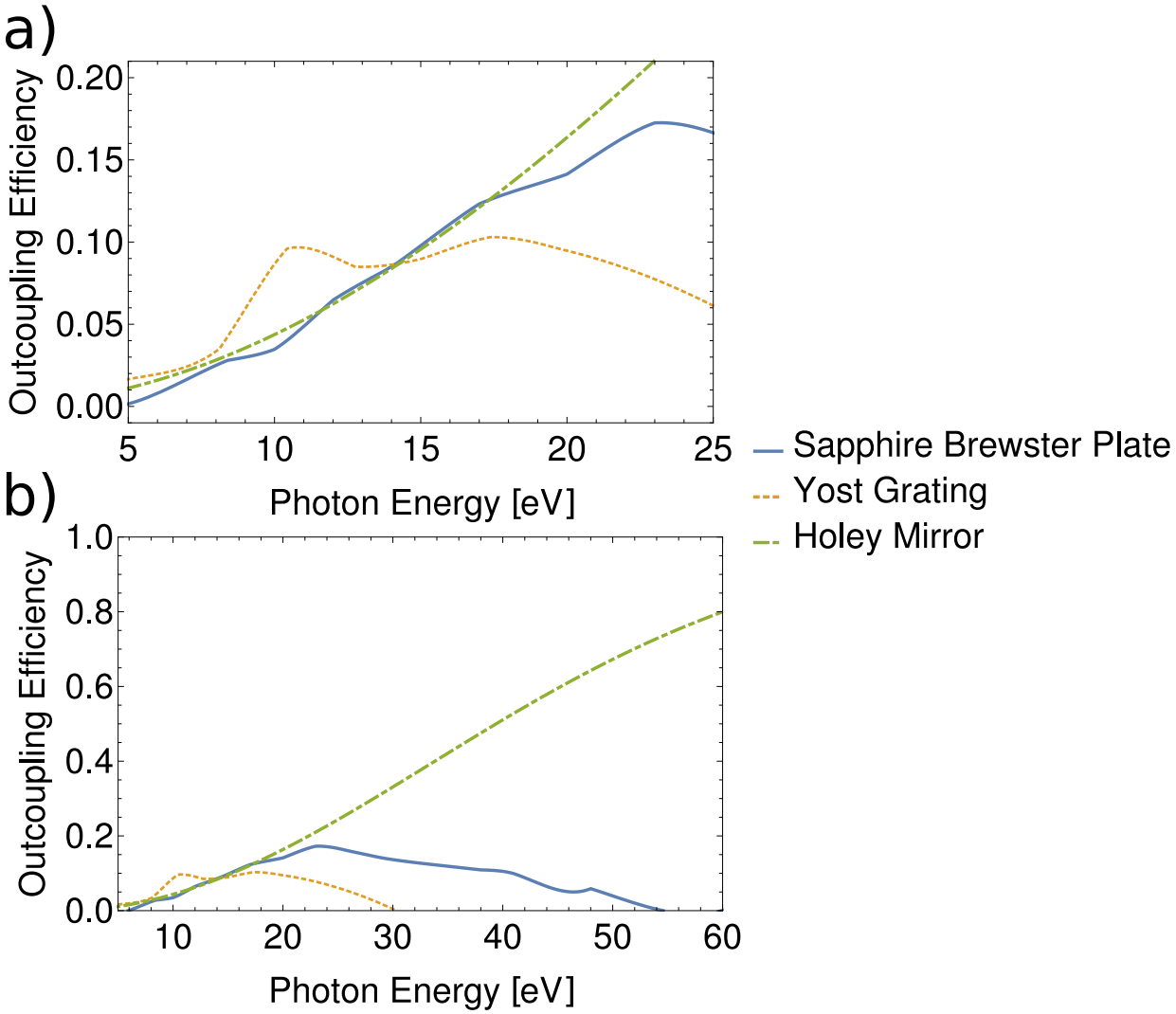

Figure 2.7: Output coupling efficiency for different methods. **a)** The low photon energy efficiencies are shown. All methods have similar performance. **b)** The high photon energy region is shown. The improvement of using a holey mirror output coupler is clearly seen and the efficiency will increase with wavelength. Only the Yost grating spectrally disperses and outcouples the harmonics in a single step forgoing the need to filter the harmonics if they are to be used for spectroscopy.

but the performance has been far from optimal. Work is still in progress.

A summary of all three output coupling schemes is shown in Fig. 2.7. For the comparison, the holey mirror has a radius of 50 μm in a curved mirror with radius of curvature (ROC) of 25 cm. The focusing optic with a ROC of 7.5 cm was chosen to give a similar spot size of about 20 μm, which is typical for our fsECs and facilitates a fair comparison to the Brewster plate and the Yost grating. All methods shown are compatible with cavities that have a $\beta = 200$. As seen in Fig. 2.7a, the low photon energy performance from all three methods does not vary greatly. However, in Fig. 2.7b, the high energy photon comparison is presented. Since the holey mirror does not rely on a reflection to output couple and since the harmonic beam diverges less at high photon energies, the output coupling efficiency increases with harmonic order. This is a very promising scheme because it does not add dispersion to the cavity (good for short pulse operation) and its efficiency increases with photon energy (great for future work requiring shorter and shorter wavelengths). This is very enticing for possible applications in isolated attosecond pulse generation experiments or virtually any other experiments where very high energy photons are needed.

2.3 The laser

The laser technology used for XUV frequency comb generation has rapidly progressed since the initial demonstration [3, 4]. In the first generation of experiments, Ti:Sapphire oscillators were used to pump fsECs. For reasons that will be outlined in Chapter 3, it is beneficial to use fsECs with relatively low finesse which puts a stringent requirement on how much average power the frequency comb must have. To satisfy the need for high average power frequency combs, Yb:fiber technology was employed because it offered a platform for robust power scaling.

In the work of this thesis, we used the laser system outlined in Ref. [73]. For completeness, we will outline the major features of the laser system and its recent modifications. The laser system starts with a Yb:fiber modelocked, similariton oscillator. This oscillator design is used throughout the Yb:fiber frequency combs used in our lab [31, 36, 84, 87, 91–93]. The entire laser system, including the oscillator details, are schematically sketched in Fig. 2.8. Modelocked operation is

achieved by a combination of nonlinear polarization rotation and a saturable absorbing mirror with a sub-ps lifetime. The dispersion of the cavity is compensated with a chirped FBG to keep the net dispersion near zero and in the similariton regime [94]. The FBG also doubles as a cavity end mirror. The oscillator exhibits exceptional noise properties for a fiber laser and robust day-to-day operation. The free running f_0 linewidth is $\sim$ 10 kHz [92]. The oscillator produces $\sim$ 100 mW of average power and pulses compressible to $<$ 80 fs at a repetition rate of 154 MHz. The spectrum is centered at 1050 nm and has 45 nm of bandwidth.

After the oscillator, a chirped pulse amplification (CPA) system is employed. Typically, CPA systems rely on a grating-based stretcher and a grating-based compressor. To make our system more robust, we replaced the grating-based stretcher with an all fiber solution making it alignment free. Over 380 m of various fibers were required to stretch the pulses to 870 ps. The various fibers were chosen so the higher order dispersion of the fiber is matched for the grating compressor used after the main power amplifier. The group delay dispersion at 1070 nm was 12.4 ps^2. Since the stretching system is very lossy, the pulses were then amplified in two stages up to $\sim$ 3 W of average power before being injected into the main power amplifier.

The main amplification stage relies on $\sim$ 9 m of polarization maintaining large mode area (LMA) photonic crystal Yb:doped fiber commercially available from NKT Photonics. This stage of the laser was damaged and rebuilt in 2012. The fiber is pumped by a 250 W, 915 nm diode. This was upgraded during 2014 to replace an aged diode and allow for $>$ 80 W operation. The long fiber length and 915 nm pump wavelength were both chosen to allow the laser spectrum to redshift during amplification. The output of the amplifier is 100 W, but it can be briefly run up to 125 W when additional cooling methods are employed. The pulses are dechirped with a pair of 1600 l/mm transmission dielectric gratings. These were an upgrade from the original polymer gratings that had 1590 l/mm. The small change in line spacing did not affect the performance, but the dielectric gratings offer higher damage thresholds and better power handling. After the compressor 80 W (or briefly 100 W) of average power is available for use with a pulse duration of 120 fs. The amplifier operates with a B-integral of $<$ 0.2 and shows no sign of nonlinearities. The laser system

runs daily with nearly alignment free operation. Only small tweaks to the grating separation in the compressor is required for peak performance.

2.3.1 Nonlinear pulse compression

One of the major drawbacks of using fiber-based ultrafast laser systems is that the gain materials typically do not have large gain-bandwidths and this limits the achievable minimum pulse duration. In fact, our laser system, up until recently, was unmatched in average power and pulse duration. Nevertheless, the convenience of fiber-based systems is so compelling that there have been many work-arounds to the pulse duration problem. The most common way to approach this is nonlinear pulse compression after amplification [95]. However, new nonlinear amplifiers have been developed, but they are still untested in XUV frequency comb applications [96, 97].

The nonlinear interaction of a laser pulse with condensed media is typically described by the non-linear Schrödinger equation (NLSE) [98]. If we ignore higher order effects (self-steepening, stimulated Raman scattering, etc) and only focus on self-phase modulation and dispersion, the NLSE is expressed as

$$i\frac{\partial A}{\partial z} = \frac{\beta_2}{2}\frac{\partial^2 A}{\partial T^2} - \gamma|A|^2 A, \tag{2.58}$$

here A is the pulse envelope, β_2 is the second order dispersion coefficient, and γ is the nonlinearity. The equation is easily numerically integrated using the split-step Fourier method. For illustrative purposes, a normalized version of Eq. 2.58 was numerically implemented and the simulation results are plotted in Fig. 2.9. The simulation parameters are chosen to simulate injecting 80 W of our 120 fs pulses into 1 cm of commercially available LMA fiber. The injected spectrum broadens by almost one order of magnitude and the spectral ripples are a hallmark of self-phase modulation. In the time domain, due to the shortness of the nonlinear medium (and hence small amounts of dispersion) hardly any perturbation is present on the pulse. However, the self-phase modulation process does impose a large temporal chirp on the pulse that can be removed. If the pulse is dechirped, the pulse duration shortens by almost one order of magnitude. The combination of self-phase modulation

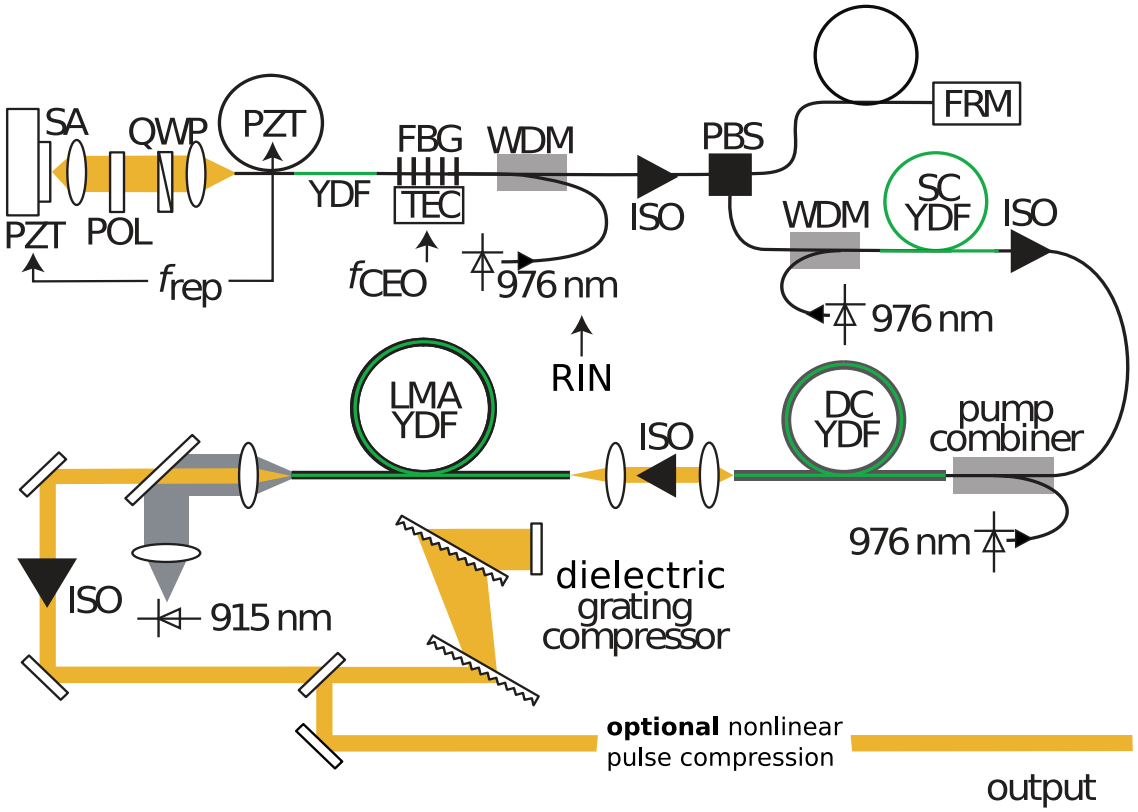

Figure 2.8: Schematic of the 80 W Yb:fiber frequency comb system. PZT, piezoelectric transducer. SA, saturable absorber. QWP, quarter waveplate. POL, polarizer. YDF, Yb-doped fiber. TEC, thermoelectric cooler. FBG, fiber Bragg grating. WDM, wavelength division multiplexer. ISO, optical isolator. PBS, polarizing beam splitter. FRM, Faraday rotating mirror. SC YDF, suspended core YDF. DC YDF, double clad YDF. LMA YDF, large mode area YDF. The LMA YDF and 240 W 915 nm pump laser were replaced from the original version due to failure and age. The original polymer grating compressor was upgraded to the dielectric grating compressor for better power handling. Nonlinear pulse compression was implemented to reduce the pulse duration. The laser can be operated up to 100 W for periods of time less than 1 hour limited by thermal management.

with temporal dechirping is a very robust way to decrease the pulse duration of fiber laser systems.

We implemented a version of this nonlinear pulse compression scheme. Instead of broadening in an optical fiber, we chose bulk sapphire as our nonlinear medium. Nonlinearly broadening in bulk materials is often met with degradation in beam quality because of the nonuniformity of the nonlinearity (the nonlinearity is proportional to the intensity profile and hence not homogeneous across the wavefront). Nevertheless, for our experiments we required only a modest amount of spectral broadening due to restrictions from our enhancement cavities (See the coupling bandwidth in Fig. 2.4d). For our implementation, the laser is focused into 3 mm of bulk c-plane sapphire. The focusing and recollimating objectives are 50 mm air-spaced doublets to ensure tight focusing and preservation of good beam quality. The chirp imposed by the self-phase modulation process was removed by 24 bounces on -100 fs^2/bounce chirped mirrors purchased from Altechna. After the chirped mirrors, part of the beam is sent to diagnostics including a frequency resolved optical-gating (FROG) apparatus for pulse characterization. The rest of the beam is sent to the enhancement cavities for use in experiments.

The results of the characterization measurements are displayed in Fig. 2.10. The increased optical bandwidth is only slightly filtered by the optical cavity as seen in Fig. 2.10a,b. This is in agreement with the dispersive properties of the mirrors provided by Layertec and the simulation results presented in Fig. 2.4. The pulse in the time domain (and its corresponding phase) was measured by FROG and is shown in Fig. 2.10c. The pulse only differs from the transform limit at the pedestal of the pulse. To verify that the cavity was not distorting the pulse in the time domain, cavity transmission light was used for second harmonic intensity autocorrelation. Assuming a Gaussian deconvolution factor, the intracavity pulse duration is 75 fs, consistent again with the simulation results. The intensity autocorrelation trace is shown in Fig. 2.10d. We are able to achieve 11.5 kW of intracavity average power with 75 fs pulses. We are typically limited to similar average powers when the Yost grating is used due to thermal heating of the optic. By reducing the pulse duration from 120 fs to 75 fs, assuming a constant average power and constant beam waist, there

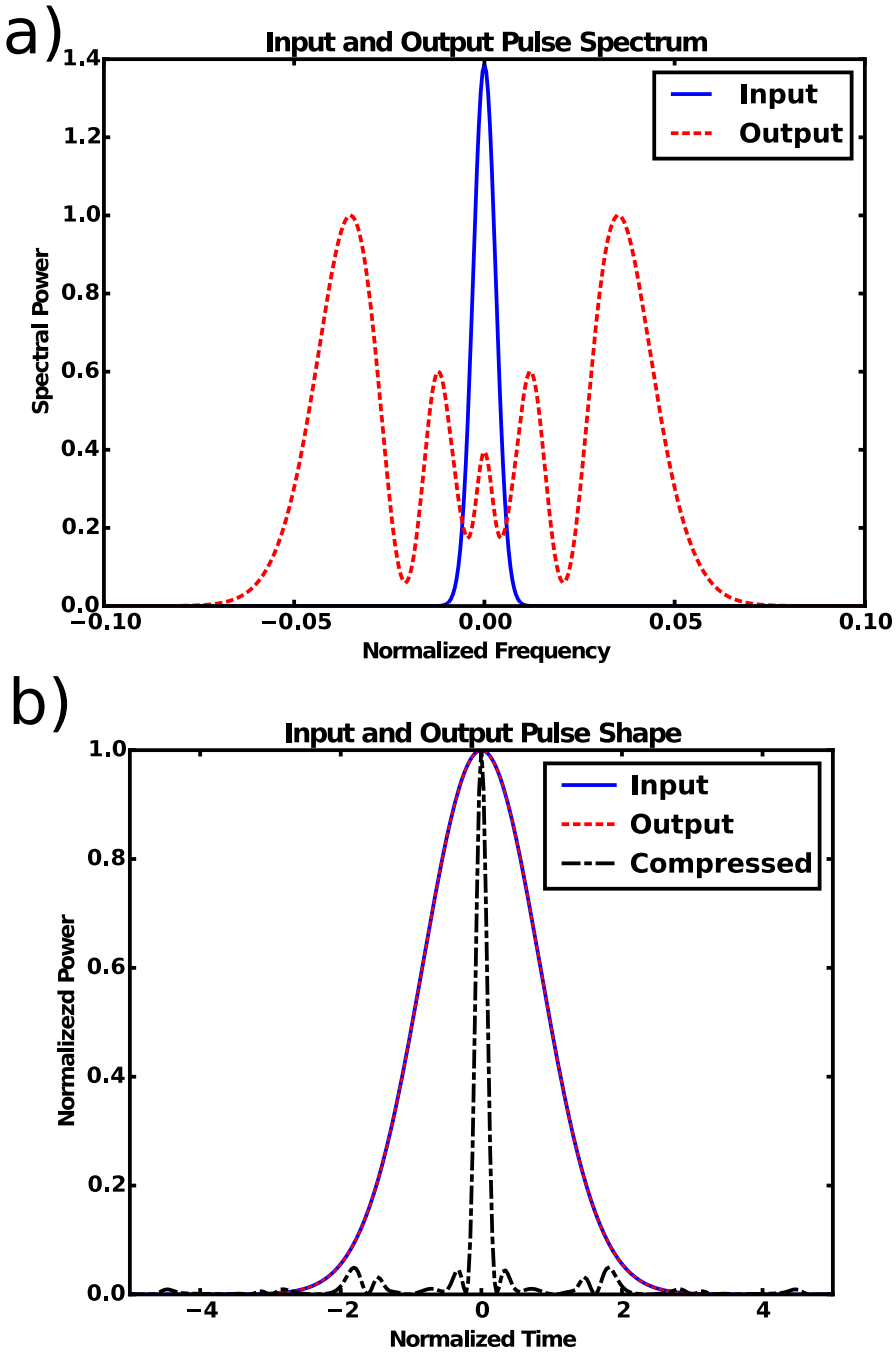

Figure 2.9: **a)** The input and output laser spectrum using the Nonlinear Schrödinger equation calculation assuming 80 W of our frequency comb power into a 1 cm piece of LMA-35 NKT Photonics fiber. **b)** The input and output temporal profile are shown in blue and red. There is nearly no observable difference between the two because the fiber is so short and does not impart dispersion of its own to the pulse. In black, the compressed pulse is shown if the chirped from the SPM broadening is removed. A nearly 10× reduction in pulse duration is achieved.

will be an immediate gain of 1.6× in the peak intensity.

We also succeeded in a nonlinear pulse compression scheme based on a large mode area fiber as a nonlinear medium. The fiber is a commercially available photonic crystal fiber from NKT Photonics (LMA-35). We achieved 40 fs pulses at an average power of 30 W. In terms of peak power, this is still an improvement upon our laser's nominal operating condition of 120 fs pulses at 80 W. The average power could have in principle been increased, but we were unable to fabricate fibers < 2 cm in house. Further, 40 fs pulses proved to be too short for our cavity mirrors (Fig. 2.4).

2.4 Typical laser-cavity operating parameters

Typical cavity-laser operating parameters are as follows. With 30 W of average power in 120 fs pulses at 154 MHz repetition rate from the laser system, a cavity with an input coupler of T = 1.5% has a buildup of 200 and does not distort the 120 fs pulse duration. Therefore, the intracavity power is 6000 W. The resonator usually operates with a 10 cm and 15 cm ROC curved mirror combination leading to a spot size of $\sim 20\,\mu$m at the inner stability edge. The peak intensity of the Gaussian beam can be calculated by

$$I = \frac{2}{\pi}\frac{P_{avg}}{f_r\,\tau_{pulse} w_0^2}, \tag{2.59}$$

where P_{avg} is the average power and τ_{pulse} is the pulse duration. With the aforementioned operating parameters, the peak intensity is 0.52×10^{14} W cm^{-2} which is very suitable to make HHG in a xenon gas target. We have demonstrated up to 14 kW of average power in the cavity (a four mirror resonator not using the Yost grating) which would correspond to a peak intensity of 1.3×10^{14} W cm^{-2} which is suitable for harder to ionize gases like argon.

2.5 The chamber

Due to the high power cavity operations, the nonlinear and dispersive properties of air will be problematic for cavity operation. Also, XUV wavelengths (< 100 nm) will not propagate in air and

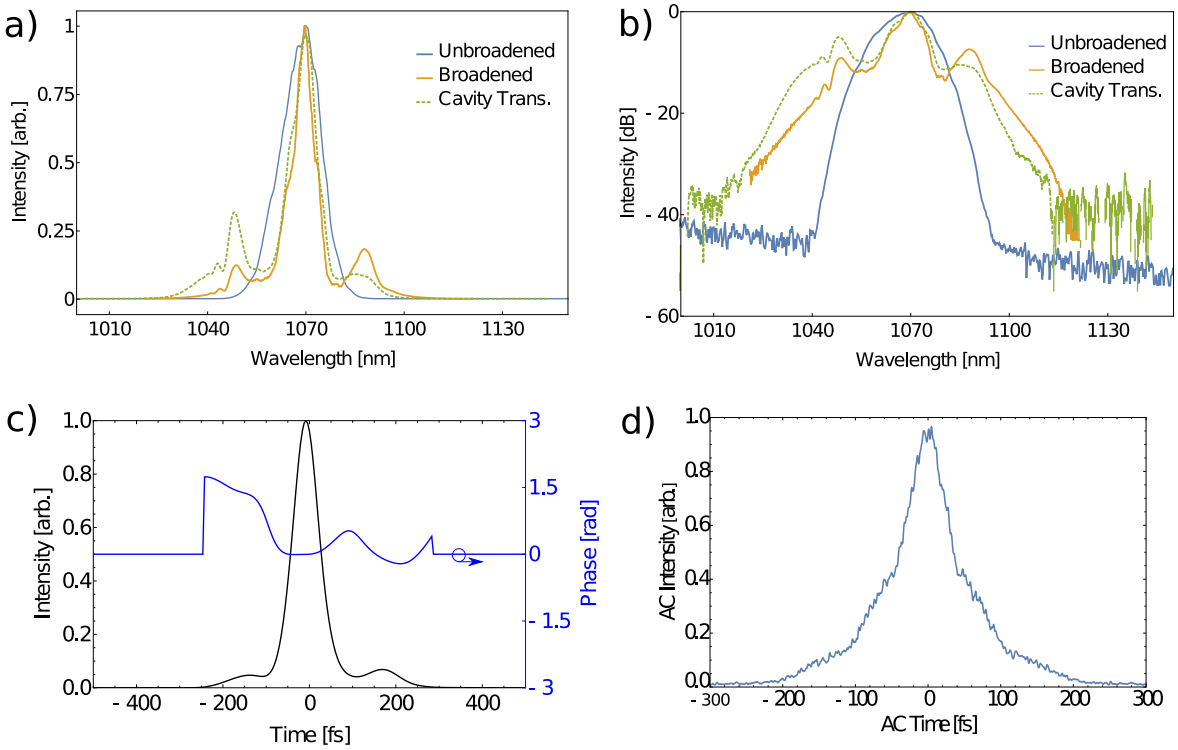

Figure 2.10: **a)** The unbroadened laser spectrum, nonlinearly broadened laser spectrum, and the cavity transmission spectrum of the nonlinearly broadened laser are shown. **b)** Same as a) but on a log scale. **c)** The time domain profile of the nonlinearly compressed pulse. The pulses were reduced from 120 fs to 70 fs in duration. The is near the transform limit of the nonlinearly broadened spectrum shown in a). **d)** The intracavity second harmonic intensity autocorrelation trace. Assuming a Gaussian deconvolution factor, the pulse in the cavity is $\sim$ 75 fs in duration. The slight increase from c) is because of the dispersion of the cavity mirrors.

are almost immediately absorbed. So, the entire experiment needs to be performed inside a vacuum chamber. We do not require ultrahigh vacuum and a pressure of < 1 mTorr is generally sufficient. This is easily accomplished with turbomolecular pumps. Due to work that involves simultaneous operation of two enhancement cavities, a large vacuum chamber needed to be constructed and is schematically shown in Fig. 2.11. The many ports are required for allowing beam access into and out of the chamber. Despite its holey design, more holes would have been nice. Nevertheless, the chamber is mainly aluminum in construction with a steel baseplate. There are holes in the chamber bottom to allow that the breadboard in the vacuum chamber be mechanically decoupled from the chamber walls. Our cavity optics are mounted on the breadboard. This is very important so that the inherent vibrations of the turbomolecular pump do not disturb the fsEC. The decoupling scheme is shown in Fig. 2.12.

We typically inject multiple atmospheres of gas pressure behind a quartz[4] nozzle of $\sim 100\,\mu$m diameter. This leads to a considerable gas load in the chamber and in order to keep the pressures below 1 mTorr (to minimize reabsorption in the gas), pumping speeds of ~ 1000 L/s are necessary. However, this situation can be improved by implementing a gas dump right below the nozzle. It is described in more detail in Ref. [89] and is shown in Fig. 2.13. A small aperture catch is placed as close to the nozzle as possible without clipping the laser beam. The catch is hooked up to a separate vacuum pump. When operating properly, the gas catch can reduce the background pressure in the chamber by $\sim 5\times$. As we will describe later, this is essential for two cavity simultaneous operation and for XUV power scaling methods. Further improvement is possible, for example, by using a wider pumping tube for the gas catch thereby increasing its conductance.

2.5.1 Ozone and plasma cleaner

There is often a small amount of residual gas present in a vacuum chamber. Of particular importance to this work are hydrocarbons. When a hydrocarbon absorbs an XUV photon, it will

[4] The nozzle material is important. Because of our extremely large average intracavity power, a borosilicate nozzle will readily melt when placed close to the laser focus. Therefore, a nozzle with a high melting temperature is needed. We have found that quartz works very nicely and can be purchased commercially.

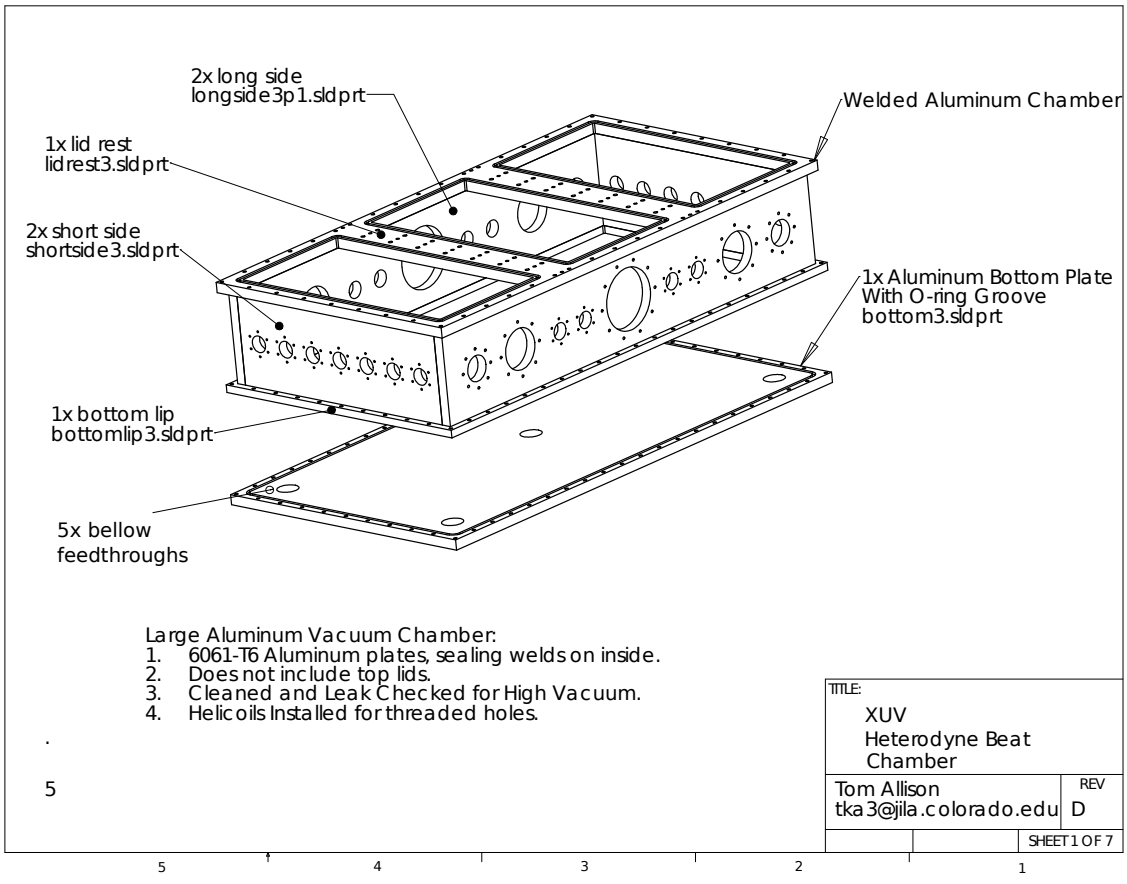

Figure 2.11: Drawing of the XUV comb vacuum chamber. Note the five holes in the baseplate that are used for vibration isolation of the optical breadboard. The many ports are use to get diagnositics in and out of the chamber.

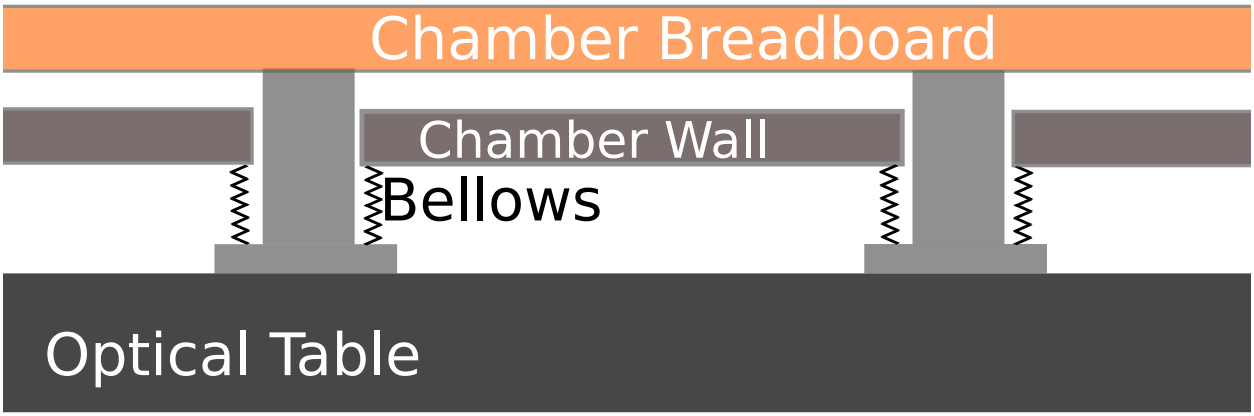

Figure 2.12: Schematic drawing of the XUV comb vacuum chamber vibration isolation scheme. Belows are used in the baseplate to separate the optical breadboard from the vacuum chamber to mechanically decouple them. This is essential for quiet cavity operation.

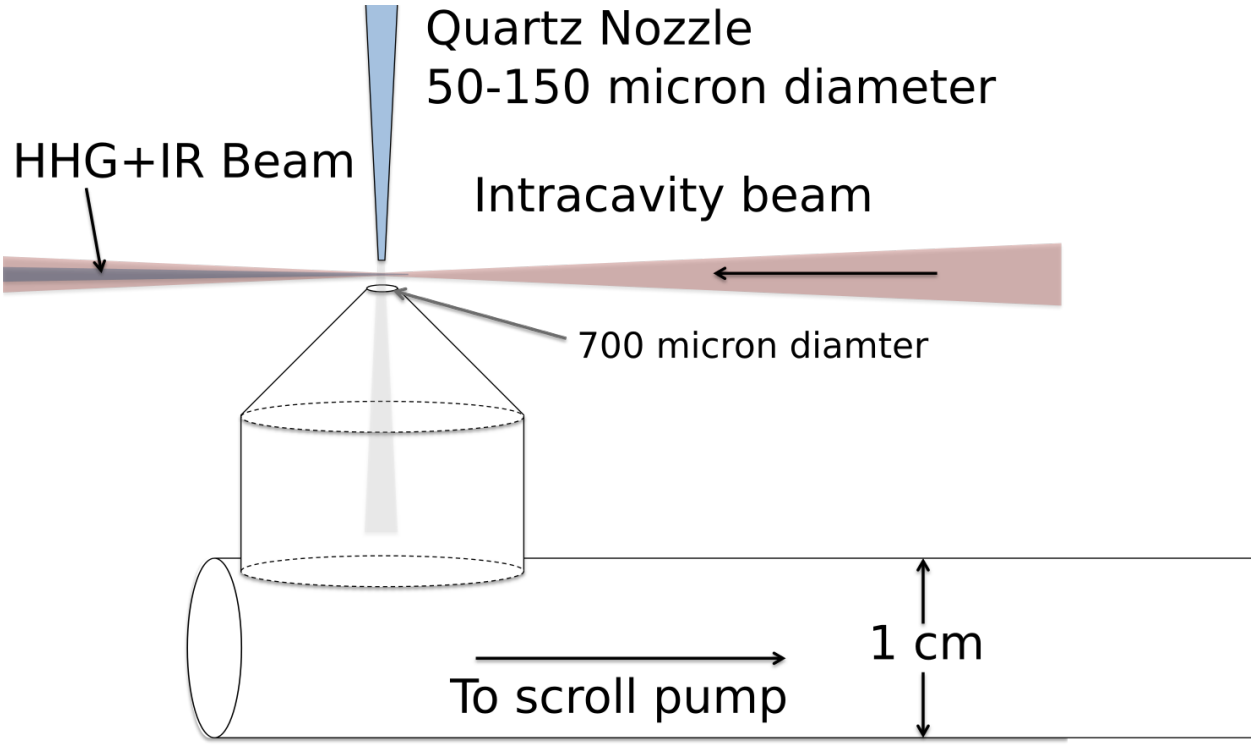

Figure 2.13: Preventing large chamber background pressures is aided by a "gas dump." A small aperture hooked up to a scroll pump attempts to catch the gas coming from the injection nozzle. We routinely observe a 5× reduction in background pressure when the dump is properly installed.

typically "crack" and stick to chamber walls or optics. After long periods of XUV operation, thin films of carbon-containing molecules deposit on the mirrors. This typically does not hurt the fsEC operation, however, the XUV performance of our optics degrades. The Yost grating grooves regularly get filled up with a film and the optic will eventually stop diffracting. Similar effects have been observed at synchrotrons for many years [99, 100]. Common cleaning methods include introducing ozone into the vacuum chamber or running oxygen discharges [101–103]. In the early days of XUV comb operation (before 2013), carbon contamination was a fact of life. After an optic had become dirty, it would need to be removed from the vacuum chamber and taken into a clean-room to use a reactive ion etcher to produce a cleaning RF oxygen discharge. This was a very time consuming cleaning process, not to mention that a cavity would typically only last about one half hour at full XUV flux before becoming too dirty to use.

Since this dirty little secret of XUV comb performance would clearly hinder future work, a solution needed to be reached. Since ozone was routinely used to clean optics, we decided to deliberately introduce ozone into the vacuum chamber in relatively small quantities during the HHG work ($\sim$1 mTorr of O_2 and $\sim$0.1 mTorr of O_3). This was done by purchasing a ozone generation unit from Ozone Solutions [104] and injecting it into the vacuum chamber. After the simple modification of introducing ozone, cavity performance can immediately recover from a contaminated state and can sustain nearly optimal performance for month timescales. Without this simple trick, some experiments in this thesis would have become so time consuming as to render them nearly impossible.

While the ozone trick is now a standard piece of our XUV comb operation, additional and stronger cleaning methods are sometimes needed if the ozone is ever not used or contamination is so bad that the ozone is no longer effective. The stronger cleaning method is to run an oxygen discharge. We developed a simple method to run a small RF discharge in the vacuum chamber to isolate individual dirty optics. A small DC-AC inverter (originally intended to power laptop screen lamps) converts a 12 V signal into a 1.5 kV signal oscillating at 50 kHz. We place this signal on a small electrode in the vacuum chamber and place it next to an optic that needs to be cleaned. There needs to be an electric ground behind the optic in order for the RF to capacitively couple

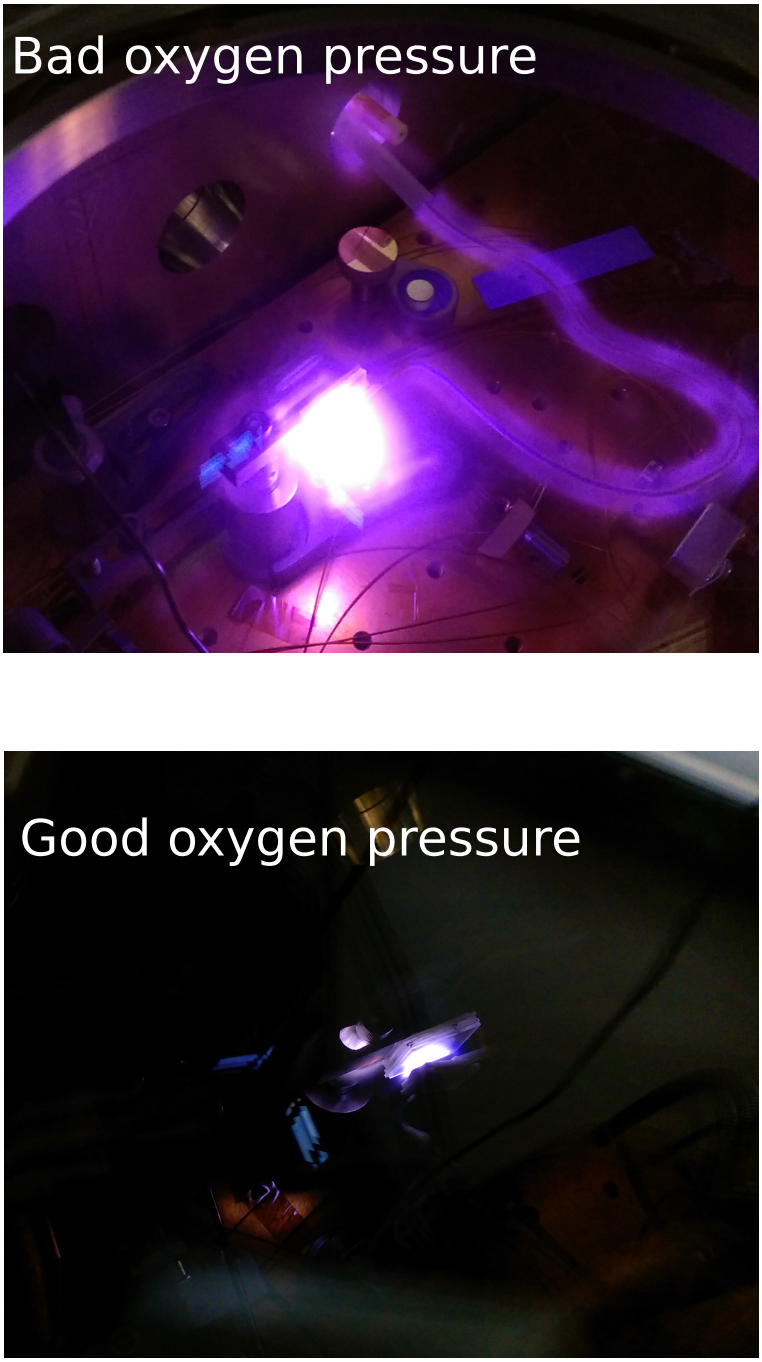

Figure 2.14: Top panel shows the plasma cleaner operation under too low oxygen flow. The bottom panel shows ideal oxygen flow. A nice, localized plasma is formed on near the mirror to perform cleaning. The *in-situ* plasma cleaner reduces the cleaning time of an optic from $\sim$ 1 hour to $\sim$ 15 minutes.

through the optic. A small, steady oxygen flow is introduced to the chamber and the electrode is then switched on. If the chamber pressure is too low, the plasma becomes very unstable (for our chamber and flow, too low means < 1 Torr). An image of non-ideal operation is shown in Fig. 2.14a. Once higher pressures are reached, the plasma stabilizes close to the electrode and the optic tends to be cleaned. This is shown in Fig. 2.14b. We tested a few optics and as long as good pressure conditions were maintained for cleaning times of about 2 minutes and electrode-optic separations of 1 cm, we did not observe any additional damage and the optics would become clean. Considering this can be done *in-situ* and does not require a specialized piece of equipment like a reactive ion etcher, it is pretty convenient.

Chapter 3

High-order harmonic generation

In this chapter, we will focus on how a single atom responds to a very intense laser field and how this interaction relates to HHG. We will focus on aspects most relevant to the XUV frequency comb experiments. We will also describe macroscopic effects and phasematching of HHG. Special attention is paid to the unique situation of HHG in a fsEC.

3.1 Single atom response to a strong laser field

Here, we will review strong-field ionization, a simple model for HHG, a quantum description based on the strong-field approximation, and finally, aspects of HHG beyond the strong-field approximation. We will focus on features most relevant to the XUV frequency comb experiment.

3.1.1 Ionization by an intense laser pulse

High-order harmonic generation falls under the discipline of strong-field physics and extreme nonlinear optical phenomena. When an atom or molecule is in an intense electric field, the valence electrons can tunnel through the severely distorted Coulomb barrier and ionize. Here, an intense electric field has a strength comparable to the Coulomb interaction responsible for binding the atom or molecule together. This is typically V/Å strengths for the noble gases. In oscillating electric fields, there is also the potential for multiphoton ionization assuming the photon energy is less than the ionization potential, a so-called "low frequency" electric field. Here, an atom or molecule will absorb multiple photons from the laser and an electron will be excited into the continuum. In 1964,

Leonid V. Keldysh produced a simple means to understand what happens to atoms or solids when they are placed in intense, low frequency electric fields [23]. The published date of 1964 (1965 in English) is quite striking. Remember, the laser was still in its infancy. Nevertheless, it pre-dated even the first observation of multiphoton ionization [105], optical tunneling [106], above-threshold ionization [107], and high-order harmonic generation [108]. The connection between Keldysh's work and these experimental results was not immediately apparent and it took nearly 40 years after publication for people to realize how useful Keldysh's physical model actually was [109]. As expressed earlier in Eq. 1.4, Keldysh derived what we know call the Keldysh parameter γ to show the transition of the multiphoton ionization to the tunnel ionization regimes. In some sense, the common interpretation of γ is problematic [23]; an interesting discourse on the meaning of γ in the case of strong-field laser-atom interactions is givent in Ref. [110].

Nevertheless, Keldysh's theory was the first implementation of the strong-field approximation (SFA) which stated that during the interaction of an intense laser field, bound states or resonances can be neglected during ionization, and the effects of the Coulomb potential on the continuum electron can be neglected. Using Keldysh's theory, Perelomov, Popov and Terent'ev developed a method to calculate ionization rates by intense laser fields (often called PPT rates) [112]. Later, Ammosov, Delone and Krainov developed a simplified formulation for arbitrary atoms in intense fields (often referred to as ADK rates or ADK theory) [25]. The ADK rates are known to be poor in the multiphoton ionization regime of $\gamma >> 1$. However, due to the ease of implementation, experimentalists often prefer ADK to PPT. A very detailed treatment can be found in Ref. [113]. Fig. 3.1 shows the ionization probability for a 120 fs, 1070 nm laser pulse using the ADK rate modified by Tong and Lin [111] to deal with the shortcomings of the pure ADK rate when in the barrier-suppressed regime (when over the barrier ionization plays a role). The ionization probably, or ionized fraction η, is defined as

$$\eta = 1 - \exp\left[-\int_{-\infty}^{\infty} \omega_{ADK}(t)\,\mathrm{dt}\right], \tag{3.1}$$

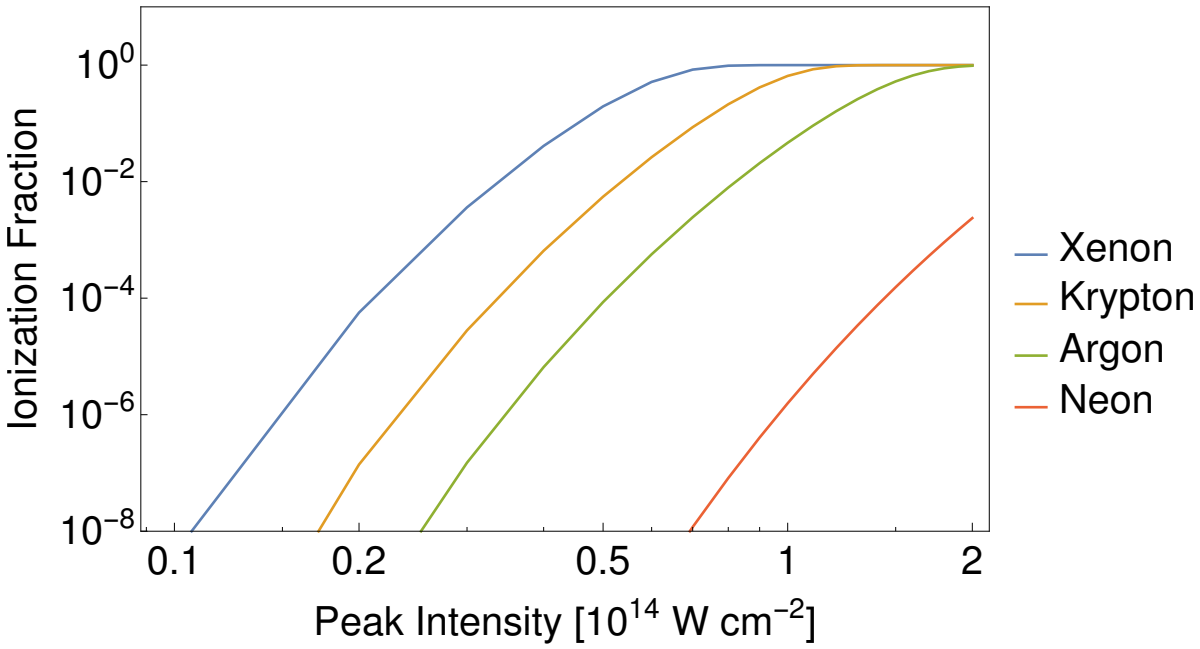

Figure 3.1: Ionization probabilities as a function of laser intensity for 1070 nm, 120 fs pulse. The ionization rate was calculated using the ADK formalism with the modifications made by Tong and Lin to include the effects of barrier-suppression [111].

where the integral is performed over the laser pulse duration and $\omega_{ADK}(t)$ is the ionization rate calculated using ADK theory. The ionization probabilities are very sensitive to the ionization potential of the atom and the laser intensity (see Table 1.1 for ionization potentials). As previously mentioned, ADK rates are generally most applicable in the limit $\gamma << 1$, however, the Tong and Lin's modification have proven to work well when this limit is not strictly true [114]. For a 1070 nm laser of 0.8×10^{14} W cm^{-2} and considering xenon's I_p, the Keldysh parameter is $\gamma = 0.842$. As we will discuss in Sect. 3.2, the ionized fraction of a gas target is very important when one considers the macroscopic response of HHG and macroscopic phasematching.

3.1.2 Simple model of high-order harmonic generation

As previously mentioned, HHG was first observed as early as 1987. However, there were many attempts to theoretically understand the phenomena and they often relied on direct integrations of the time-dependent Schrödinger equation [115–117]. In 1993, Paul Corkum developed a simple [1] model that successfully described double-ionization, above-threshold ionization, *and* HHG [24]. It is commonly referred to as the "3-step model". The three steps for HHG are: (1) ionization with rates determined by ADK theory or a similar theory, (2) propagation of the electron's motion using Newton's equations and ignoring electron-ion interactions, (3) recombination of the electron and ion to produce a dipole responsible for the generated XUV field.

The most salient features of the model are presented in Fig. 3.2. For the illustrative calculation, a single laser period is 2π. After the electron is ionized at a time t_i, it propagates in the oscillating electromagnetic field according to $F = ma$. Since the field is oscillatory, the electron will return to the ion at t_r with the possibility of recombining and emitting a high energy photon. Fig. 3.2a shows that there is a one to one correspondence between ionization time and return time. However, not all trajectories will recombine. If the electron is ionized before the peak of the field, it will simply drift away. This can be seen in Fig. 3.2c. The trajectories that have the possibility of recombining typically ionize at the peak of the field or immediately after. Despite the one to

[1] "Simple" meaning the calculation is at the undergraduate physics level, something experimentalists love.

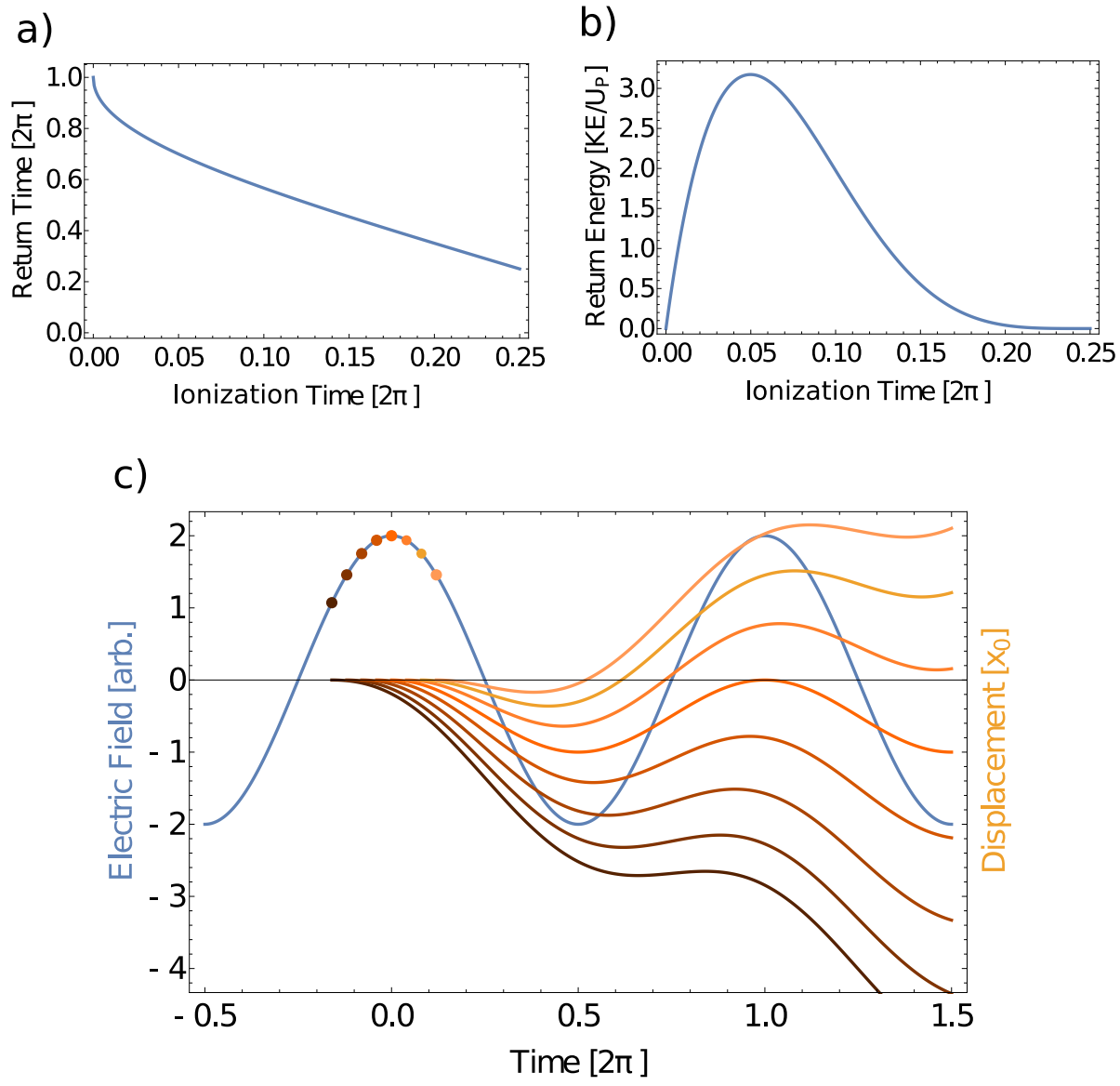

Figure 3.2: Simple man model of HHG. All units of time have been normalized to a phase of 2π. **a)** The return time of the electron as a function of emission time (time of ionization). There is a one-to-one correspondence between the two. **b)** The return kinetic energy (normalized to the pondermotive energy U_p) as a function of emission time. Two emission times correspond to the same return kinetic energy. The return kinetic energy sets the harmonic photon energy. The two times are referred to as the long and short trajectory referring to the amount of time the electron spends propagating in the continuum. **c)** An example of electron trajectories in the laser field. If the electron is ionized before the maximum of the wave, the electron drifts away and does not have the chance to recombine. Electrons ionized after the peak have a chance to return to the ion and possibly recombine and emit a high energy photon.

one correspondence between t_i and t_r, this is not true for the return kinetic energy of the electron. Shown in Fig. 3.2b is the return kinetic energy (normalized to the pondermotive energy) as a function of t_i. For a given return energy, there are two possible t_i's t_r's. These two paths are commonly referred to as the long and short trajectories indicative of the difference in the amount of time the electron spends propagating in the laser field. The maximum return kinetic energy is $3.17U_p$ and leads to the famous cutoff equation stated earlier in Eq. 1.6.

While Corkum's simple model was quite successful at capturing much of the essential physics, it is not a quantum mechanical description of the HHG process and is incapable of describing things such as the phase of the emitted XUV light and addressing the role of quantum interferences in the HHG process, if any. This would be addressed later in the work of Lewenstein *et al.* [86, 118]. While there is nothing in Corkum's model that would hinder future XUV comb performance, quantum effects may shed more light on coherence properties of the XUV light and if temporally coherent light in the XUV is even feasible.

3.1.3 The quantum description of high-order harmonic generation

The two works of Lewenstein *et al.* [86, 118] essentially built the quantum mechanical description of HHG within the SFA. The assumptions of the theory are similar to Corkum's: (1) No bound states are considered except for the ground state, (2) the ground state is not depleted, and (3) after ionization, the electron propagates as a free particle with no influence from the ion potential. The quantum treatment recovers much of the same physical insight as Corkum's model with the addition of predictions on the phase of the XUV light.

Lewenstein *et al.* [86, 118] derived an equation for the dipole moment responsible for the generated XUV field. For the moment, we switch to atomic units where $\hbar = |e| = m_e = 1$ [16]. The phase term in the dipole moment is sensitive to the electron trajectory after it has been ionized and is written

$$\Phi_q = S(\mathbf{p}, t_i, t) - q\omega t, \tag{3.2}$$

where S is the quasi-classical action defined as

$$S(\mathbf{p}, t_i, t) = \int_{t_i}^{t} \mathrm{d}\tau \left(\frac{[\mathbf{p} + \mathbf{A}(\tau)]^2}{2} + I_p \right), \tag{3.3}$$

where $\mathbf{p}$ is the electron momentum, $\mathbf{A}(\tau)$ is the vector potential of the laser field, and t_i is the time of ionization. Eq. 3.3 is reminiscent of Feynman's path integral approach. Essentially, the dipole moment contains a sum over all possible electron paths. Eq. 3.2 is in general a rapidly varying quantity and only conditions where the dipole contains a stationary phase will contribute to XUV generation. Looking for the stationary phases is often called the saddle-point approximation.

Where then can write the three saddle-point equation evaluated at the recombination time t_r as

$$\nabla_p \Phi_q|_{t=t_r} = \int_{t_i}^{t_r} \mathrm{d}\tau \, [\mathbf{p} + \mathbf{A}(\tau)]^2 = 0\,, \tag{3.4}$$

$$\frac{\partial}{\partial t} \Phi_q|_{t=t_r} = \frac{[\mathbf{p} + \mathbf{A}(t_r)]^2}{2} + I_p - q\,\omega = 0\,, \tag{3.5}$$

$$\frac{\partial}{\partial t_i} \Phi_q|_{t=t_r} = \frac{[\mathbf{p} + \mathbf{A}(t_i)]^2}{2} + I_p = 0\,. \tag{3.6}$$

Since the form of the vector potential is known, it is straightforward to numerically find the roots of this set of equations. Each of the saddle point equations gives insight into what is physically going on during the strong-field process. Eq. 3.4 is simply a statement that the electron must return to the point from which it was ionized (an assumption also made in Corkum's model [24]). This makes sense because the electron must return to the ion to rescatter or recombine. Eq. 3.5 is just a statement of the conservation of energy enforcing that the emitted photon energy is a sum of the kinetic energy of the electron plus the ionization potential. It can readily be seen Eq. 3.6 does not have a solution for real values of t_i (because I_p is positive). The imaginary part of t_i has been interpreted as the "tunneling time" which many claim exists and even try to measure. This assertion may be fanciful and can even be shown to be gauge dependent [110]. One of the cornerstones of physical theories is that measurable observables should not be gauge dependent. A discourse on the

idea of "tunneling times" can be found in Refs. [119, 120]. Nevertheless, if complex time values are assumed, roots to the saddle-point equations can easily be found.

By numerically finding the roots of Eq. 3.4–Eq. 3.6, assuming a xenon target and a 1070 nm driving laser, it is possible to calculate the dipole phase from Eq. 3.2 using the return times determined from the saddle point equations. Fig. 3.3a shows the return time (emission time) as a function of harmonic order. Two roots per harmonic order are found, corresponding to the long and short trajectories. Two sets of solutions are shown corresponding to different laser intensities. Fig. 3.3b shows the dipole phase (and hence phase of the emitted XUV light) as a function of laser intensity for the short and long trajectories of the 15^{th} harmonic. The short trajectories have nearly no dependence on intensity while the long trajectories have a quite strong dependence. The coupling between intensity and phase is parametrized in atomic units as

$$\phi = -\alpha_j \frac{U_p(I)}{\omega} = -\alpha_j \frac{I}{4\omega^3}, \tag{3.7}$$

where j is the index of the short or long trajectory. α_j is plotted in Fig. 3.3b in units of π similar to Refs. [43, 87, 121]. We will use this convention later in our experimental investigation of the intensity-dependent phase presented in Chapter 4.

3.1.4 Beyond the strong-field approximation

The SFA is not without its shortcomings, but it has nevertheless been a very useful tool. For the work in this thesis, we are typically in a regime where the SFA is certainly a bad approximation. Below- or near-threshold harmonics are the harmonics with photon energy less than or comparable to the ionization potential, respectively. These low order harmonics violate two out of the three assumptions of the SFA, namely that bound states are not important [122] and that the Coulomb potential is safe to ignore allowing the electron to be treated as a free particle when propagating the in the electromagnetic field [121, 123].

The theoretical treatments of below- or near-threshold harmonics are beyond the scope of this thesis. However, some of the outcomes of the analysis are relevant to our work. First, for

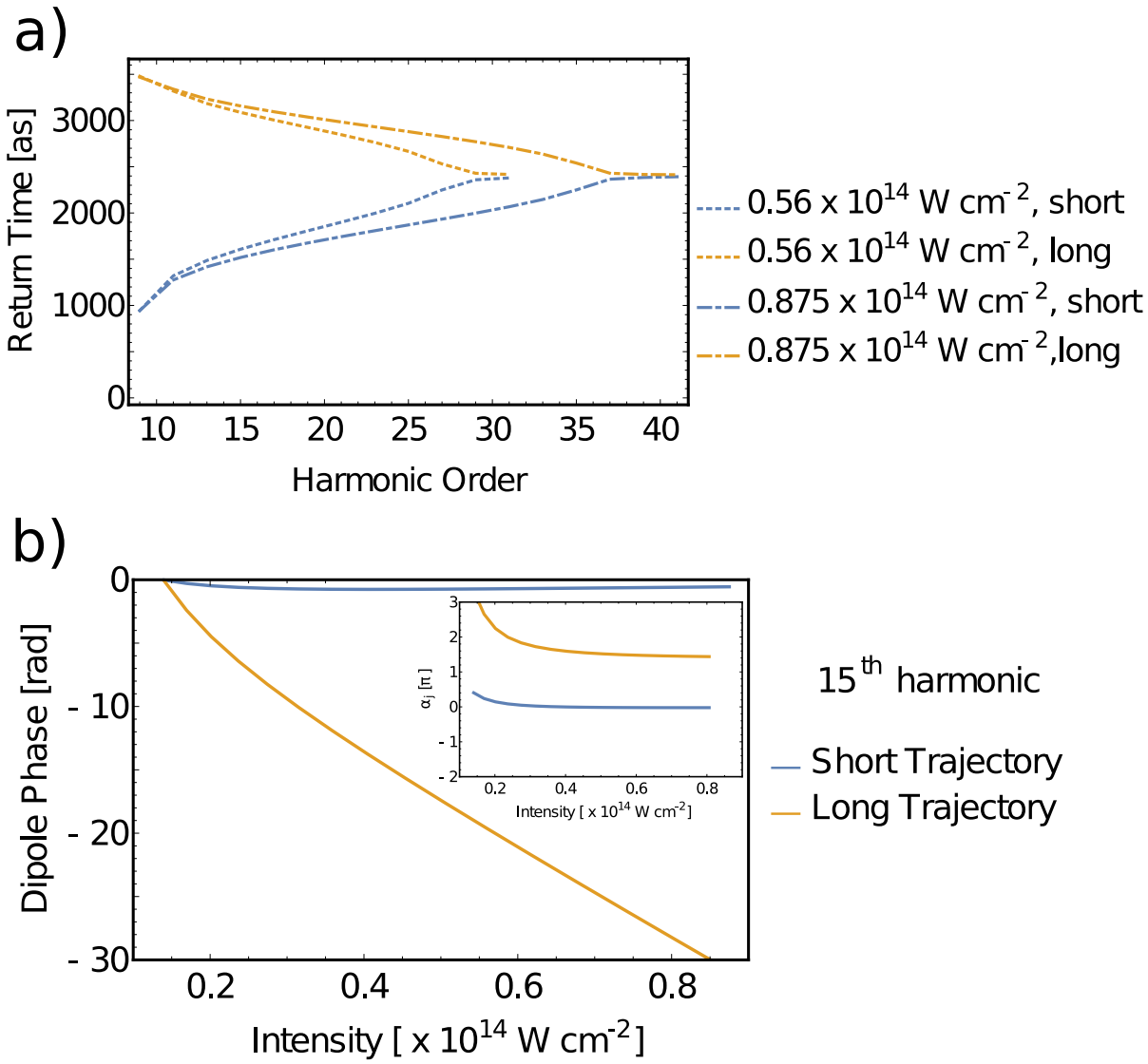

Figure 3.3: **a)** The return time (time of XUV photon emission) is plotted versus harmonic order for two laser intensities using the strong-field approximation. Two trajectories contribute to each harmonic order. **b)** The intensity dependent dipole phase for the short and long trajectory as a function of laser intensity for the 15^{th} harmonic. The inset contains the coupling parameter between intensity and phase. For all presented here, the laser wavelength was 1070 nm and the target was xenon.

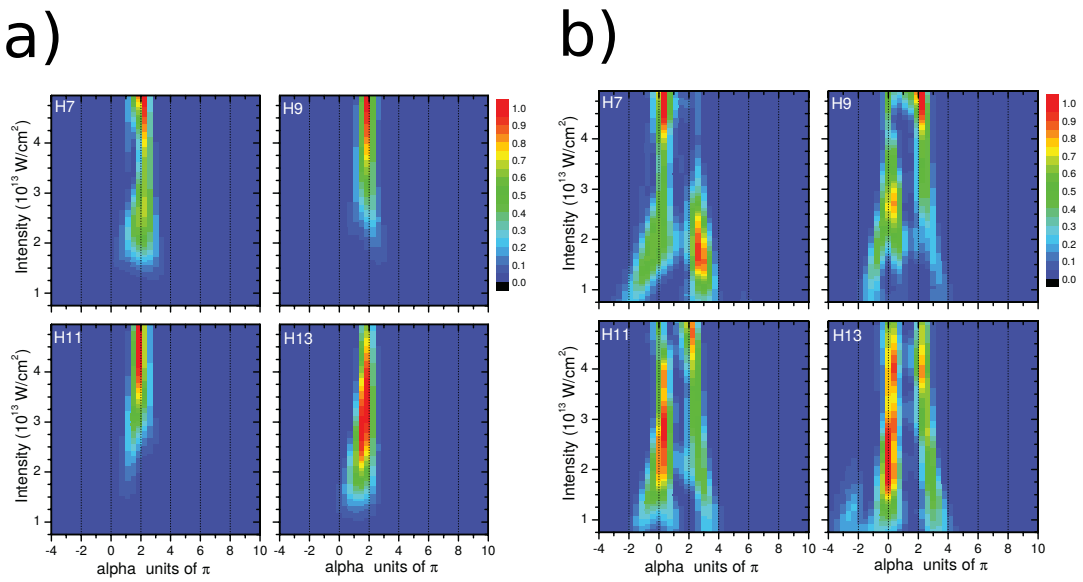

Figure 3.4: The effects of considering effects beyond the SFA. The plots were reproduced from Ref. [121]. **a)** The calculation shows the density of quantum paths when only tunnel ionization is considered. There is only one quantum path present. **b)** The calculation shows the density of quantum paths when tunnel ionization and over-the-barrier ionization (including uphill trajectories) are included. The multiple quantum paths for below-threshold harmonics were initially surprising and they do not originate from tunnel ionization like their above-threshold counterparts.

below-threshold harmonics, if only the SFA is considered, there is only a single quantum path relevant for HHG. This is shown in Fig. 3.4a which has been reproduced from Ref. [121]. The plot shows the distribution of possible α_j as a function of laser intensity assuming a xenon target and a 1070 nm driving laser. What is most apparent is that the single trajectory actually has a very strong intensity to phase coupling. Work from our group showed that below-threshold harmonics do indeed have multiple quantum paths leading to harmonic generation [87]. This surprising result has allowed our collaborators from the Schaeffer/Gaarde group to work out the origin of these harmonic paths. Fig. 3.4b shows the calculation where instead of relying only harmonics to be initiated by tunnel ionization (as in the SFA), we included over-the-barrier ionization with uphill trajectories and downhill trajectories [121]. Now, multiple quantum paths are present, which are consistent with our initial experimental observation [87]. Subsequent work reported in this thesis (see Chapter 4) was able to isolate the short quantum path component of these trajectories and make a precision measurement of the intensity-dependent dipole phase [43], thus confirming the weak intensity to phase coupling present in below- and near-threshold harmonics. These findings further emphasize their non-tunnel ionization-based origin. The often ignored below- and near-threshold harmonics are a rich system for studying strong-field light-matter interactions. Further, the presence of the short trajectory with a weak intensity to phase coupling in the below- and near-threshold harmonics is rather fortuitous for future work using the harmonic light for precision spectroscopy applications. Since the HHG process will be less sensitive to intensity fluctuations, the coherence properties of the XUV light will be much less sensitive to laser intensity noise.

3.2 Macroscopic response and phasematching

Like most nonlinear optical phenomena, the nonlinearly converted light rarely (if ever) perfectly mimics the single-atom response discussed thus far. The macroscopic emission of harmonics is dominated by phasematching. Phasematching is well understood in typical HHG experiments and we will review it within the framework of Ref. [124]. The analysis was originally formulated for HHG experiments performed by very intense, low-repetition rate laser systems. However, the

XUV frequency comb operates in a very different regime employing a much tighter laser focus and a repetition rate nearly six orders of magnitude higher than more traditional systems. The fsEC also complicates the phasematching situation. We will cover how these effects modify phase matching considerations and, despite the added difficulty, show that the XUV frequency comb is the single most powerful source of XUV radiation originating from HHG in terms of average power in its operating spectral region.

3.2.1 Single-pass case

One of the key differences between HHG and other nonlinear harmonic generation (for example, in crystals) is that the nonlinear medium is also strongly absorptive at the wavelengths being generated. Conversion efficiency can then be limited by absorption and not other phase matching conditions.

Reaching the absorption limit in phase-matching HHG requires a delicate balance of many macroscopic parameters. Ref. [124] introduced a simple formulation of the phase-matching criterion that well describes high conversion efficiency results with ∼800 nm [124] and ∼1030 nm [125] laser systems operating in a regime where the laser is focused only loosely. It was originally anticipated that it would not be experimentally feasible to reach the absorption limit in cases where the laser beam is tightly focused (a condition applicable to high repetition rate laser systems like the XUV frequency comb), but analysis and experiment have shown that it is indeed possible to reach this limit albeit in low repetition rate laser systems thus far [126, 127].

The primary distinguishing operating characteristics of the XUV frequency comb are the high repetition rate and tight laser focus needed for performing HHG. Performing HHG inside a fsEC has led to record high XUV flux from HHG systems, but has come with many additional operating constraints pertinent to proper phase matching [114, 128].

The one-dimensional model used for analysis follows the work of Ref. [124]. The harmonic flux of the q^{th} harmonic is $P_q(t)$ given by

$$P_q(t) \propto \frac{4\,\rho^2(t)\,A_q^2\,L_{abs}(t)^2}{1+4\pi^2 L_{abs}(t)^2/L_{coh}^2(t)}\left[1+e^{-\frac{L_{med}}{L_{abs}(t)}}-2\cos\left(\pi\frac{L_{med}}{L_{coh}(t)}\right)e^{-\frac{L_{med}}{2L_{abs}(t)}}\right], \tag{3.8}$$

where $\rho(t)$ is the neutral density that varies with time as $\rho(t) = \rho_0(1-\eta(t))$, with $\eta(t)$ being the ionization fraction and ρ_0 being the original target gas density. A_q is the atomic dipole of the q^{th} harmonic obtained quantum mechanically [118] or empirically [129], L_{med} is the length of the gas target, the absorption length is $L_{abs}(t) = 1/\sigma\rho(t)$ where σ is the absorption cross-section of the harmonic of interest. The coherence length $L_{coh}(t)$ measures the phase mismatch between the driving laser and harmonic q as $L_{coh}(t) = \pi/\Delta k$ with $\Delta k = |k_q - q\,k_0|$, k_0 is the wave-vector of the driving laser, and k_q is the wave-vector of the q^{th} harmonic. Details of all the relevant phase matching terms have been covered extensively elsewhere [72] and can be summarized by

$$\Delta k = \Delta k_{atomic} + \Delta k_{plasma} + \Delta k_{Gouy} + \Delta k_{dipole}, \tag{3.9}$$

where Δk_{atomic} is from the un-ionized gas dispersion, Δk_{plasma} is from the free electron dispersion, Δk_{Gouy} is from the differential Gouy phase shift (Eq. 2.37), and Δk_{dipole} is from the quantum path contribution of the HHG process [86] and depends on the laser intensity gradient.

Phase-matching occurs when $\Delta k \approx 0$ and only transiently over ultrashort laser pulses as $L_{coh}(t)$ evolves with the ionization fraction $\eta(t)$. Absorption limited phase matching is generally achieved when

$$L_{med} > 3\,L_{abs}, \tag{3.10}$$

$$L_{coh} > 5\,L_{abs}, \tag{3.11}$$

ensuring the macroscopic yield is more than half of the maximum yield [124]. An illustration of how the harmonic yield is affected by relative sizes of L_{med}, L_{coh}, and L_{abs} is in Fig. 3.5. If L_{coh} and L_{abs} are comparable in size, oscillations in the harmonic yield as a function of target length

will be present. These are often called "Maker fringes". If no absorption is present, a quadratically increasing harmonic yield is expected. However, even a slight amount of absorption will lead to a saturation of the harmonic yield as a function of target length. The reason is that for every emitter added to the target, an absorber is also added and the net harmonic flux does not increase.

While the one dimensional model was originally intended to apply in the case where the laser beam is only loosely focused, Refs. [126, 127] showed that it is still applicable to the case where the laser beam is tightly focused. A balance of the Gouy phase shift, ionization fraction, and gas density can result in $\Delta k \approx 0$. Fig. 3.6a shows the required density to achieve phase matching as a function of beam radius for different ionization conditions. The critical ionization fraction η_{crit} is the ionization fraction where the neutral atom dispersion cancels the free electron dispersion in the plasma. An important feature of Fig. 3.6a is that a tight laser focus requires commensurately high target densities (and hence nozzle backing pressure). Current fsEC technology limits the feasible spot size to the shaded region and shows that multi-atmosphere backing pressures will be required for phasematching.

3.2.2 Enhancement cavity case

One would hope that these previously discussed conditions could readily be applied to the case of HHG in fsECs. However, the cavity is very sensitive to nonlinear phase shifts present inside the resonator because the cavity effectively increases the nonlinear interaction length [114, 128, 130]. Since the repetition rate of the laser is high, the plasma does not have time to clear the focus of the laser beam, leading to a steady-state plasma during the generation process that can be $\sim 5\times$ larger than the single-pass case. The steady-state plasma leads to an intensity-dependent phase shift in the resonator and the resonator become bi-stable. The phase shift can be quantified by

$$\phi_{NL} = 2\, r_0 \rho \eta L_{med} \mathcal{F} / k_0, \tag{3.12}$$

where $\mathcal{F}$ is the cavity finesse and r_0 is the classical electron radius. While there are methods to deal with this [114, 130], they require detuning the laser from the cavity and reducing the enhancement

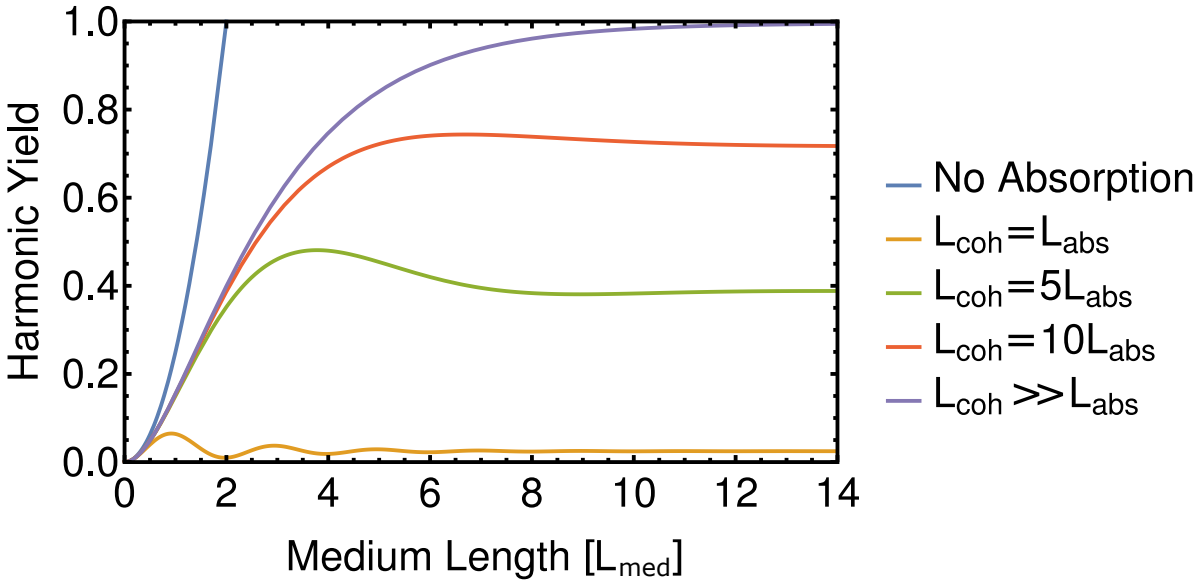

Figure 3.5: The harmonic yield plotted as a function of medium length for various ratios of the coherence and absorption lengths. In the limit that the coherence length is much larger than the absorption length, harmonic flux does not increase with increasing target length. This is in stark contrast to other nonlinear optical phenomena like second harmonic generation where absorption usually does not play a role. A typical quadratic scaling is also predicted in the absence of absorption which is what is expected when the emitters add coherently.

of the cavity. To illustrate the immediate impact of the fsEC on phase matching, Fig. 3.6b shows the nonlinear phase shift under phase matched conditions. Operating too close to the critical ionization and with too small of beams results in a cavity that will not be stable and makes reaching the phase-matched condition nearly impossible unless the thickness of the target is greatly reduced. The process of HHG has been shown to be scale invariant suggesting our operating conditions can, in principle, reach absorption limited phasematching [131]. Nevertheless, it is important to keep the nonlinear phase shift $\phi_{NL} \leq \pi$ to avoid this. We impose an additional optimization conditions and require

$$\phi_{NL} \leq \pi. \tag{3.13}$$

Fig. 3.6b contains two shaded regions corresponding to feasible spot sizes obtainable in the resonator and the region where the nonlinear phase shift is small enough to allow stable, reliable operation. The overlap of the two shaded regions is clearly very small highlighting how important effects of the cavity are for achieving phasematched operation.

To further complicate the matter, when femtosecond pulses propagate through field-ionizing media, the laser pulse spectrum shifts to higher frequencies [114, 130, 132]. Usually this effect is small for optimal HHG conditions, but in the cavity-enhanced approach, small spectral shifts cause notable effects due to the high cavity finesse [114, 130]. When the blue-shift becomes severe, the intracavity spectrum no longer matches the injected laser spectrum and the enhancement is reduced. Until now, there was no suitable method to reduce the spectral blue-shifting besides reducing the cavity finesse and requiring larger driving lasers. We speculate about a potential method at the end of Chapter 6.

To apply the one dimensional model (Eq. 3.8) to HHG in fsECs, extra considerations are required. First, the ionization fraction includes a steady-state value determined by the intracavity intensity [114, 128]. Second, the plasma ramp across the laser pulse leads to an energy loss and spectral blue shifting that reduce the intracavity intensity. The direct energy loss has little effect

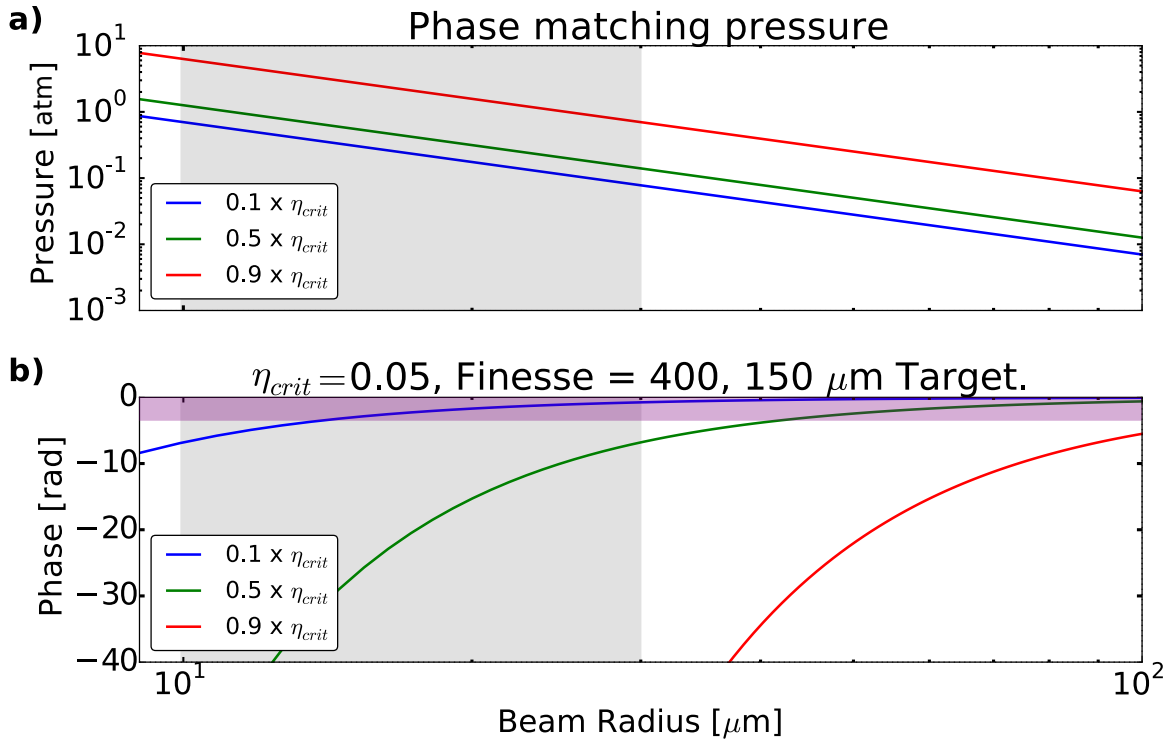

Figure 3.6: **a)** Phase matching conditions. For a given ionization fraction, the beam radius and target gas density can be tuned to achieve phase matching conditions when $\Delta k \approx 0$. **b)** Nonlinear phase shift in the cavity. The phase shift from the neutral/plasma target must be kept less than π in order to keep the fsEC stable. For the phase matching conditions in a), the nonlinear phase shift is shown as a function of beam radius and ionization fraction. The gray shaded regions correspond to regions where the beam waist in the fsEC is feasible to operate for HHG. The purple shaded region in b) is the region where the nonlinear phase shift is small enough for operation.

under our operating conditions. Most of the reductin in laser intensity comes from the mismatch between the blue-shifted intracavity field and the unshifted field we inject into the resonator [114]. Third, the nonlinear phase shift due to the steady state plasma is maintained to be small enough for practical implementation. To achieve reliable operation, we impose Eq. 3.13.

3.3 Power scaling

Up until recently, armed with the just described phasematching knowledge, it was possible to generate $\sim 200\,\mu$W/harmonic. This already makes the XUV frequency comb about 1/10 as bright as the ALS synchrotron [69]. This amount of power was sufficient to perform the first spectroscopy experiments [52]. However, as is often true in any laser-based experiment, having more power is beneficial. The greatest hindrance to further power scaling the system is the troublesome persistent plasma that remains in the laser focus for many cavity round trips. Reducing the steady state plasma will improve conversion efficiency and make the system more reliable and stable.

3.3.1 Methods

Our method for power scaling beyond the 200 μW/harmonic level is straightforward. For our investigations, we use our fsEC equipped with a diffraction grating output coupler [74], a system well suited for spectroscopy [52]. The cavity and HHG detection is schematically sketched in Fig. 3.7. To improve performance, we modify the properties of our gas target using tricks often employed in supersonic beam experiments [133]. A simple estimate and demonstration of our scheme is shown in Fig. 3.8a. For a beam waist of $w_0 = 20$ μm and a peak intensity of 0.5×10^{14} W cm^{-2}, the radial profile of the beam and the ionized fraction of the gas (calculated using ADK theory) are shown in Fig. 3.8a. We can estimate the speed of the beam using Ref. [133] and we find that the time it would take to replenish the previously ionized region is 35 ns, or about 5 cavity round trips. This is consistent with previous observations and modeling [114]. Seeding a heavy gas (like xenon) into helium molecular beam is a common method to increase the jet velocity of the heavier gas. Following Ref. [133], we can estimate the speed increase of a xenon beam mixed with helium and this

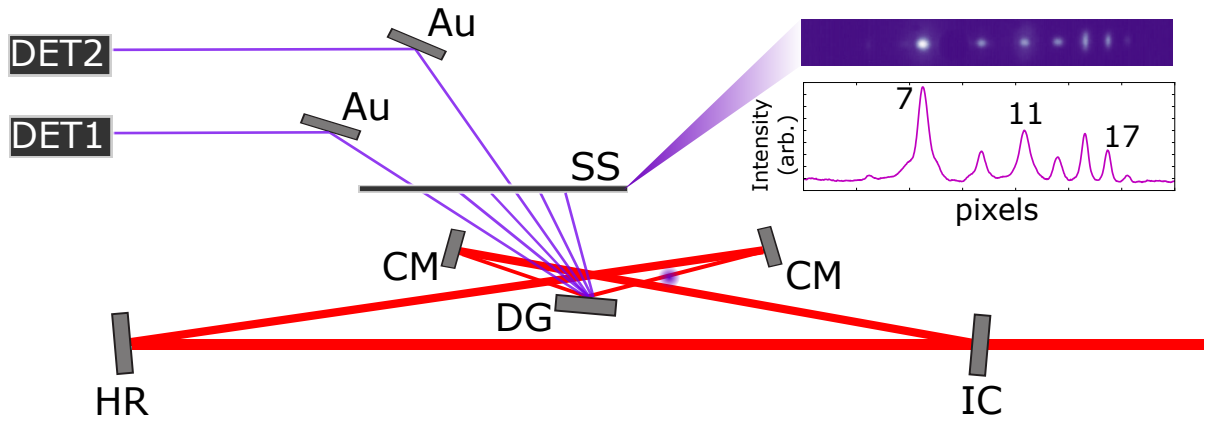

Figure 3.7: Schematic of the apparatus. The harmonics are out-coupled from the cavity using a high reflector/diffraction grating optic. The 11^{th} and the 17^{th} harmonic can optionally pass through the sodium salicylate detection plate by apertures. They can then be sent to independent detectors. The inset shows a typical harmonic spectrum with all orders incident on the sodium salicylate plate with various harmonic orders identified. The relevant harmonic orders can be identified by their horizontal spacing on the plate since this is determined by the line spacing of the diffraction grating. The image was taken with a simple CCD located outside of the vacuum chamber. CM, curved mirror. HR, high reflector. DG, diffraction grating output coupler. IC, input coupler. DET1, aluminum coated silicon photo-diode. DET2, NIST calibrated vacuum photo-diode. SS, sodium salicylate plate. Au, gold mirrors.

is shown in Fig. 3.8b. For large helium fractions, we can greatly speed up the beam and replenish the previously ionized region much more quickly. This will in turn lead to a reduced steady state ionization fraction and hence better phase matching and stability. Since we operate at intensities much too low to effectively ionize helium, we will only maintain harmonic yield from xenon. The potential cost is a reduced xenon density or requiring unfeasible backing pressures for the gas nozzle.

3.3.2 Results

In a sweeping cavity mode, a cavity mirror with a PZT sweeps the cavity resonance across the comb teeth. The cavity operates with an enhancement factor of ~ 200. The cavity is equipped with a 10 cm and a 15 cm ROC mirror and the cavity is set to near the middle of the stability range to achieve a focal beam waist of $w_0 = 25$ μm. The beam waist is determined by measuring the frequency spacings of higher order transverse modes of the cavity (see Sect. 2.2.3). Gas is injected into the focus of the cavity via a quartz nozzle. The harmonics are outcoupled from the cavity using the Yost grating (See Sect. 2.2.6 and Ref. [74]). We detect the 11^{th} harmonic and the 17^{th} harmonic independently and simultaneously. The 11^{th} harmonic is detected on a NIST calibrated vacuum photodiode [134, 135]. The photodiode was biased to -100 V, but the photocurrent was insensitive to the bias voltage between -60 and -120 V. The photocurrent was dumped over a resistor of 10 kOhm and the voltage was amplified using a low noise voltage amplifier. The NIST calibrated diode was used to calibrate the 17^{th} harmonic detector which is an aluminum-coated silicon photodiode [136]. The calibration is performed by comparing photo-currents on both diodes and comparing the relative yields on a sodium salicylate plate. The sodium salicylate acts as a uniform scintillator [13] and the fluorescence is easily measured with a camera, as seen in the inset of Fig. 3.7. The reflectivity of the gold mirrors is calculated with knowledge of the photon energy, angle of incidence, polarization and the optical constants of gold [137]. While the optical properties of gold are well known, the specific characterization of the gold mirrors employed in our measurements are unknown. It is likely that the reflectivity is lower than the theoretical value. Similarly, the performance of the NIST vacuum photodiode is assumed to be perfect. We have no way of independently verifying this, so all power

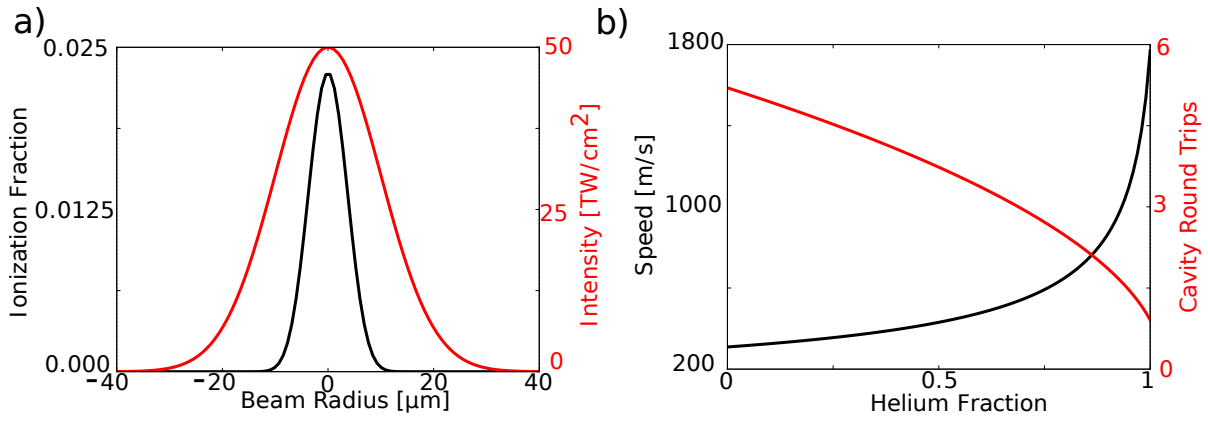

Figure 3.8: **a)** Beam radial profile and the ionization fraction radial profile. The ionization fraction is estimated by using ADK theory covered in Sect. 3.1.1. **b)** The speed of the xenon gas jet as a function of helium seeding and the number of round trips the ionization profile shown in a) will take to replenish the interaction region. The jet speeds were estimated following Ref. [133] and effects like velocity lag were ignored. Replenishment was defined by when the ionized fraction move at least one ionized fraction width away. This figure should only be interpreted as an estimate to the replenishment. More sophisticated fluid flow simulations could in principle be performed. The round trips assumed a laser with a repetition rate of 154 MHz. The round trip estimate can be easily scaled to compared with other systems by the ratio of the repetition rates under consideration. Simply dividing the repetition rate by two should lead to nice improvements on the steady state ionization problem.

levels reported here should be interpreted as lower bounds and the power levels may very likely be higher. While we have taken precaution to ensure the detector was never contaminated, these detectors are known to degrade due to air exposure or other surface contamination [135]. All detectors were verified to be blind to the driving laser.

To determine if we are reducing the steady state ionization fraction by using a faster atomic beam, we can sweep the driving laser across the cavity resonances and observe the self-locking phenomena described throughly in Ref. [114]. Simply, the more steady state ionization, the more the cavity will follow the laser as it is sweeping across the resonance, leading to a lineshape that looks similar to a saw-tooth shape and not a Lorrentzian as in the case of a normal, linear cavity (for an empty cavity, see Fig. 2.5). Fig. 3.9 illustrates this mechanism. Fig.3.9a shows the result of injecting pure xenon into the cavity through a 100 μm nozzle. The intracavity power, the 11^{th} and the 17^{th} harmonic power are monitored as a function of time while the resonance is swept. The departure from the Lorrentzian lineshape of the cavity resonance is a manifestation of self-locking. By simply switching to a 11:1 helium to xenon mixture and increasing the nozzle backing pressure until approximately the same partial pressure of xenon is achieved, the distortion becomes less severe and the harmonic yield is greatly enhanced, as seen in Fig. 3.9b.

Fig. 3.10 documents the maximum achievable harmonic yield for various mixing conditions and nozzle diameters. The laser peak intensity was kept approximately the same in all cases ($\sim 0.67 \times 10^{14}$ W cm^{-2}, or 12.2 kW of average power) and gas pressure was chosen empirically to maximize yield. We also observe a systematic increase of harmonic yield with decreasing nozzle diameter. Decreasing the nozzle diameter requires much larger backing pressures on the nozzle, making it difficult to experimentally realize with the large mixing ratios. We also verified that no measurable harmonic yield (< 0.05 μW outcoupled) was observed when using pure helium as our peak intensities were too low to effectively ionize helium.

As a final demonstration of power scaling, we moved to conditions that we have experimentally determined to optimize yield; the data is also presented in Fig. 3.10. By using a 100 μm quartz nozzle, backed by 100 psi of a 4:1 He:Xe gas mixture, we are able to outcouple 60 μW in the 11^{th}

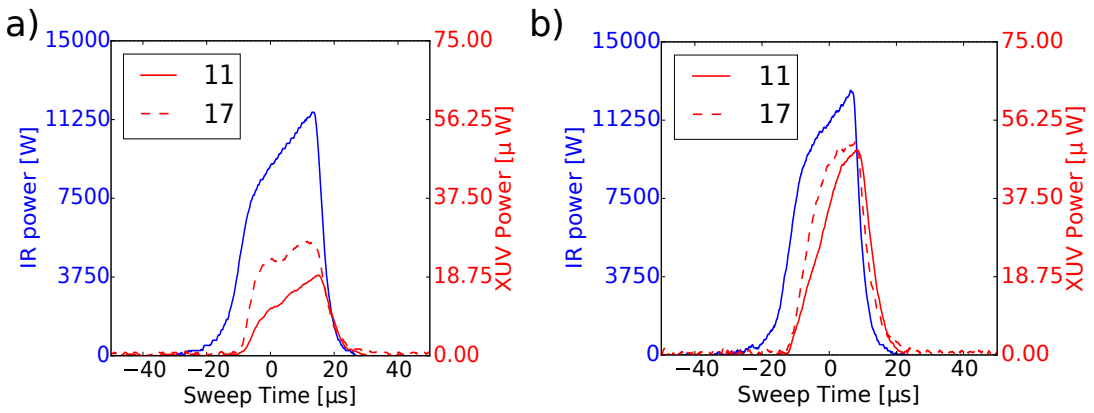

Figure 3.9: The data in both panels was aquired by sweeping the laser across the cavity resonance. A piezo on a cavity high reflector used for the sweep. All the data was recorded on photodetectors simultaneously and averaging with the oscilloscope was performed. **a)** Data for a pure xenon target. **b)** Data for an 11:1 He:Xe mixture. The harmonic yield is greatly enhanced and the self-locking phenomena is reduced compared to a). The xenon densities in these two cases is approximately the same. The nozzle diameter was ~ 100 μm. The beam waist was $w_0 = 25$ μm. The driving laser power was also approximately the same. However, due to the reduction in steady state plasma, b) sweeps to a slightly higher intracavity power. However, harmonic power levels at identical intracavity power levels show a clear improvement for the case of the 11:1 He:Xe mixture so the boost in harmonic yield is not an artifact of sweeping to a larger intracavity power and is due to improving phasematching conditions by reducing the steady state plasma.

and the 17^{th} harmonic order simultaneously. Assuming the diffraction grating output coupler is performing as well as theory predicts [74], this would correspond to a generated harmonic yield of 0.7 mW and 0.63 mW at the 11^{th} and the 17^{th} harmonic order respectively. By switching to a 50 μm quartz nozzle and applying 400 psi with a 4:1 gas mixture, we are able to outcouple 71 μW at the 11^{th} harmonic, corresponding to 0.84 mW generated at 12.7 eV photon energy (4×10^{14} photons/s). Further improvements are achieved with 275 PSI applied with the 9:1 mix resulting in 78 μW at the 11^{th} harmonic, corresponding to 0.93 mW generated at 12.7 eV photon energy (4.8×10^{14} photons/s).

We also performed HHG with nonlinearly compressed pulses (See Sect. 2.3.1). By broadening in bulk sapphire and compressing with chirped mirrors, we delivered 70 fs pulses at up to 53 W of average power to the fsEC. This method yields an optical spectrum and beam profile suitable to maintain intracavity buildups of 200. The intracavity pulse duration was 75 fs, measured by second harmonic intensity autocorrelation of the intracavity field. We are able to outcoupled harmonic flux at the 50 μW/harmonic level and we observed a 25% boost in conversion efficiency (average driving laser power to average XUV power). By using nonlinearly compressed pulses, we observed a decrease in the self-locking phenomena at similar target densities and peak intensities confirming that the shorter pulses are ionizing less of the gas at equivalent peak intensities.

It is useful to compare our results with high-flux results obtained with titanium-sapphire based XUV frequency comb generation. Ref. [138] reports outcoupled power levels of 45 -77 μW over a similar wavelength range. When one considers the inherent $\sim \lambda^{-6}$ wavelength scaling of HHG [139], it becomes clear that the improvement obtained in this work is very encouraging. If we scaled our 60 μW at the 17^{th} harmonic result (1070 nm driver) to directly compare with the titanium-sapphire results (800 nm driver), this would amount to a scaled power of 342 μW, implying generation levels of $\sim$3.4 mW. For applications that do not require very high photon energies (lower harmonic cutoff), it is worth reconsidering driving HHG at 800 nm or even possibly the second harmonic of Yb:fiber-based laser systems at $\sim$ 532 nm. It is important to note that the outcoupled power of fsEC-based XUV sources is in principle totally deliverable on target for experiments, without the need for extra

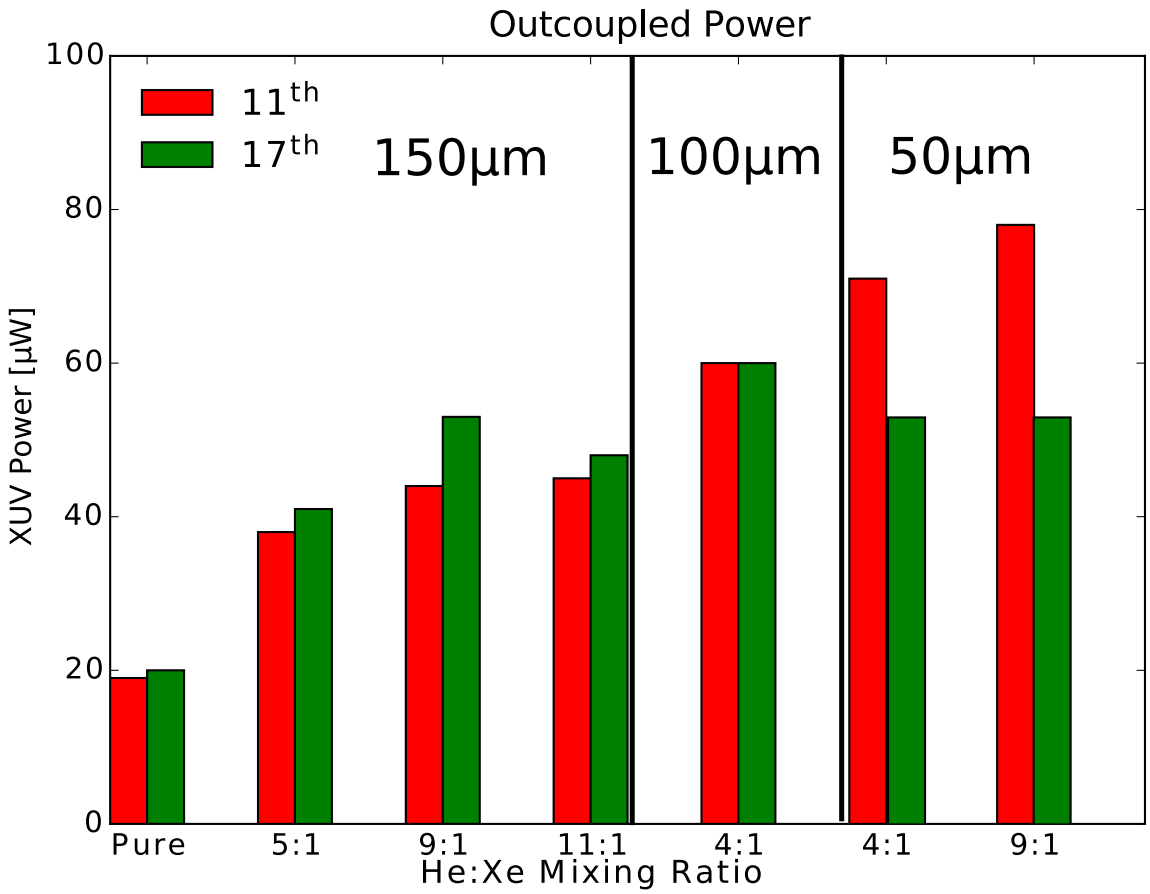

Figure 3.10: System scaling. Output coupled harmonic yields are shown as a function of nozzle diameter and mixing ratio. The laser intensity was approximately the same in all cases and the pressure was choses to maximize yield.

filtering to remove parasitic driving laser light, which is typically very lossy for the XUV light [137]. This is in sharp contrast to more traditional approaches to HHG. Therefore, for direct comparison with lower repetition rate systems, it is more useful and informative to compare generated power levels for both cases. The fsEC-based approach is much higher [125]. For implementation of the XUV light in experiments, filtering out the driving laser is almost always necessary. In the fsEC system described here, the driving laser light is effectively removed by output coupling of the XUV light from the cavity. A broad comparison of HHG sources is plotted in Fig. 3.11. The figure contains the generated XUV power as a function of repetition rate. It should be obvious that for a nominally fixed conversion efficiency, the generated power increases with repetition rate (although, pulse energy commensurately goes down). For linear spectroscopy, average power is the relevant quantity and the XUV comb clearly leads the pack.

The only drawback to our demonstrated method is the increased gas load to the vacuum chamber. However, by having sufficient pumping speed (∼700 L/s) and proper gas dump design (see Sect. 2.5 and Ref. [130]), we are able to operate under safe conditions for the turbomolecular pumps and at low enough background pressures that re-absorption of the harmonics is minimal. The improvements outlined in this chapter are simple to implement and can easily be extended to other collinear output coupling techniques [88, 90] and possibly non-collinear geometries [88, 150]. A simple estimate suggests that by using the geometric output coupling technique [88, 90], we can increase output coupling efficiency by 3× and deliver ∼ 180 μW at 19.7 eV. This will greatly aid application of XUV frequency combs for precision spectroscopy, strong-field physics, and any other application where a high photon flux source of XUV radiation is needed.

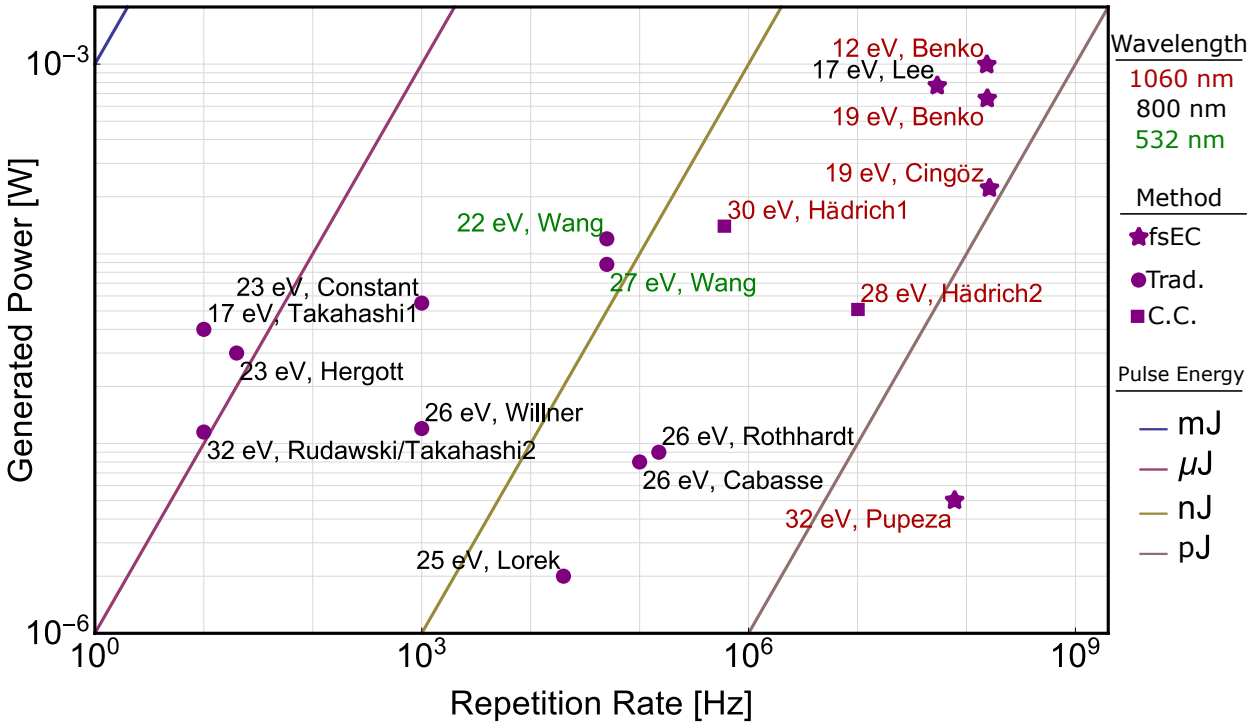

Figure 3.11: Generated power levels are plotted as a function of laser repetition rate. The XUV frequency combs clearly has the advantage in terms of photon flux. The very low XUV pulse energies delivered by the XUV frequency comb are inconsequential for linear spectroscopy. Benko [140], Cabasse [141], Cingöz [52, 130],Constant [124], Hädrich1 [125], Hädrich2 [142], Hergott [143], Lee [138], Lorek [144], Pupeza [90], Rothhardt [126], Rudawksi [145], Takashi1 [146], Takahashi2 [147], Wang [148], Willner [149].

Chapter 4

Interferometry in the extreme ultraviolet

In this chapter, we will focus on aspects related to performing interferometry in the XUV. Various components of the XUV interferometer will be discussed along with some design considerations.

4.1 Motivation and brief history

The goal of building an interferometer in the XUV is to test the temporal coherence properties of the XUV light originating from HHG. Often, we will refer to the temporal coherence level by quoting the inverse of the temporal coherence time and refer to it as the frequency resolution. [1]

Prior to this work, temporal coherence was tested at the 10 MHz frequency resolution level by multiple experiments. The first attempt by Bellini *et al.* [151] only tested coherence at the few fs level, but the experiment nevertheless showed the temporal coherence was indeed there (at least within a single pulse) [151]. Future applications in high resolution spectroscopy will require coherence at a much higher level that will potentially extend over billions of pulses.

After the pioneering work by Bellini *et al.* [151], it was not until much later that pulse-to-pulse coherence was demonstrated. Two methods were employed to test the temporal coherence. Our group employed an interferometric approach by constructing a time-delayed homodyne interferometer to measure the 7^{th} harmonic of our 1070 nm fiber laser [87]. The group of Eikema developed a

[1] This is not a rigorous definition of frequency resolution, but nevertheless useful for our discussion. In Chapt. 5, we will discuss how optical phase noise and temporal coherence are related to laser linewidth and hence frequency resolution.

spectroscopic approach akin to Ramsey spectroscopy. There, the 15^{th} harmonic of an 800 nm laser was used to perform spectroscopy in helium [56, 152]. The spectroscopic signature is evidence of pulse to pulse coherence. Both groups established frequency resolution at the ∼10 MHz level.

In a heroic experimental effort, our group also established the ability to use the frequency comb to perform absolute frequency measurements deep into the XUV by performing direct frequency comb spectroscopy on atomic argon and neon [52, 89]. This, however, still only demonstrated coherence at the ∼10 MHz level but did establish the efficacy of using XUV frequency combs for high resolution spectroscopy. Ultimately, the fractional frequency uncertainty of the transition in argon was measured to about 10^{-10} (∼ 500 kHz) which is about four orders of magnitude better than a typical spectrograph operating in the XUV can achieve [13].

The method we employ to directly measure the fundamental limits of temporal coherence in the XUV was essentially established in our group with the first XUV comb demonstration [3] with a concurrent demonstration in Garching [4]. Our original method relied on generating two UV combs, one in a gas target and one using traditional methods by tripling in crystals. The two sources had different f_0's which upon recombining would form a heterodyne beat (see Fig. 1.6c). By measuring the linewidth of the heterodyne beat, coherence properties could be determined. While this result may not be surprising since it was applied to only the 3^{rd} harmonic, it demonstrates the principle we will rely on to test coherence at harmonics much higher than the third. For our work, we will construct a heterodyne interferometer capable of operating between 1070 nm and 56 nm.

4.2 The extreme ultraviolet interferometer

Our interferometer is an extension of a traditional interferometer design known as a Mach-Zehnder interferometer shown schematically in Fig. 4.1a. A laser beam is split with a 50:50 beam splitter and then recombined, after traversing independent paths, on an additional 50:50 beam splitter. It is possible for these beam splitters to be polarizing, but it is not necessary. There are two output ports where detectors can be placed. The output ports will change from bright to dark depending on the relative phase between the two paths. In general, the two ports are anticorrelated:

meaning that if one port is bright, the other is dark such that the total optical power out of the interferometer is conserved.

The XUV version of the Mach-Zehnder interferometer is shown schematically in Fig. 4.1b. The first beam splitter will be an AOM. This will spatially split the driving laser beam and put a frequency shift on one arm relative to the other. A cavity-based HHG apparatus will be placed in each arm of the interferometer and the resulting HHG beams will be recombined in the XUV. One detection port will be available in our scheme and the interference pattern will oscillate from bright to dark at a rate proportional to the frequency set by the AOM. This is the beat frequency, or the beatnote, that we aim to detect. While what we are trying to achieve is conceptually very simple, the practical implementation is far from it.

The full schematic of the interferometer is shown in Fig. 4.2. Our driving laser is the previously described Yb:fiber comb (See Chapter 2). There are optional modulators (amplitude or phase) placed in one arm of the interferometer. Inside the vacuum chamber, each arm contains an independently stabilized fsEC. The harmonics are outcoupled using sapphire Brewster plates. The harmonic beams are then recombined on a beam combiner in space and time. The combined beam is then sent to a spatial filter and finally an XUV photodetector. There is also an optional monochromator to analyze the performance of the HHG process and XUV optics. Since this is a very non-trivial interferometer, each of the components will be described in detail.

4.2.1 The acousto-optic modulator

The first component of the XUV interferometer is the AOM. When used in conjunction with a frequency comb, the AOM acts as an f_0-shifter. The AOM can be used for high-bandwidth stabilization of f_0 with servo bandwidths of up to 250 kHz, typically limited by the propagation delay of the acoustic wave in the AOM crystal [31]. For this implementation, it will just produce a static, relative f_0 shift between the driving laser of the two arms. We would like to have the AOM put a small frequency shift between the arms since the frequency shift of the harmonics will grow as $f_{q,0} = q \times f_0$ where q is the harmonic order. Therefore f_0 needs to be kept low so it will be

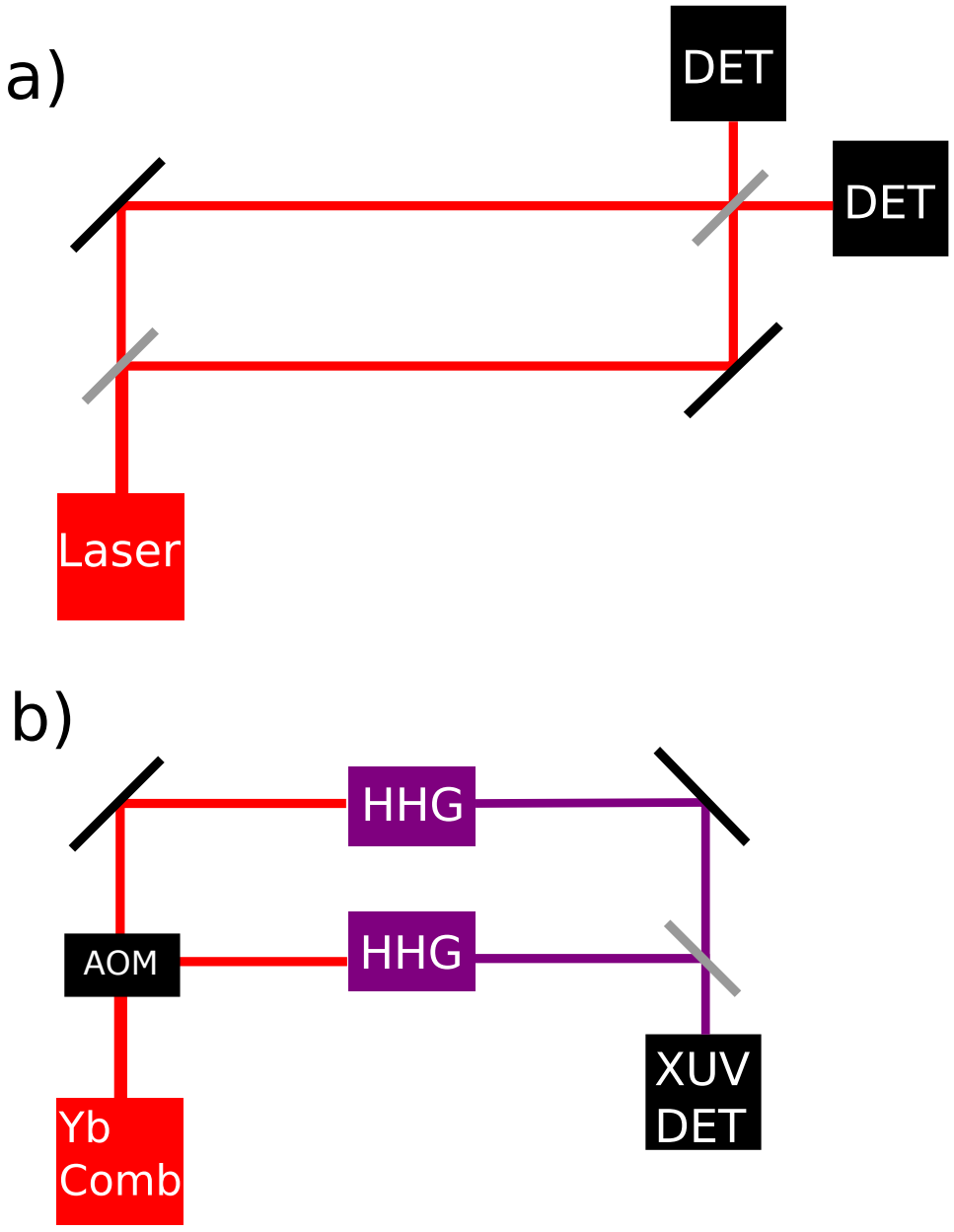

Figure 4.1: Schematics of a Mach-Zehnder interferometer and an XUV Mach-Zehnder interferometer shown in **a)** and **b)** respectively.

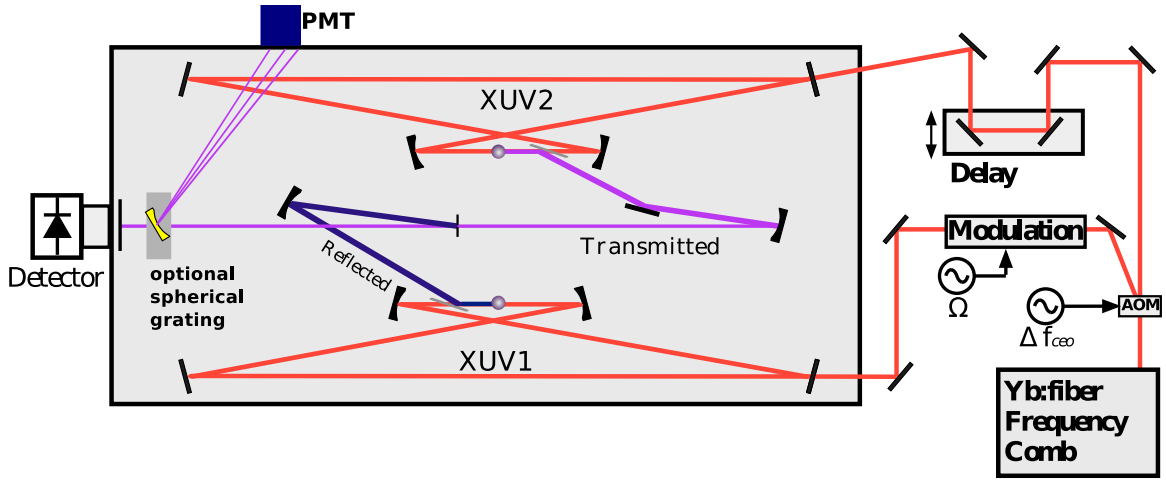

Figure 4.2: Detailed schematic of the XUV interferometer. The Yb:fiber comb is split in two with an acousto-optic modulation (AOM). One patch contains an additional AOM to act as an amplitude modulator. Each cavity is independently stabilized using the PDH method. The XUV beams are outcoupled with sapphire Brewster plates. The XUV beams are recombined (see Sect. 4.2.2) and detected after being spatially filtered (see Sect. 4.2.3 and Sect. 4.2.4). The optional spherical grating is for operation of the Seya-Namioka monochromator (see Sect. 4.2.6). Temporal overlap of the XUV pulses is achieved by temporal delay of the driving laser using a simple delay stage. PMT, photomultiplier tube.

within a possible XUV photodetector bandwidth. We settle on a 1 MHz relative detuning between the arms. However, AOMs do not operate at such low frequencies.

To overcome this, we use an AOM that operates at frequencies near f_r such that f_r - f_{aom} = 1 MHz. When a frequency comb is split by an AOM with a frequency of f_{AOM} and interferometrically recombined on a photodetector, there will actually be two beat frequencies below f_r. The possible beat frequency f_b can be $f_b = f_{AOM}$, f_r-f_{AOM}. This can be seen by referring back to Fig. 1.6. The latter option is typically referred to as the conjugate beatnote. If we simply detect the conjugate beatnote $f_b = f_r$-f_{AOM}, any fluctuations in f_r will couple into the signal. Since we do not want this, it is removed by a phase-lock trick shown schematically in Fig. 4.3 for the black signal pathway. To remove the f_r dependence of the low frequency beatnote, we enforce f_r-f_{AOM}= 1 MHz by phase locking it to an ultrastable Wentzel crystal oscillator. By doing this, the f_r dependence is transferred to the higher frequency beatnote which is left undetected in our case.

As is true of any interferometer, any acoustic noise, mechanical vibrations, or air current fluctuations that are not common to both interferometer arms will cause the relative phase of the interferometer arms to fluctuate. This can be very problematic if the goal is to test the phase stability of the optical signal; it can easily be corrupted by a poorly constructed interferometer. Since it is very difficult to construct an interferometer like ours that is passively stable to less than an optical fringe over many seconds, we must resort to actively stabilizing the interferometer.

To accomplish this, we need a method to detect fluctuations between each arm of the interferometer. When we ultimately detect XUV beatnotes in the interferometer, a small amount of our driving laser light will also make it to the detection plane. For the driving laser, there is a beatnote at 1 MHz that will be sensitive to any phase fluctuations due to the interferometer not being perfect. We use our driving laser beatnote at 1 MHz and compare it to another stable 1 MHz Wentzel source. This comparison signal is referred to as the interferometer error signal. The error signal is sensitive to any phase fluctuations and they are actively removed by slight adjustment to the AOM drive frequency phase. To accomplish this, the additional phase lock is implemented as schematically shown in Fig. 4.3 with the blue signal pathway added. With this additional phase

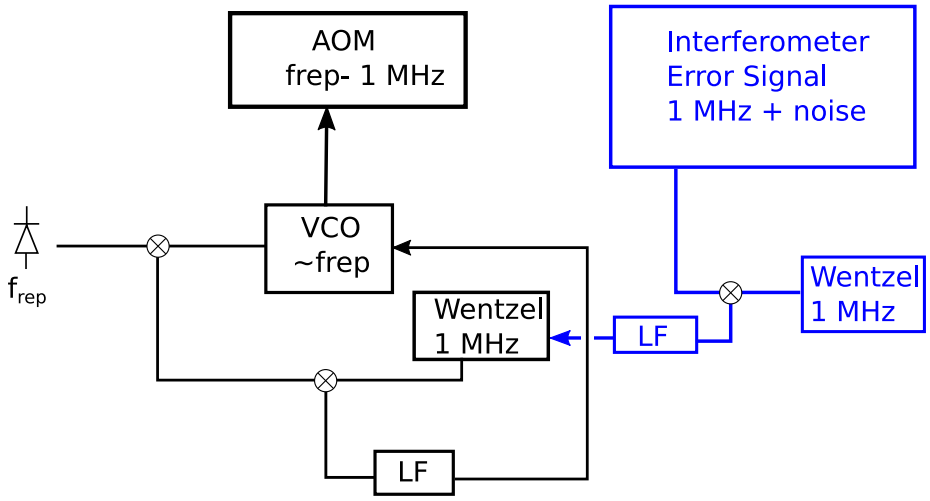

Figure 4.3: The radiofrequency drive scheme for the AOM and the optional stabilization method. An f_r signal is derived from a photodetector and compared with a voltage-controlled oscillator (VCO). The difference is then compared to 1 MHz and that is used to produce an error signal for the phase lock that sets the AOM frequency to be f_r-1 MHz exactly. When the interferometer stabilization is required, the blue signal path is added. A second error signal at 1 MHz is produced from the interferometer that is proportional to phase fluctuation in the interferometer. This is error signal is filtered with a loop filter (LF) and applied to the AOM stabilization scheme to cancel out the fluctuations.

lock, we can be free of technical noise of the interferometer and focus on the ultimate stability of the XUV light.

The choice of AOM optical material is also critical for the experiment. Initially, an AOM constructed of fused silica was chosen. Most AOMs are not designed to operate with up to 80 W of average laser power. Therefore, large beam diameters are needed as well as large RF powers in order to maintain a minimum of 50% diffraction efficiency. A fused silica AOM worked, however, at high laser power, the optical mode strongly distorts due to thermal lensing. This is a common problem with high average power laser systems like ours. To overcome thermal lensing, the laser beam waist can be made larger or additional telescopes can be used to try and manipulate the beam at high power. As it turns out, fused silica just did not have good enough thermal properties. Therefore, we had to switch to a tellurium oxide (TeO_2) AOM. It had much better thermal properties at the expense of more optical dispersion. The extra dispersion is easily compensated with the laser compressor and the residual thermal lensing was manageable with telescopes. An additional TeO_2 AOM is optionally used as an amplitude modulator in one arm of the interferometer.

4.2.2 Construction of the beam combiner

As previously discussed, there simply is not suitable optical material in the XUV that is transparent. This poses a great challenge for building an interferometer than can operate in the XUV. Beam combination is usually achieved with partially reflecting/transmitting optics or polarization beam splitters. These do not exist in the XUV. The aforementioned beam splitters are typically referred to as amplitude division beam splitters. However, there is another class of beam splitters, wavefront division beam splitters, that are suitable for application in the XUV as they only require reflections.

To combine two XUV beams, we rely on a mirror with a hole in it. This is a common trick in the XUV world. By using a mirror with a hole in it, one XUV beam is focused and transmitted through the hole while a second XUV beam reflects off the surface. The two beams will have partial overlap in the far field. To construct such a mirror, we first started with a silicon wafer with a

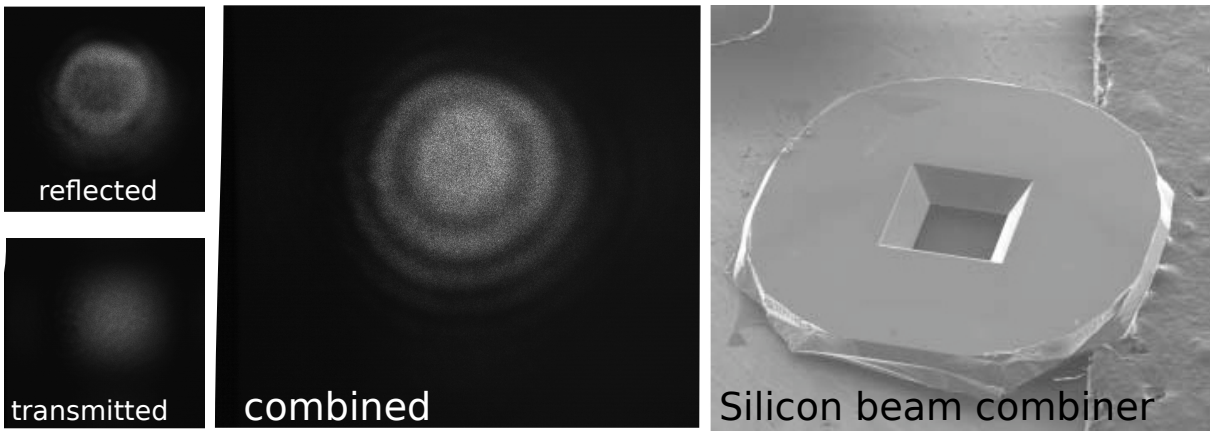

Figure 4.4: Images of the XUV beam combiner. The transmitted (XUV2), reflected (XUV1), and combined beam images were all taken with the driving laser at 1070 nm (see Fig. 4.2 for the relevant beam paths). In order to observe fringes like these with a simple CCD, the frequency detuning between XUV1 and XUV2 must be set to zero. This can be achieved by driving the AOM with the repetition rate (obtained from a simple photodetector).

100 μm square, pyramidal aperture shown in Fig. 4.4. The pyramid structure is important because it allows a larger acceptance angle for the beam that will be focused through the hole. Such a silicon wafer is an "off the shelf" item and is produced by KOH etching, but it needs to be altered to perform well as an XUV mirror. First, the silicon wafer is only 3 mm x 3 mm. To make this more robust and to facilitate polishing it later, we anodically bond the silicon wafer to a pyrex substrate that also has a large hole in it of about 1 mm diameter. It is important the substrate is pyrex or else the anodic bonding process will not work well. To anodically bond the two pieces, they are sandwiched together with a large voltage ($\sim$ 1.5 kV) applied across them and under a high temperature ($\sim$ 300 C). There is a small current that flows between the electrodes which can be monitored. Once the current has almost stopped (after a couple hours), the two optics should be bonded together after the optic cools.

After the anodic bond is formed, the silicon wafer needs to be polished so it can later be coated with a material that reflects well in the XUV. The anodic bond is strong enough to survive polishing. After the silicon is polished to an $\sim$Å rms roughness level and the surface is determined to be optically flat, it is ready for coating. We chose to coat the optics with boron carbide (B_4C) because it has a high reflectivity of about R = 0.3 out to 55 nm at normal incidence. This is a "high reflector" at normal incidence in the XUV. The coating was performed by Rigaku [153] and further discussion of XUV optics is in Sect. 4.2.5.

The nominal performance at 1070 nm wavelength is shown in Fig. 4.4. The transmitted beam retains its normal Gaussian structure. However, the reflected beam does not look quite as nice. Despite the structure on the beam, the wavefront phase is still relatively flat. When the beams are recombined, a bull's-eye fringe is present in the far-field profile. The bull's-eye structure is due to the fact that the reflected beam and transmitted beam have different wavefront curvatures. If this beam was incident on a detector, the total interference pattern would average to zero. To overcome this, the central fringe is selected out with another aperture before detection. This throws away a small amount of optical power, but it ensures a high contrast interference fringe for detection.

4.2.3 Beam combiner theory and scaling

To begin to describe the beam combiner operation, we rely on Babinet's principle (principle of complementary apertures) to describe the reflected beam. The far-field reflected beam u_R can be written as combination of a Gaussian beam and the beam generated by the inverse of the aperture. For our consideration, we will assume a circular aperture of radius a. The schematic used for calculation is in Fig. 4.5a. For the reflected beam amplitude, we have

$$u_R = u_G - u_H \tag{4.1}$$

where u_G is just a Gaussian beam with the focus of ω_1 at a distance L from the hole mirror. The functional form of the Gaussian beam can be found in Eq. 2.34. The contribution of the aperture is [14]

$$u_H(r,z)/u_0 = i\pi N e^{-i\pi N(r/a)^2} \int_0^1 \mathrm{d}\left(\frac{r'}{a}\right) u_G(r') e^{-i\pi N(r'/a)^2} \frac{r'}{a} J_0\left(\frac{2\pi r r'}{a^2}\right), \tag{4.2}$$

where N is the Fresnel number defined as $N = a^2/z\lambda$. While this equation is quite cumbersome, it can easily be treated numerically. The full far field combination is a sum of all three contributions

$$u_{total} = u_R + u_T, \tag{4.3}$$

where u_T is the transmitted beam, which is also a Gaussian of form Eq. 2.34 with a focus at $z = 0$ and a beam waist of ω_2.

As an illustrative example, the results of a numerical simulation are shown in Fig. 4.5b,c with L = 10 cm, z = 40 cm, $\lambda = 83$ nm, $\omega_1 = \omega_2 = 25\,\mu$m and the beam combiner aperture a was left to vary. The spatial filter aperture was chosen to isolate the central fringe. The signal to noise was estimated by considering the contrast of the signal illustrated in Fig. 4.5c with the in and out of phase beam profile of the combined beams. The contrast is $C = (I_{max} - I_{min})/(I_{max} + I_{min})$ and assuming a shot-noise-limited detection, the signal to noise is $\sqrt{2}\sqrt{(I_{max} + I_{min})}C$.

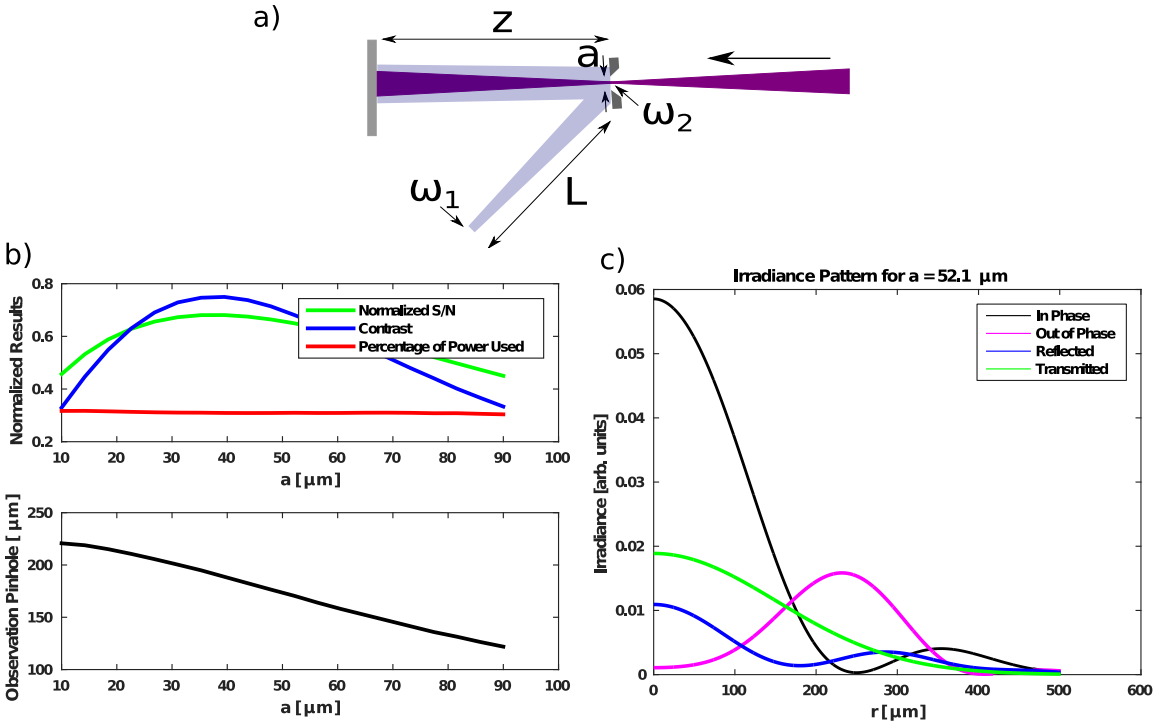

Figure 4.5: **a)** Schematic of the beam combination geometry relevant for calculation. A roughly collimated beam is used in reflection and a tightly focused beam is used for transmission. The beam combiner is assumed to have an aperture of width a. The detection plane will contain a spatial filter to select the central interference fringe. The degree of beam collimation, beam combiner aperture size, and spatial filter aperture size were all choses to maximize interference contrast and signal-to-noise. For **b,c)** the following parameters were chosen. z = 40 cm, L = 10 cm, λ = 83 nm, and $\omega_1 = \omega_2 = 25\,\mu$m. The parameter a was varied and the spatial filter size was chosen to isolate the central fringe. **b)** Shown is the compromise of SNR, power used and contrast as a function of aperture size. The bottom panel shows the optimal spatial filter size. **c)** The electric field is shown in for the transmitted and reflected beam for $a \approx 50\,\mu$m. The in and out of phase profile of the combined beam is also shown.

If briefly we ignore the effect of the aperture on the reflected beam and analyze how the different wavefront curvatures of the two combined beams affect the spatial fringe, we find that the distance from the center of the beam to the first interference minimum actually scales as $\sqrt{\lambda}$. This can be seen by looking at Eq. 2.34 and realizing the wavefront phase scales inversely to λ but proportionally to the radial distance squared. This rather favorable scaling implies that the interferometer should work over a wide range of wavelength ranges without having to constantly modify experimental parameters such as z, L, ω_1 or ω_2. By setting the aforementioned parameters, a single spatial filter at the interference plane can also be chosen to maintain near optimal performance for harmonics 7–17. As will be presented later, we observed the heterodyne beats between 56 nm and 1070 nm without changing anything but the detector.

4.2.4 Extreme ultraviolet detectors

To detect heterodyne beats in the XUV, we need a detector that is both sensitive at XUV wavelengths and has a fast response since the beatnotes will be at multi-MHz frequencies. The most common approach to detecting XUV photons is to use a scintillating material. Sodium salycilate is a good material because it absorbs light below 355 nm and fluoresces around 420 nm. Detecting 420 nm light is straightforward with a photomultiplier tube (PMT) or even a CCD camera. The upper state lifetime of sodium salycilate is also ~ 10 ns allowing for high bandwidth detection. An additional benefit is that the quantum efficiency is nearly perfectly flat between 5 eV and 15 eV making comparisons between harmonic orders very straightforward [13].

Another option is to use an electron multiplier or an multi-channel plate (MCP). Electron multipliers work in a similar way to PMTs. They can have very large internal gains (up to 10^7) and can operate directly in a vacuum chamber (unlike PMTs). The work function of common electron multipliers is typically 9 eV or higher, making them "solar blind". For us, that means they do not see the driving laser or the 3^{rd} harmonic, which is a huge benefit, and can thus allow for very sensitive detection without saturating the detector on the abundant 1070 nm or the 357 nm light. Electron multipliers can also have ~ 10 ns response times again allowing for high bandwidth detection.

In the power scaling effort reported in Chapter 3, two other detection methods are employed. A windowless silicon diode with a thin metallic coating can be used [136]. The metallic coating filters out low photon energy light and the silicon behaves in much the same way as it does with visible light. The second was a NIST calibrated vacuum photodiode [134]. The photodiode was a polished piece of aluminum oxide that serves as a photocathode. Photoelectrons emitted from the aluminum oxide are collected on a biased anode ring. The device was calibrated by NIST. These two detection methods are often the most accurate. However, they are also very difficult to operate with high gain and high bandwidth. They are therefore not ideal for the heterodyne interferometry experiment.

4.2.5 Extreme ultraviolet optics

One of the most common optical coating materials for XUV radiation is gold. At grazing incidence, gold can have excellent reflectivity from the XUV out to hard x-ray wavelengths [137]. However, for our interferometer, it is impossible to build it with only grazing incidence optics. The actual optical layout in reality is close to what is shown in Fig. 4.2. For the path of XUV2 in the figure, a 70 deg grazing incidence reflection and one normal incidence reflection will be required to get the beam to the combiner. Fig. 4.6 show the expected reflectivity if gold optics are used. The net reflectivity of both optics combined is only $\sim 2\%$ for the wavelengths of interest.

Another, less commonly used optical material is B_4C. At normal incidence, B_4C has a reflectivity 2×-3× that of gold [154–156]. Fig. 4.6 also shows the expected reflectivity for XUV2 if all B_4C mirrors are used. The advantage is clear. When one considers that the heterodyne beat between XUV1 and XUV2 will be proportional to the product of their fields, enhancing the net reflectivity by 5× for each arm of the interferometer will give 5× more heterodyne beat power. The reflectivity reported in Fig. 4.6 was calculated by the known optical constants of both materials. One drawback to using B_4C or other boron-based optical coatings is that they tend to decay over time and primarily limit the reflectivity at short wavelengths at normal incidence. We have indeed observed this decay and a mirror that was used over the course of a year experienced almost a factor

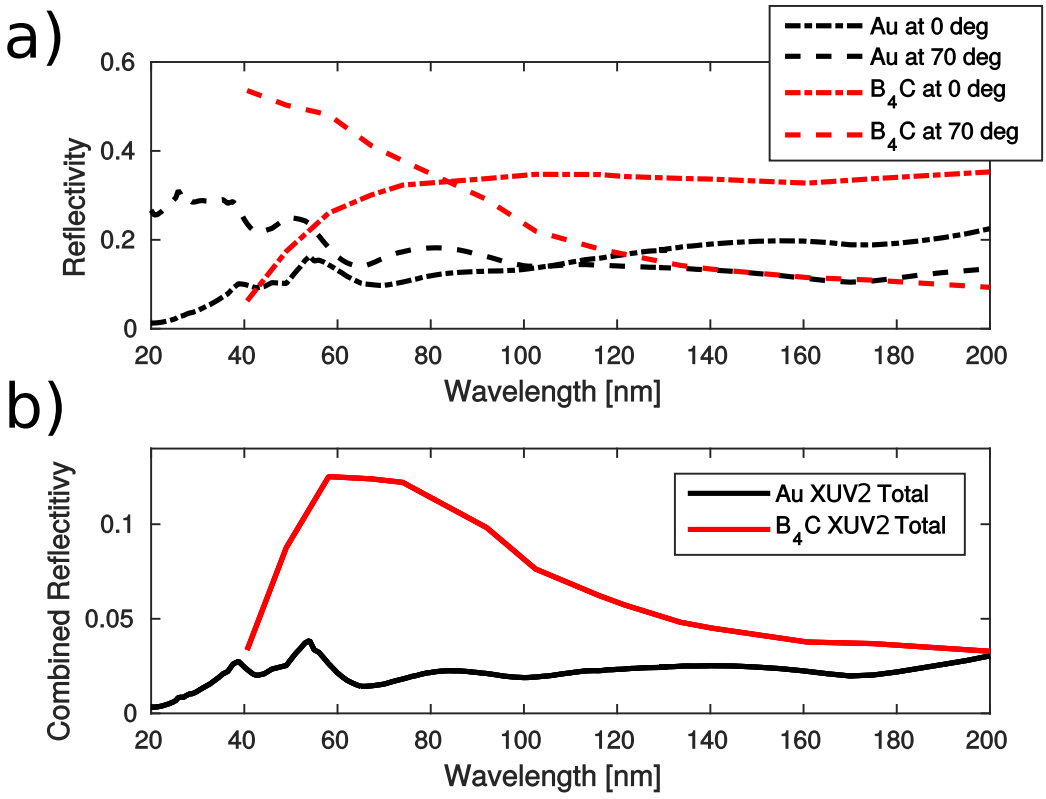

Figure 4.6: The reflectivities of boron carbide and gold. **a)** The reflectivity of both optics in the path of XUV2. **b)** The net reflectivity of both optics for XUV2 assumes both gold mirrors or both B_4C mirrors. The improvement by choosing B_4C is very clear. In all cases, the reflectivity was calculated with knowledge of the optical constants of the materials.

of 3 drop in reflectivity at 200 nm. We were unable to determine the loss at shorter wavelengths, but suspect it was even more severe.

4.2.6 The Seya-Namioka monochromator

The final piece of the experiment is not actually required for interferometer operation. However, it is a very useful tool for diagnosing the HHG process and confirming proper operation of our XUV optics. The Seya-Namioka monochromator is a simple and robust method of detecting HHG radiation [13]. We added a Seya-Namioka monochromator to our apparatus by having a removable spherical grating placed near the detection plane as seen in Fig. 4.2. The monochromator only works for the XUV2 beam path. The beam combiner acts as an entrance slit to the monochromator. The spherical grating diffracts and re-focuses the light to an exit slit. After the exit slit is a sodium salycilate coated light pipe fed to a PMT. A DC stepper motor drives a ferrofluidic feedthrough that is connected to a rotation stage that holds the grating. A key feature of the Seya-Namioka design is that the angle between the entrance slit and exit slit is fixed ($\sim$ 70 deg) and only the grating needs to rotate. This makes for easy implementation and easy interpretation. The achievable resolution is in principle a few Å.

The results of a monochromator scan are shown in Fig. 4.7. The monochromator is operated in low resolution mode ($\sim$ 1 mm exit slit) but all the harmonics orders are clearly resolved. The scan takes about 30 seconds. Harmonics 7–21 are clearly visible (and possibly the 23). The relative heights of all the harmonic orders are strongly influenced by our choice of optics. For the XUV2 path, Fig. 4.8 contains the reflectivity of all the optics. The trace labeled B_4C accounts for the normal incidence reflection and the grazing reflection in the beam path. The grating efficiency was given by the grating manufacturer. The total throughput of the system is not that great, being only 0.2% at maximum. Nevertheless, we can use this information to reconstruct the harmonic spectrum that is generated and how much will be present at the beatnote detection plane (with the grating removed). The scaled harmonic spectrum is shown in Fig. 4.9. The raw spectrum is taken from the data in Fig. 4.7. The exit plane data represents the light that will be available for heterodyne

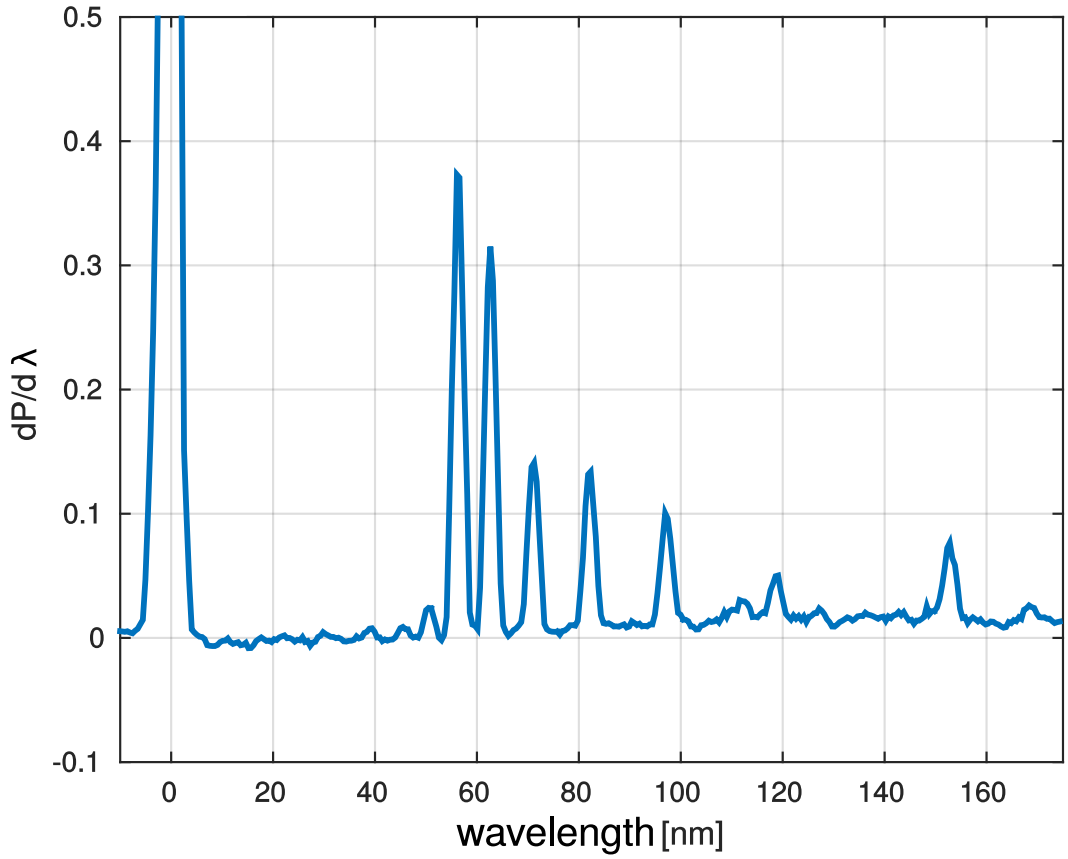

Figure 4.7: The harmonic spectrum measured with a Seya-Namioka monochromator. The spherical diffraction grating is rotated about its center while the photocurrent from a photomultiplier tube is measured. Signals that do not fall on harmonic orders are due to second order diffraction of the grating. The data is the result of a single scan that took about 30 seconds to acquire.

detection. The generated data is the inferred harmonic spectra at the focus of the cavity. Clearly, we make an enormous amount of 7^{th} harmonic, but this is consistent with previous observations and is relatively unexplained [89]. Our harmonic spectra exhibits a "traditional" plateau shape, one of the early and intriguing features of the HHG spectrum.

4.3 Putting it all together

With all of the key operating components discussed, the final operation mode can be established. The output of the Yb:fiber comb is split 50:50 by the AOM operating at f_r-1 MHz. Each path, XUV1 and XUV2, has an independent set of mode matching optics. The two arms are slightly different due to the fact that the 1070 nm beam traverses different directions in the ring resonators.

The light is coupled into independent fsECs. The input coupler is R = 0.985 so the finesse is ~ 400, and the buildup is ~ 200. Since the Yb:fiber comb only has two degrees of freedom and both cavities require a total of four degrees of freedom for simultaneous stabilization, the Yb:fiber comb is left free running and all the servo actuation to maintain stabilization is performed with the fsECs. The PDH lock is actuated on by two PZTs in each fsEC. One PZT is a fast, low voltage PZT attached to the cavity HR mirror. A second, slow but long travel PZT pushes a translation stage located underneath the same HR mirror. The servo loops for each cavity are independent. Fortunately, since both cavities have identical optics, the required f_0 was the same for both cavities (including the 1 MHz offset by the AOM) and could be adjusted by manipulating the temperature of the fiber Bragg grating inside the laser oscillator. Generally, no active feedback was necessary for f_0.

The focal spot size is 19 μm $\times$ 22 μm in both cavities, so average powers between 4 kW and 6 kW are necessary for good HHG conversion. The focal spot is determined by measuring the frequency spacing of higher order transverse modes as discussed in Chapter 2. Xenon is injected through quartz nozzles with 150 μm diameter. The light in XUV1 and XUV2 is outcoupled using a 330 μm thick sapphire Brewster plates (see Fig. 2.7 or Fig. 4.8 for expected performance). Each of the XUV beams are steered inside the vacuum chamber by motorized B_4C coated mirrors. After

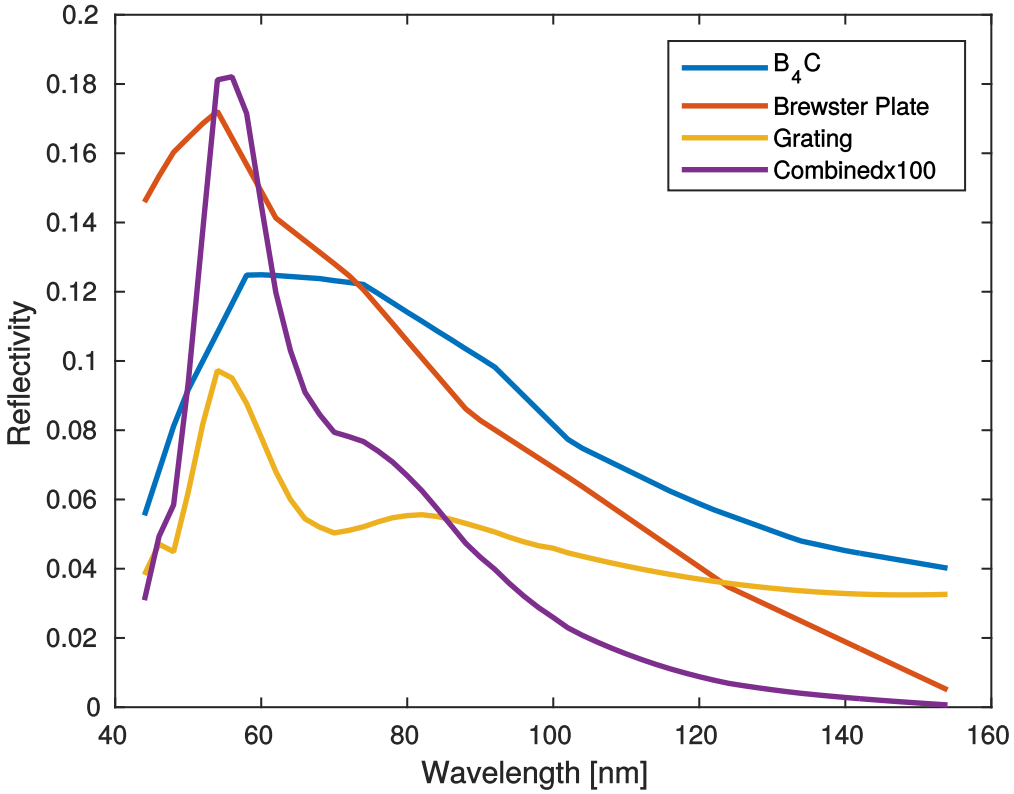

Figure 4.8: The reflectivities of various optics in the XUV interferometer and monochromator. This data is used to back out the relative amount of harmoinc power at the generation location.

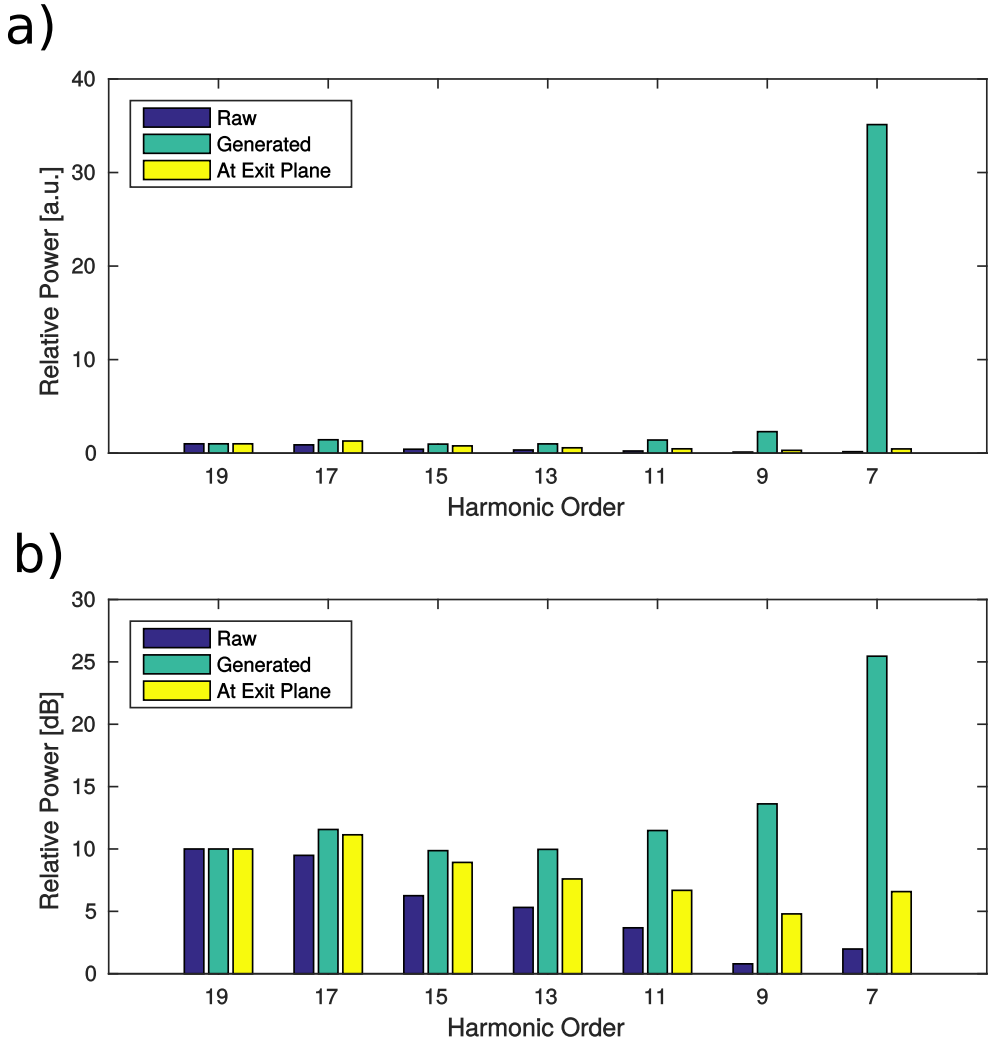

Figure 4.9: The relative harmonic powers at different points in the interferometer. The data in both figures is the same but shown in linear and log scales for **a)** and **b)** respectively. The large amount of 7^{th} harmonic is consistent with previous observation and its origin is not completely clear.

recombination in space and time, the beams are directed to a spatial filter of a 100 μm square aperture before detection. The time overlap between the XUV pulses is achieved by delaying the time of the Yb:fiber comb pulses using a delay stage in the XUV2 beam path.

Because fsECs XUV1 and XUV2 are both pumped by a common NIR laser, the noise in the radio frequency (RF) beatnotes is immune to the common-mode frequency noise of the Yb:fiber laser. Thus, the apparatus directly measures noise from the HHG process or the cavity-plasma dynamics. However, because the interferometer is not actively stabilized, there are small amounts of relative noise induced by vibrations in the optics, giving the two sources a non-zero relative linewidth that is technical in origin. This tecnical contribution can be removed by the active stabilization scheme previously discussed.

Harmonics 3–7 could be detected using a sodium salycilate screen with a PMT. Harmonics 9–19 were detected directly with an electron multiplier. The photocurrent coming from the detectors is expected to have the form

$$I(t) = I_1(t) + I_2(t) + \sqrt{I_1 I_2}\cos(q f_{AOM} t + q(f_r - f_{AOM})t + \phi(t)), \tag{4.4}$$

where $\phi(t)$ are any relative phase fluctuations. However, we have enforced $\Delta f = f_r - f_{AOM} = 1$ MHz and $q f_{AOM}$ is far too fast for our detector's response time, Eq. 4.4 reduces to

$$I(t) = I_1(t) + I_2(t) + \sqrt{I_1 I_2}\cos(q\Delta f t + \phi(t)). \tag{4.5}$$

The output of the detectors is amplified and sent to an RF spectrum analyzer. Fig. 4.10 contains the RF heterodyne beats for harmonics 3–17. The harmonic beatnotes were heterodyne translated from their 3 MHz, 5 MHz, 7 MHz, etc. tones to lower frequencies for display on an FFT analyzer. There is also a beatnote from the fundamental laser at 1 MHz, but this is not shown. It is separately detected by picking off a small fraction of the edge of the beam that would be otherwise wasted by the spatial filter. The B_4C optics and the Brewster plate still have a very small reflectivity at 1070 nm facilitating this detection. There iss also a beatnote at 19 MHz, however,

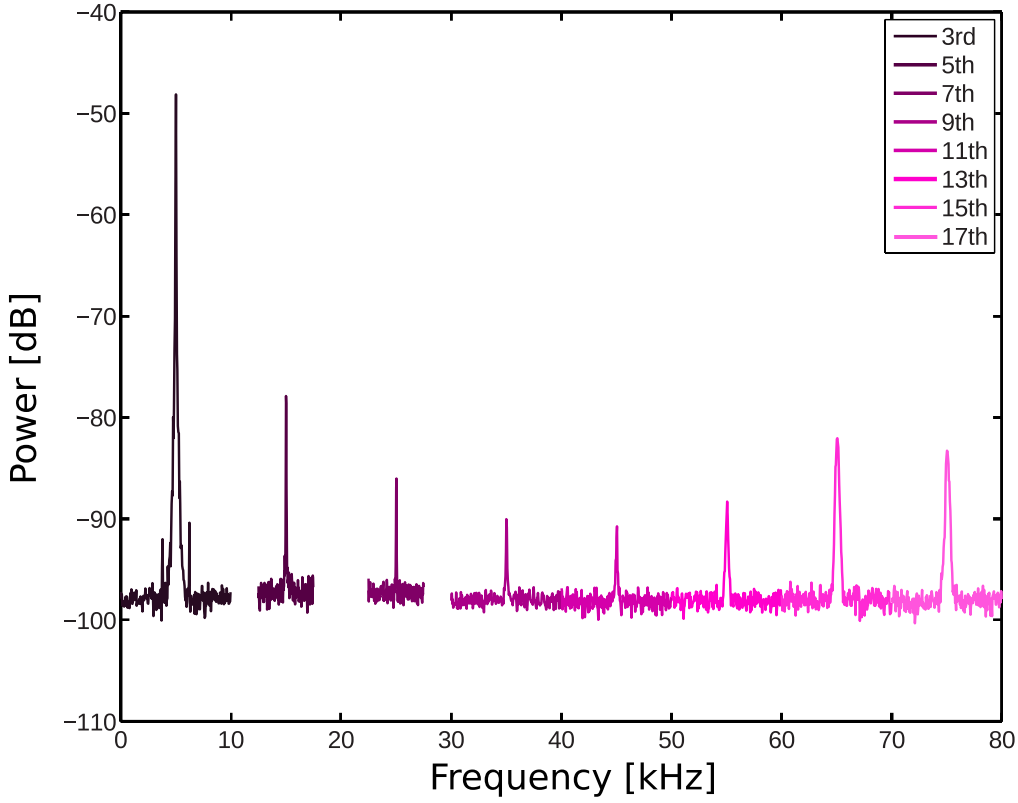

Figure 4.10: Heterodyne beats from harmonics 3–17. The harmonics were originally detected at 3 MHz – 17 MHz but were frequency shifted to much lower frequencies using RF mixing to help high resolution display on an FFT analyzer. The data is presented on a 30 Hz resolution bandwidth.

the signal-to-noise is very poor. We suspect this is due to a reduction in the B_4C reflectivity, which is hard to accurately characterize in our system [154–156]. The relative heights of the beatnotes in Fig. 4.10 also resembles the expected relative heights from Fig. 4.9.

The data in Fig. 4.10 is already great news for the XUV comb. The f_0 scaling of each harmonic order is exactly $f_{q,0} = q \times f_0$. Also, the beatnotes are clearly sub-kHz. Already this is a huge improvement over previous work and shows that nothing drastic is happening to destroy the coherence in the XUV. With each harmonic order individually accessible in the RF domain, it is now possible to analyze them independently and use them to investigate strong-field physics with phase-sensitive techniques.

Chapter 5

Phase noise and phase sensitive detection in the extreme ultraviolet

In this chapter, we will discuss and answer the basic question of "How good is the XUV frequency comb?" Here, "goodness" is referred to as a long coherence time or a narrow optical linewidth. Further, in this chapter we will describe how phase noise scales in the harmonic generation process and test the limit of XUV coherence by measuring sub-Hz linewidths at various harmonic orders. We will also demonstrate how we can use phase-sensitive detection in the XUV to probe strong-field physics which occurs at attosecond timescales.

5.1 Optical phase noise

Phase noise in periodic signals is a very well studied problem. Much of the work well predates laser development and finds most of its development in the context of RF signals and RF communications. We will focus mainly on how phase noise affects oscillators or waves (specifically, their power spectrum), but we refer to Ref. [157] for thorough investigation of amplitude, phase and frequency noise processes. For discussion related to RF oscillators, Ref. [158] is quite useful. In the context of laser stabilization, a thorough discussion is in Refs. [47, 159]. For the purposes here, we will review the most important aspects as they relate to the XUV comb experiments.

Before establishing the characteristics of optical phase noise, it is useful to consider how a coherently phase modulated wave behaves and then move to a wave modulated by random phase fluctuations. A phase modulated wave is written as

$$E = E_0\, e^{-i\omega_0 t - i\phi(t)}. \tag{5.1}$$

the instantaneous frequency is $\omega = \omega_0 + \mathrm{d}\phi(t)/\mathrm{d}t$. If we assume that $\phi(t) = \beta \sin(\Omega t)$, where β is the phase modulation depth [1] and Ω is the modulation frequency, we can expand Eq. 5.1 in a series of Bessel functions as

$$E = E_0 J_0(\beta) e^{-i\omega t} + \sum_{n=1}^{\infty} E_0 J_n(\beta) \left(e^{-i(\omega + n\Omega)t} + (-1)^n e^{-i(\omega - n\Omega)t} \right), \tag{5.2}$$

where J_n is a Bessel function of order n. An interesting property that is preserved and is not immediately obvious from the expansion is that $EE^* = E_0^2$, meaning a phase modulation process does not add to or remove from the total power of an oscillating wave. The expansion in Eq. 5.2 tells us that the sinusoidal modulation creates symmetric "sidebands" about the carrier wave at ω_0. However, the sign of the electric field amplitude at frequencies below the carrier changes with order n. If the modulation depth β is large, there will be multiple sidebands generated at integer multiples of the modulation frequency Ω. We can represent the amount of power in the first order sideband P_{SB} relative to the power in the carrier P_C by

$$\frac{P_{SB}}{P_C} = \left| \frac{J_1(\beta)}{J_0(\beta)} \right|^2. \tag{5.3}$$

In the limit that β is small, $P_{SB}/P_C \approx \beta_{rms}^2/2$ where β_{rms} is the root-mean-square of β. This is an instructive result because it shows that the amount of power moved from the carrier to the sidebands is nonlinear in the size of the phase modulation. To illustrate why this can be problematic in the context of optical harmonic generation, consider the second harmonic gerneration process in a crystal. The second harmonic field intensity will be proportional to the square of the driving laser electric field [2] $E_{2\omega} \propto E_\omega^2$. Explicity, we have

[1] Previously, we used β to refer to enhancement cavity buildup. In this chapter, we use β to mean phase modulation depth. The choice of using β is based on convention. The meaning of β will be clear from context.

[2] Note that this is E^2 and not $|E|^2$, a subtle but extremely important difference.

$$E_{2\omega} \propto E_{\omega}^2, \tag{5.4}$$

$$E_{\omega}^2 = E_0^2 e^{-i2\omega_0 t - i2\beta\sin(\Omega t)}. \tag{5.5}$$

There are two important results here. First, the modulation frequency did not change by the harmonic generation process. Second, the phase modulation depth changed and $\beta \to 2\beta$ meaning the amount of power taken from the carrier also changed to $P_{SB}/P_C \to 4\,P_{SB}/P_C$. This can be generalized to higher order harmonics (assuming they are proportional to powers of the electric field) to be $(P_{SB}/P_C)_{q\omega} = q^2\,(P_{SB}/P_C)_{\omega}$ where q is the harmonic order. If the harmonic order becomes too high, eventually all of the power can be taken away from the carrier. If we imagine that the $\phi(t)$ is no longer a pure sinusoid, but a random process, we can still decompose it into its Fourier components and we can have a similar expansion as in Eq. 5.2 but for each Fourier component (we will make this claim more rigorous shortly). What we realize is that with increasing harmonic order, the amount of power in the noise relative to the carrier will grow quadratically for frequency doubling.

Instead of dealing with discrete phase modulation frequencies, we can generalize to the case where $\phi(t)$ is a normal, random process. If we want to know how the random phase modulation affects the pure wave, we often look at the frequency power spectrum to analyze how much power is at frequencies other than the carrier. The Wiener-Khintchine theorem states that the frequency power spectrum is just the Fourier transform of the temporal autocorrelation. Explicitly, the electric field autocorrelation is

$$R(\tau) \equiv \langle E(t)E^*(t+\tau)\rangle_t. \tag{5.6}$$

Invoking the Wiener-Khintchine theorem, the power spectrum is

$$P_E(\omega) = \frac{1}{\sqrt{2\pi}} \int \mathrm{d}\tau\, e^{-i\omega\tau} R(\tau). \tag{5.7}$$

We can insert Eq. 5.1 into $R(\tau)$ to get

$$R(\tau) = E_0^2\, e^{i\omega_0\tau}\langle e^{i(\phi(\tau+t)-\phi(t))}\rangle_t, \tag{5.8}$$

and using the Gaussian moment theorem [158, 159], we can make the final manipulation

$$R(\tau) = E_0^2\, e^{i\omega_0\tau} e^{R_\phi(\tau)-R_\phi(0)}, \tag{5.9}$$

where

$$R_\phi(\tau) = \langle \phi(t)\phi(t+\tau)\rangle_t. \tag{5.10}$$

Before moving forward, we can identify important characteristics of $R_\phi(\tau)$. First, if the noise is random and uncorrelated, $R_\phi(\tau)$ has an important limiting form of

$$\lim_{\tau\to\infty} R_\phi(\tau) = 0. \tag{5.11}$$

Secondly, for $\tau = 0$, we have

$$R_\phi(0) = \langle \phi(t)\phi(t)\rangle_t = \langle \phi(t)^2\rangle_t = \Delta\phi_{rms}^2. \tag{5.12}$$

These conclusions allow us to rewrite $R(\tau)$ in the limit of large τ in a very suggestive way. We have

$$\lim_{\tau\to\infty} R(\tau) = E_0^2 e^{-\Delta\phi_{rms}^2} e^{i\omega_0\tau}. \tag{5.13}$$

This shows that the amount of power in the carrier is just $\exp\big(-\Delta\phi_{rms}^2\big)$.

We can also define the phase noise power spectral density of the electric field $S_\phi(\omega)$ using the Wiener-Khintchine theorem. It is

$$S_\phi(\omega) = \frac{1}{\sqrt{2\pi}} \int \mathrm{d}\tau e^{-i\omega\tau}\, R_\phi(\tau)\,. \tag{5.14}$$

The phase noise power spectral density is a very useful quantity. Note that is has units of $[\mathrm{rad}^2/\mathrm{Hz}]$. To illustrate its utility, we assume that our wave has small phase fluctuations. This means that

both $R_\phi(\tau)$ and $R_\phi(0)$ are small. Starting with Eq. 5.7 and expanding the exponent in $R(\tau)$, we have

$$\begin{aligned} P_E(\omega) &= \frac{E_0^2}{\sqrt{2\pi}} \int \mathrm{d}\tau\, e^{-i(\omega-\omega_0)\tau}(1 + R_\phi(\tau) - R_\phi(0)), \\ &= \frac{E_0^2}{\sqrt{2\pi}} \left[\int \mathrm{d}\tau\, e^{-i(\omega-\omega_0)\tau}(1 - R_\phi(0)) + \int \mathrm{d}\tau\, e^{-i(\omega-\omega_0)\tau} R_\phi(\tau) \right], \\ &= E_0^2 \left[(1 - R_\phi(0))\delta(\omega - \omega_0) + S_\phi(\omega - \omega_0) \right], \end{aligned} \tag{5.15}$$

where $\delta(\omega - \omega_0)$ is a Dirac delta functional for $\omega = \omega_0$. Therefore, we see that the power spectrum has a coherent carrier at $\omega = \omega_0$ that is reduced by an amounts $\Delta\phi_{rms}^2$. The second part of the power spectrum is just proportional to the phase noise power spectral density centered at $\omega = \omega_0$.

The coherence properties of a laser are often parametrize by its linewidth (inverse of the coherence time). The linewidth is usually defined as the FWHM of the power spectrum. However, the meaning of FWHM is usually restricted to cases where the function form of the power spectrum is known (for example, Gaussian or Lorrentzian. See Ref. [158] for limiting cases). A more general definition of the laser linewidth is therefore desirable. One proposed metric [47, 160] is that the linewidth is the frequency from the carrier at which half of the power spectrum is located in the noise and half is in the carrier. We can make this more explicit by using the phase noise power spectral density

$$\int_{\delta\omega}^{\infty} \mathrm{d}\omega S_\phi(\omega) \approx 1\,\mathrm{rad}^2. \tag{5.16}$$

when $\delta\omega$ is chosen so the integral totals to 1 rad^2, approximately half of the optical power is in the noise and half in the carrier frequency. We can then define the FWMH as being FWHM$= 2\delta\omega$.

Returning to our earlier example of how the phase modulation depth scaled with harmonic order, if we start with the premise that $\phi_{q\omega_0} = q\phi_{\omega_0}$, that is that the phase of the q^{th} harmonic advances at $q\times$ the phase of the fundamental frequency, our analysis results in that the phase noise power spectral density of the harmonic tone $S_{q\omega_0,\phi}$ will grow quadratically with harmonic order. That is

$$S_{q\omega_0,\phi}(\omega) = q^2 S_{\omega_0,\phi}(\omega). \tag{5.17}$$

It therefore follows that the linewidth will also grow quadratically with harmonic order. Further, if $S_{\omega,\phi}(\omega)$ is not sufficiently small before the harmonic generation process, the coherent carrier will eventually disappear for large q. This is known as carrier collapse [160] and is discussed in detail in the context for RF oscillators in Ref. [161].

5.2 Noise scaling of high-order harmonic generation

As we have just discussed, in harmonic generation of oscillating signals, the phase noise power spectral density (and hence the linewidth) is expected to grow quadratically with harmonic order from the phase noise of the driving laser, *even if the harmonic generation process is noiseless* [161]. With the XUV interferometer described in Chapter 4, we use the resulting heterodyne beatnotes presented in Fig. 4.10 to test this assertion for the case of optical HHG. The relative linewidth between the two XUV sources (refer to Fig. 4.2 for the schematic of the apparatus) is presented in Fig. 5.1. The linewidth as a function of harmonic order is fit to a quadratic function and excellent agreement is obtained. For this data, the interferometer is not phase-stabilized and all the beatnotes are shifted from the MHz frequencies to audio frequencies and analyzed on a FFT machine so a high resolution signal could be obtained allowing numerical fitting for the linewidth.

For the data in Fig. 5.1, it is worth mentioning that we approximated the linewidth using a Lorentzian function. However, nearly identical scaling results were obtained if a Gaussian was used. In reality, neither function perfectly matches our observed power spectrum. This is not surprising since the relative noise in the interferometer can arise from a wide variety of sources. We refer to Ref. [158] for examples of when a Gaussian versus a Lorentzian power spectrum is expected. In general, the power spectrum will be a convolution of these or even more complicated [159, 160].

The phase noise scaling was also tested in an independent way utilizing coherent phase modulation instead of noise. By placing phase modulation sidebands on the driving laser, we observe how

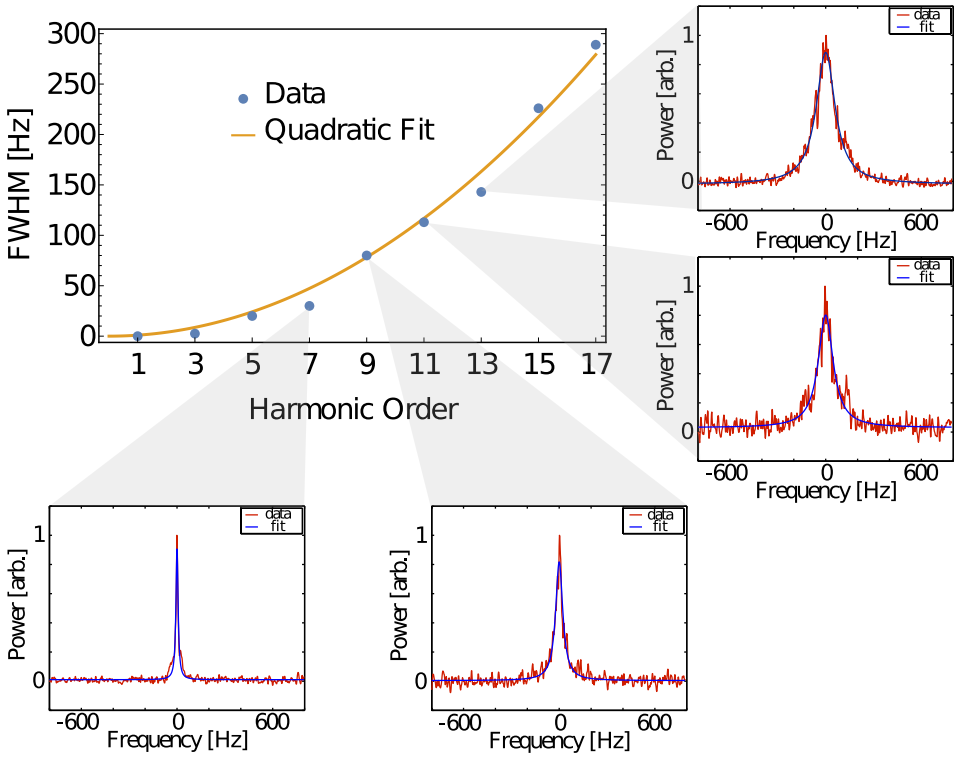

Figure 5.1: Beat linewidth versus harmonic order to show phase noise scaling. The data is the same as presented in Fig. 4.10. The interferometer was not actively stablized for this measurment. The linewidth was approximated with a Lorentzian function, but a similar results was obtained assuming a Gaussian. The shown fit is to a simple quadratic equation.

the power in the sidebands changes at various harmonic orders. By phase modulating one arm of the interferometer and using the heterodyne beat of the driving laser, the phase modulation depth is determined to be $\beta P_1 = 0.049$. At the 17^{th} harmonic, we expect this to be $\beta_{17} = 17 \times P_1$. The heterodyne beat at the 17^{th} harmonic with the modulation on and off is displayed in Fig. 5.2. A clear reduction in the carrier power is observed and large phase modulation sidebands are present. We use Eq. 5.3 to determine that the sideband should be at -6.8 dBc which is in good agreement with the measured -6.5 dBc. This sort of measurement was repeated at harmonics between 7–17 with good agreement.

The observations with the linewidth scaling and the modulation sidebands indicates that the HHG process is not adding any additional noise to the laser beyond what is expected by frequency multiplication. With this, we already have very strong predictive power on what sort of levels of coherence can be expected in the XUV. For example, if we start with a comb that has a 1 Hz absolute linewidth, we can expect to have a XUV comb with a linewidth of 441 Hz at the 21^{st} harmonic or a linewidth of 10.2 kHz at the 101^{st} harmonic.

With our interferometer not actively stabilized, it is equivalent to performing a relative phase noise characterization between two lasers that have a relative linewidth of about 1 Hz. The 1 Hz relative linewidth was not deliberate but just the natural manifestation of our apparatus. What remains to be tested is the following. Imagine our lasers had a relative linewidth of 1 mHz, what is the linewidth in the XUV? What about 1 μHz? At what level does the HHG process start to add phase noise beyond what pure frequency multiplication dictates? To answer these questions, we need the interferometer to be completely phase stable so that the relative linewidth between the two sources at the driving laser wavelength is non-existent (at least to the degree that we can make a good phase lock). Fortunately, we have the ability to do exactly that.

5.3 Testing the limits of coherence in the extreme ultraviolet

As previously described in Sect. 4.2.1, we use the heterodyne beat from the driving laser at 1 MHz to actively phase stabilize the relative path lengths of the two arms in the interferometer.

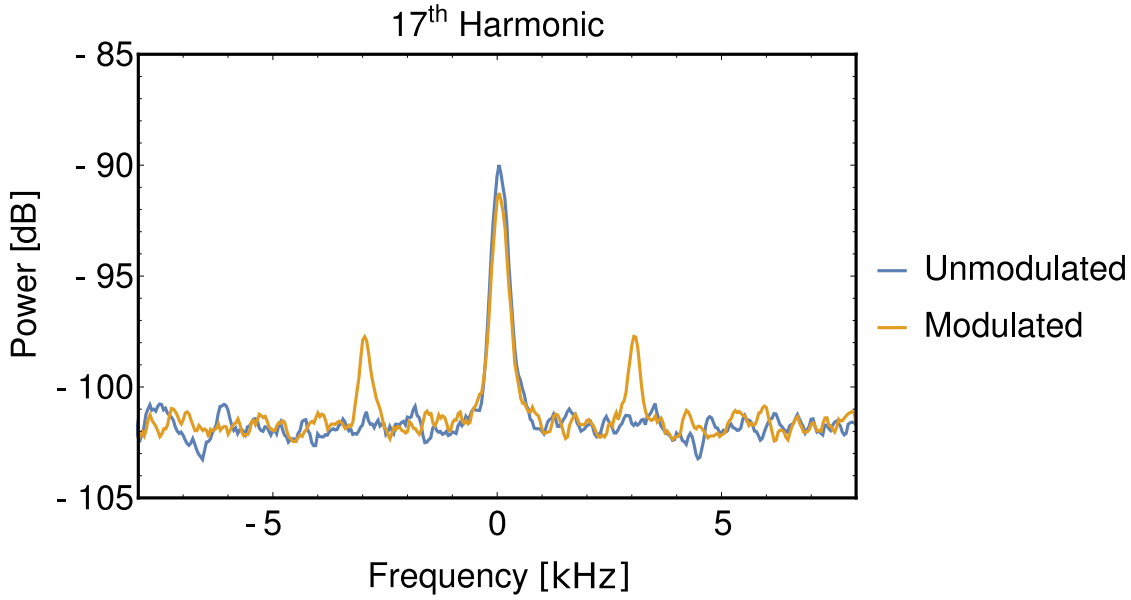

Figure 5.2: The 17^{th} harmonic with and without the presence of phase modulation on the driving laser. A clear reduction in the carrier is present. The size of the phase modulation sidebands at the 17^{th} harmonic is consistent with the measured sidebands of the driving laser. The modulation sidebands were places on the driving laser by the AOM used as a beam splitter for the interferometer. The data is shown on a 30 Hz resolution bandwidth.

The feedback loop parameters were chosen to have a deliberately low feedback bandwidth as to not interfere with any subsequent and deliberate laser modulation (amplitude or phase). Since the noise in the interferometer was already made small at low frequencies due to its passive stability, a high bandwidth feedback loop was not necessary to remove most of the noise. Fig. 5.3a,b show the heterodyne beat between the driving laser with the interferometer unstabilized and stabilized, respectively. Only a subtle change is observed due to the action of the phase lock, but it is clear that the fluctuations have been removed. Fig. 5.3c,d show the results of the heterodyne beats for the 17^{th} harmonic with the interferometer unstabilized and stabilized. The change is much more dramatic and note the difference in the x-axis of the plot. The beat in Fig. 5.3d appears to be a δ-function and its narrowness is limited by the observation time. This is often referred to as being limited by the resolution bandwidth. For this data, the resolution bandwidth was 1 Hz and this level of coherence was confirmed at all harmonics from the 3^{rd} to the 19^{th}. We can further increase the observation time of the heterodyne beat to 16 seconds. Fig. 5.3f shows a near resolution limited beat of 62.5 mHz. This linewidth implies a coherence time of 16 seconds. This also demonstrates that we were able to maintain perfect phase stability for over 10^9 optical pulses at our repetition rate of 154 MHz. At this level of investigation, we do not observe any deleterious effects to the phase coherence from the HHG process, a testament to its coherence maintaining properties despite its enormous nonlinearity. We also confirmed that our observation was not a coincidence of picking the same nonlinear medium for both cavities (in this case xenon). By injecting xenon into XUV1 and krypton into XUV2, we observed a 1 Hz resolution limited beat at the 15^{th} harmonic, again limited by the resolution bandwidth of this measurement.

Coherence at the 62.5 mHz level is great news for future prospects of performing high-resolution spectroscopy in the XUV. The best available lasers in the near IR have linewidths down to 30 mHz [80]. Assuming we discipline our driving laser to this, we can expect to start with a frequency comb with comparable linewidth. Due to the quadratic scaling of the phase noise, we expect to have a linewidth of 8.7 Hz at the 17^{th} harmonic. The data presented in Fig. 5.3 shows that the XUV frequency comb can indeed support this level of coherence. Current laser technology

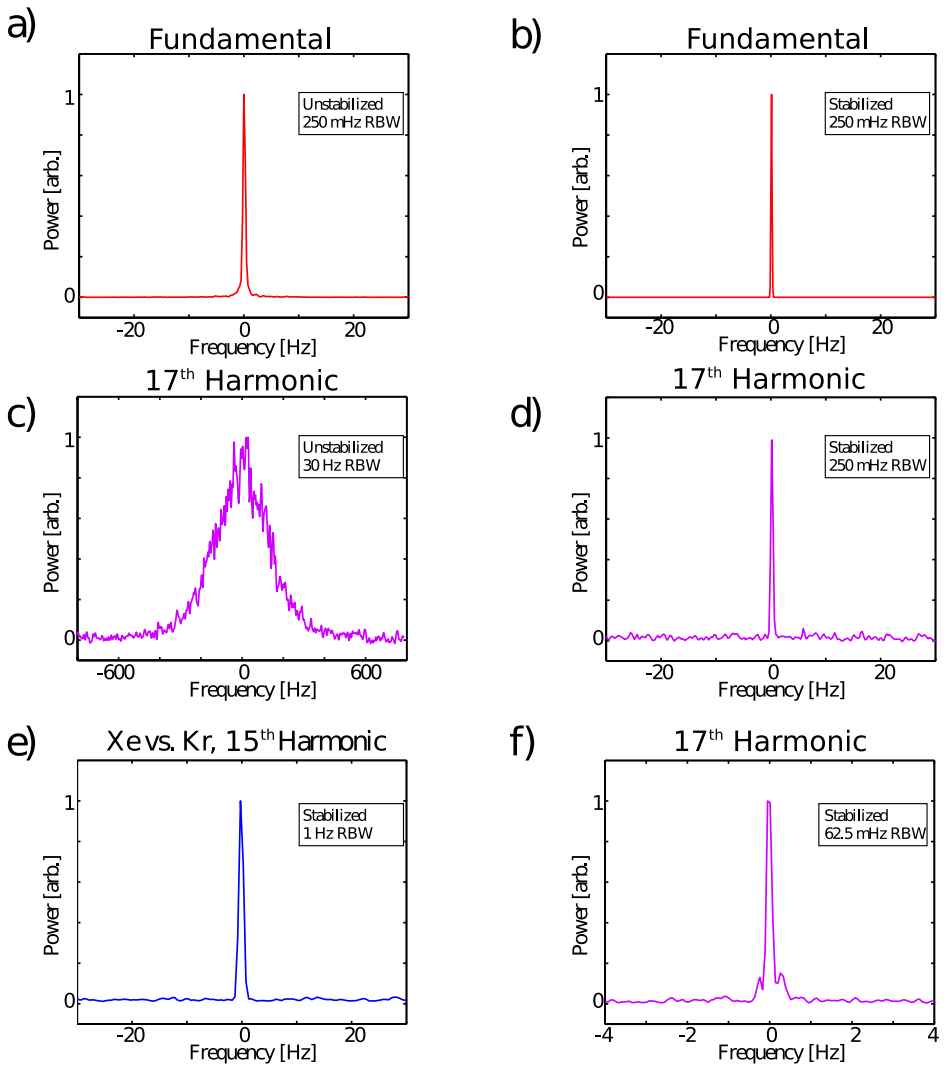

Figure 5.3: Ultra narrow heterodyne beats test XUV comb coherence at long time scales. **a)** and **b)** show the beatnote between the driving laser with the interferometer unstabilized and stabilized respectively. A subtle change to the IR heterodyne beat power spectrum is observed. **c)** and **d)** show the beatnote between the 17^{th} harmonic with the interferometer unstabilized and stabilized respectively. A dramatic difference is observed. Note the difference in the x-axis of the plots. We can further zoom in to d) and uncover an ultranarrow beat, resolution limited at 62.5 mHz in **f)**. To show that the observed heterodyne beats were possible if different gases were used, the 15^{th} harmonic beat between XUV1 making harmonics in xenon and XUV2 making harmonics in krypton is shown in **e)** with a 1 Hz resolution bandwidth limited heterodyne beat. At 1 Hz, the XUV frequency comb already exceeds the capabilities of current laser stabilization techniques in the visible and near-infrared. RBW, resolution bandwidth.

(in terms of linewidth) would need to improve by nearly two orders of magnitude to justify testing the XUV comb linewidth beyond the level presented here. Our result of no additional noise at the 62.5 mHz level is eight orders of magnitude better than previous demonstrations [52, 56, 87].

5.4 Measurement of intensity dependent dipole phase

Access to phase-stable light in the XUV opens up many exciting possibilities. For example, two-dimensional spectroscopy in the XUV, XUV holography, and of course, high-resolution spectroscopy. To demonstrate the power of having access to optical phase in the XUV, we decided to investigate one of the most salient features of HHG presented in Sect. 3.1.3. The quantum description of HHG predicts that the phase of the XUV light will be linked to the driving laser intensity. The relationship is parametrized as $\phi = -\alpha_j I/4\omega^3$, where α_j is the coupling constant and the index j refers to the index of the different possible quantum paths (typically, just the short and long trajectories). Ref. [87] established that below threshold harmonics contained both long and short trajectory contributions to the overall HHG yield. The investigation relied heavily on theory to extract values for α_j but was nevertheless successful. Most investigations of the intensity dependent dipole phase of above threshold harmonics rely on the interference of the long and short trajectories with each other, and rarely direct, independent investigation of an isolated trajectory was performed [87, 162]. Our heterodyne interferometry scheme has the ability to isolate the short trajectory by observing the heterodyne beats directly on axis where the contribution from the long trajectory is expected to be very negligible due to its much larger diffraction angle in the far field and its reduction due to macroscopic phasematching. With systematic variation of the laser intensity, phase shifts on the heterodyne beats can be linked directly to this sub-laser cycle (and hence attosecond timescale) physics of HHG.

To illustrate the principle of this measurement, Fig. 5.4 shows the heterodyne beats at the 15^{th} harmonic and at the fundamental at two different intracavity laser powers. The 15^{th}harmonic in Fig. 5.4a shows a clear phase shift (and slight reduction in beat power) as a laser intensity is changed while there is hardly a difference in fundamental shown in Fig. 5.4b. The phase shift in the

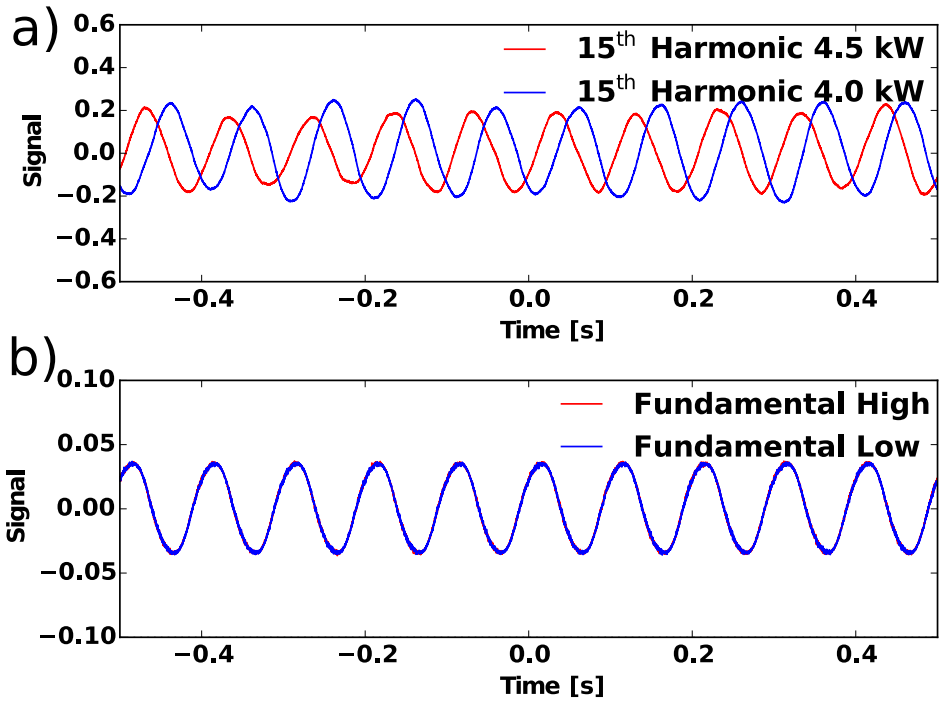

Figure 5.4: Heterodyne beats at 15^{th} harmonic and fundamental in the time domain for two differrent laser powers shown in **a)** and **b)** respectively. The phase shift in the XUV is clearly present while there is virtually no detectable phase shift at the fundamental beat (due to the phaselock).

15^{th} harmonic originates from the intensity dependent phase. However, one must be very careful in a measurement like this. For example, by changing the laser intensity, we may inadvertently change the driving laser phase. Since we have already established that small phase shifts at the fundamental scale with harmonic order in the XUV, small perturbations can be very important. Therefore, we will rely on modulation techniques and lock-in detection methods to make measurements of the intensity dependent phase. Simultaneous monitoring of the XUV beats and the fundamental beat will be necessary to correct the signal for any parasitic phase modulation on the fundamental. The schematic for the modulation/demodulation scheme is shown in Fig. 5.5. As describe earlier, an additional AOM is placed in the beam path to act as an amplitude modulator. The following section will describe the signal extraction and analysis scheme.

5.4.1 Theory of measurement

By trying to measure the intensity dependent phase that results from HHG, we are effectively measuring the AM-PM coupling with the AM (amplitude modulation) being on the driving laser and the PM (phase modulation) being on the XUV light. We can mathematically describe a beat signal as

$$S(t) = (1 + \mathrm{A}\,\mathrm{Sin}(\Omega\,t + \phi_m))\,\mathrm{Cos}(\omega\,t + \mathrm{P}\,\mathrm{Sin}(\Omega\,t + \phi_m)). \tag{5.18}$$

ω is the frequency of the beat and Ω is the frequency of the applied modulation and ϕ_m is its phase. A is the amplitude modulation depth and P is the phase modulation depth. The phase response is directly proportional to the amplitude response, when we assume that these two response are in phase with each other. Each beatnote is characterized by its own values for A and P. To avoid confusion, the subscripts will refer to the signal it represents. For example, $\mathrm{A_{IR}}$ is for the amplitude modulation of the driving (fundamental) laser and $\mathrm{P_q}$ is the phase modulation of the q^{th} harmonic. Our task is to determine the values for A and P at the fundamental and the harmonics. By taking the ratio of $\mathrm{P_q}$ to $\mathrm{A_{IR}}$ and using proper units, we can extract the intensity dependent phase coefficient

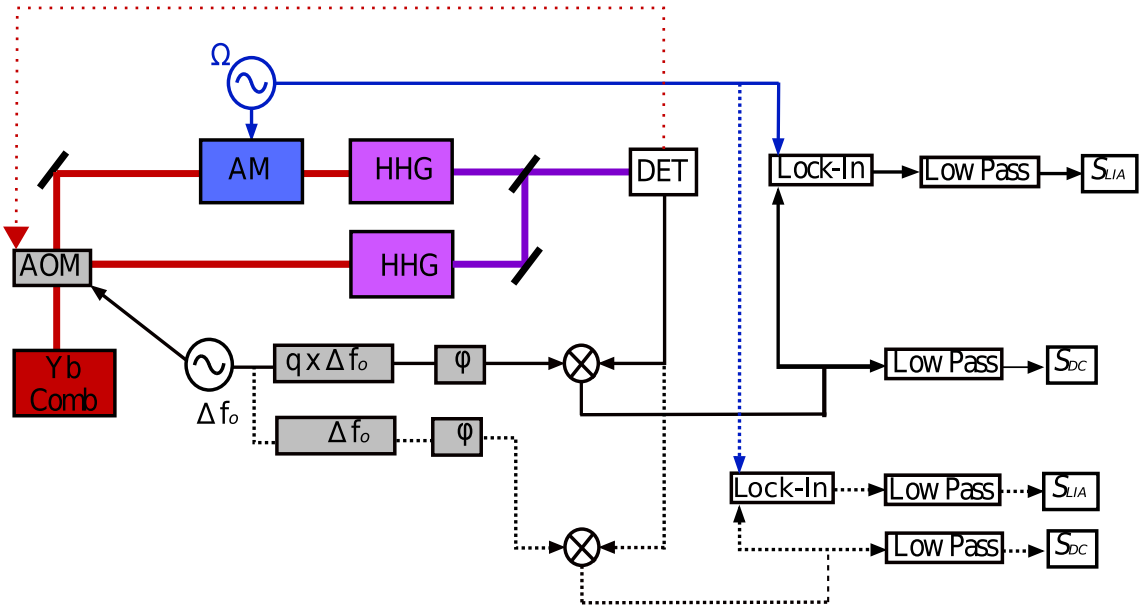

Figure 5.5: Detailed schematic of the measurement scheme for the intensity dependent dipole phase. AOM, acousto-optic modulation. AM, amplitude modulation. Ω, the modulation frequency. DET, photodetector. ϕ, a phase shifter in the RF signal chain. The dashed lines represent the signal chain for the fundamental detection and the solid lines represent the signal chain for harmonic detection. It is very important that the interferometer is phase stabilized during the data detection process lest the double demodulation scheme will not work. It is also important that all RF sources involved in the heterodyne beats and interferometer stabilization are mutually phase coherent.

α_j.

We need to extract the relevant parameters of Eq. 5.18 at both the harmonic of interest and the driving laser simultaneously. To do this, we use a two step demodulation process. By taking Eq. 5.18 and mixing it with a stable RF signal (LO1) at a frequency of ω and relative phase offset ϕ, we get

$$S(t) \otimes V_1 \mathrm{Cos}(\omega\, t\, +\, \phi) = S_1(t) \tag{5.19}$$

$$S_1(t) \approx V_1(\mathrm{Cos}(\phi) - \frac{\mathrm{AP}}{2}\,\mathrm{Sin}(\phi) + \mathrm{A}\,\mathrm{Cos}(\phi)\mathrm{Sin}(\Omega\, t + \phi_m) - \mathrm{P}\,\mathrm{Sin}(\phi)\,\mathrm{Sin}(\Omega\, t + \phi_m)). \tag{5.20}$$

Where we have ignored terms at 2ω. We can further low pass the signals at Ω and obtain a "DC" signal

$$S_1(t) \overset{\text{Low Pass}}{\rightarrow} S_{DC} = V_1(\mathrm{Cos}(\phi) - \frac{\mathrm{AP}}{2}\,\mathrm{Sin}(\phi)). \tag{5.21}$$

Eq. 5.21 will be one of our primary signals. Note that the phase is set by the phase of LO1. This also assumes that the phase of the XUV beat is stable. This is true if we phase stabilize our interferometer which we do for this measurement.

The signal S_1(t) contains terms that oscillate at the applied modulation frequency Ω. We can demodulate our signal once more at the correct phase ϕ_m and ignore terms at 2Ω to obtain

$$S_1(t) \otimes V_2 \mathrm{Sin}(\Omega t + \phi_m) = S_{LIA} \approx V_1 V_2 \mathrm{A}\,(\mathrm{Cos}(\phi)\, -\, \frac{\mathrm{P}}{\mathrm{A}}\,\mathrm{Sin}(\phi)) \tag{5.22}$$

S_{LIA} is our second signal. With Eq. 5.21, Eq. 5.22 and some independently measured parameters, we can extract our parameters of interest.

By applying AM to the pump laser on one arm of the interferometer, we can control $\mathrm{A_{IR}}$ very well. It is also easily measured with a photodetector. By varying the phase of LO1, we can measure S_{DC} and S_{LIA} (Eq. 5.21 and Eq. 5.22) simultaneously. With the modulation (A,P) turned off, S_{DC}

tells us the phase of the beat. With the modulation on, the relative phase between S_{DC} and S_{LIA} can tell us the ratio of A/P. Since A can be measured independently, we can extract the amount of phase modulation, P. This procedure needs to be done with the IR signal and the XUV signal simultaneously recorded to prevent any systematic errors. Due to the nonlinear nature of HHG, simply measuring $\mathrm{A_{IR}}$ and $\mathrm{P_{IR}}$ does not give us enough information about the XUV light. This is because $\mathrm{A_{IR}} \neq \mathrm{A_q}$. However, as we discovered in our linewidth studies $\mathrm{P_q} = \mathrm{q} \times \mathrm{P_{IR}}$. This will be an important point for calibrating our signal.

To measure the AM-AM coupling, we can use our beat signals. Our XUV beatnotes are directly proportional to the amount of XUV power in each beam. The amount of beat power can also be easily measured on an RF spectrum analyzer. By changing the amount of power in one of the fsECs and observing how the beat power changes, we can determine how much the XUV power must have changed for a given laser intensity change. Since A_q is no longer a fit parameter, we can use the measurements of S_{DC} and S_{LIA} with the XUV signal to extract $\mathrm{P_q}$. Once we have both $\mathrm{P_q}$ and $\mathrm{A_{IR}}$, we need to correct the measurement of $\mathrm{P_q}$ to account for any small amount of $\mathrm{P_{IR}}$ that may have been in the system. We do this by simply $\mathrm{P_q} \rightarrow \mathrm{P_q} - q \times \mathrm{P_{IR}}$. This is to remove any residual phase modulation that does not originate from the dipole response in HHG. From here, we can take the ratio of $\mathrm{P_q}/\mathrm{A_{IR}}$ and scale by appropriate units to determine α_j.

5.4.2 Measurement systematics

In order to determine α_j, we need to determine $\mathrm{A_{IR}}$, $\mathrm{P_{IR}}$, ϕ_{IR}, $\mathrm{A_q}$, $\mathrm{P_q}$, and ϕ_{q}. It is easy to directly control and measure $\mathrm{A_{IR}}$, but due to various imperfections in the system, attempts to put pure amplitude modulation on the IR light results in small amounts of $\mathrm{P_{IR}}$. However, by measurements of S_{DC} and S_{LIA} with the IR signal, we can extract the amount of $\mathrm{P_{IR}}$ and use it to correct our system. This is important to do because $\mathrm{P_q} = q \times \mathrm{P_{IR}}$ and this $\mathrm{P_q}$ does not originate from the atomic dipole phase of interest. This is just a manifestation of how the phase of the XUV light is tied to the phase of the IR light via the harmonic process. Modulating the intensity has notable effects on the neutral/plasma density ratio inside the fsEC. However, the modulation is slow

(at 2 kHz) and the PDH lock can easily follow it to maintain resonance. Due to the neutral/plasma density changes, there is a small amount of PM induced by AM on the driving laser. This was verified by measuring the effect of AM with gas present and absent. This can easily corrupt the intensity-dependent phase measurement and necessitates the correction described previously. Furthermore, any cavity oscillation due to bistability [114] can render the signals too noisy. Further, to avoid the aforementioned bistability, we deliberately lock the laser off the peak of the cavity resonance by adding a small DC offset to the PDH error signal. This is problematic because as the amplitude of the driving laser is modulated, so will the size of the PDH error signal be modulated. The effective detuning from the laser to the cavity resonance is set by the ratio of the DC offset value to the peak-peak value of the PDH signal. This is now dynamically modulated by our imposed AM and thus the cavity/feedback loop is now converting this to PM by modulating the cavity-laser relative detuning. This was systematically measured on both the fundamental and harmonic light to ensure proper correction and no nonlinearity. A final systematic check was performed with "dummy signals" originating from RF synthesizers. The dummy signals were injected into the electronics at the location of the photodetectors. The signals were then analyzed by the electronics to ensure no artificial AM-PM couplings due to nonlinearities in either the lock-ins or the RF mixers. Similarly, AM-PM conversion of the photodetectors was also verified to be of negligible sizes by studying their response to controlled light amplitude variations.

5.4.3 Results and data analysis

The results of the intensity dependent phase measurement for harmonics 3–17 are shown in Fig. 5.6. This is the main result of our attempt to measure the intensity dependent dipole phase. The laser peak intensity was 0.34×10^{14} W cm^{-2} with an intensity modulation of 15%. Each data point is determined by fitting ~ 10 runs of beat measurement. By combing multiple runs of data, we can construct a weighted average and determine a final value for α_j at a given harmonic. The case of the 15^{th} harmonic is shown in Fig. 5.7. The error bars seem to be larger than the actual scatter of the data. This just means there is some "over-scatter" indicating we did not make a large

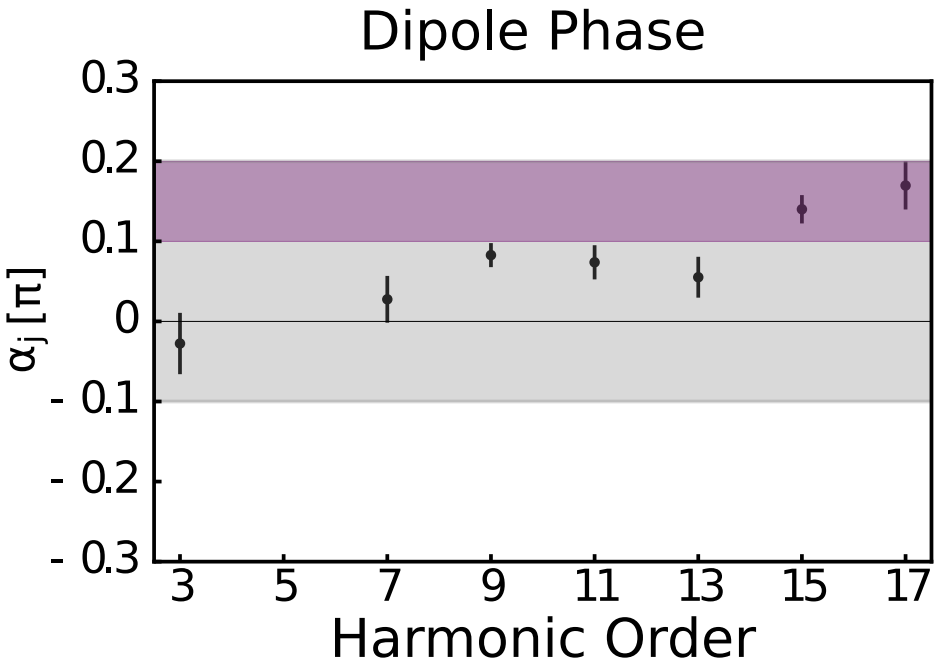

Figure 5.6: Data summary of the intensity dependent dipole phase as a function of harmonic order. The purple regions is where the SFA predicts the values to lie for above-threshold harmonics. The gray regions is where the near-threshold harmonics are expected to lie. The sign depends on contributions from uphill or downhill over-the-barrier ionization trajectories.

enough statistical average for each run, but clearly the systematics were small. Normalizing the final error bar by the χ^2_{red} will account for this. An example of an individual run of data for the IR and the 15^{th} harmonic data is shown in Fig. 5.8. The data is displayed as signal voltages as a function of ϕ (the phase of the LO1). From these two traces and the measured value of A_{IR}, we can measure any unintended P_{IR}. Each run yields a value of α_j with an error bar determined by the statistical noise in the data. All the data is then fit to a standard mean, weighted by the standard uncertainty of the individual fits to α_j, and an error bar is given by the standard error of the pooled data normalized to the χ^2_{red} of the fit to a constant.

5.4.4 Conclusion

Our data, summarized in Fig. 5.6, shows the intensity dependent dipole phase as a function of harmonic order from below-threshold to above-threshold. Our method of measurement is unique because it directly determines the contribution of the short trajectory by sampling of optical phase and does not rely on spatial interference between multiple pathways. It is complementary to RABBITT and related methods based on photoelectron spectroscopy [72, 163], which seek to determine the time delay (or equivalently phase shift) between adjacent harmonic orders at a given intensity.

Our data also has the ability to help distinguish important aspects of near-threshold harmonic generation. For example, in the theory work of Ref. [121], the treatment of the atomic potential and ionization dynamics is very important for determining the intensity dependent phase of the near-threshold harmonics. By using the semi-classical model (SCM) or using over-the-barrier corrections (OTB), the sign of the intensity dependent phase parameter α_j can change and the trajectory contributions are modified. Our data is more consistent with theory when the OTB corrections are included. This confirms the claim that short trajectories of the below-threshold case do not originate from tunnel ionization, unlike short trajectories of the above-threshold harmonics which do originate from tunnel ionization. We previously presented Fig. 3.4 that shows the difference between the SCM and OTB case.

Our phase measurement technique is able to resolve phase shifts with uncertainties at the 10^{-2}

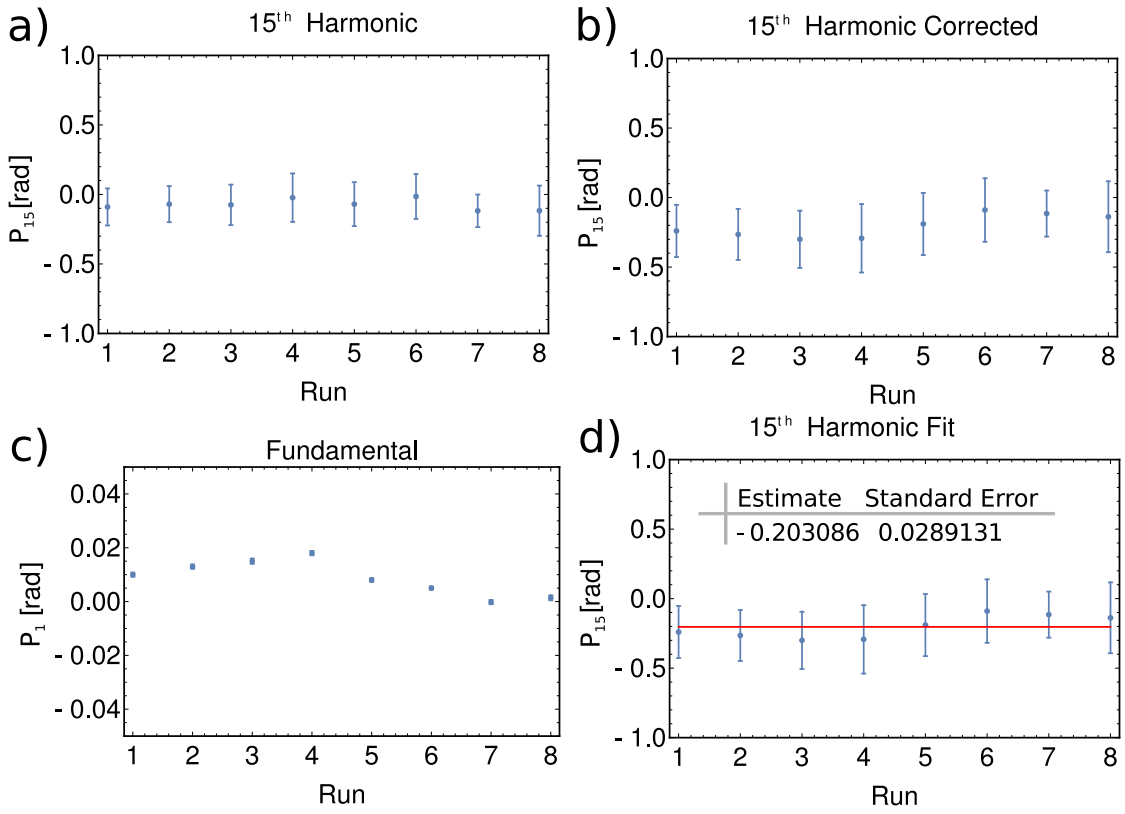

Figure 5.7: A dataset for the intensity dependent dipole phase measurement at the 15^{th} harmonic. **a)** The raw phase modulation depth of the 15^{th} harmonics. **b)** The scaled phase modulation depth. The scaling factor is determined from the amount of phase modulation present on the fundamental light which is shown in **c)**. **d)** The total dataset for the 15^{th} harmonic with a fit shown in red. The mean values and the χ^2_{red} normalized standard error is reported in the inset.

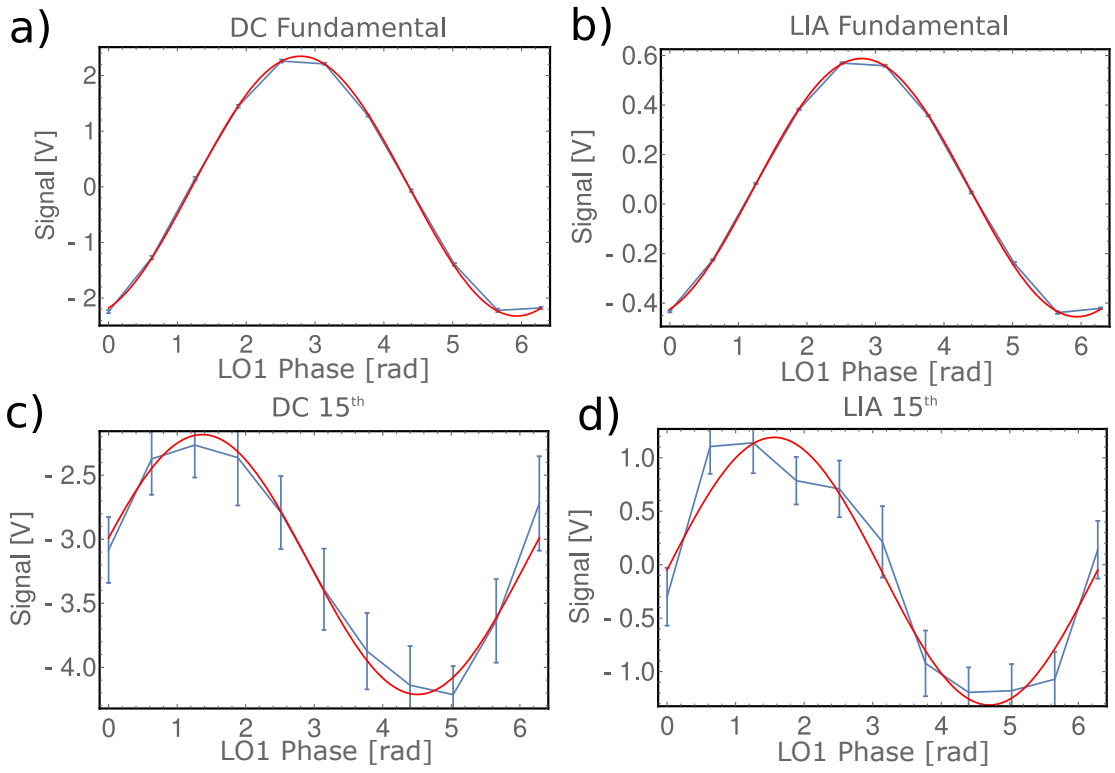

Figure 5.8: An example of a single data run measuring the intensity dependent dipole phase at the 15^{th} harmonic. The phase of LO1 is scanned as the voltages from the DC detector and the LIA are measured. **a,b)** contains the DC signal for the fundamental and the 15^{th} harmonic respectively. **c,d)** contains the LIA signal for the fundamental and the 15^{th} harmonic respectively.

rad level, which corresponds to a time uncertainty of 6 as. In contrast to typical experiments that utilize direct attosecond timing resolution, we measure the attosecond electron dynamics imprinted on the phase of the emitted XUV light originating from HHG. With system improvements, it is feasible to extend this into the $\leq$1 as regime, rivaling the highest achievable temporal resolution of attosecond electron dynamics provided that a direct link between XUV phase and time can be established.

To conclude this detour into attosecond physics, our apparatus provides a unique ability to directly sample optical phase in the XUV. We performed a proof of principle experiment where we measure the intensity dependent dipole phase from below-threshold to above-threshold. Our technique can be further extended to probe attosecond physics in other atomic samples or aligned molecules.

Chapter 6

Strong-field physics with molecules

The motivation for studying strong-field physics of molecules is based on the success of Chapter 5 where we were able to extract the intensity dependent dipole phase, a signature of the strong-field light-matter interaction responsible for HHG. The hope is that we can do similar work with molecules and investigate HHG physics as a function of molecular alignment and laser intensity, for example. The work of Ref. [164] essentially started the field of high-harmonic spectroscopy for molecular orbitals. The current status of the HHG spectroscopy/attosecond science is well summarized by a series of review articles [165–168]. An interesting perspective of high harmonic spectroscopy from someone at the frontline of the high harmonic spectroscopy battleground is in Ref. [169]. We seek to offer a clean, highly sensitive measurement of HHG phenomena and without the need to invoke too complicated theories.

6.1 Impulsive stimulated Raman scattering

Raman scattering and stimulated Raman scattering (SRS) [170] are ubiquitous processes in optical science. Some notable examples include manipulation of ultracold molecules [171], nonlinear spectroscopy [172] and microscopy [173], and ultrafast molecular phase modulators [174]. Of particular interest for ultrafast science is the use of SRS as an ultrafast phase modulator capable of generating multi-octave spanning optical spectra [174, 175]. The resulting spectrum is capable of supporting sub-fs optical pulses [176] or generating complex optical waveforms [177]. In these experiments, intense, short laser pulses are ideally suited to investigate SRS and use SRS as a tool

to manipulate optical fields. SRS generates a coherent vibration or rotation in a molecular system (typically H_2 or isotopologues). The molecular vibration or rotation modulates the index of refraction in the gas, producing sidebands at the corresponding frequencies.

In some SRS experiments, two separate pulses of ∼ns−ps durations at two different frequencies are used to stimulate the Raman responses from the molecules. These long pulses operate in the adiabatic regime where the modulation process persists during the entire laser pulses. However, with a broad spectrum being generated from the modulation process, trains of ultrashort (possibly sub-fs) pulses may emerge within the long parent pulses [174]. It is also possible to perform SRS with pulses of ∼fs durations. In this regime, known as impulsive stimulated Raman scattering (ISRS), a single pulse has a sufficiently wide spectral bandwidth to provide Raman coherence. Unlike the case with longer pulses, the coherent vibration or rotation can persist long after the pulse has passed through the molecular sample [178]. On a rotational excitation, this is field-free molecular alignment (FFMA) in the ISRS limit [179, 180].

Impulsive, field-free molecular alignment has greatly aided the study of molecular systems because it is a simple and robust way to create an aligned molecular sample in the absence of any electromagnetic fields [179, 181]. The impulsive molecular phase modulation has also been demonstrated to produce ultrashort laser pulses [182]. More importantly, this technique has led to major advancements in strong-field physics with high-order harmonic generation (HHG) experiments performed in molecules [163, 164, 183, 184]. In the impulsive regime, the pulse duration is much shorter than the characteristic vibrational or rotational period of the system. Therefore, assumptions made in describing adiabatic SRS are no longer valid. The impulsive nature has important effects on the driving laser [178, 185, 186]. The laser pulse experiences a self-phase modulation-like process, which leads to a red-shifting of the original optical spectrum. This features is distinct from SRS in the adiabatic regime [178, 185, 186]. Impulsive FFMA also has important consequences for strong-field physics [163, 164, 179, 183] since the HHG-producing laser pulse will experience spectral and phase shifts related to ISRS during the HHG process. Indeed, we can now provide a clean measurement of this effect with our fsEC approach.

6.2 Field-free molecular alignment

Field-free molecular alignment is an elegant way to use ultrashort laser pulses to coherently excite molecules such that at later times after the initial excitation the molecular axis will become periodically aligned with respect to the laser polarization. This method is not restricted to linear molecules, but for this work we will focus on those solely. Here, we briefly outline the basic formalism of FFMA for linear molecules as it pertains to our experiments. A more detailed treatment can be found in Ref. [179, 180]. During the laser pulse interaction with the molecules, the effective Hamiltonian is,

$$H_{eff}(t) = \frac{B}{\hbar^2}\mathbf{J}^2 - \frac{1}{4}\Delta\alpha E^2(t)\cos^2\theta. \tag{6.1}$$

Here, B is the rotational constant, $\mathbf{J}$ is the angular momentum operator, $E(t)$ is the electric field, and θ is the angle between the primary molecular axis and the laser polarization. The anisotropic polarizability $\Delta\alpha$ is defined as $\Delta\alpha = \alpha_{||} - \alpha_{\perp}$, where $\alpha_{||} - \alpha_{\perp}$ are the polarizabilities of the molecule parallel and perpendicular to the molecular axis, respectively. The time-dependent Schrödinger equation can be solved by expanding the wave function in the rigid rotor basis, and the degree of alignment can be quantified by the expectation value of $\langle\cos^2\theta\rangle = \langle\psi(t)|\cos^2\theta|\psi(t)\rangle$. To compare with experiments, gas samples usually begin in thermal equilibrium, so the expectation value of $\langle\cos^2\theta\rangle$ needs to be thermally averaged, denoted as $\langle\langle\cos^2\theta\rangle\rangle$ (this will be described shortly). In the rigid rotor basis, the $\cos^2\theta$ operator can connect only $J \rightarrow J' = J, J \pm 2$ in a two-photon, Raman-like process. The molecules receive an impulsive kick from the field, and many rotational states are coupled owing to the large bandwidth associated with the short pulse. After the pulse has passed through the gas target, the molecular wave function then evolves freely as

$$\psi(t) = \sum_{J,M} a'_{J,M} e^{-i\frac{B}{\hbar}J(J+1)t}|J, M\rangle, \tag{6.2}$$

where $a'_{J,M}$ is the amplitude of the $|J, M\rangle$ state right after the interaction with the pulse has ended. Eq. 6.2 shows that the laser pulse has created a coherent superposition of rotational states that evolve coherently after the pulse. It is evident that at time $t = 2\pi\hbar/B$ and its integer multiples, the wave function will repeat itself. At these wave-packet revival times, the $\langle\langle\cos^2\theta\rangle\rangle$ expectation value will be maximized. The thermal average to obtain $\langle\langle\cos^2\theta\rangle\rangle$ is performed in the usual way by

$$\langle\langle\cos^2\theta\rangle\rangle = \mathcal{Z}^{-1}\sum_J \exp\left[\frac{-BJ(J+1)}{k_BT}\right]\sum_{M=-J}^{M=J}\langle\cos^2\theta\rangle_{J,M}, \tag{6.3}$$

where $\mathcal{Z}$ is the rotational partition function, k_B is the Boltzmann constant, and T is the rotational temperature. The rotational partition function is given by

$$\mathcal{Z} = \sum_J w_J(2J+1)\exp\left[\frac{-BJ(J+1)}{k_BT}\right], \tag{6.4}$$

where w_J is the weight of the J^{th} energy level determined by nuclear statistics. Despite the thermal nature of the gas jet we are attempting to align, the coherences are still present as manifested by the dynamic evolution of $\langle\langle\cos^2\theta\rangle\rangle$. There may be times of strong alignment at fractions of $t = 2\pi\hbar/B$ that depend on the molecule under investigation [179, 180].

To illustrate the alignment phenomena, a numerical implementation is shown in Fig. 6.1. For Fig 6.1a,b a 5 TW cm^{-2} laser pulse of 130 fs duration and a rotational temperature of 70 K was assumed for N_2 and N_2O respectively. The field-free evolution is shown after the laser pulse at $t = 0$. A list of common molecular parameters is shown in Table 6.2 for reference. It is clear that the N_2 and N_2O have quite different behaviors. The obvious features are the different timescales for the dynamics which is due to the difference in rotational constants. Further, the degree of alignment is stronger in N_2O because of the larger anisotropic polarizability. A more subtle differences is that N_2O only has full and half revivals while N_2 has full, half, *and* quarter revivals. This difference is due totally to nuclear statistics.

Impulsive FFMA can also have important consequences for precision studies of strong-field physics [163, 164, 179, 181, 183, 184, 187] in aligned molecules since the HHG-driving laser pulse

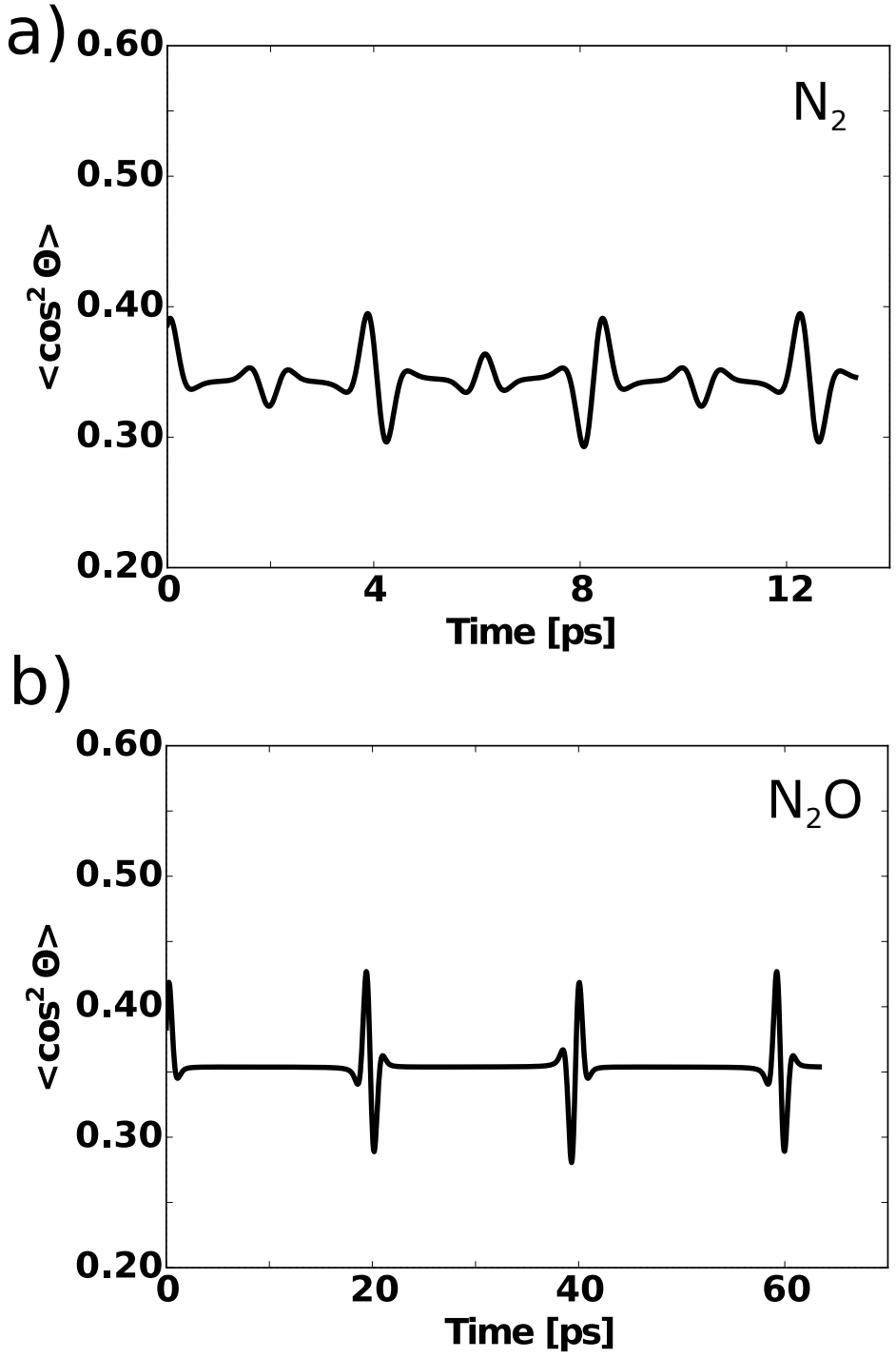

Figure 6.1: Rotational revivals shown for N_2 and N_2O in **a)** and **b)** respectively at 70 K interacting with a 5 TW cm^{-2}, 130 fs pulse. The expectation value $\langle\langle\cos^2\theta\rangle\rangle$ is plotted as a function of field-free evolution time.

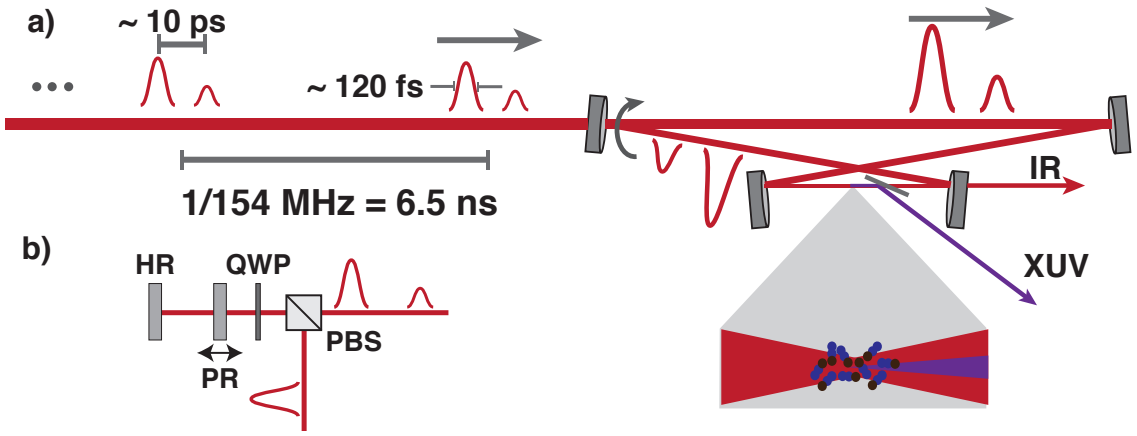

Figure 6.2: **a)** Schematic of the experiment. A high repetition-rate train of dual pulses, one for alignment and the second for HHG, are coherently coupled into a high-finesse, femtosecond enhancement cavity. At the focus of the cavity, the molecules are aligned by the first pulse and high-order harmonic generation is performed by the second pulse. The XUV light can be extracted from the cavity using a sapphire plate placed at Brewster's angle for the driving laser. **b)** The dual pulse feature of femotsecond pulse train is produced from a Gires-Tournois interferometer, with a tunable delay between the two pulses. HR, high reflector. PR, partial reflector. QWP, quarter waveplate. PBS, polarizing beamsplitter.

Molecule	$B(cm^{-1})$	$T_{rot}(ps)$	$\Delta\alpha(\text{Å}^3)$	I_p (eV)	w_J (even J)	w_J (odd J)
N_2	1.9896	8.383	0.93	15.58	2	1
O_2	1.4297	11.67	1.099	12.07	0	1
N_2O	0.4190	39.8	2.8	12.89	1	1
CO_2	0.3902	42.74	2.11	13.78	1	0

Table 6.1: A table containing the rotational constants, rotational periods, anisotropic polarizabilities of common molecules used in field-free molecular alignment.

will experience spectral and phase shifts related to ISRS during the HHG process. Despite FFMA being a well understood phenomenon [179, 181], the effects on the driving laser originating from ISRS are often ignored in HHG and FFMA experiments due to their small effects when thin, freely expanding gas targets are used at low densities. However, in the cavity-enhanced approach described here, we are more sensitive to the effects of ISRS on the driving laser due to the cavity effectively increasing the interaction length of our sample by a factor proportional to the cavity finesse. Indeed, we can now provide a clean measurement of the effects of ISRS with our fsEC approach while maintaining otherwise similar experimental conditions to conventional molecular HHG experiments. Our measurements indicate that modulations (amplitude and phase) of the driving laser cannot be ignored in future experiments utilizing fsECs and must be characterized to properly describe the XUV frequency comb spectral amplitude and phase.

6.3 Field-free molecular alignment experiments

The apparatus is schematically shown in Fig. 6.2. The intracavity pulse duration is verified with second-harmonic intensity autocorrelation. The intracavity spectrum is measured with an optical spectrum analyzer using the light transmitted through a cavity high-reflecting mirror. Performing HHG with aligned molecules requires two successive pulses, the first to rotationally excite the molecules and the second to drive HHG (henceforth, pump and probe respectively). To accomplish this goal, we use a mirror combination similar to a Gires-Tournois interferometer (GTI) to convert the original laser pulse train into two with a tunable timing delay, schematically shown in Fig. 6.2 b). The combination of a partial reflector (R $\approx$ 0.1) and a high reflector (R $\approx$ 1) along with

a quarter ($\lambda/4$) waveplate and a polarizing beamsplitter cube generates the dual-pulse train. This combination of optics also generates weaker pulses after the probe pulse, but these do not affect the rotational dynamics generated by the pump and observed by the much larger probe. Additionally, the GTI combination of optics is more efficient in generating the pulse train than a more traditional Michelson-type interferometer that relies on polarization optics. By tuning the value of the partial reflector, the relative heights of the pump and probe can be adjusted. By simply changing the distance between the partial and high reflector, the timing delay between the pulses can be tuned. The pulse train after the GTI combination was analyzed with second-harmonic intensity autocorrelation to ensure the pulse separation and ultrashort pulse durations were maintained. For our experiment, the intensity ratio of alignment pulse (pump) to HHG-driving pulse (probe) is 1:8; however, this value can easily be varied from 1:3 to 1:30 limited only by the available PR mirrors. The pulse train is coherently coupled into the fsEC, and at the cavity focus we inject N_2O gas through a quartz nozzle with a $\sim$ 120 μm diameter with up to $\sim$ 3 atmospheres (atm) of constant backing pressure. XUV light produced with HHG is outcoupled from the cavity using a 250 μm thick sapphire plate placed at Brewster's angle for the fundamental driving laser.

6.3.1 Single-pulse case

We begin with investigating the effects of a single pulse propagating and interacting with an N_2O gas jet inside the fsEC. N_2O was chosen because of the relatively large anisotropic polarizability to facilitate alignment, the small rotational constant to create a large delay between revivals, and the low ionization potential to facilitate observation of above-threshold harmonics. We estimate the rotational temperature of the N_2O gas to be 30-60 K [133]. The pulse has a peak intensity of 0.7×10^{14} W cm^{-2} in the absence of molecules. We monitor both the intracavity spectrum and power as a function of the applied pressure to the gas nozzle. As shown in Fig. 6.3, we observe a clear red shift of the spectrum, accompanied with a systematic decrease of the power. The power decrease results from spectral red-shifting decreasing the enhancement of the cavity and not from light scattering out of the cavity. The red shift by ISRS is contrary to what is usually observed

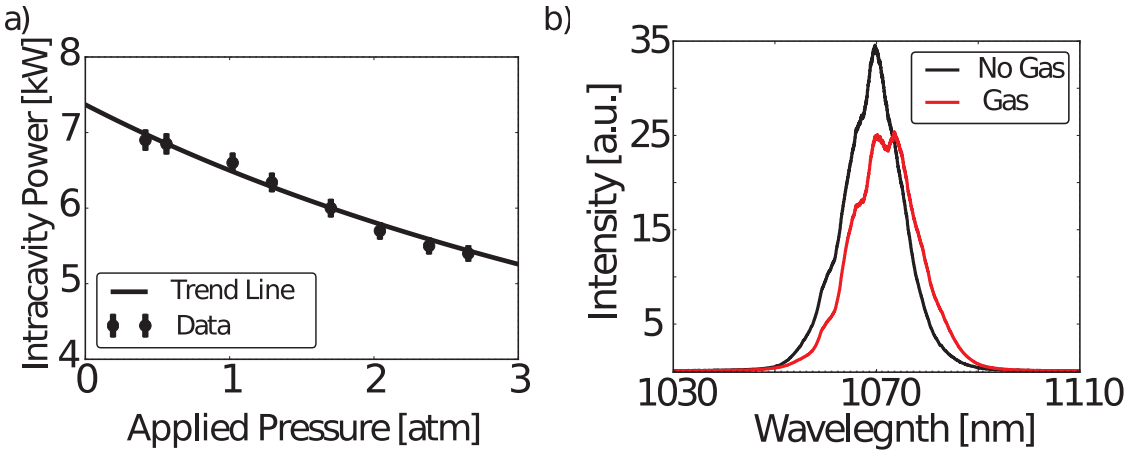

Figure 6.3: **a)** Pressure dependence of the buildup power when a single pulse is interacting with molecules inside the cavity. As the N_2O pressure is increased, a decrease in the intracavity power is observed due to loss of power enhancement in the cavity. A trend line is shown with the data. The loss is due to the spectral red-shift from ISRS. **b)** The intracavity spectrum exhibits a clear shift to the red when gas is present, a signature of impulsive stimulated Raman scattering. The red shift is dominant even in the presence of strong ionization, which would shift the spectrum to the blue. The red shifted spectra corresponds to the data in a) at 1.7 atm of applied pressure. An interesting application of the spectral red-shift could be to counteract the spectral blue-shift of ionization to aid in maintaining high buildup during HHG in atomic systems.

– spectral blue shift – when a femtosecond pulse propagates through field-ionizing media [114]. This demonstrates that ISRS has a more dominant effect on the pulse when interacting with N_2O at these intensities and densities. The red shift is a manifestation of energy transfer from the field to the molecular rotations.

6.3.2 Multi-pulse case

We proceed to inject two pulse trains into the fsEC. The first pulse (pump) excites a rotational wave-packet. The second pulse (probe) is of greater intensity and generates high-order harmonics. We observe two important features as a function of delay between the two pulses. First, the HHG yield of the probe pulse is modulated at the revivals of N_2O (more on this in Sect. 6.4). Second, thanks to the cavity-based measurement and the multi-pass effect, we observe clear effects of the pump pulse on the probe pulse that occur at the rotational revivals of N_2O. We observe these effects by monitoring the intracavity spectrum and power relying on the fact that the intracavity spectrum is dominated by the much more intense probe pulse and that the delay-dependent effects can only affect the probe. The effects on the probe pulse persist even if the probe intensity is too weak for appreciable HHG ($< 0.2 \times 10^{14}$ W cm^{-2}) further showing that the observed modulations are not purely an ionization related phenomena.

The effects on intracavity power are presented in Fig. 6.4. At ∼20 ps and ∼40 ps of delay between the pump and probe, the half- and full-revival of N_2O alignment, respectively, modulate the intracavity power of the probe, as shown in Fig. 6.4a,b. The intensity uncertainty is $\sim 1\%$. This power modulation is related to spectral shifts of the intracavity spectrum, shown in Fig. 6.5a,b as a function of pump-probe delay for the half- and full-revival respectively. The dominant contribution to the modulations in the power arises from the reduced overlap between the intracavity comb and the incident probe. The center of the intracavity spectrum shifts as the delay is scanned, along with the corresponding intracavity power, as shown in Fig. 6.5a,b. The conditions for the half-revival and full-revival data were the same as Fig. 6.4a,b at 2 atm of nozzle backing pressure. The increase in intracavity power occurs with a slight blue-shift in the spectrum and the decrease with a slight

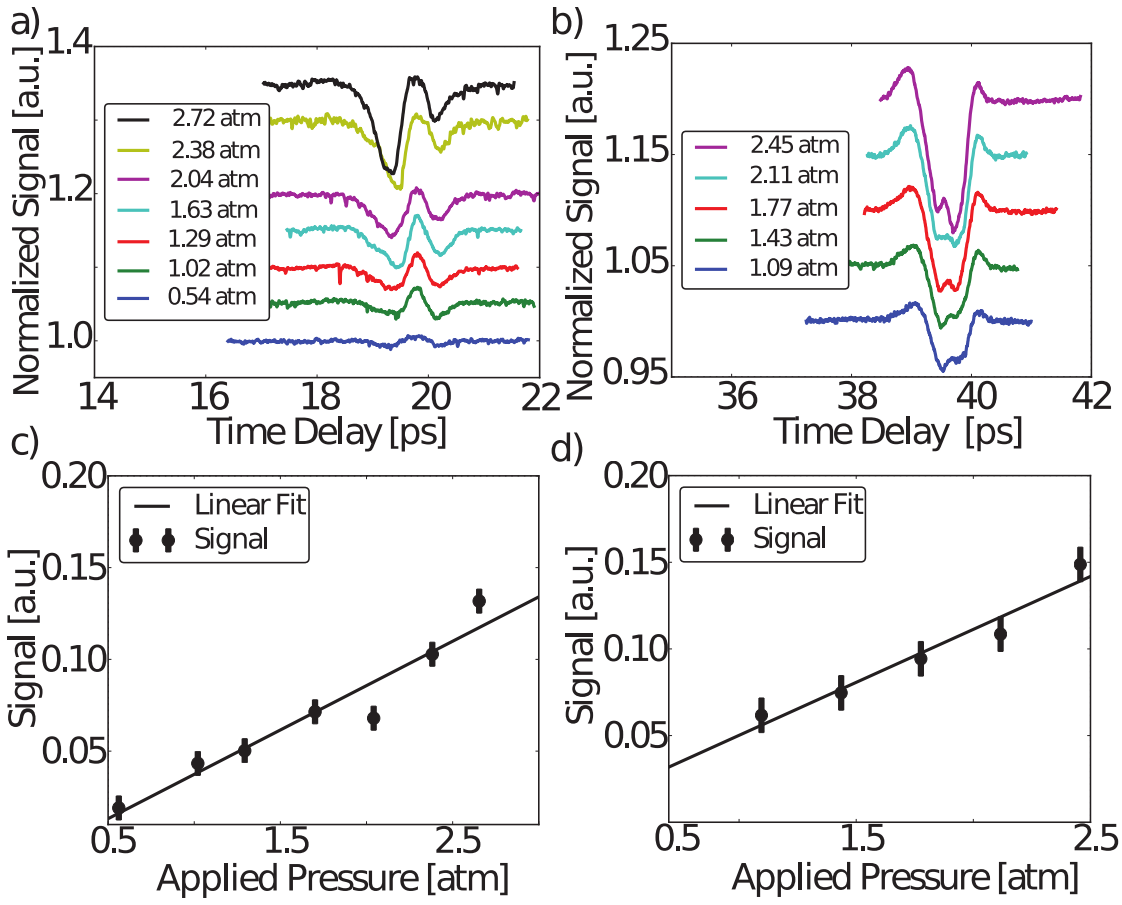

Figure 6.4: **a,b)** The effects of the half-revival (a) and full-revival (b) on the probe pulse as a function of pressure on the intracavity power. The signal is normalized to the baseline ($\sim$ 16 ps and $\sim$ 36 ps, respectively) and offset vertically for clarity. The pressure reflects what is applied to the 120 μm diameter quartz nozzle. **c,d)** The size of the half (c) and full (d) revival signals, determined with |max(signal)-min(signal)| of the revival structure. The dependence of the signal size on sample density is fit to a linear function.

red-shift. When the laser spectrum shifts to the blue, the spectrum becomes closer to the empty cavity case. The improved overlap leads to an increase of the intracavity power. Conversely, a red-shift reduces the spectral overlap further and the intracavity power decreases. It is important to note that in the single pulse case (e.g., Fig. 6.3), only red shift of the spectrum is observed because only one laser pulse interacts with the target. However, with the combination of pump and probe pulses, we measure the effects on the probe field. The molecular alignment/coherent rotation can transfer energy back and forth between the molecule and the probe field, depending on the pump-probe delay time [178].

To provide a systematic investigation of the intracavity response, we have measured its dependence on a number of important parameters including the target gas density and pump/probe intensities. As the molecular density is increased, we observe a linear increase in the size of the revival effect on the intracavity power (measured by |max(signal)-min(signal)| of the revival structure), as shown in Fig. 6.4c,d. This dependence is consistent with ISRS [178]. We also see a linearly increasing response as either the pump or probe is increased independently. This effect is also consistent with ISRS and the degree of alignment $\langle\langle\cos^2\theta\rangle\rangle$ increasing linearly in the small intensity limit. These observations have been verified by numerically simulating the alignment process.

To complete our investigation of the field-molecule interaction, we use the observed spectral shifts to estimate the effects of ISRS on the phase of the probe pulses. We determine the phase shifts by analyzing the measured central wavelength of the intracavity spectrum as a function of pump-probe delay. The delay dependent spectral shifts are smaller than the red-shift observed when the gas is introduced (see Fig. 6.3b.). The spectral shifts and their corresponding intracavity power are shown in Fig. 6.5a,b for the half- and full-revival respectively. Using the relation $\omega(t) = \omega_0 + d\phi/dt$, we extract the phase dependence as a function of delay [188]. The phase shift results are shown in Fig. 6.5c,d for half- and full-revival respectively. Large phase shifts are introduced to the driving laser. This will be important to understand and control for experiments with HHG because small phase shifts on the pump will be transferred to the harmonic light and scale with harmonic order (as discussed in Chapter 5).

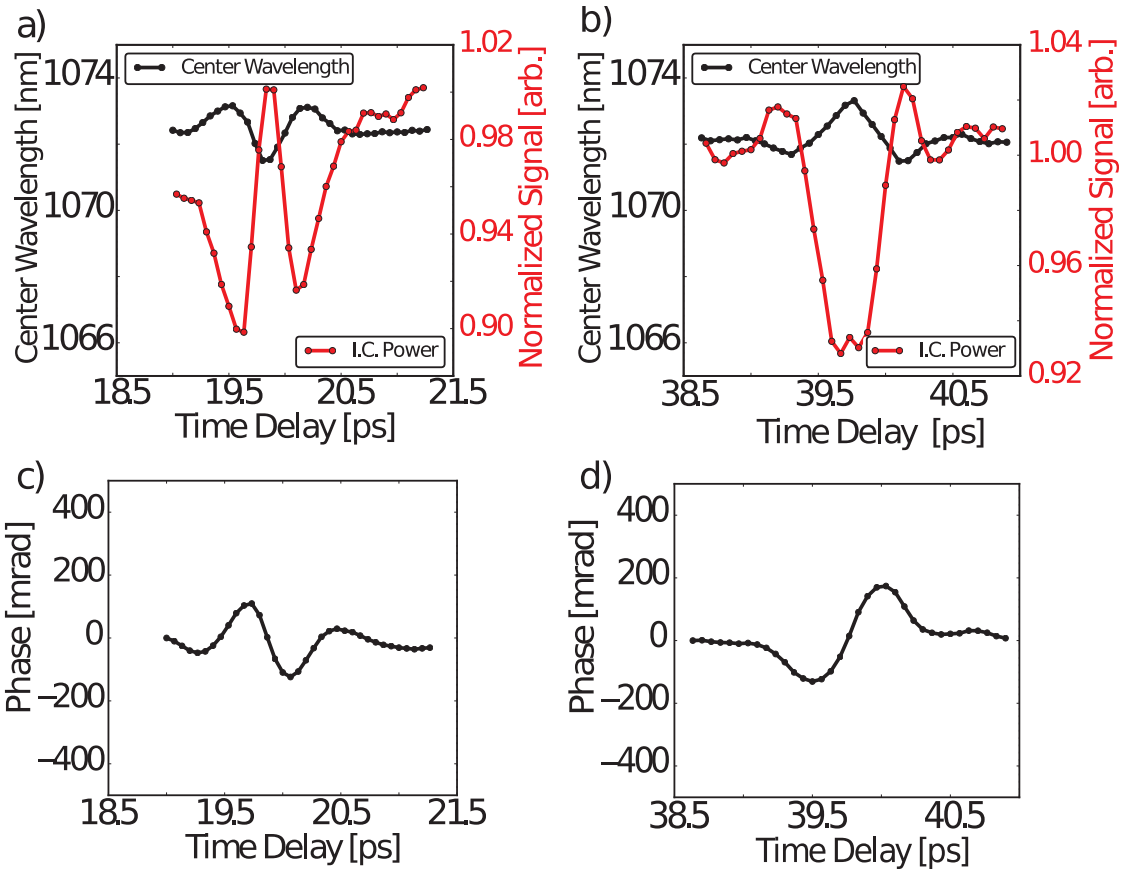

Figure 6.5: **a,b)** The intracavity central wavelength and the intracavity power are shown as a function of pump-probe delay for the half-revival (a) and full-revival (b) of N_2O. **c,d)** The phase as a function of delay for the half-revival (c) and full-revival (d) of N_2O respectively using the relation $\omega(t) = \omega_0 + d\phi/dt$. The conditions for the data were the same as Fig. 6.4a,b with 2 atm of pressure for the half-revival and full-revival data.

6.4 High-order harmonic generation with molecules.

With this clear determination of the molecular alignment effect on the probe pulse that is used to drive HHG, we now turn our attention to the measurement of the HHG yield as a function of molecular alignment. A pump pulse of 7.5×10^{12} W cm^{-2} is used to prepare a rotational wavepacket before a probe pulse of 0.6×10^{14} W cm^{-2} is used to perform HHG. The total yield of harmonics 15 - 19 is detected simultaneously with an electron multiplier as the delay between the pump and probe pulses is scanned. These harmonics are isolated with an aluminum filter and the bandwidth of our B_4C optics. The data is documented in Fig. 6.6. The XUV yield is normalized to the baseline at t $\sim$ 5 ps. The delay is scanned continuously at a rate of at 1 ps/s and no averaging of the data is performed besides low-pass filtering at 300 Hz. Further averaging could be performed to improve signal to noise and is not presented here. In Fig. 6.6b, we report the observation of a nearly 50% modulation in the XUV yield. The XUV yield is shown with the $\langle\langle\cos^2\theta\rangle\rangle$ expectation value for reference. The similarity between the data and $\langle\langle\cos^2\theta\rangle\rangle$ is expected when the harmonics are far from an interference region [189, 190]. This XUV yield does not mimic the effect on the driving laser, meaning that the modulation in the XUV yield are not driven by modulation in the driving probe power but is an intrinsic signal from the molecular dynamics. With our fsEC apparatus we are easily able to achieve probe intensities of 1×10^{14} W cm^{-2} and we have also performed HHG experiments with molecules of higher ionization threshold such as CO_2 or harder to ionize molecules like O_2 and observed similar modulations in the HHG yield arising from rotational revivals. We also observed a weaker harmonic modulation from O_2, but O_2 proved to be much harder to ionize than the I_p suggests resulting in lower harmonic yields and a much noisier signal.

6.5 Future potential of cavity-based field-free molecular alignment

Observing HHG from aligned molecules at high repetition rates opens exciting avenues for probing molecular rotational dynamics [184, 191] with more rapid data acquisition and increased measurement precision. It may also be possible to enhance the degree of alignment with repetitive

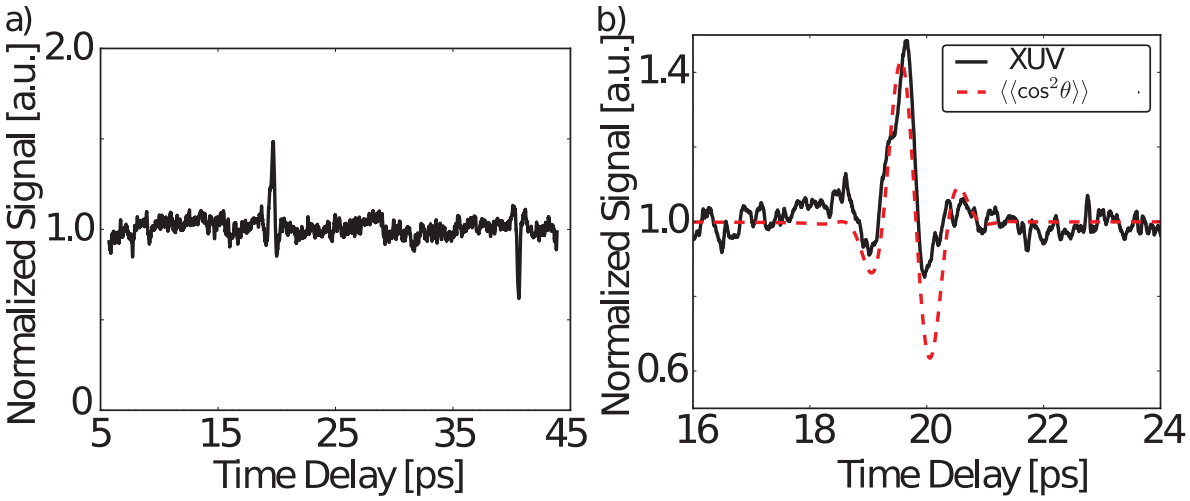

Figure 6.6: **a)** High harmonic signal generated from aligned N_2O molecules. Harmonics 15-19 are measured as a function of pump-probe delay. The half and full revival of N_2O is shown at ∼19 and ∼ 39 ps of delay, respectively. Revival signals on the harmonic yield are observable out to ∼ 80 ps. **b)** The amplitude modulation on the XUV yield is shown in detail. The $\langle\langle\cos^2\theta\rangle\rangle$ expectation value is shown for reference. It is assumed that the harmonic yield will approximately follow the $\langle\langle\cos^2\theta\rangle\rangle$ value if the harmonic order is far from a resonant feature. Strong harmonic modulations were also present down to the 3^{rd}harmonic. The harmonic modulations are not identical to the IR modulations shown in Fig. 6.4.

impulsive kicks [192]. With the demonstration of heterodyne interferometry with XUV combs [43] we expect to measure both the amplitude and phase of XUV light from aligned molecules [164].

There are also a few open questions about the system. First, we observed the higher fractional revivals in N_2O than what is predicted by $\langle\langle\cos^2\theta\rangle\rangle$. These are shown in the highlighted section of Fig. 6.7a. The higher order fractional revivals could be used to probe additional light-molecule interaction dynamics [179]. Second, the coherence decays much faster than we expected. The decay of the driving laser revival signal is shown in Fig. 6.7b. It is possible that the presence of the plasma is affecting the rotational coherence at these fast timescales. The collisional dynamics of the molecules and the plasma are potentially interesting to study. Third, there is a possibility to use the modulations from the molecule to tune the nonlinearities in the cavity. This can be used to compensate for plasma blue-shifting or to tune phase shifts for possible attosecond pulse generation experiments. This effect is shown in Fig. 6.7c. We tested the hypothesis by measuring the intracavity spectrum using pure xenon, pure N_2O, and a mix of xenon and N_2O such that the xenon density was the same as in the pure xenon case. The inset to the figure shows the differential spectra relative to the empty cavity case.

Another possibility is to use the cavity-enhanced FFMA signals to non-resonantly detect molecules. An example of where this could be useful is detecting OH in the presence of H_2O. OH and H_2O have very close and congested absorption spectra in the mid-IR, however they have very different rotational constants. Therefore, the revival features of the two molecules would be very different. It should then be possible to pick a pump-probe detuning to focus on OH rather than H_2O and use highly-sensitive detection techniques (such as lock-in detection on intensity modulations or polarization modulations) to look for the revival signal. Using a much higher finesse cavity than the one used for this work can also increase the sensitivity. An added benefit of a method like this is that it can also be very flexible with the specific molecule to be detected since the wavelength of the laser is essentially irrelevant and only the pump-probe delay is selected in order to isolate a certain molecule. It may also be possible to use multiple probe pulses at different times to multiplex the detection. It is unclear whether absolute concentrations can be determined, but if polarization

modulation is used for detection, it should be possible.

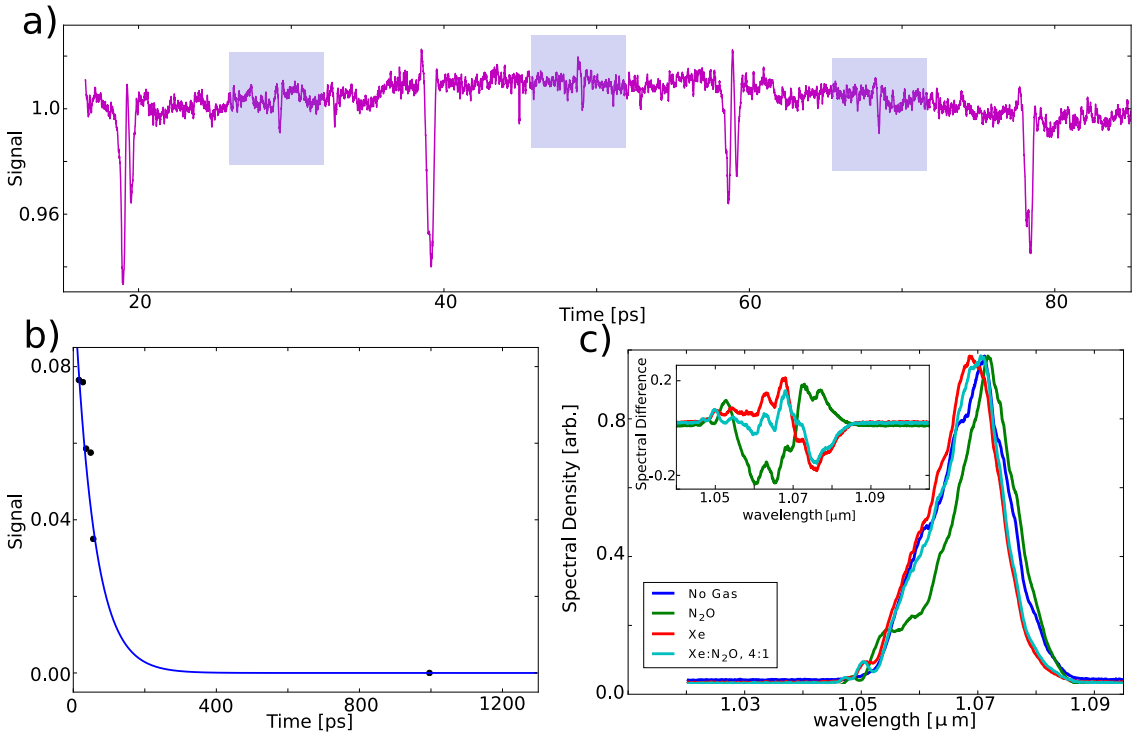

Figure 6.7: **a)** The data is the IR intensity modulations from N_2O. The highlighted regions show revival struction at the quarter of the full rotational period. These do not originate from the $\langle\langle\cos^2\theta\rangle\rangle$ expectation value. **b)** The decay of the revivals as a function of time. The lifetime is much shorter than is expected. This could be a method to determine if there is collisional decoherence in the jet. **c)** Use of molecules and a traditional HHG target, xenon. The xenon causes an ionization blue-shift. The N_2O causes a ISRS-induced red-shift. Together, they can cancel each other. The insert is the difference spectra of each case relative to no gas. The small reduction in blue-shift can be seen in the cyan trace which corresponds to the mixed gases. Further optimization could yield more dramatic results.

Chapter 7

Conclusion and Future Prospects

The riddles of God are more satisfying than the solutions of man.

–G. K. Chesterton

7.1 Conclusion

We have shown that the XUV frequency comb is not only one of the brightest sources of XUV light originating from HHG, it is also by far the most temporally coherent of all available XUV light sources. Certainly, it is now in an excellent position to leverage both of these properties for future spectroscopy application. Picking the perfect spectroscopy target will be left up to future generations of the experiment. We have also shown that there is a good amount of strong-field physics that can be investigated with the XUV comb apparatus. Certainly there will be more opportunities in the future. For instance, measuring harmonic phases as a function of molecular alignment is completely feasible and the XUV comb promises a level of sensitivity not reached in any other effort to date. Further, the possibility of turning the XUV comb into an attosecond pulse machine is intriguing (if not for the amazingly short pulse duration but for the continuous XUV spectrum these pulses require). We have helped show a few tricks that may help in future efforts, but progress is being made in other groups around the world. It seems only a matter of time before it becomes a reality. Another interesting avenue is using an optical parametric oscillator (OPO) to pump the enhancement cavity [93]. The OPO is a tunable source outputing at wavelengths of 3-5 μm. Due to the favorable scaling of HHG with driving laser wavelength, building a soft X-ray

frequency comb seems within reach. A modest power scaling of the OPO technology would be required from the current 1 W of power to about 10 W of power. However, the OPO pumping laser technology is certainly available. The only remaining question would be if an enhancement cavity that can support 10 kW of average power in the mid IR is possible [193].

The fact that there are femtosecond pulses circulating inside the fsEC is definitely under utilized. We made an effort to exploit this with the field-free molecular alignment work, but beyond using them for just making harmonics, little work has been done in the time domain. This is set to change with recent experiments in transient-absorption spectroscopy and should start a whole new wave of cavity-based ultrafast experiments [194]. There are a whole host of possible pump-probe-style experiments that can now be envisioned with increased power, sensitivity, and statistics. This will definitely be a very exciting direction if not completely orthogonal to our groups efforts focusing on high-resolution spectroscopy.

Bibliography

[1] J. L. Hall. Nobel lecture: Defining and measuring optical frequencies. *Rev. Mod. Phys.* **78**, 1279–1295 (2006).

[2] T. W. Hänsch. Nobel lecture: Passion for precision. *Rev. Mod. Phys.* **78**, 1297–1309 (2006).

[3] R. J. Jones, K. Moll, M. Thorpe & J. Ye. Phase-coherent frequency combs in the vacuum ultraviolet via high-harmonic generation inside a femtosecond enhancement cavity. *Phys. Rev. Lett.* **94**, 193201 (2005).

[4] C. Gohle *et al.* A frequency comb in the extreme ultraviolet. *Nature* **436**, 234–7 (2005).

[5] W. Ubachs, E. Salumbides, K. S. E. Eikema, N. de Oliveira & L. Nahon. Novel techniques in VUV high-resolution spectroscopy. *Journ. of Elect. Spect. and Rel. Phenom.* **196**, 159 – 164 (2014).

[6] J. P. Gordon, H. J. Zeiger & C. H. Townes. Molecular microwave oscillator and new hyperfine structure in the microwave spectrum of NH_3. *Phys. Rev.* **95**, 282–284 (1954).

[7] J. P. Gordon, H. J. Zeiger & C. H. Townes. The maser–new type of microwave amplifier, frequency standard, and spectrometer. *Phys. Rev.* **99**, 1264–1274 (1955).

[8] A. L. Schawlow & C. H. Townes. Infrared and optical masers. *Phys. Rev.* **112**, 1940–1949 (1958).

[9] T. H. Maiman. Stimulated optical radiation in ruby. *Nature* **187**, 493 (1960).

[10] A. Javan, W. R. Bennett & D. R. Herriot. Population inversion and continuous optical maser oscillation in a gas discharge containing a He-Ne mixture. *Phys. Rev. Lett.* **6**, 106 (1961).

[11] L. Hollberg, S. Diddams, A. Bartels, T. Fortier & K. Kim. The measurement of optical frequencies. *Metrologia* **42**, S105–S124 (2005).

[12] D. E. Spence, P. N. Kean & W. Sibbett. 60-fsec pulse generation from a self-mode-locked Ti:Sapphire laser. *Opt. Lett.* **16**, 42–44 (1991).

[13] J. A. R. Samson. *Techniques in vacuum ultraviolet spectroscopy* (PIED Publications, 1967).

[14] A. E. Siegman. *Lasers* (University Science Books, 1986).

[15] M. Niering *et al.* Measurement of the hydrogen $1S$- $2S$ transition frequency by phase coherent comparison with a microwave cesium fountain clock. *Phys. Rev. Lett.* **84**, 5496–5499 (2000).

[16] H. A. Bethe & E. E. Salpeter. *Quantum mechanics of one- and two-electron atoms* (Springer Science & Business Media, 2012).

[17] P. A. Franken, A. E. Hill, C. W. Peters & G. Weinreich. Generation of optical harmonics. *Phys. Rev. Lett.* **7**, 118–119 (1961).

[18] N. Bloemgergen. *Nonlinear optics* (Addison-Wesley, 1965).

[19] T. Braebec & F. Krausz. Intense few-cycle laser fields: Frontiers of nonlinear optics. *Rev. Mod. Phys.* **72**, 545–591 (2000).

[20] A. Spott, A. Jaroń-Becker & A. Becker. Ab initio and perturbative calculations of the electric susceptibility of atomic hydrogen. *Phys. Rev. A* **90**, 013426 (2014).

[21] A. Spott, A. Becker & A. Jaroń-Becker. Transition from perturbative to nonperturbative interaction in low-order-harmonic generation. *Phys. Rev. A* **91**, 023402 (2015).

[22] J. Hall, E. Robinson & L. Branscomb. Laser double-quantum photodetachment of I^-. *Phys. Rev. Lett.* **14**, 1013 (1965).

[23] L. V. Keldysh. Ionization in the field of a strong electromagnetic wave. *Sov. Phys. JETP.* **20**, 1307 (1965).

[24] P. Corkum. Plasma perspective on strong field multiphoton ionization. *Phys. Rev. Lett.* **71**, 1994–1997 (1993).

[25] M. Ammosov, N. Delone & V. Krainov. Tunnel ionization of complex atoms and of atomic ions in an alternating. *Sov. Phys. JETP* **64**, 1191–1194 (1986).

[26] J. Ye & S. Cundiff. *Femtosecond optical frequency comb: principle, operation and applications* (Springer Science & Business Media, 2005).

[27] A. Marian, M. C. Stowe, J. R. Lawall, D. Felinto & J. Ye. United time-frequency spectroscopy for dynamics and global structure. *Science* **306**, 2063–2068 (2004).

[28] D. J. Jones *et al.* Carrier-envelope phase control of femtosecond mode-locked lasers and direct optical frequency synthesis. *Science* **288**, 635–639 (2000).

[29] S. A. Diddams *et al.* Direct link between microwave and optical frequencies with a 300 THz femtosecond laser comb. *Phys. Rev. Lett.* **84**, 5102–5105 (2000).

[30] J. M. Dudley, G. Genty & S. Coen. Supercontinuum generation in photonic crystal fiber. *Rev. Mod. Phys.* **78**, 1135 (2006).

[31] C. Benko *et al.* Full phase stabilization of a Yb:fiber femtosecond frequency comb via high-bandwidth transducers. *Opt. Lett.* **37**, 2196–2198 (2012).

[32] R. Ell *et al.* Generation of 5-fs pulses and octave-spanning spectra directly from a Ti:sapphire laser. *Opt. Lett.* **26**, 373–375 (2001).

[33] T. Fortier, D. J. Jones & S. Cundiff. Phase stabilization of an octave-spanning Ti:sapphire laser. *Opt. Lett.* **28**, 2198–2200 (2003).

[34] A. D. Ludlow, M. M. Boyd, J. Ye, E. Peik & P. O. Schmidt. Optical atomic clocks. *Rev. Mod. Phys.* **87**, 637–701 (2015).

[35] T. Nicholson *et al.* Systematic evaluation of an atomic clock at 2×10^{-18} total uncertainty. *Nat. Comm.* **6**, 1–8 (2015).

[36] G. D. Cole, W. Zhang, M. J. Martin, J. Ye & M. Aspelmeyer. Tenfold reduction of brownian noise in high-reflectivity optical coatings. *Nat. Photon.* **7**, 644–650 (2013).

[37] N. R. Newbury & B. R. Washburn. Theory of the frequency comb output from a femtosecond fiber laser. *IEEE Journ. of Quant. Elect.* **41**, 1388–1402 (2005).

[38] N. R. Newbury & W. C. Swann. Low-noise fiber-laser frequency combs. *JOSA B* **24**, 1756–1770 (2007).

[39] A. Cingöz *et al.* Broadband phase noise suppression in a Yb-fiber frequency comb. *Opt. Lett.* **36**, 743–745 (2011).

[40] T. Kessler *et al.* A sub-40-mhz-linewidth laser based on a silicon single-crystal optical cavity. *Nat. Photon.* **6**, 687–692 (2012).

[41] T. M. Fortier *et al.* Generation of ultrastable microwaves via optical frequency division. *Nat. Photon.* **5**, 425–429 (2011).

[42] A. Ruehl *et al.* Ultrabroadband coherent supercontinuum frequency comb. *Phys. Rev. A* **84**, 011806 (2011).

[43] C. Benko *et al.* Phase coherent extreme ultraviolet radiation with coherence time greater than 1 s. *Nat. Photon.* **8**, 530–536 (2014).

[44] S. Schiller. Spectrometry with frequency combs. *Opt. Lett.* **27**, 766–768 (2002).

[45] I. Coddington, W. C. Swann & N. R. Newbury. Coherent multiheterodyne spectroscopy using stabilized optical frequency combs. *Phys. Rev. Lett.* **100**, 013902 (2008).

[46] P. Del'Haye, O. Arcizet, A. Schliesser, R. Holzwarth & T. J. Kippenberg. Full stabilization of a microresonator-based optical frequency comb. *Phys. Rev. Lett.* **101**, 053903 (2008).

[47] J. L. Hall & M. Zhu. An introduction to phase-stable optical sources. *of the International School of Physics Enrico Fermi, edited by E. Arimondo, W.D. Phillips, and F. Strumia (North-Holland)* (1992).

[48] M. Martin *et al.* A quantum many-body spin system in an optical lattice clock. *Science* **341**, 632–636 (2013).

[49] M. D. Seaberg *et al.* Ultrahigh 22 nm resolution coherent diffractive imaging using a desktop 13 nm high harmonic source. *Opt. Exp.* **19**, 22470–22479 (2011).

[50] Y. Mairesse *et al.* Attosecond synchronization of high-harmonic soft x-rays. *Science* **302**, 1540–1543 (2003).

[51] H. Fattahi *et al.* Third-generation femtosecond technology. *Optica* **1**, 45–63 (2014).

[52] A. Cingöz *et al.* Direct frequency comb spectroscopy in the extreme ultraviolet. *Nature* **482**, 68–71 (2012).

[53] M. I. Eides, H. Grotch & V. A. Shelyuto. Theory of light hydrogen-like atoms. *Phys. Rep.* **342**, 63–261 (2001).

[54] K. S. E. Eikema, W. Ubachs, W. Vassen & W. Hogervorst. Precision measurements in helium at 58 nm: Ground state lamb shift and the 1^1S-2^1P transition isotope shift. *Phys. Rev. Lett.* **76**, 1216–1219 (1996).

[55] K. S. E. Eikema, W. Ubachs, W. Vassen & W. Hogervorst. Lamb shift measurement in the 1 ^{1}S ground state of helium. *Phys. Rev. A* **55**, 1866–1884 (1997).

[56] D. Z. Kandula, C. Gohle, T. J. Pinkert, W. Ubachs & K. S. E. Eikema. Extreme ultraviolet frequency comb metrology. *Phys. Rev. Lett.* **105**, 063001 (2010).

[57] L. Schmöger *et al.* Coulomb crystallization of highly charged ions. *Science* **347**, 1233–1236 (2015).

[58] M. T. Murphy, J. Webb & V. Flambaum. Further evidence for a variable fine-structure constant from Keck/HIRES QSO absorption spectra. *Monthly Notices of the Royal Astronomical Society* **345**, 609–638 (2003).

[59] J. C. Berengut, V. A. Dzuba & V. V. Flambaum. Enhanced laboratory sensitivity to variation of the fine-structure constant using highly charged ions. *Phys. Rev. Lett.* **105**, 120801 (2010).

[60] J. C. Berengut, V. A. Dzuba, V. V. Flambaum & A. Ong. Electron-hole transitions in multiply charged ions for precision laser spectroscopy and searching for variations in α. *Phys. Rev. Lett.* **106**, 210802 (2011).

[61] M. Zolotorev & D. Budker. Parity nonconservation in relativistic hydrogenic ions. *Phys. Rev. Lett.* **78**, 4717–4720 (1997).

[62] E. Reinhold *et al.* Indication of a cosmological variation of the proton-electron mass ratio based on laboratory measurement and reanalysis of H_2 spectra. *Phys. Rev. Lett.* **96**, 151101 (2006).

[63] P. C. Hinnen, S. E. Werners, S. Stolte, W. Hogervorst & W. Ubachs. XUV-laser spectroscopy of HD at 92-98 nm. *Phys. Rev. A* **52**, 4425–4433 (1995).

[64] J. Liu *et al.* Determination of the ionization and dissociation energies of the hydrogen molecule. *The Journ. of Chem. Phys.* **130**, 174306 (2009).

[65] C. J. Campbell *et al.* Single-ion nuclear clock for metrology at the 19th decimal place. *Phys. Rev. Lett.* **108**, 120802 (2012).

[66] F. Asaro & I. Perlman. Isomeric state of uranium-235. *Phys. Rev.* **107**, 318–319 (1957).

[67] J. R. Huizenga, C. L. Rao & D. W. Engelkeikeir. 27-minute isomer of U^{235}. *Phys. Rev.* **107**, 319 (1957).

[68] D. Attwood. *Soft x-rays and extreme ultraviolet radiation: principles and applications* (Cambridge university press, 1999).

[69] ALS. http://www-als.lbl.gov/index.php/beamlines/photon-source-parameters.html (2016).

[70] J. D. Koralek *et al.* Laser based angle-resolved photoemission, the sudden approximation, and quasiparticle-like spectral peaks in $Bi_2Sr_2CaCu_2O_{8+\delta}$. *Phys. Rev. Lett.* **96**, 017005 (2006).

[71] F. Krausz & M. Ivanov. Attosecond physics. *Rev. Mod. Phys.* **81**, 163–234 (2009).

[72] Z. Chang. *Fundamentals of Attosecond Optics* (CRC Press 2011, 2011).

[73] A. Ruehl, A. Marcinkevicius, M. E. Fermann & I. Hartl. 80 W, 120 fs Yb-fiber frequency comb. *Opt. Lett.* **35**, 3015–3017 (2010).

[74] D. C. Yost, T. R. Schibli & J. Ye. Efficient output coupling of intracavity high-harmonic generation. *Opt. Lett.* **33**, 1099–101 (2008).

[75] R. J. Jones & J. Ye. Femtosecond pulse amplification by coherent addition in a passive optical cavity. *Opt. Lett.* **27**, 1848 (2002).

[76] J. Petersen & A. Luiten. Short pulses in optical resonators. *Opt. Exp.* **11**, 2975–2981 (2003).

[77] S. Holzberger *et al.* Enhancement cavities for zero-offset-frequency pulse trains. *Opt. Lett.* **40**, 2165–2168.

[78] M. R. Kozlowski, M. C. Staggs, F. Rainer & J. Stathis. Laser conditioning and electronic defects of HfO_2 and SiO_2 thin films. In *Laser-Induced Damage in Optical Materials: 1990*, 269–282 (International Society for Optics and Photonics, 1991).

[79] R. Drever *et al.* Laser phase and frequency stabilization using an optical resonator. *Appl. Phys. B* **31**, 97–105 (1983).

[80] M. Bishof, X. Zhang, M. J. Martin & J. Ye. Optical spectrum analyzer with quantum-limited noise floor. *Phys. Rev. Lett.* **111**, 093604 (2013).

[81] BP Abbott *et al.* (LIGO Scientific Collaboration and VIRGO Collaboration). Observation of gravitational waves from a binary black hole merger. *Phys. Rev.Letters* **116**, 061102 (2016).

[82] E. D. Black. An introduction to Pound–Drever–Hall laser frequency stabilization. *Am. Journ. of Phys.* **69**, 79–87 (2001).

[83] W. Nagourney. *Quantum electronics for atomic physics* (Oxford University Press, 2010), 1 edn.

[84] F. Adler, P. Masłowski & A. Foltynowicz. Mid-infrared Fourier transform spectroscopy with a broadband frequency comb. *Opt. Exp.* **18**, 21861–21872 (2010).

[85] A. Foltynowicz, T. Ban, P. Masłowski, F. Adler & J. Ye. Quantum-noise-limited optical frequency comb spectroscopy. *Phys. Rev. Lett.* **107**, 233002 (2011).

[86] M. Lewenstein, P. Salieres & A. L'Huillier. Phase of the atomic polarization in high-order harmonic generation. *Phys. Rev. A* **52**, 4747–4754 (1995).

[87] D. C. Yost *et al.* Vacuum-ultraviolet frequency combs from below-threshold harmonics. *Nat. Phys.* **5**, 815–820 (2009).

[88] K. D. Moll, R. J. Jones & J. Ye. Output coupling methods for cavity-based high-harmonic generation. *Opt. Exp.* **14**, 8189–97 (2006).

[89] D. C. Yost. *Development of an extreme ultraviolet frequency comb for precision spectroscopy.* Ph.D. thesis, University of Colorado (2011).

[90] I. Pupeza *et al.* Compact high-repetition-rate source of coherent 100 ev radiation. *Nat. Photon.* **7**, 608–612 (2013).

[91] I. Hartl *et al.* Cavity-enhanced similariton Yb-fiber laser frequency comb: 3×10^{14} W/cm^2 peak intensity at 136 MHz. *Opt. Lett.* **32**, 2870–2 (2007).

[92] T. R. Schibli *et al.* Optical frequency comb with submillihertz linewidth and more than 10 W average power. *Nat. Photon.* **2**, 355–359 (2008).

[93] F. Adler *et al.* Phase-stabilized, 1.5 W frequency comb at 2.8–4.8 μm. *Opt. Lett.* **34**, 1330–1332 (2009).

[94] F. O. Ilday, J. R. Buckley, W. G. Clark & F. W. Wise. Self-similar evolution of parabolic pulses in a laser. *Phys. Rev. Lett.* **92**, 213902 (2004).

[95] C. Jocher, T. Eidam, S. Hädrich, J. Limpert & A. Tünnermann. Sub 25 fs pulses from solid-core nonlinear compression stage at 250 W of average power. *Opt. Lett.* **37**, 4407–4409 (2012).

[96] W. Liu *et al.* Pre-chirp managed nonlinear amplification in fibers delivering 100 W, 60 fs pulses. *Opt. Lett.* **40**, 151–154 (2015).

[97] Y. Liu *et al.* High-power pre-chirp managed amplification of femtosecond pulses at high repetition rates. *Las. Phys. Lett.* **12**, 075101 (2015).

[98] G. P. Agrawal. *Nonlinear fiber optics* (Academic press, 2007).

[99] R. A. Rosenberg & D. C. Mancini. Deposition of carbon on gold using synchrotron radiation. *Nucl. Inst. and Meth. in Phys. Res. Sect. A* **291**, 101–106 (1990).

[100] J. Hollenshead & L. Klebanoff. Modeling radiation-induced carbon contamination of extreme ultraviolet optics. *Journ. of Vac. Sci. & Tech. B* **24**, 64–82 (2006).

[101] T. Koide *et al.* Resuscitation of carbon-contaminated mirrors and gratings by oxygen-discharge cleaning. 1: Efficiency recovery in the 4–40-ev range. *Appl. Opt.* **26**, 3884–3894 (1987).

[102] R. W. Hansen, M. Bissen, D. Wallace, J. Wolske & T. Miller. Ultraviolet ozone cleaning of carbon-contaminated optics. *Appl. Opt.* **32**, 4114–4116 (1993).

[103] F. Eggenstein, F. Senf, T. Zeschke & W. Gudat. Cleaning of contaminated XUV-optics at BESSY II. *Nucl. Inst. and Meth. in Phys. Res. Sect. A* **467**, 325–328 (2001).

[104] Ozone solutions. http://www.ozonesolutions.com.

[105] G. Voronov & N. Delone. Many photon ionization of the xenon atom by ruby laser radiation. *Sov. Phys. JETP* **23**, 54–58 (1966).

[106] S. Chin, G. Farkas & F. Yergeau. Observation of Kr and Xe ions created by intense nanosecond CO_2 laser pulses. *J. Phys. B* **16**, L223 (1983).

[107] P. Agostini, F. Fabre, G. Mainfray, G. Petite & N. K. Rahman. Free-free transitions following six-photon ionization of xenon atoms. *Phys. Rev. Lett.* **42**, 1127 (1979).

[108] A. McPherson *et al.* Studies of multiphoton production of vacuum-ultraviolet radiation in the rare gases. *JOSA B* **4**, 595–601 (1987).

[109] L. DiMauro, M. Frolov, K. L. Ishikawa & M. Ivanov. 50 years of optical tunneling. *J. Phys. B* **47**, 200301–200304 (2014).

[110] H. R. Reiss. Limits on tunneling theories of strong-field ionization. *Phys. Rev. Lett.* **101**, 043002 (2008).

[111] X. Tong & C. Lin. Empirical formula for static field ionization rates of atoms and molecules by lasers in the barrier–suppression regime. *Journ. of Phys. B* **38**, 2593 (2005).

[112] A. Perelomov, V. Popov & M. Terent'ev. Ionization of atoms in an alternating electric field. *Sov. Phys. JETP* **23**, 924–934 (1966).

[113] F. H. Faisal. *Theory of multiphoton processes* (Springer Science & Business Media, 2013).

[114] T. K. Allison, A. Cingöz, D. C. Yost & J. Ye. Extreme nonlinear optics in a femtosecond enhancement cavit. *Phys. Rev. Lett.* **107**, 183903 (2011).

[115] A. L'Huillier, K. J. Schafer & K. C. Kulander. Theoretical aspects of intense field harmonic generation. *J. Phys. B* **24**, 3315 (1991).

[116] J. L. Krause, K. J. Schafer & K. C. Kulander. High-order harmonic generation from atoms and ions in the high intensity regime. *Phys. Rev. Lett.* **68**, 3535 (1992).

[117] K. J. Schafer, B. Yang, L. F. DiMauro & K. C. Kulander. Above threshold ionization beyond the high harmonic cutoff. *Phys. Rev. Lett.* **70**, 1599–1602 (1993).

[118] M. Lewenstein, P. Balcou, M. Y. Ivanov, A. L'Huillier & P. B. Corkum. Theory of high-harmonic generation by low-frequency laser fields. *Phys. Rev. A* **49**, 2117 (1994).

[119] E. H. Hauge & J. A. Støvneng. Tunneling times: a critical review. *Rev. Mod. Phys.* **61**, 917–936 (1989).

[120] H. G. Winful. Tunneling time, the Hartman effect, and superluminality: A proposed resolution of an old paradox. *Phys. Rep.* **436**, 1 – 69 (2006).

[121] J. Hostetter, J. Tate, K. Schafer & M. Gaarde. Semiclassical approaches to below-threshold harmonics. *Phys. Rev. A* **82**, 23401 (2010).

[122] M. Chini *et al.* Coherent phase-matched VUV generation by field-controlled bound states. *Nat. Photon.* **8**, 437–441 (2014).

[123] W.-H. Xiong, J.-W. Geng, J.-Y. Tang, L.-Y. Peng & Q. Gong. Mechanisms of below-threshold harmonic generation in atoms. *Physical review letters* **112**, 233001 (2014).

[124] E. Constant *et al.* Optimizing high harmonic generation in absorbing gases: Model and experiment. *Phys. Rev. Lett.* **82**, 1668–1671 (1999).

[125] S. Hädrich *et al.* High photon flux table-top coherent extreme-ultraviolet source. *Nat. Photon.* **8**, 779–783 (2014).

[126] J. Rothhardt *et al.* Absorption-limited and phase-matched high harmonic generation in the tight focusing regime. *New Journ. of Phys.* **16**, 033022 (2014).

[127] C. M. Heyl, J. Güdde, A. L'Huillier & U. Höfer. High-order harmonic generation with μJ laser pulses at high repetition rates. *J. Phys. B: At. Mol. Opt. Phys.* **45**, 074020 (2012).

[128] D. R. Carlson, J. Lee, J. Mongelli, E. M. Wright & R. J. Jones. Intracavity ionization and pulse formation in femtosecond enhancement cavities. *Opt. Lett.* **36**, 2991–3 (2011).

[129] S. Kazamias *et al.* Pressure-induced phase matching in high-order harmonic generation. *Phys. Rev. A* **83**, 063405 (2011).

[130] D. C. Yost *et al.* Power optimization of XUV frequency combs for spectroscopy applications [Invited]. *Opt. Exp.* **19**, 23483–93 (2011).

[131] C. Heyl *et al.* Scale-invariant nonlinear optics in gases. *Optica* **3**, 75–81 (2016).

[132] M. Geissler *et al.* Light propagation in field-ionizing media: Extreme nonlinear optics. *Phys. Rev. Lett.* **83**, 2930–2933 (1999).

[133] D. R. Miller. Free jet sources. In G. Scoles (ed.) *Atomic and Molecular Beam Methods*, vol. 1, chap. 2, 17–53 (Oxford University Press, 1988).

[134] Al_2O_3 Detector. http://www.nist.gov/calibrations/radiometric-far-uv.cfm (2016).

[135] L. R. Canfield, R. G. Johnston & R. P. Madden. NBS detector standards for the far ultraviolet. *Appl. Opt.* **12**, 1611–1617 (1973).

[136] AXUV100G. http://optodiode.com/ (2016).

[137] Optical constants. http://henke.lbl.gov/optical_constants/.

[138] J. Lee, D. Carlson & R. Jones. Optimizing intracavity high harmonic generation for XUV fs frequency combs. *Opt. Exp.* **19**, 23315–23326 (2011).

[139] A. D. Shiner *et al.* Wavelength scaling of high harmonic generation efficiency. *Phys. Rev. Lett.* **103**, 073902 (2009).

[140] C. Benko *et al.* Power scaling XUV frequency combs to the mW level. *In preparation* (2016).

[141] A. Cabasse, G. Machinet, A. Dubrouil, E. Cormier & E. Constant. Optimization and phase matching of fiber-laser-driven high-order harmonic generation at high repetition rate. *Opt. Lett.* **37**, 4618–4620 (2012).

[142] S. Hädrich *et al.* Exploring new avenues in high repetition rate table-top coherent extreme ultraviolet sources. *Light:Sci. and App.* **4**, e320 (2015).

[143] J.-F. Hergott *et al.* Extreme-ultraviolet high-order harmonic pulses in the microjoule range. *Phys. Rev. A* **66**, 021801 (2002).

[144] E. Lorek *et al.* High-order harmonic generation using a high-repetition-rate turnkey laser. *Rev. Sci. Instr.* **85**, 123106 (2014).

[145] P. Rudawski *et al.* A high-flux high-order harmonic source. *Rev. Sci. Instr.* **84**, 073103 (2013).

[146] E. Takashi *et al.* Generation of 10-Âţj coherent extreme-ultraviolet light by use of high-order harmonics. *Opt. Lett.* **27**, 1920 (2002).

[147] E. J. Takahashi, P. Lan, O. D. Mücke, Y. Nabekawa & K. Midorikawa. Attosecond nonlinear optics using gigawatt-scale isolated attosecond pulses. *Nat. Comm.* **4**, 2691 (2013).

[148] H. Wang *et al.* Bright high-repetition-rate source of narrowband extreme-ultraviolet harmonics beyond 22 eV. *Nat. Comm.* **6**, 7459 (2015).

[149] A. Willner *et al.* Coherent control of high harmonic generation via dual-gas multijet arrays. *Phys. Rev. Lett.* **107**, 175002 (2011).

[150] M. Louisy *et al.* Gating attosecond pulses in a noncollinear geometry. *Optica* **2**, 563–566 (2015).

[151] M. Bellini *et al.* Temporal coherence of ultrashort high-order harmonic pulses. *Phys. Rev. Lett.* **81**, 297–300 (1998).

[152] D. Z. Kandula, C. Gohle, T. J. Pinkert, W. Ubachs & K. S. E. Eikema. XUV frequency-comb metrology on the ground state of helium. *Phys. Rev. A* **84**, 062512 (2011).

[153] Rigaku. http://www.rigaku.com/en/industry/coatings.

[154] J. I. Larruquert & R. A. M. Keski-Kuha. Multilayer coatings with high reflectance in the extreme-ultraviolet spectral range of 50 to 121.6 nm. *Appl. Opt.* **38**, 1231–1236 (1999).

[155] G. Monaco *et al.* Optical constants in the EUV soft x-ray (5–152 nm) spectral range of B_4C thin films deposited by different deposition techniques.

[156] M. Vidal-Dasilva, M. Fernández-Perea, J. A. Méndez, J. A. Aznárez & J. I. Larruquert. Electron-beam deposited boron coatings for the extreme ultraviolet. *Appl. Opt.* **47**, 2926–2930 (2008).

[157] D. Middleton. LXXI. The distribution of energy in randomly modulated waves. *The London, Edinburgh, and Dublin Philosophical Magazine and Journal of Science* **42**, 689–707 (1951).

[158] D. Elliott, R. Roy & S. Smith. Extracavity laser band-shape and bandwidth modification. *Physical Review A* **26**, 12 (1982).

[159] M. Zhu & J. L. Hall. Stabilization of optical phase/frequency of a laser system: application to a commercial dye laser with an external stabilizer. *JOSA B* **10**, 802–816 (1993).

[160] H. R. Telle. *Frequency control of semiconductor lasers*, chap. 5, 137–172 (Springer, 1996).

[161] F. L. Walls & A. Demarchi. RF spectrum of a signal after frequency multiplication; measurement and comparison with a simple calculation. *Instrumentation and Measurement, IEEE Transactions on* **24**, 210–217 (1975).

[162] A. Zair *et al.* Quantum path interferences in high-order harmonic generation. *Phys. Rev. Lett.* **100**, 143902 (2008).

[163] Y. Mairesse *et al.* High-order harmonic transient grating spectroscopy in a molecular jet. *Phys. Rev. Lett.* **100**, 143903 (2008).

[164] J. Itatani *et al.* Tomographic imaging of molecular orbitals. *Nature* **432**, 867–871 (2004).

[165] S. R. Leone *et al.* What will it take to observe processes in "real time"? *Nat. Photon.* **8**, 162–166 (2014).

[166] K. T. Kim, D. Villeneuve & P. Corkum. Manipulating quantum paths for novel attosecond measurement methods. *Nat. Photon.* **8**, 187–194 (2014).

[167] F. Lépine, M. Y. Ivanov & M. J. Vrakking. Attosecond molecular dynamics: fact or fiction? *Nat. Photon.* **8**, 195–204 (2014).

[168] F. Krausz & M. I. Stockman. Attosecond metrology: from electron capture to future signal processing. *Nat. Photon.* **8**, 205–213 (2014).

[169] S. B. Schoun. *Attosecond High-Harmonic Spectroscopy of Atoms and Molecules Using Mid-Infrared Sources*. Ph.D. thesis, The Ohio State University (2015).

[170] Y. R. Shen & N. Bloembergen. Theory of stimulated brillouin and raman scattering. *Phys. Rev.* **137**, 6A (1965).

[171] S. Ospelkaus *et al.* Efficient state transfer in an ultracold dense gas of heteronuclear molecules. *Nat. Phys.* **4**, 622–626 (2008).

[172] P. D. Maker & R. W. Terhune. Study of optical effects due to an induced polarization third order in the electric field strength. *Phys. Rev.* **137**, A801–A818 (1965).

[173] J.-X. Cheng & X. S. Xie. Coherent anti-stokes Raman scattering microscopy: Instrumentation, theory, and applications. *The Journ. of Phys. Chem. B* **108**, 827–840 (2004).

[174] S. Baker, I. A. Walmsley, J. W. G. Tisch & J. P. Marangos. Femtosecond to attosecond light pulses from a molecular modulator. *Nat. Photon.* **5**, 664–671 (2011).

[175] S. E. Harris & A. V. Sokolov. Broadband spectral generation with refractive index control. *Phys. Rev. A* **55**, R4019–R4022 (1997).

[176] S. E. Harris & A. V. Sokolov. Subfemtosecond pulse generation by molecular modulation. *Phys. Rev. Lett.* **81**, 2894–2897 (1998).

[177] H.-S. Chan *et al.* Synthesis and measurement of ultrafast waveforms from five discrete optical harmonics. *Science* **331**, 1165–1168 (2011).

[178] Y. Yan, E. B. G. Jr. & K. A. Nelson. Impulsive stimulated scattering: General importance in femtosecond laser pulse interactions with matter, and spectroscopic applications. *The Journ. of Chem. Phys.* **83**, 5391–5399 (1985).

[179] T. Seideman. Rotational excitation and molecular alignment in intense laser fields. *The Journ. of Chem. Phys.* **103**, 7887 (1995).

[180] J. Ortigoso, M. Rodríguez, M. Gupta & B. Friedrich. Time evolution of pendular states created by the interaction of molecular polarizability with a pulsed nonresonant laser field. *The Journ. of Chem. Phys.* **110**, 3870 (1999).

[181] H. Stapelfeldt & T. Seideman. Colloquium: Aligning molecules with strong laser pulses. *Rev. Mod. Phys.* **75**, 543–557 (2003).

[182] N. Zhavoronkov & G. Korn. Generation of single intense short optical pulses by ultrafast molecular phase modulation. *Phys. Rev. Lett.* **88**, 203901 (2002).

[183] R. Velotta, N. Hay, M. B. Mason, M. Castillejo & J. P. Marangos. High-order harmonic generation in aligned molecules. *Phys. Rev. Lett.* **87**, 183901 (2001).

[184] J. Itatani *et al.* Controlling high harmonic generation with molecular wave packets. *Phys. Rev. Lett.* **94**, 123902 (2005).

[185] A. Nazarkin & G. Korn. Raman self-conversion of femtosecond laser pulses and generation of single-cycle radiation. *Phys. Rev. A* **58**, R61–R64 (1998).

[186] G. Korn, O. Dühr & A. Nazarkin. Observation of raman self-conversion of fs-pulse frequency due to impulsive excitation of molecular vibrations. *Phys. Rev. Lett.* **81**, 1215–1218 (1998).

[187] P. Salières, A. Maquet, S. Haessler, J. Caillat & R. Taïeb. Imaging orbitals with attosecond and Ångström resolutions: toward attochemistry? *Rep. on Prog. in Phys.* **75**, 62401 (2012).

[188] R. A. Bartels *et al.* Phase modulation of ultrashort light pulses using molecular rotational wave packets. *Phys. Rev. Lett.* **88**, 013903 (2001).

[189] M. Lein *et al.* Interference effects in high-order harmonic generation with molecules. *Phys. Rev. A* **66**, 023805 (2002).

[190] C. Vozzi *et al.* Controlling two-center interference in molecular high harmonic generation. *Phys. Rev. Lett.* **95**, 153902 (2005).

[191] R. Lock *et al.* Extracting continuum electron dynamics from high harmonic emission from molecules. *Phys. Rev. Lett.* **108**, 133901 (2012).

[192] J. P. Cryan, P. H. Bucksbaum & R. N. Coffee. Field-free alignment in repetitively kicked nitrogen gas. *Phys. Rev. A* **80**, 063412 (2009).

[193] G. D. Cole *et al.* High-performance near-and mid-infrared crystalline coatings. *arXiv:1604.00065* (2016).

[194] M. A. R. Reber, Y. Chen & T. K. Allison. Cavity-enhanced ultrafast spectroscopy: ultrafast meets ultrasensitive. *Optica* **3**, 311–317 (2016).

Appendix A

Numerical Code Repository

Github During the course of this work, a decent amount of code was generated to numerically simulate various things relevant to the XUV frequency comb project. The numerical code is stored on Github at `https://github.com/c-benko`. A very brief description of the repositories relevant to this work are below. It is written almost entirely in Python.

Cavity

This contains an implementation of ABCD matrices for ring resonators. It also contains simulations of how dispersion affects the fsEC intracavity spectrum and pulse duration. This code was used in Chapter 2.

crankyc

This contains a small library of functions to load data from various experimental equipment used in lab. It also contains simple functions for commonly used mathematical manipulations such as Allan deviations and FFTs.

HHG

Contains a numerical implementation of Corkum's three step model [24] and the quantum version of Lewenstein [86, 118]. It also contains an implementation of and ionization rate calculation using ADK theory. This code was used in Chapter 3.

HHG_Phasematching

A general HHG phasematching simulation in a single-pass geometry. It is based on the absorption-limited phase matching work of Constant [124] and can be applied to a wide variety of

experimental conditions. This code was used in Chapter 3.

HHG_phasematching_fsEC

A general HHG phasematching simulation in a single-pass geometry. It is based on the absorption-limited phase matching work of Constant [124] and can be applied to a wide variety of experimental conditions. This code attempts to include the effects of the fsEC.

Molecular_Alignment

A variety of numerical implementations of FFMA using various methods within the Python programming language. The code highlights methods to integrate C/C++ with Python for faster computation. This code was used in Chapter 6.

NLSE

A simple implementation of the normalized nonlinear Schrödinger equation to simulate nonlinear broadening of ultrashort pulses in optical fibers or materials. This code was used in Chapter 2.

XUV

A set of scripts to calculate mirror reflectivity in the XUV. This was used in Chapter 4

Appendix B

Publication list

Since I spent almost two years of my graduate career on the strontium lattice clock experiments, I have added my full list of publications which includes a handful of papers relevant to the strontium experiments in context of many-body physics, clock operation, frequency comb development, and laser stabilization.

Publications

[B.1] J. R. Jameson, D. Ngo, **C. Benko**, J. P. McVittie, Y. Nishi, and B. A.Young, "Dielectric relaxation study of hydrogen exposure as a source of two-level systems in Al_2O_3," Journal of Non-Crystalline Solids **357**, 2148–2151 (2011).

[B.2] C. P. Weber, **C. Benko**, and S. C. Hiew, "Measurement of spin diffusion in semi-insulating GaAs," Journal of Applied Physics **109**, 106101 (2011).

[B.3] A. Ruehl, M. J. Martin, K. C. Cossel, L. Chen, H. McKay, B. Thomas, **C. Benko**, L. Dong, J. M. Dudley, M. E. Fermann, I. Hartl, and J. Ye, "Ultrabroadband coherent supercontinuum frequency comb," Physical Review A **84**, 011806 (2011).

[B.4] M. Bishof, M. J. Martin, M. D. Swallows, **C. Benko**, Y. Lin, G. Quéméner, A. M. Rey, and J. Ye, "Inelastic collisions and density-dependent excitation suppression in a ^{87}Sr optical lattice clock," Physical Review A **84**, 052716 (2011).

[B.5] **C. Benko**, A. Ruehl, M. Martin, K. S. E. Eikema, M. E. Fermann, I. Hartl, and J. Ye, "Full phase stabilization of a Yb:fiber femtosecond frequency comb via high-bandwidth transducers," Optics Letters **37**, 2196–2198 (2012).

[B.6] A. Ruehl, **C. Benko**, M. J. Martin, K. S. E. Eikema, M. E. Fermann, I. Hartl, and J. Ye, "Phase stabilization of a Yb:fiber frequency comb via high-bandwidth transducers," in "CLEO: Science and Innovations," (Optical Society of America, 2012), pp. CTh1J–1.

[B.7] M. D. Swallows, M. J. Martin, M. Bishof, **C. Benko**, Y. Lin, S. Blatt, A. M. Rey, and J. Ye, "Operating a ^{87}Sr optical lattice clock with high precision and at high density," IEEE Transactions on Ultrasonics, Ferroelectrics and Frequency Control. **59**, 416–425 (2012).

[B.8] M. J. Martin, M. Bishof, M. D. Swallows, X. Zhang, **C. Benko**, J. von Stretcher, A. M. Rey, and J. Ye, "A quantum many-body spin system in an optical lattice clock," Science **341**, 632–636 (2013).

[B.9] T. K. Allison, A. Cingöz, **C. Benko**, D. C. Yost, A. Ruehl, M. Fermann, I. Hartl, and J. Ye, "High brightness XUV frequency combs via intracavity high harmonic generation," EPJ Web of Conferences **41**, 11006 (2013).

[B.10] A. M. Rey, A. V. Gorshkov, C. V. Kraus, M. J. Martin, M. Bishof, M. D. Swallows, X. Zhang, **C. Benko**, J. Ye, N. D. Lemke, and A. Ludlow, "Probing many-body interactions in an optical lattice clock," Annals of Physics **340**, 311–351 (2014).

[B.11] W. Zhang, M. J. Martin, **C. Benko**, J. L. Hall, J. Ye, C. Hagemann, T. Legero, U. Sterr, F. Riehle, G. D. Cole, and M. Aspelmeyer, "Reduction of residual amplitude modulation to 1×10^{-6} for frequency modulation and laser stabilization," Optics Letters **39**, 1980–1983 (2014).

[B.12] **C. Benko**, T. K. Allison, A. Cingöz, L. Hua, F. Labaye, D. C. Yost, and J. Ye, "Extreme ultraviolet radiation with coherence time greater than 1 s," Nature Photonics **8**, 530–536 (2014).

[B.13] **C. Benko**, L. Hua, T. K. Allison, F. Labaye, and J. Ye, "Cavity-enhanced field-free molecular alignment at a high repetition rate," Physical Review Letters **114**, 153001 (2015).

[B.14] **C. Benko**, N. Dörre, and J. Ye, "Power scaling extreme ultraviolet frequency combs to the mW level," in preparation. (2016).